

3
003

This is to certify that the

dissertation entitled

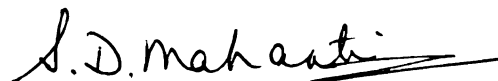
Studies of Current-Perpendicular-to Plane
(CPP) Magnetoresistance

presented by

Khalid Fatthi Eid

has been accepted towards fulfillment
of the requirements for

Ph.D. degree in Physics



J. Bass, Major professor
S.D. Mahanti, Associate
Chairperson for Graduate
Studies

Date 08/15/02

LIBRARY
Michigan State
University

PLACE IN RETURN BOX to remove this checkout from your record.
TO AVOID FINES return on or before date due.
MAY BE RECALLED with earlier due date if requested.

DATE DUE	DATE DUE	DATE DUE

**STUDIES OF CURRENT-PERPENDICULAR-TO-
PLANE (CPP) MAGNETORESISTANCE**

By

Khalid Fatthi Eid

A DISSERTATION

Submitted to

Michigan State University

in partial fulfillment of the requirements

for the degree of

DOCTOR OF PHILOSOPHY

Department of Physics and Astronomy

2002

ABSTRACT

STUDIES OF CURRENT-PERPENDICULAR-TO-PLANE (CPP)

MMAGNETORESISTANCE

By

Khalid Fatthi Eid

Scientificallly, measurements of Giant Magnetoresistance (GMR) in ferromagnetic/non-magnetic (F/N) metal multilayers with Current flow Perpendicular to the layer Planes (CPP-MR) are of interest because they can provide unique insights into the physical phenomena underlying GMR. Technologically, the CPP-MR is of growing interest because it may be able to provide the larger MRs needed for next generation devices. Most CPP-MR data have been reasonably well described by two simple models, the two-current series-resistor (2CSR) model, in which the only lengths are the thicknesses of the F- and N-metals, t_F and t_N , and the Valet-Fert extension to when spin-flipping occurs, where the characteristic lengths are the spin-flipping (or spin-diffusion) lengths l_{SF}^F and l_{SF}^N . This thesis consists of several experiments that test and/or use these models.

(1) Recently, new data were claimed to be evidence that there are additional length scales in the CPP-MR, the mean-free-paths for elastic scattering, λ_N and λ_F (actually two lengths in the F-metal). After reproducing the reported results, we extended them in three different ways to test the claimed interpretation. We conclude that the mean-free-paths are not responsible for the behavior of the data; rather we propose spin-memory-loss at the F/N interfaces as the primary explanation.

(2) The CPP-MR would be more competitive for devices if the total specific resistance, area times resistance, AR , the change in AR with magnetic field, ΔAR , or both can be increased. We investigated three potential ways to increase them: (a) by alloying the F metal layer with an impurity expected to produce a large change in resistivity without decreasing the anisotropic scattering that is fundamental to GMR, (b) by creating additional interfaces within individual ferromagnetic layers, and (c) by inserting a source of strong spin-flipping, in hopes of reducing the contribution of contact or lead resistances to ΔAR .

(3) Ruthenium (Ru) is now of great interest in GMR because Ru layer inserts as thin as 0.6 nm can 'pin' the magnetizations of thin Co layers anti-parallel to each other, forming an 'artificial anti-ferromagnet'. For CPP-MR use, it is necessary to know various properties of Ru and of Ru-based interfaces. We present a study of the CPP-MR properties of Ru and its interfaces with Co and Cu. The most important results for devices are that the resistivity of sputtered Ru is small enough and the spin-flipping distance (spin-diffusion length) is large enough so that they don't constitute problems for device use.

(4) We also use Ru to provide a sensitive new way to study spin-asymmetric scattering at some interfaces of interest.

(5) Lastly, there is now great interest, both for basic physics and for devices, in studying the CPP-MR and current-driven excitations in submicron-size multilayer pillars. We describe a method for producing such pillars by combining optical and electron beam lithographies, and present a few measurements on samples we have prepared this way.

COPYRIGHT
KHALID FATTHI EID
2002

إلى أبي و أمي و إخوتي

ACKNOWLEDGEMENTS

I would like to thank my thesis advisor Professor Jack Bass for his encouragement, criticism, and guidance. He always had the time to patiently discuss my thesis research with me and give advice. I also thank Professor William P. Pratt Jr. for useful discussions and insightful evaluation of research ideas, and Professor Norman Birge for encouragement and valuable discussions.

I would like to thank Professor Kamal Rashid from En-Najah University for helping me apply to the graduate school and encouraging me during my studies.

I also wish to thank Dr. Reza Loloee for teaching and helping me in the lab. Reza's friendship and support made the lab a pleasant place to do research.

I would also like to thank Dr. B. Bi and Dr. J. Caballero for teaching me many of the lithography skills and Dr. R. Slater and N. Verhanovitz for helping me with the equipment and the programming. I also thank the people I worked with in the labs: M. Darwish, A. Zambano, H. Kurt, M. Crosser and S. Urazhdin.

Finally, I would like to thank my friends in Lansing for friendship and for making my life in Michigan State a memorable experience. They include M. Hozain, M. Al Haj Darwish, A. Shinnaq, Dr. A. Ahmad, J. Siryani, Dr. K. Ghosheh, S. Armagan, Dr. N. Saglam, G. Mustafa, G. Al zoubi, S. Ahmad, 'M & M' Al khasawneh, A. Masadeh, A. Abdo, M. Shatnawi, S. Berber, M. Chatal, and M. Sayyaheen.

TABLE OF CONTENTS

List of Tables	ix
List of Figures	x
1 Introduction	1
1.1 Definitions and background	1
1.2 Basic ideas in GMR	4
1.3 GMR Device Applications	11
1.4 CPP-MR Theory & History Crucial to the Present Thesis	13
1.4.1 High Current-Density Effects in F/N Multilayers	21
1.5 The Present Thesis	23
2 Sample Preparation, Characterization, and Measurement	26
2.1 Introduction	26
2.2 Common Preparation Procedures	28
2.3 Characterizing Samples	30
2.4 Microscopic Samples	40
2.4.1 Preparation	41
2.4.2 Characterization	53
2.4.3 Measurement	54
3 Theoretical Background	55
3.1 Free-Electron-Based Semi-Classical Models	55
3.2 Real Fermi Surface Effects	66
3.3 High Current Density Effects on Magnetization	67
3.3.1 Spin-Transfer Switching	68
4 Search for Mean-Free-Path Effects in the CPP-MR	72
4.1 Introduction	72
4.2 $AR(H)$ from the initial state to first saturation	77
4.3 Magnetic Order	81
4.4 Magnetoresistance Tests of Mean-Free-Path Effects	93
4.5 Effect of Spin-Memory-Loss	100
4.6 Studies of CIP-MR in Co/Cu based multilayers and CPP_MR in Co/Ag Based Multilayers	110
4.7 Summary and Conclusion	113
5 Methods for Enhancing the CPP-MR	116
5.1 Introduction	116
5.2 Enhancing the CPP-MR by Alloying Co with Zr	117

5.2.1	Giant Magnetoresistance of CoZr/Cu systems	120
5.2.2	Dusting CoZr/Cu Interface with Co	130
5.2.3	GMR in CoZr/Ag	133
5.2.4	Effect of FeMn growth on MR	136
5.2.5	Search for Magnetically dead layers	140
5.2.6	Co ₉₅ Zr ₅ and Co ₈₀ Zr ₂₀	143
5.3	Internal Interfaces	147
5.3.1	Data and analysis	151
5.3.2	Incomplete Interfaces versus Interfacial Spin Memory Loss	156
5.4	Spin-Memory-Loss to enhance GMR	166
5.4.1	Data and Analysis	167
5.4.2	Fitting Data to the 2CSR Model	172
6	CPP-MR studies with Ruthenium (Ru)	177
6.1	Ru for CPP-MR	178
6.1.1	CPP-MR of Co/Ru	181
6.2	Studies of Spin-Asymmetries at Interfaces using Ru.	192
7	GMR in Multilayers with Submicron Area	204
8	Summary and Conclusions	209
	Appendix	211
	Bibliography	217

LIST OF TABLES

2.1	VdP resistivity and superconducting transition temperature of sputtered Nb. $T_C(\text{Nb})$ bulk ≈ 9.2 K.	34
2.2	VdP Resistivity of CuGe Films.	35
2.3	Van der Pauw Resistivities of Co, Py, Cu and Ag films. Last Column shows if each sample was sputtered at the beginning or end of each sputtering run.	35
2.4	Van der Pauw Resistivity of CoZr films.	36
2.5	Average resistivities (in $\mu\Omega\text{cm}$) both at 4.2 K and room temperature.	37
2.6	Ion-Milling rates of materials used in the lab.	50
5.1	CoZr parameters found from the fits to our data.	126
5.2	The Composition of the samples used to study the effect of incomplete interfaces and separated-like effect (due to the internal interfaces).	159

LIST OF FIGURES

1.1.	Cartoon of the s- and d- subbands of a ferromagnetic metal and a normal metal. There is a net magnetic moment in the ferromagnet but not the normal metal.	9
1.2.	Schematic diagram of scattering in the ‘up’ and ‘down’ channels when the magnetizations of the ferromagnetic layers are (A) antiparallel or (B) parallel to each other. The star indicates stronger scattering. Scattering is only shown in bulk F.	10
1.3.	$AR(H)$ for (A) an EBSV, and (B) a hybrid spin valve. $AR(H)$ for the hybrid SV is symmetric around $H = 0$, while that for the EBSV is not. Numbers indicate layer thicknesses in nm.	11
1.4.	Square root test of the 2CSR model. Adding Ge impurities that greatly reduce the value of λ in Cu does not affect the applicability of the model. (From [68]).	19
1.5.	Testing the 2CSR and VF models. Adding Sn to Ag reduces the mean-free-path without greatly reducing the spin-diffusion-length. The Co/Ag and Co/AgSn data fall on the 2CSR model prediction of a single straight line going through the origin. Adding Pt or Mn, in contrast, reduces the spin-diffusion length, and causes the data to fall below the 2CSR model line (see text). (From [68]).	20
1.6.	$A\Delta R$ vs. t_{Py} for $Py(t_{Py})/Cu(20nm)/Py(t_{Py})$ EBSVs. Filled circles are the data, along with the 2CSR (dashed line) and the VF (solid line) model with $l_{SF}^{Py} = 5.5$ nm. From [74].	21
1.7.	$AR(H)$ for an interleaved sample (A) and a separated sample (B). Samples were already taken to saturation in the $-H$ direction. There are differences both in shape and size of the change in AR with H .	24
2.1.	(A) A CPP mask. A screw through the middle circular hole holds the mask in place, but allows it to be rotated. The three openings are used to sputter the bottom Nb (1), the multilayer (2), and the top Nb (3). The blocking position protects the sample before and after sputtering. (B) A finished sample with Indium blobs on the Nb strips.	30
2.2.	EDX spectrum of a CuGe film. The table on the bottom shows the detailed analysis of the spectrum.	31

2.3.	EDX spectrum of a CoZr film, with a small concentration of Zr. The analysis on the bottom of the plot shows 2.5% Zr.	32
2.4.	EDX spectrum of a CoZr film. The percentage of Zr given by the analysis is 19%, which is expected to be well in the amorphous regime.	33
2.5.	AR of two different thicknesses of CoZr in Nb/CoZr/Nb sandwiches. Any dependence of AR on magnetic field H is small.	38
2.6.	Dependence of AR on t_{CoZr} . Samples both with and without Cu are used in the straight line fit. The fit gives $AR_{\text{CoZr/Nb}} = 5.8 \pm 1 \text{ f}\Omega\text{m}^2$ and $\rho_{\text{CoZr}} = (19 \pm 1 \text{ }\mu\Omega\text{cm})$.	39
2.7.	AR versus t_{Co} for Nb/Co(t_{Co})/Nb sandwiches. Data are shown for two different sputtering runs. The two straight lines are best fits, giving an average value of $2AR_{\text{Nb/Co}} = 6.5 \pm 1 \text{ f}\Omega\text{m}^2$, and $\rho_{\text{Co}} = 3.9 \pm 0.7 \text{ }\mu\Omega\text{cm}$.	39
2.8.	Au electrodes deposited on a 0.5"x0.5" Si substrate using photolithography. The outside pads are large so that measuring electrodes can be connected to them. The small samples will be deposited in the middle of those electrodes. All the Au pads are connected to avoid shocking the sample; these connections are removed when the sample is ready to be measured. The crosses are alignment marks for subsequent steps.	42
2.9.	(A) Schematic diagram of the double exposure to the electron beam. After baking the first layer, all the area enclosed by the dotted line is exposed to electrons. The area enclosed by the solid line is then exposed to electrons after spinning and baking the second electron-beam-resist layer. After developing, the part of the second layer between the dotted line and the solid line will be 'free hanging', creating an undercut. (B) shows what the substrate should look like after developing. The shaded area is the undercut.	44
2.10.	Photomicroscope picture showing the undercut (discoloration of the top layer) of Fig. 2.9B. The electron-beam resist is washed out completely from the center area where the multilayer will be sputtered.	45
2.11.	SEM images of the Al/Ti/Cu masks. Masks were dipped in PR developer for 5 seconds. Ideally the mask should look like the mushroom shape shown in Fig. 2.12. In A and B the substrate was tilted by 30° . In C there is no tilt.	47

- 2.12. Cartoon of the ideal shape of the Al/Ti mask after the short wet etching in PR developer. Ideally the mask would look a mushroom to protect the Al part from SiO to be able to dissolve the mask after the ion milling and SiO evaporation. 48
- 2.13. Ion milling thickness as a function of ion milling time. The slope gives the ion-milling rate in nm/min. The intercept with the horizontal axis indicates the existence of an oxide layer that ion mills slowly on the Cu surface. The ion milling rate of Cu is (26 ± 1) nm/min. 50
- 2.14. Picture of a sample after the ion milling of the multilayer (the line in the middle) and depositing the SiO insulating layer. SiO is the dark rectangular window in the middle. There are four crosses on the corners of the picture (inside the dark squares) that serve as alignment marks during the electron beam exposure. These alignment marks are covered by SiO, which makes them less visible. 51
- 2.15. A finished device ready to be measured. Each of the top contacts (5 Ag slabs) connects one of the top Au fingers with one from the bottom and, hopefully, has electrical contact with the top layer of the pillar in the middle. The pillars appear as dark spots in the middle of the overlap between the top contact and the multilayer. 53
- 3.1. Cartoon of an $[F1/N/F2/N]_N$ multilayer sandwiched between two superconducting layers, the arrows indicate the magnetization directions of the magnetic layers, showing an AP alignment. 57
- 3.2. 2CSR model representation of the multilayers when $l_{SF}^F \ll t_F$. The two spin channels mix completely in the middle of each ferromagnetic layer then split at around l_{SF}^F from the F/N interface. So the two spin channels are no longer independent. 64
- 4.1. $AR(H)$ vs H at 4.2K for interleaved (top of each pair) and separated (bottom of each pair) multilayers of Co/Cu with $N=4, 6$, and 8 . The unit scales for each coupled pair are identical. The open squares and dashed curves show how $AR(H)$ varied when first taken from the as-prepared state to the saturated state. The filled circles and solid curves show how it varied after having been taken to saturation. 78
- 4.2. $AR(H)$ vs. H curves for interleaved (top) and separated (bottom) samples. Both samples on the left have the thinner Co layer with $t_{Co}=1$ nm sputtered before the layer with $t_{Co}=6$ nm. The two samples on the right have the opposite order. 79

4.3.	Schematic, approximate pictures of inferred magnetic ordering for interleaved and separated samples in their ‘as-prepared’ state and after they have been taken to saturation and then the field reversed only enough to flip the thicker Co layers.	81
4.4.	M vs H at 12K for interleaved (x) and separated (+) samples with Cu and CuGe with $N = 8$ for $t_{\text{Cu}} = t_{\text{CuGe}} = 20$ nm. P and AP states are indicated.	84
4.5.	M vs H at 12K for center-cut pieces of Cu interleaved (top) and separated (lower) samples including both data from the as-prepared state to saturation and then from positive saturation to negative saturation and back again.	85
4.6.	Specular neutron reflectivity data and fits plotted as a function of the wavevector Q_z of an interleaved sample $[\text{Co}(6)/\text{Cu}(20)/\text{Co}(1)/\text{Cu}(20)]_8$ at 18 K in a 250 G field. Only the R^{--} (dark squares) and R^{++} (open circles) reflectivities are shown. (The SF reflectivities are effectively at the background level). The magnetization profile for the Co layers that is shown in the bottom graph was obtained from the fit. The apparent differences in moments in the thin and thick layers are artifacts (see text).	89
4.7.	Specular neutron reflectivity data and fits plotted as a function of the wavevector Q_z of a separated sample $[\text{Co}(6)/\text{Cu}(20)]_8[\text{Co}(1)/\text{Cu}(20)]_8$ at 18 K in a 250 G field. Only the R^{--} (dark squares) and R^{++} (open circles) reflectivities are shown. (The SF reflectivities are effectively at the background level). The magnetization profile for the Co layers that is shown in the bottom graph was obtained from the fit. The apparent differences in moments in the thin and thick layers are artifacts (see text).	90
4.8.	Specular and diffuse reflectivity data for the separated sample $[\text{Co}(6)/\text{Cu}(20)]_8[\text{Co}(1)/\text{Cu}(20)]_8$ at 18 K in the as-prepared state. The data were taken in a 3 G guide field. The R^{--} (dark squares), R^{++} (open squares), R^{+-} (dark circles), and R^{-+} (open circles) reflectivities are all shown. The diffuse data have not been corrected for polarization efficiencies. The dotted lines mark the superlattice peaks in the diffuse data.	92
4.9.	AR of interleaved and separated samples identical to samples in Fig. 4.1 except that CuGe replaces Cu. Symbols and curves have the same meaning as in Fig. 4.1.	94
4.10.	Effect of further increasing CuGe thickness on AR of interleaved and separated samples. The convention for symbols is the same as in the previous figures.	95

- 4.11. AR vs H for Cu, CuGe with $t_{\text{CuGe}} = 10, 20, 30, \text{ and } 40$ nm. The number of repeats is 3 for all samples. The specific resistance AR_{p} increases with CuGe thickness, and $A\Delta R$ decreases, but the difference between separated and interleaved samples persists. Data shown are after samples were taken to saturation. 96
- 4.12. AR vs H for multilayers with short λ/l in all layers. The difference between separated and interleaved samples has grown, disagreeing with mean-free-path effects. 98
- 4.13. AR vs H curves. All samples are of the separated type. The bottom two have a 1 nm FeMn layer in the middle of the Cu layer that separates the Co(6) layers from the Co(1). Strong spin-flipping by FeMn decouples the two sides of the multilayers giving two separate peaks on each side of $H = 0$. 99
- 4.14. $(A\Delta R)_{\text{sep}}/(A\Delta R)_{\text{int}}$ vs N . The dotted and long-dashed curves are predictions using VF theory with the parameters for Co/Cu of [25] plus $l_{\text{SF}}^{\text{Co}} = 60$ nm, $l_{\text{SF}}^{\text{Cu}} = 500$ nm, and $l_{\text{SF}}^{\text{CuGe}} = 130$ nm. The vertical bars indicate the ranges of uncertainties due to uncertainties in these values of l_{SF} . The short-dashed curve for Co/Cu and the solid curve for Cu/CuGe add $\delta_l = 0.25$ to the prior calculations. Now the error bars indicate the ranges of predictions for $\delta_l = 0.25 \pm 0.1$. For these curves, the error bars due to uncertainties in l_{SF} are smaller than the symbols for the data. $(A\Delta R)_{\text{sep}}/(A\Delta R)_{\text{int}}$ should be equal to 1 for all N , according to the 2CSR model. The uncertainties in the data are comparable to the symbol sizes. 101
- 4.15. Calculated values of $A\Delta R$ vs δ_l for interleaved and separated multilayers with $N = 6$. The solid curves include the Co/Nb contacts; the dashed curves are the same calculations but without those contacts. The filled circles correspond to Eq. 4.1 with $n = 5$ for the interleaved case and $n = 1$ for the separated one. 105
- 4.16. Calculated values of AR_{AP} (left scale) and $\sqrt{AR_{\text{AP}} \cdot A\Delta R}$ (right scale) for multilayers with total thickness = 360 nm and either fixed $t_{\text{Co}} = 6$ nm or $t_{\text{Co}} = t_{\text{Cu}}$. Filled circles are for the 2CSR model. Solid curves are VF calculations with $l_{\text{SF}}^{\text{Cu}} = 500$ nm, $l_{\text{SF}}^{\text{Co}} = 60$ nm, and $\delta_l = 0.25$. 107
- 4.17. $A\Delta R$ vs t_{Co} for symmetric (filled triangles) and asymmetric (open circles) Co/Cu exchange-biased spin-valves. The dashed curves are prior fits [25] assuming no spin-memory-loss at the Co/Cu interfaces. The solid curves just add an interfacial spin-memory-loss of $\delta_l = 0.25$. 110

- 4.18. Comparison of CPP-MR and CIP-MR for separated and interleaved Co/Cu multilayers. Symbols and curves have the same meanings as in Fig. 4.1. The open squares for the separated CPP-MR were noisy, as shown by the fluctuations in the points for $H = 200\text{-}500$ Oe. To reduce uncertainty at $H \approx 0$, that square is the average of six very low field measurements. All other points are single measurements. 111
- 4.19. $AR(H)$ vs H at 4.2K for interleaved (top) and separated (bottom) multilayers of Co/Ag with $N = 8$. The scale units for each coupled pair are identical. The open squares and dashed curves are for the initial state and the filled circles and solid lines are after samples were taken to saturation. 112
- 5.1. Predicted $A\Delta R$ of CoZr/Cu symmetric EBSVs using parameters given in the text and assuming infinite spin-diffusion-length, l_{SF}^{CoZr} , (solid line) or $l_{SF}^{CoZr} = 8$ nm (dotted line). The predictions are compared to data for Co/Cu and CoFe/Cu EBSVs. 119
- 5.2. AR_{AP} for CoFe and Co EBSVs as functions of layer thickness along with the predicted AR_P for CoZr using the parameters given in the text. 119
- 5.3. AR_{AP} vs t for CoZr/Cu EBSV data, compared with ‘best fit lines’ for CoFe/Cu EBSVs (broken curve), Co/Cu EBSVs (dotted curve), and the 2CSR model for CoZr/Cu described in the text above. 124
- 5.4. $A\Delta R$ vs t for Co, CoFe, and CoZr symmetric EBSVs. This figure is a replot of Fig. 5.1 with the addition of our CoZr symmetric EBSV data. 125
- 5.5. $A\Delta R$ vs t_{CoZr} for symmetric EBSVs. The dotted curve is a best fit to just the three EBSV data sets for $A\Delta R$. The solid curve is the best ‘common fit’ to all of the samples, exchange biased and hybrid. 127
- 5.6. Using the parameters from the fits to $A\Delta R$ fits the data for AR_{AP} quite well. The dashed curve is the 2CSR model fit described in the text above. The best fits are closer to the data than the 2CSR model prediction. 127
- 5.7. AR vs H for symmetric EBSVs with $t_{CoZr} = 8$ nm (A) and 25 nm (B). In both cases, the hysteresis curves are nicely square, indicating well-formed AP states. 128
- 5.8. $A\Delta R$ vs t_{CoZr} for EBSVs. (A) Symmetric EBSVs; (B) Asymmetric EBSVs with $t_{Py} = 24$ nm; (C) Asymmetric EBSVs with $t_{Py} = 6$ nm. The dashed curves represent a fit to just these three sets of data. The solid curves represent a ‘common fit’ to all of the exchange biased and hybrid samples with CoZr/Cu. In C, the two fits fall on top of each other. 129

- 5.9. $A\Delta R$ vs t_{CoZr} for hybrid SVs with $t_{\text{Py}} = 24$ nm (A) or 6 nm (B). The dashed curves represent a fit to just these two sets of data. The solid curves represent a 'common fit' to all of the CoZr/Cu data in Figs. 5.8 and 5.9. 130
- 5.10. Co dusting of CoZr/Cu symmetric EBSVs. Sputtering a 1 nm thick layer of Co at each CoZr/Cu interface does not increase $A\Delta R$. 132
- 5.11. Comparing $A\Delta R$ for dusting CoZr/Cu interfaces by Co, dusting Co/Cu interfaces by CoZr, and no dusting. There is a systematic reduction in $A\Delta R$ with the order of preparing the sample (indicated by numbers) in the sputtering run. Dusting a Co/Cu interface with CoZr reduces $A\Delta R$, and dusting a CoZr/Cu interface with Co increases it. 132
- 5.12. $AR(H)$ curves for EBSVs with Cu spacer layers (A), and Ag spacerlayers (B and C). The pinning is strongest for the Cu sample A and the total specific resistance, AR_{p} , is lowest. Pinning the Ag sample at a higher temperature (C) gave a slightly better result than at the usual pinning temperature (B). 134
- 5.13. $A\Delta R$ of CoZr/Ag based symmetric EBSVs and a comparison with Cu. Ag gives larger $A\Delta R$ values, especially at small thicknesses, indicating the CoZr/Ag interface gives a larger contribution to MR than the CoZr/Cu interface. 135
- 5.14. $A\Delta R$ vs t_{CoZr} in CoZr/Ag/Py hybrid samples. The fit uses the same parameters as in Fig.5.13 plus $\gamma = 0.8$ for the CoZr/Py interface. As in the Cu-based samples the fit is below data, requiring a slightly larger value of γ . 136
- 5.15. $A\Delta R$ vs t_{CoZr} in symmetric EBSVs. Changing the metal on which FeMn is grown affects $A\Delta R$. Growing FeMn on Ag gives the highest $A\Delta R$. 138
- 5.16. Effect of FeMn growth on AR_{AP} . Growing FeMn on Ag gives a significantly higher AR_{AP} than when growing it on Cu or CoZr. The V-F model predicts only a slight increase in AR_{AP} for the Ag samples over the Cu samples. The fits for Ag and Cu are on top of each other. 139
- 5.17. AR_{AP} vs t_{CoZr} . As predicted by the 2CSR model, AR_{AP} grows linearly with t_{CoZr} . The slope is the same for Ag and Cu samples, showing that CoZr has the same resistivity in both. But the intercepts are different, pointing to the FeMn as the source of the larger AR_{AP} for Ag. 139
- 5.18. Hysteresis loops of $[\text{CoZr}(t)/\text{Cu}]_N$ multilayers with fixed total CoZr thickness, $t_{\text{T}} = 480$ Å. The saturation magnetization is almost the same for all samples, regardless of the individual CoZr layer thicknesses. Any magnetically dead CoZr layer at the CoZr/Cu interface must be thin. 141

5.19.	μ/N vs t_{CoZr} thickness for CoZr/Cu multilayers. The ordinate intercept gives the thickness of any dead layer.	142
5.20.	μ/N versus CoZr layer thickness for CoZr/Ag multilayers. The ordinate intercept indicates little or no magnetically dead layer at the CoZr/Ag interface	142
5.21.	$AR(H)$ versus H , for $[\text{Co}_x\text{Zr}_{100-x}(5)/\text{Cu}(20)/\text{Py}(6)/\text{Cu}(20)]_{10}/\text{Py}(6)$. x is 97.5 in A and 95 in B. Vertical and horizontal scales are the same for direct visual comparison.	144
5.22.	$A\Delta R$ vs t_{CoZr} . Different fits are shown: $l_{\text{SF}} = \text{infinity}$ or 2 nm, $\beta = 0.5$ or 0.03, $\gamma = 0.77$, and $AR_{\text{CoZr/Cu}}^* = 0.51$.	145
5.23.	$A\Delta R$ vs t_{CoZr} for CoZr(t)/Cu(20)/Py(6) EBSVs.	145
5.24.	AR vs H for a CoZr/Cu symmetric EBSV. The amorphous CoZr does not give a noticeable $A\Delta R$ within the fluctuations of the data.	146
5.25	Predicted change in $A\Delta R$ (A) and AR_p (B) and $\Delta R/R_p$ (C) with number of inserted internal Co/Cu interfaces.	150
5.26.	$AR(H)$ curves for samples (A) with 4 internal interfaces and (B) without. To allow direct comparison, both the vertical and horizontal scales are the same for both samples. Introducing the interfaces increases AR , $A\Delta R$, and the H_s for the Co.	152
5.27.	Increase of AR_p with M in $[\text{Py}(6)/\text{Cu}(5)/(\text{Co}(t/n)/\text{Cu}(0.5))_n/\text{Cu}(4.5)]_3$ multilayers versus prediction (solid curve).	153
5.28.	$A\Delta R$ vs M . compared with 2CSR prediction. Data shows a significant increase in $A\Delta R$ at $M = 4$, then $A\Delta R$ levels off faster than predicted.	154
5.29.	Effect of the thin Cu spacer layer thickness on $A\Delta R$. When Cu layer thickness is 0.4 nm (filled boxes) $A\Delta R$ is smaller than when Cu thickness is 5 nm (filled circles). The one sample with $t_{\text{Cu}} = 0.6$ nm (filled triangle) is slightly higher than the 0.5 nm.	155
5.30.	$AR(H)$ curves for (A) Interleaved, (B) Separated and (C) Regular samples. Regular means samples without any internal interfaces. The reduction in $A\Delta R$ due to the difference in ordering of the layers between A and B was already seen in Ch. 4. Note that samples A and B also have larger AR s than sample C.	160

- 5.31. AR vs H for samples identical to the sample in Fig. 5.30 except for the Cu thicknesses. In A the Cu layer between neighboring Co layers is 0.5nm and the rest are 20nm. In B the Cu layer between neighboring Py layers is 0.5 nm and the rest are 20 nm. In C the Cu layer between neighboring Co or neighboring Py layers is 0.5 nm and the Cu layer between Co and Py is 5 nm. 161
- 5.32. $R(H)$ for an Ag based multilayer. Using a 4 nm thick Ag spacer layer is not enough to decouple Py and Co layers and an AP state is not achieved in this sample, giving sharp instead of rounded or flat peaks. 163
- 5.33. Effect of internal interfaces on $AR(H)$ curves for samples with Ag spacer layers. Introducing eight internal interfaces(part A) increases $A\Delta R$ and AR_P . 164
- 5.34. Dependence of AR_P on the total number of internal interfaces M . solid boxes are for data and solid line is the 2CSR model prediction. The data agree with prediction within the fluctuations. 165
- 5.35. $A\Delta R$ dependence on the number of internal interfaces in Co/Ag based multilayer. 165
- 5.36. Cartoon of the multilayer (with $N = 1$) with FeMn layers to enhance GMR. A single FeMn layer is inserted in the middle of the Cu layer next to Nb on each side of the multilayer. The Cu layers in direct contact with Nb are assumed to become superconducting by the proximity effect. 167
- 5.37. $A\Delta R(N)$ in $[Co(6)/Cu(20)/Co(1)/Cu(20)]_N$ multilayers. The filled circles are data points and the solid line is a no-adjustable-parameters prediction of the 2CSR model. There is a good agreement between the two, especially at small N . 168
- 5.38. Comparison of 2CSR model prediction of $AR_P(N)$ with data for $[Co(6)/Cu(20)/Co(1)/Cu(20)]_N$ multilayers. The data falls below the predictions, which may be because the Co/Cu interfaces are not fully established in the 1 nm Co layers. 168
- 5.39. $A\Delta R$ vs N for multilayers with (filled boxes) or without (filled circles) FeMn. Structure is $[Cu(10)/FeMn(1)/Cu(10)/[Co(6)/Cu(20)/Co(1)/Cu(20)]_N/FeMn(1)/Cu(5)$. The 'regular' samples are identical, just without the FeMn layers. $A\Delta R$ increases by $\sim 90\%$ for $N = 2$ to $\sim 9\%$ for $N = 4$. 169
- 5.40. AR_P vs N . Effect of the FeMn layers on the total specific resistance, AR_P . Boxes and circles have the same meaning as in the previous figure. 170

- 5.41. $\Delta R/R$ vs N with (circles) and without (squares) FeMn inserts. Since both $A\Delta R$ and AR_P increase with introducing the FeMn layers, the magnetoresistance, $\Delta R/R$, changes only slightly. 171
- 5.42. $A\Delta R$ versus N . Data (filled boxes) for samples with FeMn thin layers, 2CSR model predictions for the case without FeMn (solid curve), assuming that FeMn just removes $2AR_{S/F}$ (dashed curve), and assuming that FeMn removes $2AR_{S/F}$ and turns on asymmetry at the outer two Co/Cu interfaces (dotted curve). 173
- 5.43. Effect of t_{FeMn} on AR_P (top) and $A\Delta R$ (bottom) for Nb/Cu(10)/FeMn(t)/Cu(10)/[Co(6)/Cu(20)/Co(1)/Cu(20)]₂/FeMn(t)/Cu(10)/Nb samples. Increasing t_{FeMn} beyond 1 nm essentially does not change AR_P and reduces $A\Delta R$ slightly. 174
- 5.44. AR_P (top) and $A\Delta R$ (bottom) vs N for FeMn inserts with (triangles) or without (squares) additional thin Co layers outside of the FeMn layers. Adding the Co layer gives no gain in $A\Delta R$, but increases AR_P . 175
- 5.45. Effect of the position of FeMn on (A) AR_P and (B) $A\Delta R$. Growing the FeMn on the top of the multilayer gives a larger $A\Delta R$ and a slightly smaller AR_P than when FeMn is grown before the multilayer. 176
- 6.1. Spin-memory-loss detector. In the experiments to be described, X is either a single layer of Ru or a Cu/Ru multilayer. 178
- 6.2. $A\Delta R$ on a log scale vs t_{Ru} . The steep drop at small t_{Ru} is due to the formation of two Cu/Ru interfaces. After the two interfaces are established, $A\Delta R$ drops exponentially with t_{Ru} , and the slope of the straight line on this semi-log graph is the inverse of the spin-diffusion-length in Ru $l_{SF}^{Ru} = (14 \pm 1)$ nm. 180
- 6.3. AR_{AP} vs N for a Py-based with EBSV with an [Cu/Ru]_N insert. The slope of the best fit line gives $2AR_{Cu/Ru} = 2.0 \pm 0.2$ f Ωm^2 . 180
- 6.4. $A\Delta R$ on a log scale vs the number of [Ru(3)/Cu(5)] bilayer inserts. This straight line fit (on the log scale) of the data gives a spin-flip probability of electrons at the Cu/Ru interface $\sim 35\%$ per interface. 181
- 6.5. AR vs H curve showing an inverse CPP-MR, i.e., $AR_{AP} < AR_P$. The small $A\Delta R$ compared to noise, and the background change with H , make it hard to quantify the data. 181
- 6.6. $AR(H)$ for the hybrid sample [Py(6)/Cu(20)/Ru(2)/Co(1.5)/Ru(2)/Cu(20)]₆ showing inverse CPP-MR. 184

6.7.	CIP R(H) loop for the sample of Fig. 6.6. The CIP-MR is also inverse.	185
6.8.	Progression of $AR(H)$ curve with increasing Co layer thickness. MR is inverse for small thicknesses of Co and switches to normal for large Co thickness.	186
6.9.	$A\Delta R$ vs t_{Co} . The data follow a nearly straight line, allowing an estimate of $\chi_{Co/Ru} = (-0.15 \pm 0.05)$. Arrows in the plot indicate that those data points involve only a lower bound on the AP state.	187
6.10.	$AR(H)$ of a $[Co/Ru]_{20}$ multilayer. The antiferromagnetic coupling is too strong to be overcome even at our highest applied field of about 8 kG.	188
6.11.	Average $AR(H)$ for a $[Co(3)/Ru(1.6)]_{10}/Co(3)$ multilayer vs H. Each point is repeated 100 times and averaged to get reliable results.	189
6.12.	AR_{AP} vs N . Analysis of the slope of the straight-line fit gives $2AR_{Co/Ru} = (1.2 \pm 0.23) \text{ f}\Omega\text{m}^2$, and analysis of the intercept gives $2AR_{Co/Nb} = (7.3 \pm 2.3) \text{ f}\Omega\text{m}^2$ (see text).	190
6.13.	2CSR Model predicted $A\Delta R$ as a function of t_{Co} for a $Co(t)/Ru(10)/Co(t)$ EBSV. $A\Delta R(t)$ is non-monotonic due to the competition between the contributions from the Co/Ru interfaces and bulk Co.	191
6.14.	$AR(H)$ for $Co(15)/Ru(10)/Co(15)$. Fields were chosen based on the $AR(H)$ curves of $Co(15)/Cu(20)/Co(15)$ EBSVs. $A\Delta R$ is much less than predicted in Fig. 6.13.	192
6.15.	Drawing of the “spin-asymmetry-scattering detector” used to study Co/X interfacial $\chi_{Co/X}$. If $\chi_{Co/X} = 0$, then $A\Delta R$ is also zero. Even small values of $\chi_{Co/X}$ will give nonzero MR, making the detector quite sensitive.	195
6.16.	Reference sample: $A\Delta R \approx 0.4 \text{ f}\Omega\text{cm}$, is non-zero when there is no Ru in contact with the Co.	196
6.17.	$AR(H)$ curve. $A\Delta R$ is very small in the curve. Solid boxes are taken for the AP state and solid circle are for the P state.	197
6.18.	$AR(H)$ for samples with $X = FeMn(2, 5)$. The values of $A\Delta R$ are very close to zero in this case, just as in Fig. 6.17.	198
6.19.	AR for samples with $X = Cu(10)/FeMn(1)/Cu(10)$. $A\Delta R$ is now a non-zero positive value, which indicates that the Co/Cu interface is now contributing to GMR.	199

6.20.	<i>AR</i> for samples with $X = \text{Cu}(10)/\text{FeMn}(2)/\text{Cu}(2)/\text{Co}(2)/\text{Cu}(3)$. The $A\Delta R$ values are almost identical to the ones without the Co layer.	200
6.21.	<i>AR</i> for samples with $X = \text{Ru}(2)/\text{Cu}(20)$. Putting the Ru next to Co gives a negative $A\Delta R$ indicating that the outer Co/Ru interface is active and contributes to GMR.	202
6.22.	<i>AR</i> for samples with $X = \text{Ru}(1 \text{ or } 2)/\text{Cu}(5 \text{ or } 10)/\text{FeMn}(2)/\text{Cu}(10 \text{ or } 15)$. Adding the FeMn layer changes $A\Delta R$ very slightly from its value without FeMn.	203
7.1.	<i>R</i> vs <i>H</i> at room temperature. The sharp drop on the outer side of the two peaks indicates a single-domain magnetization in the lithographed Co layer.	205
7.2.	<i>R</i> vs <i>H</i> of the same sample in Fig. 7.1 taken at 4.2 K. The <i>R</i> (<i>H</i>) curve is asymmetric now probably due to the formation of an antiferromagnetic CoO layer on one or both Co layers. Arrows indicate the direction of changing <i>H</i> .	206
7.3.	<i>R</i> vs <i>I</i> curve at 4.2 K of the same sample of Figs. 7.1 and 7.2. There is an overall drop of resistance with current. The two hysteretic loops between ± 10 and ± 20 mA are probably due to current-driven switching of the magnetization. Open boxes and filled circles are for two sweeps of current.	207
7.4.	<i>R</i> vs <i>H</i> at room temperature. Relatively flat peaks indicate a good AP alignment. The change in resistance is higher than in Fig. 7.4, and the drop in the resistance after the AP peak is sharp indicating single domain switching of the magnetization.	208
A.1.	<i>AR</i> vs <i>H</i> for CoZr/Cu/Py asymmetric EBSVs. A good AP state is produced in samples with thin CoZr, while the samples with thicker CoZr show a poorer AP alignment. This behavior is common for both $t_{\text{Py}} = 6$ or 24 nm. Horizontal scale is the same for all samples to allow direct comparison of the switching fields.	212
A.2.	<i>AR</i> vs <i>H</i> for CoZr/Cu/Py hybrid spin valves. Curves are sharper for samples with thicker CoZr layers indicating the lack of a good AP alignment.	213
A.3.	<i>AR</i> vs <i>H</i> for CoZr/Ag/Py hybrid spin valves. The AP alignment gets quite uncertain as the CoZr layers become thicker, as seen from the bottom part.	214
A.4.	<i>AR</i> vs <i>H</i> for CoZr/Ag symmetric EBSVs. Unlike in the asymmetric and the hybrid spin valves that contain Py, the AP alignment seems good for both thin and thick CoZr in the symmetric EBSVs. Pinning is poorer than the Cu-based EBSVs (see Figs. 5.7 and 5.12).	215

- A.5. AR_{AP} vs t_{CoZr} for $[Py(t_{Py})/Cu(20)/CoZr(t)/Cu(20)]_{10}/Py(24)$ hybrid multilayers with $t_{Py} = 6\text{nm}$ (top) or 24 nm (bottom). The figure shows data, best common fit to all ARs of CoZr samples (solid line), and best fit to ARs of the hybrid samples alone (dotted line). The offset is most likely because the resistivity of Py is less than the value used in the fits.

216

Chapter 1

INTRODUCTION

1.1. DEFINITIONS AND BACKGROUND

Magnetoresistance, MR, is the fractional change in resistance of a sample upon the application of a magnetic field. For the samples studied in this thesis, it is now traditional to define its magnitude as the difference between the sample resistance, $R(H)$, at magnetic field H and at the saturation field, H_s , $R(H_s)$, divided by $R(H_s)$:

$$MR(H) = [R(H) - R(H_s)]/R(H_s).$$

H_s is the field above which $R(H)$ becomes constant (independent of H).

When the sample is a ferromagnetic/normal metal, F/N, multilayer this MR is called Giant magnetoresistance, GMR [1-6], because one of the original experiments on F/N multilayers in 1988 [1] gave a room temperature MR $\sim 50\%$ ($\sim 100\%$ at 4.2K). This MR is much larger than the MRs of both non-magnetic and magnetic metals at room temperature; for example, the 2% MR of the magnetic alloy Permalloy ($Ni_{1-x}Fe_x$ with $x \sim 0.8$) [7] is large enough that Py thin films were used as the read-head sensors in computers until they were recently replaced by GMR multilayers [8,9]. The MR of a simple film made of a ferromagnet like Py is called anisotropic MR (AMR), because the resistance is different for current flow parallel or perpendicular to the direction of the applied magnetic field. AMR is also present in GMR multilayers, but is usually small compared to the GMR. However, GMR is now used as a universal descriptor of the MR

of magnetic multilayers, even though in some cases the GMR can be less than the AMR [3]

In the original GMR experiments [1,2], the direction of current flow was in the plane of the layers of the multilayer (i.e. parallel to the F/N interfaces). This sense of current flow is called Current-in-Plane (CIP) and gives rise to CIP-MR. Current can also flow perpendicular to the plane of the layers giving Current Perpendicular to Plane (CPP)-MR.

The discovery of GMR stimulated great interest not only to understand the physics underlying GMR, but also to exploit it technologically and to use it as a sensor for probing other phenomena. GMR has been used as a sensor to study the coupling between ferromagnetic layers when separated by nonmagnetic spacer layers [10-14] and, more recently, generation of magnons and magnetization switching by high intensity polarized direct electric current [15-21]. The discovery of GMR accelerated the emergence of a new technology called spintronics [22-24], in which the spin-dependent properties of electrons are crucial for devices, and that has potential to replace much of the traditional silicon-based electronics technology based only upon the electron's charge.

The earliest experiments on GMR, and all of the device applications so far, involved the CIP geometry, where a typical thin film multilayer has a resistance of several ohms, making measuring GMR simple.

The first CPP-MR measurements were reported in 1991 by our group, and showed that the CPP-MR could be several times larger than the CIP-MR [25]. It also quickly became clear that the CPP-MR can often be described by simpler equations than the CIP-MR, allowing simpler analysis of experimental data [26,27]. These initial measurements involved samples with macroscopic area through which the CPP-current

flows ($A \sim 1 \text{ mm}^2$), and thus very small resistance $\sim 10 \text{ n}\Omega$. To obtain uniform current flow through the sample, and thus to be able to measure the specific resistances of main interest (AR_{AP} , AR_P (defined below), and their difference, $AR_{AP} - AR_P = A\Delta R$) all quantitatively, the measuring technique used crossed superconducting strips and required low temperatures and sophisticated equipment [25,28]. AR , the product of A and the sample resistance R , is the intrinsic quantity in the CPP geometry [29] (i.e., it is the inverse of the conductance per unit area). AR_{AP} and AR_P represent the values of AR when the magnetizations of adjacent F-layers in the multilayer are aligned anti-parallel (AP) or parallel (P) to each other. $A\Delta R$ represents the maximum change in specific resistance with change in magnetic field, and the CPP-MR $= A\Delta R/AR_P$.

Soon afterward, CPP resistances ranging from fractions of ohms to ohms were achieved by using optical lithography to prepare multilayer samples with areas $A \sim (\mu\text{m}^2)$ [30-33], or by electrodepositing multilayers into nanotubes with diameters $\geq 30 \text{ nm}$ in plastics subjected to radiation and then etched [6, 34-39]. Both techniques allow CPP-MR measurements to be extended to room temperature. For the lithographed samples, however, because they were wider than long, the current density was not uniform, making it difficult or impossible to reliably determine AR . While the electrodeposited samples were long and thin enough to give uniform current flow, until recently measurements involved an unknown number of wires in parallel and, so far, electrodeposition has been limited to only a few F/N metal (or alloy) pairs [39]. Measurements have also been made of the MR with current-at-an-angle to the planes (CAP-MR) [4,40-42], and a combination of CIP-MR and CAP-MR data extrapolated to the CPP-MR [4,41]. The present thesis focuses upon measurements of the CPP-MR

using the low temperature, ‘large area’ technique just noted, and some preliminary studies of the CPP-MR using a combination of optical and electron-beam lithography to produce samples with areas $A \sim 0.01 \mu\text{m}^2$. Measurements of the CIP-MR will only be presented occasionally for purposes of comparison.

In section 1.2 we review the simple phenomenological picture of the source of GMR outlined in ref. [1]. Section 1.3 describes present uses of the CIP-MR for devices, the potential for use of the CPP-MR, and the main problems to be solved if the CPP-MR is to become competitive. Section 1.4 briefly reviews those facets of the field of CPP-MR that are of direct relevance to the topics of this thesis. More complete reviews can be found in [3-5, 43] and the theses of S. F. Lee [44] and Qing Yang [45]. The chapter concludes with Section 1.5, an outline of the studies in this thesis.

1.2. BASIC IDEAS IN GMR

GMR arises from spin-dependent scattering in the F-metal and at the F/N interfaces [1]. Such scattering depends upon the band structures of the F and N metals, the impurities present in both the F and N metals, and the intermixing of the F and N metals at the F/N interface. The band structure of a ferromagnetic metal is moment-dependent; that is, the d-bands with one moment direction are shifted relative to the d-bands with the opposite moment direction. At the Fermi surface this shifting leads to a difference in the density of states for d-band electrons depending on their moment direction. Fig.1.1 shows a cartoon of the s-bands and d-bands of an N-metal and an F-metal.

This unbalanced occupation of the d-bands gives rise to a net magnetization in the F-metal, even without the presence of an external field. The direction in which more electron moments point is called the majority direction, and the direction in which fewer

point is called the minority direction. In the simplest picture, the s-electrons are assumed to carry most of the current. If electrons don't flip their moments, then majority s-electrons will scatter mostly into other majority s-electron states, because there are only few majority d-electron states available at the Fermi energy. Minority electrons, in contrast, can scatter more often into the larger number of minority d-states at the Fermi energy. These different scattering processes give rise to a different scattering probability for electrons with moments opposite to the local magnetization of the ferromagnetic metal, and electrons with moments along the local magnetization. This difference is called spin-anisotropy [4]. If no moment flipping occurs, then these two 'moment channels' (or 'spin channels') will not mix, and can be treated as two separate channels of conduction equivalent to resistances in parallel. Flipping of the electron moments mixes these channels, making the picture more complex.

These different scattering rates can be described phenomenologically in terms of different resistivities for majority and minority electrons—i.e. electrons with their moments along or opposite to the local magnetization M [46]. The different scattering rates make the resistivity of the majority electrons, ρ^\uparrow , different from that of the minority ones, ρ^\downarrow . The F/N interfaces also have spin-dependent scattering, which we characterize similarly by specific resistances AR^\uparrow and AR^\downarrow . Instead of using the four parameters ρ^\uparrow , ρ^\downarrow , R^\uparrow , and R^\downarrow , we use a dimensionless bulk spin-asymmetry parameter, $\beta = \frac{\rho^\downarrow - \rho^\uparrow}{\rho^\downarrow + \rho^\uparrow}$,

a dimensionless interfacial spin-asymmetry parameter, $\gamma = \frac{R^\downarrow - R^\uparrow}{R^\downarrow + R^\uparrow}$, the measured bulk

resistivity of the F-metal, ρ_F , and an interfacial specific resistance, $AR_{F/N}$. Chapter 3 will describe in more detail the use of these parameters to describe the CPP-MR.

To explain how GMR results from such spin-dependent scattering, consider the F/N/F trilayer in Fig.1.2 and assume that minority electrons are more strongly scattered than majority ones, both in the F-metal and at the F/N interfaces (i.e., assume $\beta_F > 0$ and $\gamma_{F/N} > 0$). Further, consider a fixed direction in space (e.g. the direction of the initially applied magnetic field H), and that the magnetizations of the F-layers are allowed only to be AP (Case A) or P (case B) to each other. Lastly, divide the electrons entering the trilayer into ones with moments up (in the direction of the initially applied H) and moments down, and do not allow their moments to flip as they cross the multilayer.

When the F-layer moments are (AP) to each other (case A), both up and down electrons will be scattered strongly in one F-layer and weakly in the other, and their resulting resistances will be identical. The net resistance will be half of each of these two equal resistances. When, in contrast, the F-layer moments are parallel (P) to each other (Case B), one of the electron channels (the ‘up’ electrons in Fig. 1.2) will be scattered only weakly in both F-layers, the resistance of this channel will be small, and will ‘short’ out the total resistance. The net resistance will now be even smaller than this shorting resistance, and thus smaller (perhaps even much smaller) than the resistance in the AP case, $R_P \ll R_{AP}$. If the relative alignment of magnetizations is between parallel and antiparallel, electron moments will sometimes flip as the electrons transit the multilayer (since the electrons will no longer be in quantum eigenstates of the system). While the total resistance will usually be intermediate between those of the parallel and antiparallel states, the analysis becomes much more complex. Because of the resulting simplicity of

analysis, we will limit our study to only the P and AP states, focusing on AR_{AP} , AR_P , and their difference $\Delta AR = AR_{AP} - AR_P$.

We assumed above that the electrons don't flip their moments as they transit the multilayer. If the electrons flip their moments as they pass through the N-layer, the GMR will be reduced. In the extreme case of many flips, the electrons will no longer care whether the F-layer moments are aligned P or AP, and the GMR will vanish. We call such effects of spin-flipping 'losing spin-memory'.

In a bulk metal, spin flipping leads to spin-memory-loss, and is measured by a length called the 'spin-diffusion length' l_{SF} [47-50]. Because spin-flip scatterings are usually only a small fraction of the total scattering events (at low temperatures, the fraction coming from spin-spin exchange coupling and spin-orbit coupling), l_{SF} is usually longer than the electron mean-free-path, λ , in the same layer. Thus we normally expect the inequality $l_{SF} \gg \lambda$ to be valid in a given F- or N-metal.

We assumed in the above analysis that we could produce both AP and P states. The P-state can be produced by applying a magnetic field strong enough to align the moments of all F-layers along the field. The AP state, however, is more elusive and three different ways have been used to produce it.

1. Using the antiferromagnetic exchange coupling that occurs between two F-layers separated by a certain small thickness of a given N-layer [1, 2, 10-14]. The discovery of this coupling originally lead to the discovery of GMR. For even smaller N-layer thicknesses the exchange coupling is ferromagnetic, and for larger N-layer thicknesses it oscillates with N-layer thickness, getting weaker as that

thickness increases until its effect becomes negligible at thicknesses of a few nm [11,13].

2. Using an exchange biased spin valve, EBSV, in which one of two F-layers is heated and cooled in a field while in contact with an antiferromagnetic (AF) layer. The exchange coupling between these layers increases the switching field H_{sw} of the F-layer [51,52], in many cases to a value much larger than that of a second 'free' F-layer separated from the first by an N-layer thick enough to minimize exchange coupling between the two F-layers. The moment of the 'free' F-layer can then be switched back and forth while that of the 'pinned' F-layer is held fixed.
3. Using a hybrid multilayer (or hybrid spin-valve (SV), composed of two F-layers (again separated by a sufficiently thick N-layer) with very different switching fields. These different fields can be achieved by using either: (a) two different F-metals with very different switching fields, or (b) only one F-metal, but with two very different layer thicknesses, since the switching field depends upon the layer thickness.

The first method, using antiferromagnetic coupling, was widely used in early GMR studies, but will not be used in this thesis because it does not allow variation of the N-layer thickness continuously to make systematic studies. We will use the other two methods. Fig. 1.3 shows examples of AR(H) curves for an EBSV (A) and a hybrid spin valve (B) studied in the present thesis. The main difference between the two is the shift in the AR(H) curve to one field direction from $H = 0$ in the EBSV, which is characteristic of exchange biased samples [51]. Such EBSVs are often the structure of choice for CIP

devices because they allow reversible CIP-MR measurements at low fields and because the magnetization of the pinned layer remains stable over many free layer switches [53, 54].

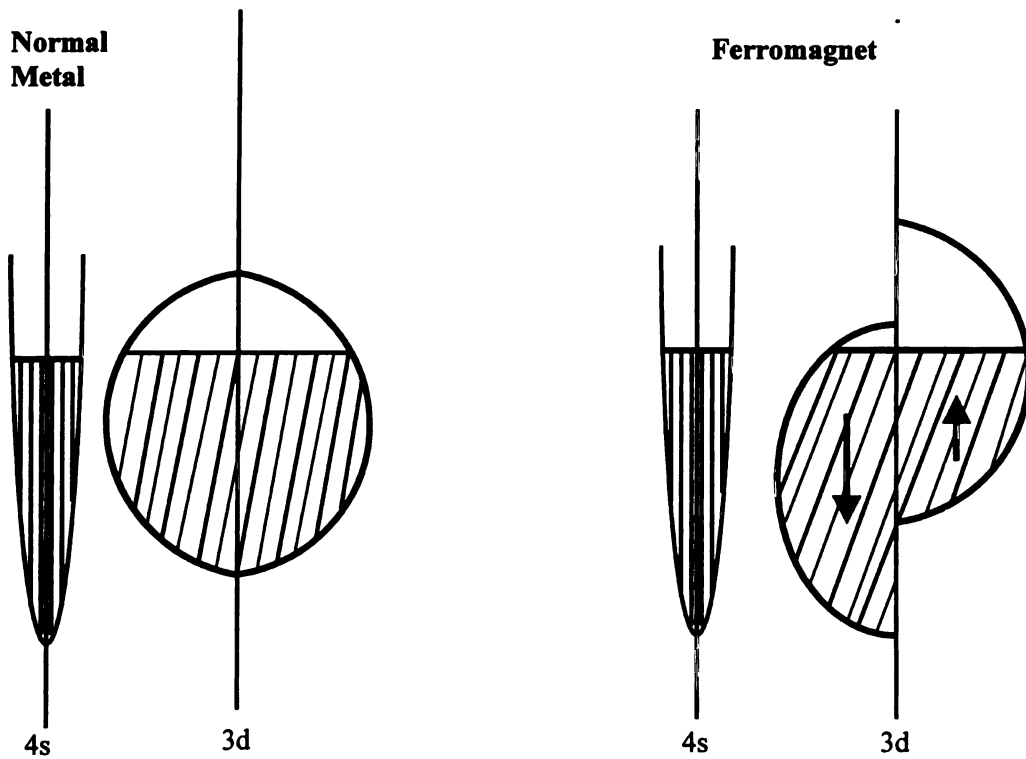


Fig. 1.1. Cartoon of the s- and d- subbands of a ferromagnetic metal and a normal metal. There is a net magnetic moment in the ferromagnet but not the normal metal.

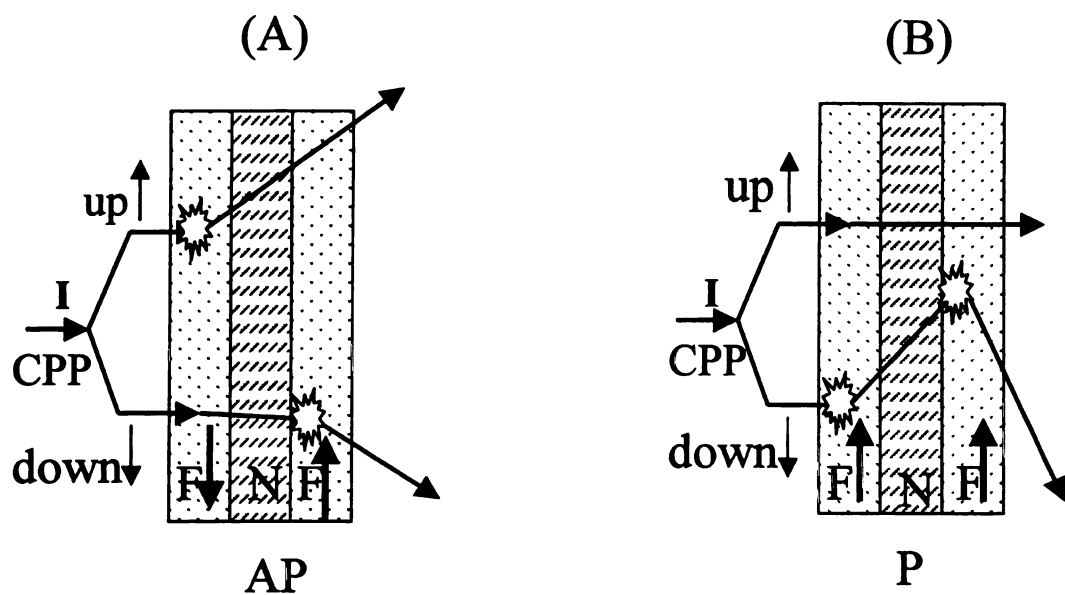


Fig. 1.2. Schematic diagram of scattering in the 'up' and 'down' channels when the magnetizations of the ferromagnetic layers are (A) antiparallel or (B) parallel to each other. The star indicates stronger scattering. Scattering is only shown in bulk F.

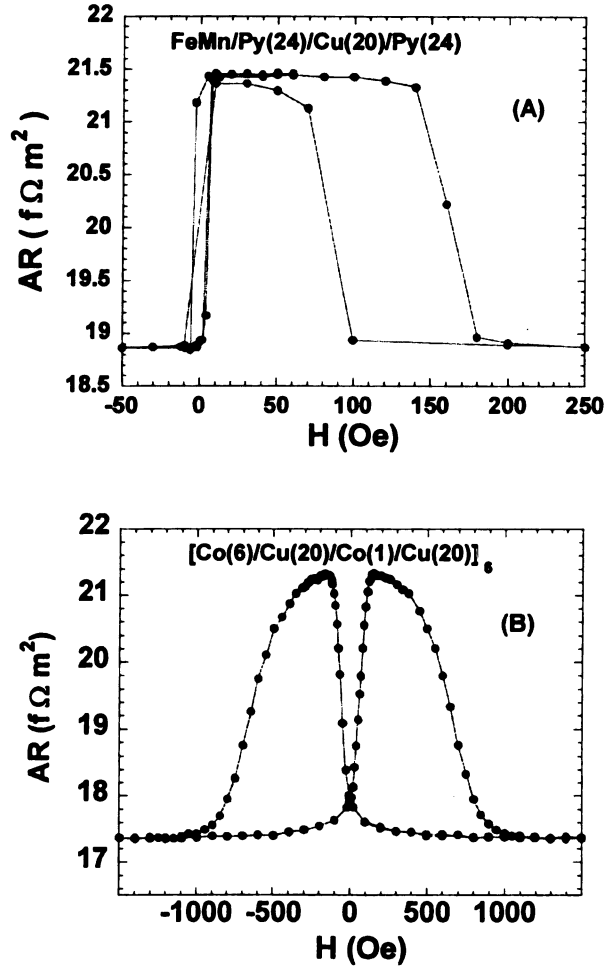


Fig. 1.3. $AR(H)$ for (A) an EBSV, and (B) a hybrid spin valve. $AR(H)$ for the hybrid SV is symmetric around $H = 0$, while that for the EBSV is not. Numbers indicate layer thicknesses in nm.

1.3. GMR DEVICE APPLICATIONS

CIP-GMR found its way into devices in a relatively short time [24,55,56], and is an elegant example of how advances in solid state physics can lead to technology.

The first GMR-based general-purpose motion detector became commercially available in 1994, just six years after the discovery of GMR [57]. In a motion detector, the GMR multilayer sensor is placed in the vicinity of the moving part of interest, which is shaped so as to give a time varying magnetic field at the sensor. The moving part can

either be magnetic (e.g., steel), or coated with a magnetic material. The sensor changes its resistance in response to the changing field. This technique can be used to detect rotational motion (such as for motors), or linear displacement (such as for automatic breaking systems) [56,58].

In 1998, IBM offered the first large-scale commercial application of GMR as the magnetic field sensor in the read heads of magnetic hard discs in computers [24]. This rapid implementation of GMR into read heads occurred because a GMR thin film with $R \sim 20 \, \Omega$ and CIP-MR $\sim 6\%$ (by now somewhat larger) simply replaced a very similar Py thin film with $R \sim 20 \, \Omega$ and AMR $\sim 2\%$. Read heads require the ability to switch resistance from high to low values in a relatively low magnetic field and stability over a range of temperatures. These requirements exclude some samples with very high MR, such as single crystal Fe whiskers [59] and the colossal magnetoresistance, CMR, observed in oxides [60,61].

Demonstrations of GMR random access memory were made as early as 1997. Several companies now have established research programs for developing nonvolatile GMR memory devices [24].

All the devices mentioned above use the traditional CIP geometry, because of its easy-to-measure resistance. However, the CIP-MR looks as if it has leveled off. Companies are now looking for systems with larger MRs to read the smaller bits under development for higher density magnetic memory, or to serve as switchable, non-volatile magnetic memory elements. Some companies [62] are investigating F/N metal CPP-based read heads and memories, due to the large potential CPP-MR. However, an obstacle to implementing CPP-MR devices with all-metal systems is the small specific

resistance of present day multilayers, $AR \sim 10 \text{ f}\Omega\text{m}^2$ in samples with total layer thicknesses limited to $\sim 50 \text{ nm}$. Even at $A = 0.01 \text{ micron}^2$ the total CPP resistance is only $\sim 1 \Omega$. A competitor for both read heads and magnetic memories, is magnetic tunnel junctions, giving tunneling MR (TMR) [56,63]. Present junctions with large room temperature TMRs (30-40%) have AR s ($\geq 60,000 \text{ f}\Omega\text{m}^2$) too large for read heads [56]. Research is underway to find ways to reduce AR without reducing the TMR. Large AR is not a fundamental problem in magnetic memory, for which TMR is under intense investigation [64].

Extensive spintronics studies of semiconductors are now also underway. Some semiconductors have been shown to conserve the current polarization over fairly long distances [65,66]. But how to inject a large spin-polarized current into them from physical contacts is still a topic of intense discussion and research [67].

We will explore in this thesis some of the potential ways to increase the total specific resistance, AR , and/or $A\Delta R$ of metallic multilayers, in hopes of making the CPP-MR more viable for devices.

1.4. CPP-MR THEORY & HISTORY CRUCIAL TO THIS THESIS

Fert initially explained GMR phenomenologically in terms of the two-current model discussed above [1]. This picture was quickly converted into transport equations to describe the CIP-MR in multilayers. Because of the low symmetry of the CIP-MR, these transport equations for a simple F/N multilayer contain many parameters [3], among which are the mean-free-path in the N-layer, λ_N , and the mean-free-paths in the F-layer, λ_F^\uparrow and λ_F^\downarrow . Qualitatively, for an electron crossing the multilayer to recognize the relative

orientation of the moments of two adjacent F-layers, the N-layer thickness must be less than λ_N . More quantitatively, λ_N appears in the transport equations as a ratio with the layer thickness t_N in the argument of exponential functions—functions involving $\exp(-t_N/\lambda_N)$ —making λ_N (and similarly λ_F^\uparrow and λ_F^\downarrow) ‘characteristic lengths’ in the CIP-MR. In addition, current flow through the layers of multilayer in the CIP geometry is not uniform; the current tends to shunt through the lower resistivity layers (usually the N-layers). Lastly, the CIP-MR seems to be very sensitive to roughness of the F/N interfaces, since the electrons, on average, move parallel to these ‘thin film’ interfaces.

Zhang and Levy [26], based upon a free-electron analysis assuming diffuse scattering of electrons, first pointed out that, if no spin flipping occurs, the CPP-MR transport equations should be very simple, just series resistor equations for two parallel current channels. Unlike the CIP-MR equations, the mean-free-path lengths in the N and F metals are not characteristic lengths, but enter only via the layer resistivity parameters ρ_N and ρ_F . Qualitatively, in the CPP geometry, the current-carrying electrons must travel through every layer and interface, and thus must ‘experience’ the actual magnetic order, regardless of the mean-free-path lengths. The only lengths in the CPP-MR equations are then the F- and N-layer thicknesses, t_F and t_N .

Lee et al. [27] (and later Valet and Fert [47]) first wrote down the two-current series-resistor, 2CSR, model equations using the parameters β_F , $\gamma_{F/N}$, ρ_F , and $AR_{F/N}$ defined above. Defining an alternative F-layer resistivity, $\rho_F^* = \frac{(\rho_F^\uparrow + \rho_F^\downarrow)}{4} = \frac{\rho_F}{1 - \beta^2}$ and

similarly, $AR_{F/N}^* = \frac{(AR_{F/N}^\uparrow + AR_{F/N}^\downarrow)}{4} = \frac{AR_{F/N}}{1-\gamma^2}$, leads to the following 2CSR model

equations for AR_{AP} and $A\Delta R$ for a simple $[F/N]_N$ multilayer with N repeats.

$$AR_{AP} = N\rho_N t_N + N\rho_F^* t_F + 2NAR_{F/N}^* \quad (1.1a)$$

$$A\Delta R = \frac{N^2 [\beta\rho_F^* t_F + 2\gamma AR_{F/N}^*]^2}{AR_{AP}} \quad (1.2)$$

An alternative form of Eq. 2 that we will use in this thesis is

$$\sqrt{(A\Delta R)(AR_{AP})} = N(\beta\rho_F^* t_F + 2\gamma AR_{F/N}^*) \quad (1.3)$$

If the left hand side of Eq. 1.3 is plotted against N for samples with fixed t_F , the data should fall on a straight line passing through the origin, and the slope of this line should be independent of the non-magnetic metal resistivity, ρ_N , and also independent of the total sample thickness, t_T .

The samples in this thesis are all made with superconducting (S) leads. All experimental evidence so far indicates that the contribution of these leads can be incorporated into the above equations simply by adding to Eq. 1.1a a constant (and independently measured) term $2AR_{S/F}$, to give Eq. 1.1b.

$$AR_{AP} = 2AR_{S/F} + N\rho_N t_N + N\rho_F^* t_F + 2NAR_{F/N}^* \quad (1.1b)$$

However, the validity of this procedure is yet to be proved theoretically. Eqs. 1.2 and 1.3 remain unchanged. These 2CSR model equations (1.1b-1.3) have been found to work surprisingly well for Co/Cu and Co/Ag multilayers, which consist of pure metals with long spin-diffusion lengths. That is, a wide variety of data in these systems have been found to be consistent with the forms of Eqs. 1.1b-1.3 with parameters that are independent of the layer thicknesses t_F and t_N [27,28]. Eq. 1.3 predicts that a plot of the

left-hand-side ‘square root’ versus N for multilayers with fixed $t_{Co} = 6$ nm should fall on a straight line passing through the origin, independent of the total multilayer thickness or the resistivity of any N-metal or N-alloy in which spin-flipping is weak. Fig. 1.4 for Co/Cu and Cu/CuGe, and Fig. 1.5 for two different sets of Co/Ag plus Co/AgSn, both show exactly this predicted behavior for non-magnetic metals Cu or Ag. Adding a little Ge to Cu or Sn to Ag increased the resistivity by about a factor of 20 [27,68], but produced only weak spin-flipping [50], thereby still leaving the 2CSR model applicable. These data were taken as strong evidence that Eqs. 1.1-1.3 contain the essential physics of the CPP-MR for systems where spin-flipping is negligible, and that the mean-free-paths in the F- and N-layers do not play a significant separate role from their appearance simply within the parameters ρ_F and ρ_N .

In 1993, Valet and Fert [47] argued that the characteristic lengths in the CPP-MR are the spin-diffusion lengths, l_{SF}^N in the N-metal and l_{SF}^F in the F-metal. Using a free-electron Boltzmann Equation model, they showed that the 2CSR model only describes the CPP-MR in the limit $l_{SF}^N \gg t_N$ and $l_{SF}^F \gg t_F$. They wrote down the more general equations (which we call the Valet and Fert (VF) model) that applies when the spin-diffusion-lengths are not that long.

For later use, we note that the VF model assumes no band structure and is also strictly valid only when $l_{SF} \gg \lambda$, a condition expected to be valid for most metals [47,69,70]. Said another way, the VF equations are the leading terms in a Boltzmann equation analysis and the corrections are $\sim \lambda/l_{SF}$. While it is not clear that this condition has always been met in experimental studies [43], the results of those studies have seemed to be consistent with the VF equations [47]. As one example, derivations of values of l_{SF} in

N-metal alloys applying the VF equations to data such as those in Fig. 1.5 were found [50,68] to be consistent with independent estimates from measurements of spin-orbit scattering [71] or, where appropriate, with calculations of spin-spin exchange [72]. The heavy impurity Pt is expected to produce strong spin-orbit scattering, and the ‘magnetic’ impurity Mn is expected to produce spin-spin exchange scattering. In both cases, the presence of spin-flipping causes the data to fall below the straight line of Eq. 1.3 (Fig. 1.5), and the values of l_{SF} were derived by fitting the data to the VF model. Measurements of l_{SF}^N were extended to additional alloys in [73].

The VF model was also found to be necessary to understand measurements of how $A\Delta R$ for symmetric Py-based EBSVs varied with the Py thickness, t_{Py} . Instead of $A\Delta R$ continuing to grow with increasing t_{Py} as expected from the 2CSR model, $A\Delta R$ saturated in value, becoming constant beyond a certain value of t_{Py} (Fig. 1.6). This behavior was attributed to a finite $l_{SF}^{Py} \sim 5.5$ nm [74], a value subsequently confirmed independently from studies of electrodeposited nanowires [39]. Also, with this finite l_{SF}^{Py} , VF theory was found to describe surprisingly well the values of AR_{AP} and $A\Delta R$ for Co/Cu/Py/Cu hybrid spin-valves, using only the previously determined parameters for Co/Cu and Py/Cu without adjustment [75]. Later studies of spin-memory-loss in Co suggest that it has a much longer value, $l_{SF}^{Co} = 60 \pm 20$ nm [76,77]. All of these results constitute evidence that the characteristic lengths in the CPP-MR are spin-diffusion lengths, not mean-free-paths.

We conclude this discussion of prior work with brief mention of three additional studies of importance to the present thesis.

From studies of Deviations from Matthiessen's rule due to addition of two different impurities at once to a host F-metal, Campbell and Fert [46] list estimated values of β for alloys of Co, Fe, and Ni with a variety of impurities. For certain impurities (especially Cr, V, and Ru), these values of β are negative, i.e. the scattering anisotropy is opposite to the usual one. Our group performed experiments both to look for negative β s in appropriate alloys and to test the absolute values of the Campbell-Fert estimates in a few cases. As predicted, evidence of negative β s were found for FeV, NiV, FeCr, and NiCr [78-80]. Reasonable agreement in magnitudes with the Campbell-Fert values were found for NiFe and CoFe (both with positive β) and for NiCr (negative β) [81,82]. The method and equations used for determining the sign of β will be described in Chapter 3.

In an attempt to test the applicability of the 2CSR model, our group examined AR for Co and Py based hybrid spin-valves in two different forms: 'interleaved' $[Co/N/Py/N]_N$, and 'separated' $[Co/N]_N/[Py/N]_N$, with $N = Cu$ or Ag [83]. When these measurements were first made, the spin-diffusion lengths in both Co and Py were expected to be long. In such a case, $AR(H)$ should be the same for interleaved and separated samples, because the 2CSR model doesn't change as the order of the layers varies. To initial surprise, a clear difference was found between the values and shapes of $AR(H)$ for the two kinds of samples (see, e.g. Fig. 1.7 below). This difference led to the measurements of $AR(H)$ for Py-based EBSVs described above, and the discovery of a short l_{SF}^{Py} . Subsequently, Bozec et al. found similar differences in $[Co/Cu/Fe/Cu]_N$ hybrid spin-valves [84]. They tentatively attributed the differences either to a short l_{SF} in Fe or to spin-memory-loss at the F/N interfaces.

Lastly, as will be discussed in Ch. 3, VF theory predicts that inserting a source of spin-memory-loss judiciously into a multilayer with large lead resistance can reduce the effect of the lead resistance on $A\Delta R$, and thereby increase $A\Delta R$. Indirectly, such behavior is already evident in the fitting of the Py-based EBSV data described above. Direct evidence for such behavior was presented by Gu et al., who inserted a strong spin-flipping alloy, FeMn, into one of the Py layers in a Py-based EBSV [85].

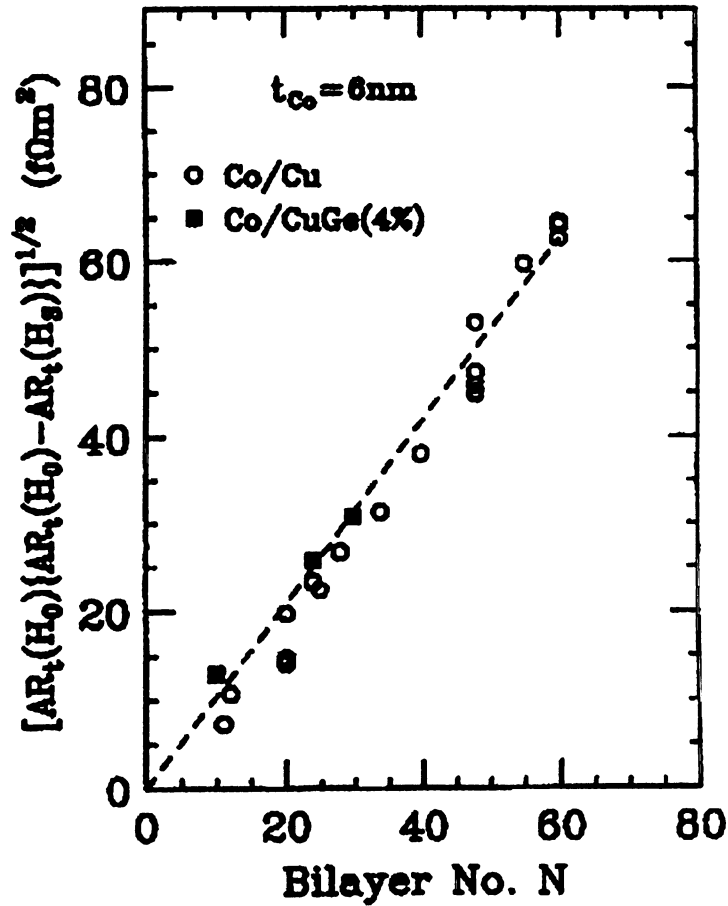


Fig.1.4 Square root test of the 2CSR model. Adding Ge impurities that greatly reduce the value of λ in Cu does not affect the applicability of the model. (From [68]).

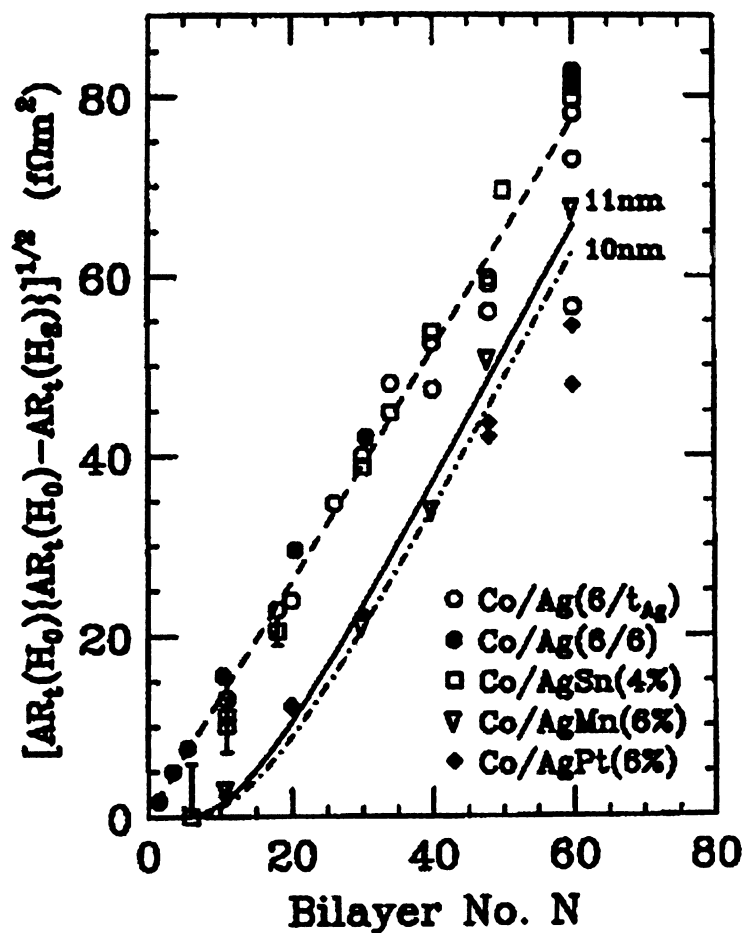


Fig.1.5 Testing the 2CSR and VF models. Adding Sn to Ag reduces the mean-free-path without greatly reducing the spin-diffusion-length. The Co/Ag and Co/AgSn data fall on the 2CSR model prediction of a single straight line going through the origin. Adding Pt or Mn, in contrast, reduces the spin-diffusion length, and causes the data to fall below the 2CSR model line (see text). (From [68]).

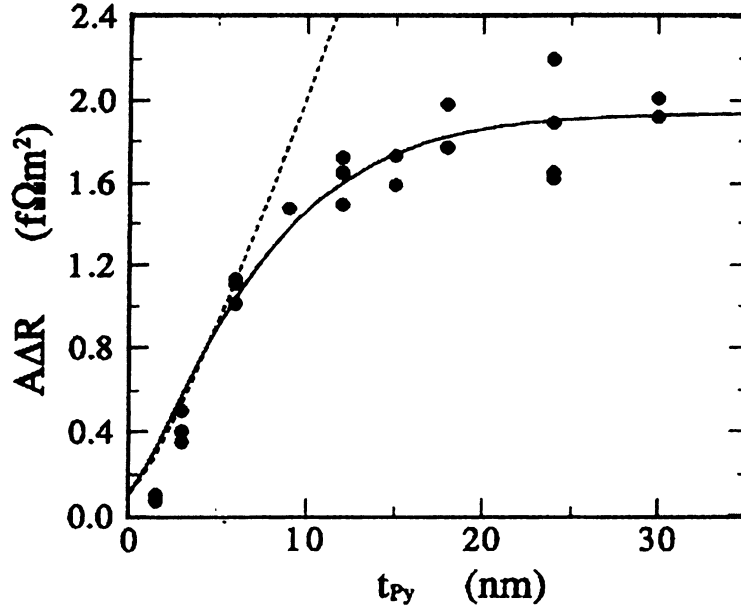


Fig. 1.6. $A\Delta R$ vs. t_{Py} for $Py(t_{Py})/Cu(20nm)/Py(t_{Py})$ EBSVs. Filled circles are the data, along with the 2CSR (dashed line) and the VF (solid line) model with $l_{SF}^{Py} = 5.5$ nm. From [74].

1.4.1. High Current-Density Effects in F/N Multilayers

A new avenue for GMR related studies in sub-micron sized samples emerged in 1996, when Slonczewski [15] and Berger [16] predicted that the magnetization direction of magnetic layers could be switched in a controlled way by a large enough electric current density. In a sense, this phenomenon is the inverse of GMR, where controlled changing of the relative magnetic order of a multilayer leads to a change in the current flowing through it (via a change in resistance). They predicted also [15,16] that a high current density could excite magnons (quantized spin waves) in the magnetic materials when an applied field limited the ability of the magnetization to completely switch. Such current-induced switching makes CPP-MR potentially attractive for devices like MRAM, because current-induced switching would be more localized, and probably also allow simpler circuit design, than magnetic-field-induced switching. The magnon generation

opens the possibility for high frequency generation. The large current densities needed for such switching cannot be applied to macroscopic samples with superconducting contacts, making it impossible to study current induced switching in them. These phenomena need small areas of current flow, which have been achieved using point contacts [17,18], e-beam lithographically produced submicron sized samples [19-21], or electrodeposited nanowires [6,39].

Tsoi et al [17], using point contacts, first observed current-induced spin waves. The Cornell group [19] soon observed the current-induced switching of magnetization in nano-patterned, pillar shaped trilayers of Co/Cu/Co, and such switching has been confirmed by others [20,21]. There are two different switching mechanisms, the self magnetic field of the current [21], and spin transfer from the polarized current to the layers [19,20]. From simple arguments, one expects the self-field switching to scale as $\sim 1/d$, and the spin-transfer switching to scale as $\sim 1/d^2$, where d is the sample diameter. Thus, self-field switching should dominate for large samples, and spin-transfer switching for small ones (e.g. $d \leq 200$ nm). More precisely, the crossover diameter depends upon the magnetic and GMR parameters of the materials, including those determining the torque, magnetization relaxation, and magnetic anisotropy. The two sources can be distinguished experimentally by their different hysteresis curves for R vs I . Self field switching should give an $R(I)$ symmetric about $I = 0$, with peaks in resistance on each side of $I = 0$ (like the $MR(H)$ curve for a simple F/N multilayer— Fig. 1.3B). The peaks are at the AP states, with the high field limits in both directions always being P-states. Spin-transfer torque, in contrast, is present only when the two F-layer magnetizations are not collinear (or anti-collinear). This torque depends upon the direction of current flow

and is characterized by an asymmetric $R(I)$ curve. Current flow in one direction stabilizes antiparallel alignment of two magnetic layers and current flow in the opposite direction stabilizes parallel alignment. The switching from one alignment to the other causes a jump in sample resistance, up in one case, down in the other. The dominant physics underlying these phenomena is still a matter of debate among theorists [15,21,22].

1.5. THE PRESENT THESIS

After this introduction, we briefly describe sample preparation and characterization in Ch. 2 and provide background on theory in Ch. 3. The rest of the thesis then consists of a variety of experiments as follows.

Ch. 4 involves a search for mean-free-path effects. As noted above, several searches for evidence that mean-free-paths might be characteristic lengths in the CPP-MR did not find any clear evidence of such effects. However, in 2000, Bozec et al [88] claimed to have seen ‘mean-free-path effects’. They used multilayers composed of alternating layers of 6 nm and 1 nm thick Co layers (separated by thick Cu layers) having the two different orderings described above: $[\text{Co}(6)/\text{Cu}(20)/\text{Co}(1)/\text{Cu}(20)]_N$ = interleaved, and $[\text{Co}(6)/\text{Cu}(20)]_N/[\text{Co}(1)/\text{Cu}(20)]_N$ = separated. Similarly to what was described above for Co/Ag/Py/Ag and Co/Cu/Fe/Cu, they found qualitative and quantitative differences between the MR curves of the two types of samples. Fig. 1.7 shows an example of our confirmation of the presence of such differences. Because of the relatively long spin-diffusion lengths in Co (~ 60 nm) and Cu (~ 500 nm) [5,76], they argued that the differences could not be accounted for by either the 2CSR model (which predicts that the two curves should be the same), or by the VF model (since the spin-diffusion lengths in

Co and Cu are too long). They attributed the differences to mean-free-path effects, claiming that the difference is due to ‘real-metal’ effects that appear when the layer thicknesses are shorter than the λ s in the Co and Cu layers. In Ch. 4 we test these claims.

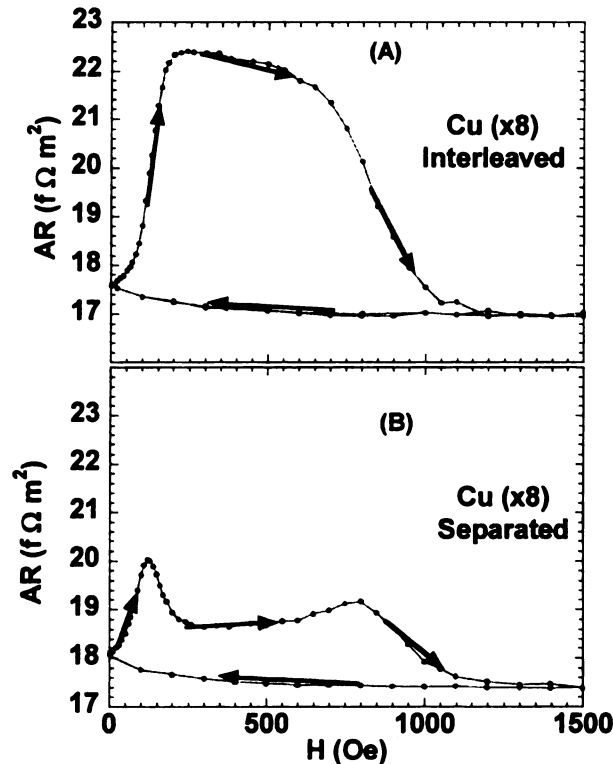


Fig. 1.7 $AR(H)$ for an interleaved sample (A) and a separated sample (B). Samples were already taken to saturation in the $-H$ direction. There are differences both in shape and size of the change in AR with H .

Ch. 5 describes studies designed to enhance the CPP-MR. By enhancing CPP-MR, we mean increasing the total specific resistance AR and/or the specific resistance change, ΔAR . As described earlier, such enhancement would help to make the CPP-MR in metallic multilayers more viable for devices. In this thesis, we tried to enhance CPP-MR in three different ways. A) By alloying ferromagnetic Co with an impurity Zr that greatly increases its resistivity, yet is not expected to reduce its spin-asymmetric scattering parameter β . B) By introducing ‘internal’ interfaces within an F-layer, which we

expected to increase both AR and $A\Delta R$ without substantially increasing the total sample thickness. The interface contribution is particularly significant when the resistivity of the bulk metal is small, as in Co/Cu multilayers. C) By introducing a source of strong spin-memory-loss into the superconducting layers of an EBSV. The arguments for why this introduction might increase $A\Delta R$ are given in Chs. 3 and 5.

In Ch. 6 we determine the GMR properties of Ru and Co/Ru interfaces. Co/Ru multilayers have acquired importance lately because of strong antiferromagnetic coupling between Co layers separated by a very thin layer of Ru. This coupling is now used in devices with structure: Co(3)/Ru(0.6)/Co(3)/Cu(t_{Cu})/F, where F is any ferromagnetic metal of suitable GMR properties, and thicknesses are in nm. This structure is called a synthetic antiferromagnet and is characterized by a very stable anti-parallel magnetization structure for the two 3 nm thick Co layers. The net moment in the two Co layers is zero, which makes them insensitive to external magnetic fields, while a third F layer is free to rotate in small fields. To provide the basic understanding needed to evaluate the potential of Ru in CPP-MR devices, we study the spin-memory loss in bulk Ru and at the Cu/Ru interface and the spin-dependant scattering at the Co/Ru interface. We will also discuss other aspects of Ru in CPP devices.

In Ch. 6 we also use Ru and the CPP-MR to probe spin-dependent scattering at several different interfaces.

In Ch. 7 we present some CPP-MR measurements on such samples at both room temperature and 4.2 K. This work was intended as the start of a program of systematic studies of current-driven excitations.

Ch. 8 contains a summary and our conclusions.

Chapter 2

SAMPLE PREPARATION, CHARACTERIZATION AND MEASUREMENT

2.1 INTRODUCTION

The process of sample preparation, as well as characterization and CPP-MR measurement in our F/N multilayered samples, varies substantially depending on sample area. All samples in this study are prepared in our labs and fall into one of two categories:

- 1) Macroscopic samples, with area of current flow $A \approx 1.25 \text{ mm}^2$.
- 2) Microscopic samples, with area $\sim 1 \times 10^{-8} \text{ mm}^2$.

Multilayers of both types are deposited by sputtering onto single-crystal Si substrates with dimensions 0.5"x0.5" and a native SiO₂ thin layer on the substrate surface.

In addition to its importance to the preparation process, sample area is of key importance because it determines the resistance of the multilayer. The two types of samples also have very different contact materials. Macroscopic samples are sandwiched between two crossed superconducting leads to provide a uniform current through the sample. The large resistances of microscopic samples make it unnecessary to have superconducting contacts, since noble-metal contacts have low enough resistivities compared with the multilayer that the current in the multilayer should be near uniform.

We use the same sputtering system to deposit the multilayers of both the macroscopic and microscopic samples. Except for some details, the same steps are used in preparing

both kinds of samples. The macroscopic samples are sputtered through a special mask, rotatable in situ, that has three openings of different shapes and a blank ‘blocking position’ that protects the substrate before and after sputtering. The microscopic samples are sputtered through a mask with a single square opening plus a blocking position.

In the next section we discuss the sputtering process that is common to both kinds of samples. We then describe characterization studies, also relevant mostly to both kinds of samples. Except for some data specific to the present samples, most of what we describe here has been presented in prior theses [44,45] and publications [28,29]. We conclude with a more detailed discussion of the preparation and characterization of microscopic samples, a topic newer to this thesis.

The small ($R \sim 10^{-8} \Omega$) resistances of the macroscopic samples are measured at 4.2K with a Superconducting Quantum Interference Device (SQUID) based bridge circuit described elsewhere [28,44]. The sample holder, including a cylindrical hand wound superconducting magnet (capable of fields up to 1.5T [44]) around the sample, is lowered into a standard 100 liter liquid helium dewar so that both the sample and the SQUID are below the helium level. It takes about 20 minutes to cool the sample slowly in the helium gas above the liquid helium and about 20 minutes to warm the sample up again to room temperature in the neck of the helium dewar. This ability to cool and warm a sample in well under an hour has led to the name ‘quick dipper’ for the sample holder.

The large resistances ($R \sim 1 \Omega$) of the microscopic samples allow them to be measured at room temperature and 4.2K with a standard digital nanovoltmeter.

2.2 COMMON PREPARATION PROCEDURES

We start the fabrication process by cleaning the substrates with Alconox, rinsing them thoroughly with water, and then cleaning them with acetone and alcohol, using ultrasonic agitation in each step. The substrates are dried using nitrogen gas to remove any traces of alcohol from the surface. Cleaned substrates are loaded into sample holders and placed on a rotating sample positioning and movement assembly (SPAMA) plate in an ultra-high-vacuum-compatible sputtering chamber. To achieve the desired low pressure, the chamber is baked for a few hours to reduce the amount of water vapor, while a high-speed cryopump pumps upon the chamber. A liquid nitrogen cold (Meissner) trap inside the sputtering system freezes out water molecules both before and during sputtering, thus further improving the effective background vacuum.

A chimney is placed over each target to collimate the particle flow to the substrate, eliminating cross contamination. A shutter is placed between the targets and the sample holder, to open or block particles from reaching the substrates.

Four dc magnetron triode sputtering guns, plus two diode guns, give us the ability to make sophisticated multilayers. Target materials are high-purity metals or alloys, mostly purchased from commercial companies. A CuGe target was prepared in our laboratory using RF melting. A CoZr target was originally a pure-Co target, into which we drilled small holes and then inserted Zr pieces in the holes. We tuned the concentration of Zr by adjusting the number of holes with Zr inserts.

Two film-thickness monitors, placed on the same plate as the substrates, and at the same distance from the sputtering guns, monitor the deposition rates from the different

targets. These rates are measured for all guns being used, just before each multilayer is sputtered.

The motion of the sample plate, and the shutter assembly, are both controlled by a computer, which also calculates the time needed for depositing different layers to get the right thicknesses. The background pressure before admitting Ar gas is $\leq 2 \times 10^{-8}$ Torr. The Ar sputtering pressure is 2.5 mTorr. During sputtering, the substrates are held at temperatures (measured by a thermocouple on the SPAMA plate) between -30°C and 20°C . Each sample has its own separate mask, which protects the sample when other samples are being sputtering. A mask for the macroscopic samples is shown in Fig. 2.1A. Opening 1 is used to sputter the bottom Nb lead, opening 2 to sputter the multilayer, and opening 3 to sputter the top Nb lead. After the sample is finished, the mask is rotated back to the initial blocking position. A vacuum-compatible wobble stick allows in situ manual rotation of the mask into these four positions. Fig. 2.1B shows a finished macroscopic sample, onto which Indium contacts have already been soldered. Contacts to the sample from the SQUID-based measuring system (described elsewhere [29]) are made by pressing superconducting leads into the Indium contacts. Simple square CIP masks are used to prepare films for Van der Pauw [90] measurements and for sputtering microscopic samples.

Since the intrinsic quantity in the CPP geometry is the specific resistance, AR , we must also measure the area of overlap A of the two crossed superconducting strips. We do this using a Dektak surface profiler [44,45] to measure the widths of the two Nb leads. The area A is then just the product of their widths. Uncertainties in determining these widths lead to an uncertainty in the area of about $\pm 5\%$.

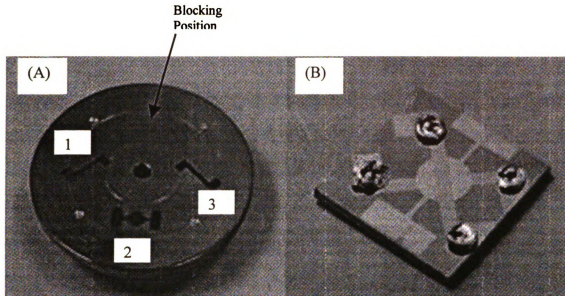


Fig. 2.1. (A) A CPP mask. A screw through the middle circular hole holds the mask in place, but allows it to be rotated. The three openings are used to sputter the bottom Nb (1), the multilayer (2), and the top Nb (3). The blocking position protects the sample before and after sputtering. (B) A finished sample with Indium blobs on the Nb strips.

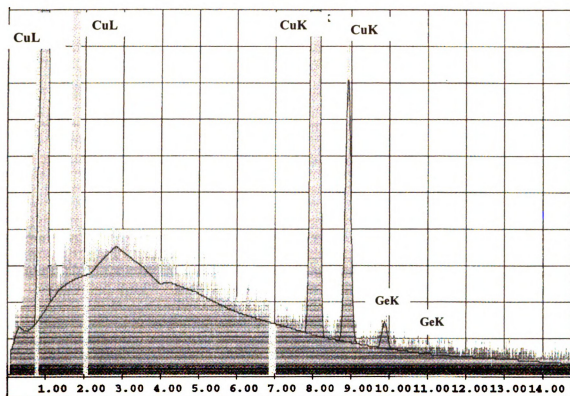
2.3 CHARACTERIZING SAMPLES

Samples are characterized by Electron Energy Dispersive X-Ray Scattering (EDX), resistivity measurements, and magnetization measurements. The periods of repeated multilayers are also checked with x-rays, examples of which are given elsewhere [44].

A) EDX Studies

EDX allows us to find the concentrations of impurities in alloys. High-energy electrons in an electron microscope hit the target film of interest, and some excite core electrons from target atoms. An electron from a higher energy level jumps down to the vacancy, emitting an x-ray photon with energy characteristic of the particular initial and final orbits and, thus, of the atom producing it. The x-rays are detected by a

crystal kept at liquid nitrogen temperature, and analyzed to determine the target composition. Sample x-ray spectra are shown in Figs. 2.2-2.4. Such spectra gave concentrations of CuGe = 2.5 ± 0.2 at. % and CoZr = 2.5 ± 0.2 at.% and 20 ± 1 %.

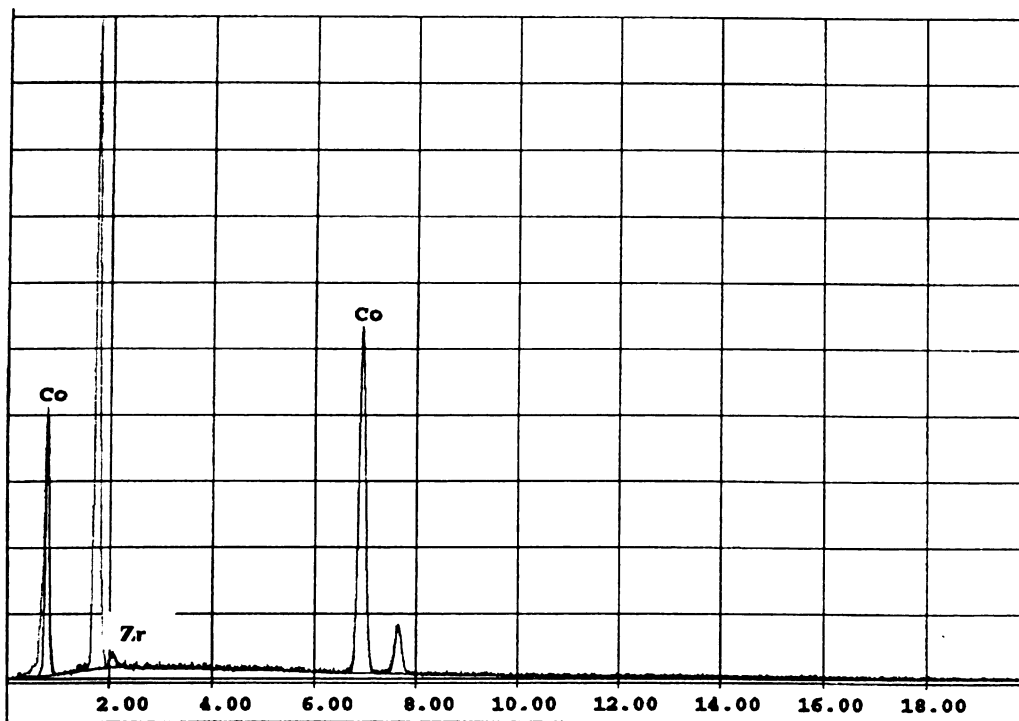


EDAX PhiRhoZ Quantification (Standardless)
Element Normalized

Element	Wt %	At %	K-Ratio	Z	A	F
CuK	97.22	97.56	0.9762	1.0013	0.9998	1.0030
GeK	2.78	2.44	0.0247	0.9522	0.9337	1.0000
Total	100.00	100.00				

Element	Net Inte.	Bkgd Inte.	Inte. Error	P/B
CuK	196.27	4.16	0.71	47.18
GeK	2.57	3.10	9.13	0.83

Fig. 2.2. EDX spectrum of a CuGe film. The table on the bottom shows the detailed analysis of the spectrum.

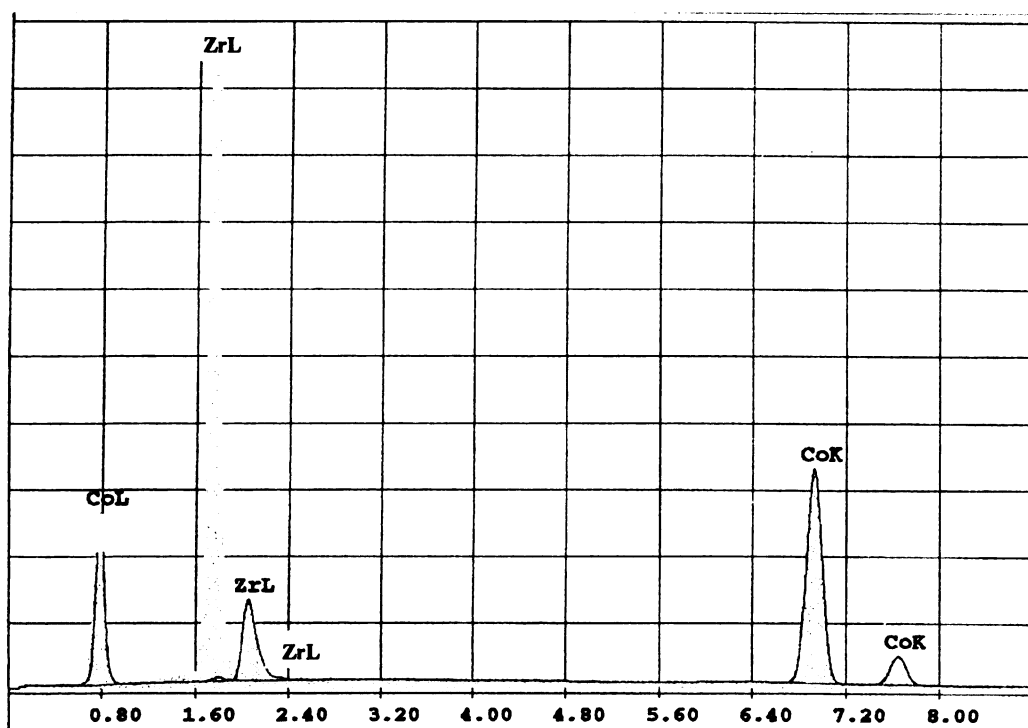


EDAX PhiRhoZ Quantification (Standardless)
Element Normalized

Element	Wt %	At %	K-Ratio	Z	A	F
ZrL	3.84	2.52	0.0210	0.9299	0.5875	1.0000
CoK	96.16	97.48	0.9610	1.0031	0.9962	1.0000
Total	100.00	100.00				

Element	Net Inte.	Bkgd Inte.	Inte. Error	P/B
ZrL	15.16	16.60	6.73	0.91
CoK	590.43	11.00	0.75	53.66

Fig. 2.3. EDX spectrum of a CoZr film, with a small concentration of Zr. The analysis on the bottom of the plot shows 2.5% Zr.



EDAX PhiRhoZ Quantification (Standardless)
Element Normalized

Element	Wt %	At %	K-Ratio	Z	A	F
ZrL	26.70	19.05	0.1665	0.9450	0.6600	1.0000
CoK	73.30	80.95	0.7302	1.0222	0.9745	1.0000
Total	100.00	100.00				

Element	Net Inte.	Bkgd Inte.	Inte. Error	P/B
ZrL	53.55	6.41	1.44	8.36
CoK	199.10	6.63	0.72	30.05

Fig. 2.4. EDX spectrum of a CoZr film. The percentage of Zr given by the analysis is 19%, which is expected to be well in the amorphous regime.

B) Resistivity

We separately measure the resistivities of all components of the multilayers to provide parameters for our fits and to check for reproducibility of the sputtered metals. We measure these resistivities by two methods: the Van der Pauw (VdP) method [44, 45] for all metals, and by sandwiching F-metals between superconducting strips.

VdP measurements are made at both 4.2 K and room temperature (RT), the latter used to check for reasonable values of the ‘phonon-resistivity’. For Nb, we also measure its superconducting transition temperature, T_C . Tables 2.1-2.4 contain detailed measured VdP resistivities for most of the metals and alloys used in this thesis. Table 2.5 contains a summary of the results with uncertainties (2 standard deviations).

Table 2.1. VdP resistivity and superconducting transition temperature of sputtered Nb. $T_C(\text{Nb})$ bulk ≈ 9.2 K.

Sample#	T	Thickness (\AA)	$\rho(\mu\Omega\text{cm})$	T_C (K)
1074-1a	room	3000	23.1	
1074-1a	12K		6.9	
1180-8b	12K	2000	5.5	9.1
1190-7b	12K	3000	5.1	9.15
1201-7b	room	3000	19.7	
1201-7b	12K		5.0	9.13

Table 2.2. VdP Resistivity of CuGe Films

Sample #	Description	Temp. (K)	ρ ($\mu\Omega$ cm)
1169-8a	CuGe(3000)	300	9.3
1169-8a	CuGe(3000)	4	7.4
1169-8b	CuGe(3000)	300	9.5
1169-8b	CuGe(3000)	4	7.5
1171-8b	CuGe(3000)	300	10.0
1171-8b	CuGe(3000)	4	8.0
1182-8a	CuGe(2000)	300	10.7
1182-8a	CuGe(2000)	4	8.7
1182-8b	CuGe(2000)	300	10.3
1182-8b	CuGe(2000)	4	8.3
1190-8a	CuGe(5000)	300	10.2
1190-8a	CuGe(5000)	4	8.2
1190-8b	CuGe(5000)	300	10.0
1190-8b	CuGe(5000)	4	8.0

Table 2.3. Van der Pauw Resistivities of Co, Py, Cu and Ag films. Last Column shows if each sample was sputtered at the beginning or end of each sputtering run.

sample#	material	t(nm)	$\rho_{room}(\mu\Omega cm)$	$\rho_{4.2K}(\mu\Omega cm)$	Order of sputtering
1150-8a	Co	225	13	6.1	beginning
1150-8b	Co	225	12.5	3.8	end
1151-8A	Co	270	12.8	6	beginning
1151-8B	Co	180	13.2	6.7	end
1152-8A	Co	300	11.3	4.1	end
1201-7a	Co	300	11.6	4.8	beginning
1201-8a	Co	300	11.4	4.4	end
1179-8a	Co	200	11.5	4.9	
1191-8a	Co	300	11.1	4.6	
1094-8B	Py	300		11.1	
1153-8A	Py	300	21.6	10.6	
1197-8a	Cu	500	2.71	0.7	beginning
1197-8b	Cu	500	2.68	0.8	end
1198-8a	Cu	500	2.94	1.1	beginning
1199-8a	Cu	500	3.15	1.2	middle
1198-8b	Ag	500	2.49	0.8	end
1199-8b	Ag	500	2.73	1.0	end

Table 2.4. Van der Pauw Resistivity of CoZr films

Sample#	Thickness (Å)	$\rho_{\text{Room}}(\mu\Omega\text{cm})$	$\rho_{4.2\text{K}}(\mu\Omega\text{cm})$
	Co_{97.5}Zr_{2.5}		
1007-8a	3000		20.6
1008-8a	3000		23.5
1042-8a	3000		20.3
1043-8b	3000		20.25
1040-8a	3000		20.9
1040-8b	3000		20
1074-1b	3000	28.9	21.1
1074-8b	3000	29.2	21.7
1089-8b	3000	30.8	22.8
1106-5a	3000		18.6
1106-5b	3000		17.7
	Co₈₀Zr₂₀		
1173-8a	3000	132.4	136.4
1173-8b	3000	132.6	136.1

For CoZr, Bass [91] and Campbell and Fert [46] list a resistivity increase of 4 $\mu\Omega\text{cm}$ per percent of Zr impurity, but this value is uncertain since it comes from only a single source. Assuming additivity of residual resistivities (Matthiessen's rule for alloying), and our measured value of $\sim 5 \mu\Omega\text{cm}$ for ρ_{Co} , our estimated values of ρ_{CoZr} for our nominally 2.5% Zr suggest a higher value of about 5 $\mu\Omega\text{cm}$ per atomic percent Zr.

Table 2.5. Average resistivities (in $\mu\Omega\text{cm}$) both at 4.2 K and room temperature.

Material	$\rho(4.2\text{K})$	$\rho(RT)$	$\Delta\rho = \rho(RT) - \rho(4.2\text{K})$	ρ_{Phonon} [91]
Nb	5.1 ± 1.6	20.6 ± 1.8	15.5	14.4
CuGe(2.5%)	8.0 ± 0.9	10.0 ± 1.0	2.0	1.65
Cu	0.96 ± 0.46	2.86 ± 0.50	1.9	1.65
Ag	0.9 ± 0.1	2.55 ± 0.15	1.65	1.6
Py	10.9 ± 0.3	21.9 ± 0.5	11	
Co	5.1 ± 1.9	12.1 ± 2.2	7	5.5
CoZr(2.5%)	21 ± 2	28.8 ± 2	7.8	5.5
Ru	≈ 8.5			

The residual resistivity at 4.2 K comes from scattering by imperfections in the metals and impurities in the alloys. $\rho(RT)$ has an extra contribution from scattering by phonons. The third column in Table 2.5 lists the measured increase in resistivity ($\Delta\rho$) for each metal. The fourth column lists the room temperature phonon resistivity (ρ_{Ph}) for the high purity metal from [91]. In all cases, $\Delta\rho$ and ρ_{Ph} are similar.

One exception from the observed increase of resistivity with temperature is $\text{Co}_{80}\text{Zr}_{20}$. For the $\text{Co}_{80}\text{Zr}_{20}$ alloy the room temperature resistivity is smaller than that of liquid helium temperature. Combined with a resistivity, $\rho > 100 \mu\Omega\text{cm}$, this behavior suggests an amorphous structure of those samples.

For F-metals or F-alloys, we also measure AR vs t for a sandwich structure of the form $\text{Nb}(100)/\text{F}(t)/\text{Nb}(100)$. The slope of the AR versus t gives the F-metal resistivity ρ_F , and the ordinate intercept is $2AR_{\text{Nb/F}}$. The sandwich method is limited to 4.2 K by the use of superconducting Nb leads. Fig. 2.5 shows that any magnetic field dependence of AR for sandwiched single F-layers is small. Fig. 2.6 shows AR vs t_{CoZr} for CoZr inserts. The CoZr plot shows that results with and without 10 nm inserts of Cu between the CoZr and the Nb are similar, strongly suggesting that the Cu becomes superconducting by

proximity with the superconducting Nb. Since the differences between data with and without Cu are modest, we fit both kinds of samples together to a single straight line, the slope of which is $\rho_{\text{CoZr}} = (19 \pm 1) \mu\Omega\text{cm}$. Happily, this value is consistent with the value of $\rho_{\text{CoZr}} = 21 \pm 2 \mu\Omega\text{cm}$ found from VdP measurements (table 2.5). This consistency is heartening, since the CPP and CIP resistivities of layers need not be identical, because of the columnar growth of the layers perpendicular to their layers [5]. The intercept with the ordinate axis is $2AR_{\text{CoZr/Nb}} = 5.8 \pm 1 \text{ f}\Omega\text{m}^2$, a value compatible both with the independent value of $6.5 \pm 1 \text{ f}\Omega\text{m}^2$ for Co/Nb shown in Fig. 2.7 and with earlier values [5]. Finally, Fig. 2.7 shows AR vs t_{Co} for Nb/Co/Nb sandwiches for two different sputtering runs. The intercept with the AR axis is already discussed above, and the slopes give $\rho_{\text{Co}} = 3.9 \pm 0.7 \mu\Omega\text{cm}$, consistent with the VdP value, $\rho_{\text{Co}} = 5.1 \pm 2 \mu\Omega\text{cm}$.

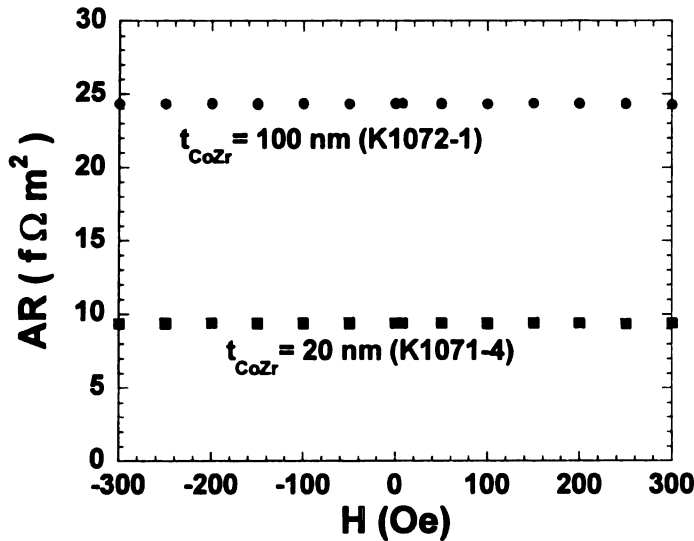


Fig. 2.5. AR of two different thicknesses of CoZr in Nb/CoZr/Nb sandwiches. Any dependence of AR on magnetic field H is small.

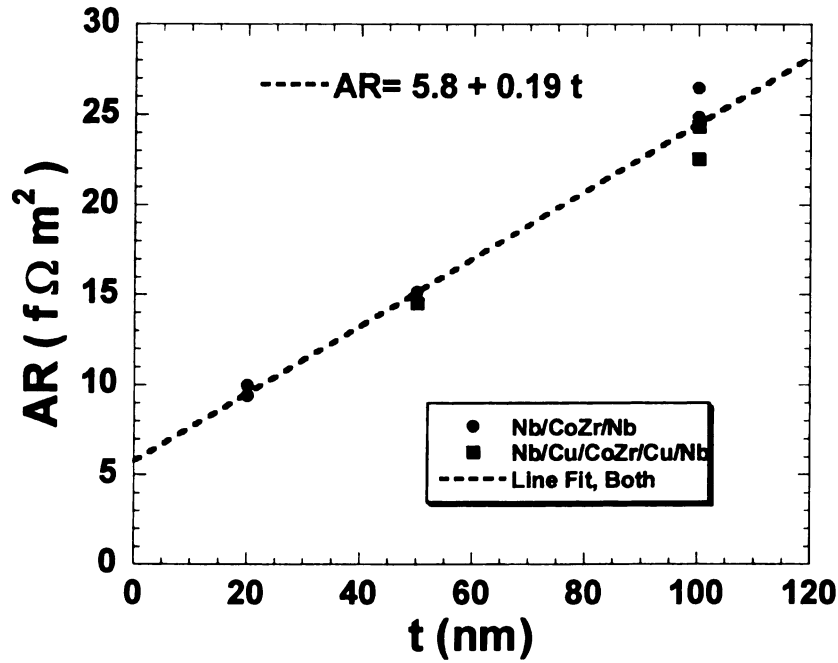


Fig. 2.6. Dependence of AR on t_{CoZr} . Samples both with and without Cu are used in the straight line fit. The fit gives $AR_{CoZr/Nb} = 5.8 \pm 1 f\Omega m^2$ and $\rho_{CoZr} = (19 \pm 1 \mu\Omega cm)$.

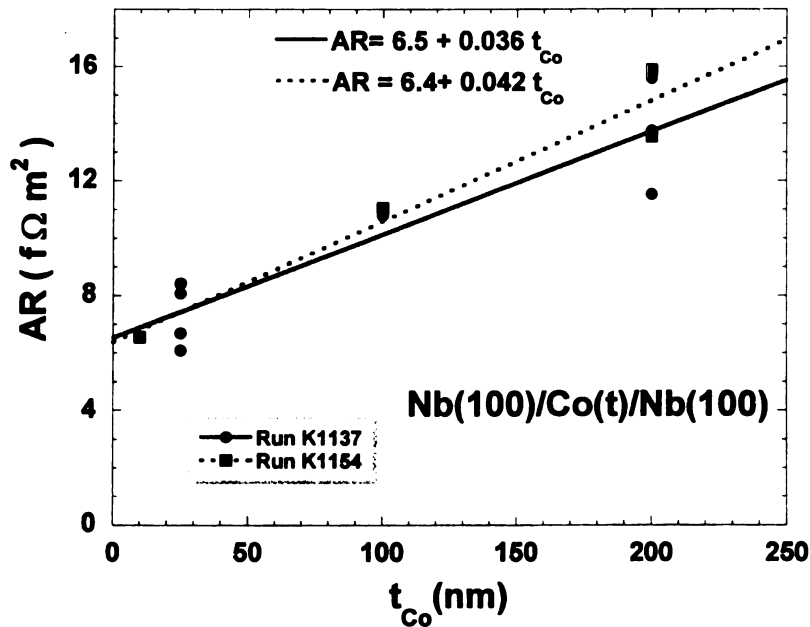


Fig. 2.7. AR versus t_{Co} for Nb/Co(t_{Co})/Nb sandwiches. Data are shown for two different sputtering runs. The two straight lines are best fits, giving an average value of $2AR_{Nb/Co} = 6.5 \pm 1 f\Omega m^2$, and $\rho_{Co} = 3.9 \pm 0.7 \mu\Omega cm$.

C) Magnetization

Finally, we also used magnetization measurements to determine the magnetic states of multilayers, switching fields, and to search for magnetically dead layers. Some magnetization studies are presented in Chapter 4, and the results of a search for magnetically dead layers in CoZr/Cu and CoZr/Ag multilayers will be described in Ch. 5.

2.4 MICROSCOPIC SAMPLES

Microscopic samples need far more care in preparing and handling than do large ones. After the sample is sputtered, most of the subsequent preparation is carried out in a class 100 Cleanroom facility in our department. Cleanroom atmosphere is required for such small samples, since a tiny piece of dust can ruin the whole device. Once samples are taken into the Cleanroom, they are only taken outside for ion milling followed by evaporating a SiO insulator and top contacts. Preparing microscopic-area samples involves a series of lithographic steps as well as thermal evaporation, sputtering, and ion milling.

Equal care has to be exercised while measuring the resistance of the finished pillar-shaped microscopic samples. Their high resistance and small size make a small instantaneous current flow due to the discharge of static electricity from the operator enough to destroy the sample. To avoid this possibility, all features are shorted until the connections to the measuring equipment are established. Only then is shorting removed and the measurement process started. Both before and during measurements, anyone handling the samples must be grounded.

In the following, we discuss briefly each step in the preparation process of the small samples, and characterization and measurement procedures.

2.4.1 Preparation

Step 1. Photolithography (Patterning the large Pads)

Before the multilayer sample is sputtered, current and voltage electrodes must be deposited onto the substrate. We use clean, single-crystal (100) Si wafers of 3" diameter to deposit electrodes simultaneously on as many as 18 of the 0.5"x0.5" substrates. We begin the process by spinning S1805 photoresist (PR) to get a thickness $t \sim 500$ nm. We then bake in an oven in ambient atmosphere at 95C for 45 minutes to remove the solvent material and harden the PR layer. The PR is sensitive to UV light, which breaks chains between molecules, making the exposed material easy to dissolve in a liquid called the developer (KOH). PR that has not been exposed to UV is less soluble in the developer. The wafer is then placed under UV (~ 3 seconds) through a Cr mask that blocks light from the substrate, except for the areas chosen to be the current and voltage pads. After selective exposure of the features, the wafer is immersed in the developer # (452) for 45 seconds. The developing process washes out the exposed PR, opening the Si surface to the outside but leaving the unexposed areas intact. After developing, the wafer is placed in a Phillips Thermal Evaporator where we evaporate ~ 1 nm of Ti followed by ~ 70 nm of Au under a vacuum $\sim 2 \times 10^{-7}$ Torr. The Ti layer is to improve the adhesion of the deposited Au to the Si substrate, since Au does not adhere strongly to SiO_2 .

We then put the wafer in acetone for some time. This step is called lift-off. Acetone dissolves the PR layer, washing out the metal layers on top of it and leaving only the metal layers (Ti/Au) that have landed directly on the Si surface.

At this stage the sample looks like Fig. 2.8. The light parts are Au electrodes that will carry the current to the sample and will be used to measure the voltage drop across the sample. The dark parts are where the Si substrate is not covered by Au.

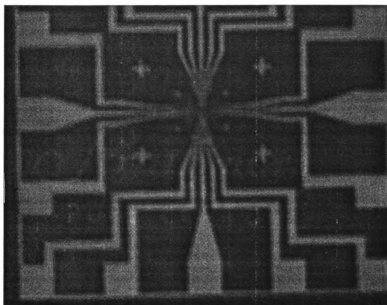


Fig. 2.8. Au electrodes deposited on a 0.5"x0.5" Si substrate using photolithography. The outside pads are large so that measuring electrodes can be connected to them. The small samples will be deposited in the middle of those electrodes. All the Au pads are connected to avoid shocking the sample; these connections are removed when the sample is ready to be measured. The crosses are alignment marks for subsequent steps.

The crosses in Fig. 2.8 are alignment marks that will be crucial in subsequent electron-beam lithography steps, where features must be aligned to within $\sim 0.1 \mu\text{m}$.

Step 2. Depositing the Multilayer

Since all our multilayers are prepared by sputtering, which produces an uncollimated flux of atoms, we need to have a large undercut. To obtain this undercut we use a bilayer of electron beam resist, Copolymer 9%/ PMMA 4%, where we first spin the Copolymer

9% for 60 seconds at 2500 RPM, bake it at 147° C and then expose it to an e-beam over a chosen area #1 (enclosed by the dashed line in Fig. 2.9A). This exposure step is followed directly by spinning PMMA 4% for 60 seconds at 3000 RPM, baking at 147° C for at least 1 hr, and then exposing the bilayer to an e-beam for a second time, but now over an area #2 (enclosed by the solid line in Fig. 2.9A), which is smaller than area #1 by 1 μ m on each side (see Fig. 2.9). Note that there was no developing after the first exposure. Proper alignment is essential for this and all other steps. The next step is developing, where the sample is dipped in EBL developer for 65 seconds, followed by Isopropanol for 30 seconds then water for 25 seconds. EBL attacks both PMMA and Copolymer, while Isopropanol mainly attacks Copolymer, adding to the undercut size. Since the bottom layer was originally exposed to the e-beam over a wider area than the top layer, all area #1 in the bottom layer gets dissolved, while the top only develops to the limits of the smaller area #2. This procedure gives a 1 μ m wide undercut, large enough for sputtering the multilayer and successful lift off, without any sharp edges that can make it impossible to deposit top contacts properly. If desired, the 1 micron undercut could be varied just by changing the borders of areas one and two in Fig. 2.9. Fig. 2.10 shows a picture of the sample at this stage, with the light areas around the developed feature indicating undercuts. We check for the presence and extent of the undercut by examining the sample under a photo-microscope. As an alternative, a trilayer layer technique involving Copolymer 9%/Al/PMMA 4%, was tried for this step. But the above technique proved to be easier and better for subsequent lift off.

The shape of the multilayer is chosen to allow for a large contact area with the bottom leads to reduce the contact resistance, but narrower in the middle to minimize the overlap

area between the bottom portion of multilayer left after ion milling (bottom electrode) and the top-contact leads. The smaller this overlap area, the less the chance of pinholes through the SiO insulating layer.

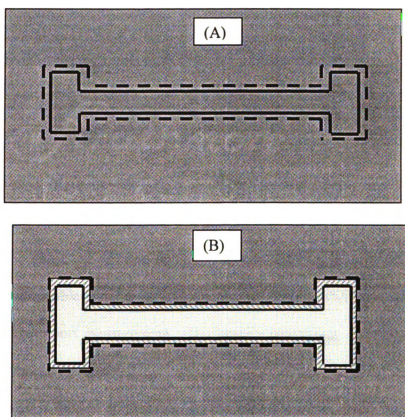


Fig. 2.9. (A) Schematic diagram of the double exposure to the electron beam. After baking the first layer, all the area enclosed by the dotted line is exposed to electrons. The area enclosed by the solid line is then exposed to electrons after spinning and baking the second electron-beam-resist layer. After developing, the part of the second layer between the dotted line and the solid line will be 'free hanging', creating an undercut. (B) shows what the substrate should look like after developing. The shaded area is the undercut.

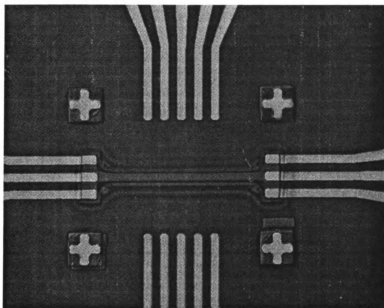


Fig. 2.10. Photomicroscope picture showing the undercut (discoloration of the top layer) of Fig. 2.9B. The electron-beam resist is washed out completely from the center area where the multilayer will be sputtered.

After developing, the sample is loaded into the sputtering system, and the multilayer is created. Starting from its bottom, the structure of the multilayer is: thick noble metal electrode/ thick bottom Co layer/ thin noble metal layer/ thin Co layer/ thick noble metal top cap. The bottom noble metal layer will not be ion milled and will provide the bottom electrode for the transport measurement. To simplify processing, the thick bottom Co layer will be only partially milled.

A shadow mask is used to sputter only on the middle portion of the sample, making the lift off easier. For lift off, samples are inserted into Acetone for nearly 1 hr, during which everything gets washed out except the multilayer in the area within the solid lines in Figs. 2.9A and 2.9B. Preparing the multilayer by sputtering is advantageous over evaporation, since the poor collimation leads to very smooth edges, which helps make the insulator cover the multilayer properly and make the top pads continuous.

Step 3. Ion Milling Mask (Al/Si bilayer or Al/Ti/Cu trilayer)

The next step is to create a sub-micron sized mask to protect the portion of the multilayer underneath, while unmasked parts are ion milled down to within the bottom Co layer. This mask has to be created using electron beam lithography and thermal evaporation. The first step is to spin a layer of Copolymer 9% at 3000 RPM for 60 seconds followed by baking at 147 °C for 1 hr. Then we spin a layer of PMMA 2% at 5900 RPM for 60 seconds and bake it at 147 °C for at least 1 hr. The use of PMMA 2% rather than 4%, and high spinning speed, are to minimize the thickness, to improve resolution and ultimately the size and shape of the mask feature. Five spots are then exposed to electron beam (since we have five masks or pillars on each multilayer). Careful focusing and correction for astigmatism are crucial in this step. The sample is then developed exactly as in step 2, and the mask is evaporated. Historically, this mask was either a bilayer of Al/Si or a trilayer of Al/Ti/Cu. Upon dipping the sample in photoresist developer (KOH), the Al dissolves much faster than the other materials, creating a mushroom-like undercut as shown for an Al/Ti/Cu trilayer in figure 2.11A, B, and C. It takes only 3 to 6 seconds to create a decent undercut. The creation of the undercut helps get a good top contact, as will be seen in the next section. Unlike in step 2, here we expose the bilayer of electron beam resist only once, since the mask material is evaporated and not sputtered.

Figs. 2.11 and 2.12 show an Al/Ti/Cu mask at this stage and a cartoon showing the ideal shape of the mask. The elongated shape of the mask is to impose shape anisotropy

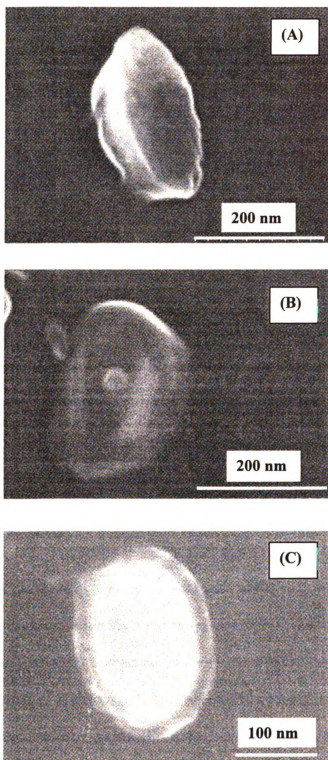


Fig. 2.11. SEM images of the Al/Ti/Cu masks. Masks were dipped in PR developer for 5 seconds. Ideally the mask should look like the mushroom shape shown in Fig. 2.12. In A and B the substrate was tilted by 30° . In C there is no tilt.

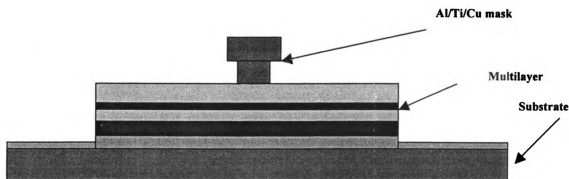


Fig. 2.12. Cartoon of the ideal shape of the Al/Ti mask after the short wet etching in PR developer. Ideally the mask would look a mushroom to protect the Al part from SiO₂ to be able to dissolve the mask after the ion milling and SiO₂ evaporation.

on the magnetic layers, which will take the shape of the mask, so that we have a single easy axis along the longer side, to control the magnetic states of the multilayer during measurements.

Step 4. Ion Milling and Insulator Evaporation

At this point, we could in principle, start ion milling the multilayer to shape the pillar-like samples. However, gold ion mills much faster than the multilayer, and our 75 nm thick gold electrodes would disappear before the sample was ion milled. To solve this problem, we protect the pads with a bilayer of electron beam resist, opening a small window through the resist around the multilayer by exposure to electrons and developing. All the area within the window gets ion milled, including the multilayer, but the covered gold pads remain protected by the electron beam resist. The electron beam resist bilayer is made of Copolymer 9% / PMMA 4%, baked, exposed, and developed as in step 3, except that the exposed area is the window that defines the ion milling area. During ion milling, the sample has to be anchored to a good heat sink, so that the sample temperature doesn't get too high. Overheating the sample can burn the electron beam resist, making it difficult to dissolve in acetone during lift off. Ion milling is performed after reaching a

background pressure $\sim 10^{-7}$ Torr, and samples are loaded using a magnetic arm to avoid breaking the vacuum. The Ar pressure during the ion milling is 3×10^{-4} Torr, and the voltage and current readings are 500 Volts and 20 mA, respectively. To insure reproducibility in our ion milling rates, we delay the milling until after the ion mill stabilizes. Unmasked parts of the multilayer are then ion milled all the way down to the bottom Co layer, which is only ion milled partly through. Leaving the bottom Co layer unpatterned helps controlling the magnetic state of both Co layers since it reduces the magnetostatic dipolar interaction that favors antiparallel coupling between patterned Co layers. The depth to which we ion mill through the multilayer is controlled by independently measuring the ion milling rates of all constituents of the multilayer. We measure the ion-milling rate for each metal by preparing films, spinning, and baking photoresist on it, exposing to UV radiation through a photo mask, then developing in KOH. Each film is then ion milled for some time, dipped in acetone to remove the photoresist, and the depth is measured using AFM or a Dektak. The ion-milling rate is the slope of the line of thickness versus time. Fig. 2.13 shows the ion milling results of Cu with a straight-line fit. The straight line does not go through zero but intercepts the time-axis, which seems to indicate a Cu oxide layer that ion mills slower than Cu. Table 2.6 shows the ion milling rates of other materials that we have measured. The error is taken from the scatter in the data (twice the standard deviation), or by trying two extreme fits, whichever is larger.

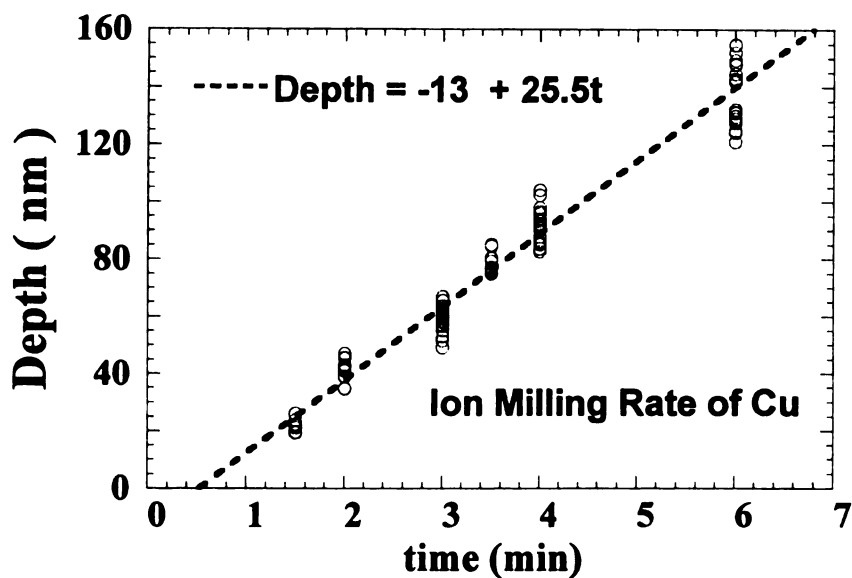


Fig. 2.13. Ion milling thickness as a function of ion milling time. The slope gives the ion-milling rate in nm/min. The intercept with the horizontal axis indicates the existence of an oxide layer that ion mills slowly on the Cu surface. The ion milling rate of Cu is (26 ± 1) nm/min.

Table 2.6. Ion-Milling rates of materials used in the lab

material	Rate (nm/MIn)
Cu	26 ± 1
Al	11 ± 2
Au	38 ± 2
Co	8.8 ± 0.4
FeMn	7 ± 2
Py	5.5 ± 2.5
Nb	3.0 ± 0.2

After the multilayer is ion milled and the pillar shapes created, we evaporate SiO onto the sample in the same chamber with the ion mill. The SiO is evaporated while the sample is rotating at 200 - 300 RPM, to minimize the chance of pinholes through the ~ 35

nm thick SiO layer. After evaporating the insulating SiO layer, the sample is dipped in acetone to wash out both the electron beam resist bilayer and the SiO over it, leaving SiO only in the window that was defined earlier by electron beam lithography. Finally, the sample is dipped in KOH for a few minutes, in hopes of completely dissolving the Al layer and exposing the top capping metal on the now pillar-shaped multilayer.

The sample at this stage is shown in figure 2.14. The dark rectangle surrounding the multilayer is the window opened using electron-beam lithography, which has been ion milled and then covered by a SiO insulating layer.

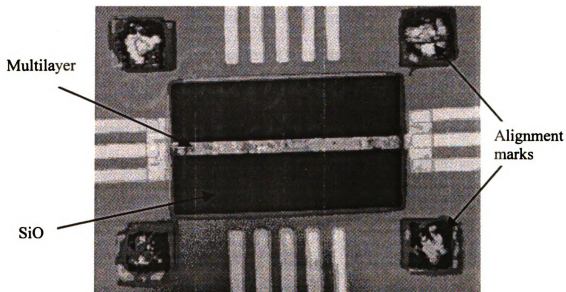


Fig. 2.14. Picture of a sample after the ion milling of the multilayer (the line in the middle) and depositing the SiO insulating layer. SiO is the dark rectangular window in the middle. There are four crosses on the corners of the picture (inside the dark squares) that serve as alignment marks during the electron beam exposure. These alignment marks are covered by SiO, which makes them less visible.

5) Top Contact

The top pads are also patterned using electron beam lithography. A bilayer of Copolymer 9% / PMMA 4 % electron beam resist is spun, baked, and exposed as in steps 3 and 4. We try to make as large as possible overlap or contact area between those top

pads and the original electrodes laid down using photolithography. The top pads are chosen narrow (3 microns), to reduce the chance of a short with the bottom electrode through possible pinholes in the insulator. After developing the sample, it is taken to the ion milling chamber, where a quick ion mill is performed to expose a fresh metal layer on top of the pillar capping layer. This milling is followed directly by evaporation of the top-contact metal, either Ag or Au, without breaking vacuum between the ion milling and evaporation. Evaporating immediately is important to minimize any oxide layers that would give a high contact resistance. As seen in figure 2.15 the only places where the top pads touch another metal are at the point of contact with the pillar multilayer, in the middle, and at both ends where they touch the extension pads. Only the middle portion of the sample is left open for the quick ion milling and for evaporation, since the whole sample is covered with an Aluminum-foil mask with a $\sim 2\text{mm}$ diameter hole in the middle. This masking makes lift off easier and faster. After lift off and removal of the electron beam resist bilayer and the metal covering it, the sample is ready to be measured.

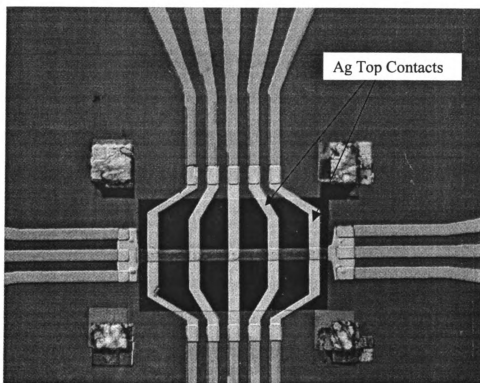


Fig. 2.15. A finished device ready to be measured. Each of the top contacts (5 Ag slabs) connects one of the top Au fingers with one from the bottom and, hopefully, has electrical contact with the top layer of the pillar in the middle. The pillars appear as dark spots in the middle of the overlap between the top contact and the multilayer.

2.4.2 Characterization

Characterization is most important during the lithography steps, as a lot of time can be wasted on undiscovered bad samples. Most characterization is done using the optical microscope in the clean room to inspect samples and check for proper developing time, adequate cleanliness, proper lift off, and basically any step in the lithography process. When trying to create the mushroom-shaped mask, sometimes the whole mask gets dissolved and the step needs to be repeated. Failure to do so would waste much time on a sample that can never work. Figs. 2.8, 2.10, 2.11, 2.14, and 2.15 are examples of pictures taking during preparation.

2.4.3 Measurement

As seen from Fig. 2.8, the Au pads are initially all shorted together. After the sample is prepared and ready to be measured, it is mounted in a quick dipper that has all of its terminals shorted and grounded as a precaution to not burn out the samples. The quick dipper has six current wires and six voltage wires, each of which can be shorted to the ground by a switch. The operator is also grounded by a bracelet to discharge any static electricity. Silver paint is used to connect the current and voltage wires to the Au pads on the sample. After the silver paint dries, the shorting connections between the different Au pads (see Fig. 2.8) are opened, after which they are electrically connected only through the pillar-shaped multilayer. After the Quick Dipper is attached to the current source, and the nanovoltmeter switched on, the particular current and voltage terminals to be used are opened to let current flow through the multilayer. The magnetic field, H , used to measure the $R(H)$ curves at room temperature is provided by an electromagnet with a computer controlled power supply. For $R(H)$, the voltage across the sample is measured six times; once at zero current, then two repeats at pre-selected positive current and the same-magnitude negative current, and finally at zero current. This procedure eliminates the effects of any offset in the nanovoltmeter. Switching of current direction for each measurement cannot be used for current-driven magnetization switching, because the current direction must be fixed. For measurements at 4.2 K the quick dipper is inserted into the liquid-helium dewar and a superconducting magnet is used to provide the magnetic field.

Chapter 3

THEORETICAL BACKGROUND

As described in Chapter 1, theoretical analysis of transport in F/N multilayers began with a phenomenological two-current model by Baibich et al. [1] in which electron spins never flip. Subsequently, more rigorous theories, both semi-classical and fully quantum mechanical, were developed [3,4], some including spin-flipping. Initial models addressed the CIP-MR, but since we study the CIP-MR only peripherally in this thesis, we do not go into those models, referring the interested reader to appropriate reviews [3]. Rather, we focus on analyses of the CPP geometry, where higher symmetry usually simplifies the analysis [3,4,26,47]. Since all of our experimental data are taken on samples with collinear magnetizations, we limit our discussion to calculations for which the layer magnetizations are mono-domain and collinear. It is convenient to divide the discussion in this chapter of models of the CPP-MR into two categories: free-electron based models involving diffuse scattering—essentially semi-classical models neglecting quantum size effects; and real Fermi surface based models, which are inherently fundamentally quantum mechanical. We describe the main features of, and issues underlying, these models in sections 3.1 and 3.2, respectively. In section 3.3, we provide a brief description of the concepts underlying a new phenomenon that can be viewed as the inverse of the CPP-MR, current-driven magnetization reversal.

3.1 FREE-ELECTRON-BASED SEMI-CLASSICAL MODELS

As first pointed out by Zhang and Levy [26], free electron analysis (i.e., assuming single parabolic conduction bands for both the F- and N-metals, but different scattering

times along with spin-dependent scattering in the F-metal), for the case of diffuse electronic transport and neglecting spin-flipping, together lead to a 2CSR model for the CPP-MR [26]. In this model, the only lengths are the layer thicknesses t_F and t_N , and all of the parameters (both ‘bulk’ and ‘interfacial’) that we defined in Chapter 1 are independent of the layer thicknesses. Valet and Fert (VF) used a Boltzmann equation formalism to extend this model to include spin-flipping within the N- and F-metals [47], adding as parameters the spin-diffusion lengths in the F- and N-layers, l_{SF}^F and l_{SF}^N . Later studies based upon the Kubo formalism or the Landauer-Buttiker formalism confirmed these results under the conditions specified. Another way to describe these models is to say that the 2CSR and VF models are expected to apply if the transport is diffuse and if scattering from adjacent interfaces is completely incoherent. For details see [3,4].

In Chapter I, we wrote down the 2CSR model equations (1.1-1.3) for a simple $[F/N]_N$ multilayer. For AR_{AP} we gave first the equation (1.1a) neglecting contacts, and then the equation (1.1b) including superconducting contacts. Eqs. 1.2 and 1.3 remain the same with or without the superconducting contacts, because such contacts just add a constant term to AR_{AP} .

In this section we analyze in detail the 2CSR model equations for a more complicated hybrid multilayer of the form $[F1/N/F2/N]_N$ (see cartoon in Fig. 3.1). We choose this more complicated multilayer because the simple $[F/N]_N$ multilayers were worked out in detail in other dissertations [44,45], because hybrid multilayers are used repeatedly in this thesis, and because the hybrid case has important differences with the simple case. The essential equations for a hybrid multilayer were first written down in [92]. We assume that the two F-metals have switching fields different enough to produce AP alignment, as

discussed in Ch.1. Fig. 3.1 shows the AP state, with arrows indicating the direction of magnetization of each metal.

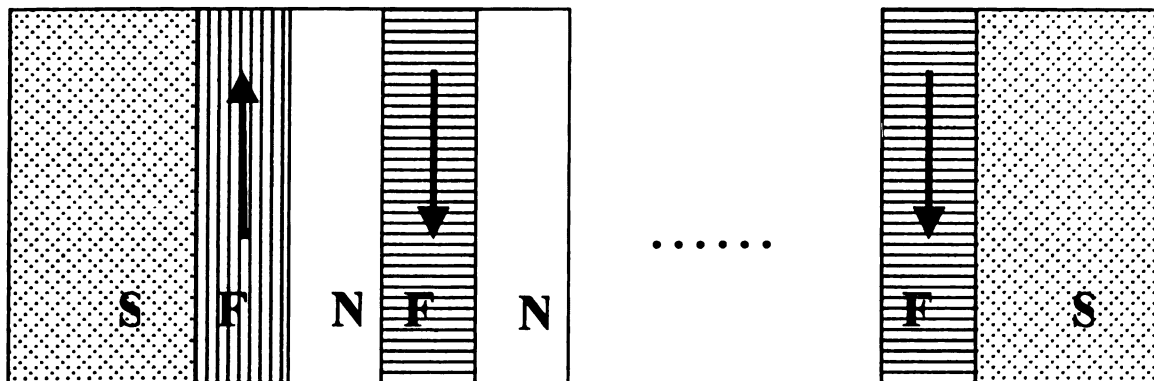


Fig. 3.1. Cartoon of an $[F1/N/F2/N]_N$ multilayer sandwiched between two superconducting layers, the arrows indicate the magnetization directions of the magnetic layers, showing an AP alignment.

The total CPP specific resistance, AR , in each of the AP or P states equals the parallel sum of specific resistances of the two spin channels; the specific resistance of each channel is the series sum of resistivities of individual layers times their thicknesses, plus the interfacial specific resistances.

AP State

In the AP state the total specific resistance for spin up electrons is:

$$AR_{AP}(up) = 2AR_{S/F}^{\uparrow} + 2N\rho_N^{\uparrow}t_N + N\rho_{F1}^{\uparrow}t_{F1} + 2NAR_{F1/N}^{\uparrow} + N\rho_{F2}^{\downarrow}t_{F2} + 2NAR_{F2/N}^{\downarrow}.$$

Using the conventions for $\rho_F^{\uparrow,\downarrow}$ and $AR_{F/N}^{\uparrow,\downarrow}$ in Chapter 1, and assuming that

$$AR_{S/F}^{\uparrow} = AR_{S/F}^{\downarrow} = 2AR_{S/F} \text{ and } \rho_N^{\uparrow} = \rho_N^{\downarrow} = 2\rho_N \text{ (i.e. no spin asymmetry in electron}$$

scattering in the normal metal or at the interface with the superconductor), gives :

$$\begin{aligned}
AR_{AP}(up) &= 4AR_{S/F} + 4N\rho_N t_N + 2N\rho_{F1}^* t_{F1}(1 - \beta_1) + 4NAR_{F1/N}^*(1 - \gamma_1) + \\
&\quad 2N\rho_{F2}^* t_{F2}(1 + \beta_2) + 4NAR_{F2/N}^*(1 + \gamma_2) \\
&= 2(2AR_{S/F} + 2N\rho_N t_N + N\rho_{F1}^* t_{F1} + 2NAR_{F1/N}^* + N\rho_{F2}^* t_{F2} + 2NAR_{F2/N}^*) \\
&\quad - 2[N\rho_{F1}^* t_{F1}\beta_1 + 2NAR_{F1/N}^*\gamma_1 - (N\rho_{F2}^* t_{F2}\beta_2 + 2NAR_{F2/N}^*\gamma_2)]
\end{aligned}$$

Similarly:

$$\begin{aligned}
AR_{AP}(down) &= 2(2AR_{S/F} + 2N\rho_N t_N + N\rho_{F1}^* t_{F1} + 2NAR_{F1/N}^* + N\rho_{F2}^* t_{F2} + 2NAR_{F2/N}^*) \\
&\quad + 2[N\rho_{F1}^* t_{F1}\beta_1 + 2NAR_{F1/N}^*\gamma_1 - (N\rho_{F2}^* t_{F2}\beta_2 + 2NAR_{F2/N}^*\gamma_2)]
\end{aligned}$$

The net specific resistance in the AP state is given by:

$$\frac{1}{AR_{AP}} = \frac{1}{AR_{AP}^{\uparrow}} + \frac{1}{AR_{AP}^{\downarrow}}$$

or

$$\begin{aligned}
AR_{AP} &= 2AR_{S/F} + 2N\rho_N t_N + N\rho_{F1}^* t_{F1} + 2NAR_{F1/N}^* + N\rho_{F2}^* t_{F2} + 2NAR_{F2/N}^* \\
&\quad - N^2 \frac{[\rho_{F1}^* t_{F1}\beta_1 + 2AR_{F1/N}^*\gamma_1 - (\rho_{F2}^* t_{F2}\beta_2 + 2AR_{F2/N}^*\gamma_2)]^2}{2AR_{S/F} + 2N\rho_N t_N + N\rho_{F1}^* t_{F1} + 2NAR_{F1/N}^* + N\rho_{F2}^* t_{F2} + 2NAR_{F2/N}^*}
\end{aligned} \tag{3.1}$$

P State

The same analysis for the AP state also applies for the P state giving:

$$\begin{aligned}
AR_P(up, down) &= 2(2AR_{S/F} + 2N\rho_N t_N + N\rho_{F1}^* t_{F1} + 2NAR_{F1/N}^* + N\rho_{F2}^* t_{F2} + 2NAR_{F2/N}^*) \\
&\quad \mp 2N[\rho_{F1}^* t_{F1}\beta_1 + 2AR_{F1/N}^*\gamma_1 + \rho_{F2}^* t_{F2}\beta_2 + 2AR_{F2/N}^*\gamma_2]
\end{aligned}$$

Thus:

$$\begin{aligned}
AR_P &= 2AR_{S/F} + 2N\rho_N t_N + N\rho_{F1}^* t_{F1} + 2NAR_{F1/N}^* + N\rho_{F2}^* t_{F2} + 2NAR_{F2/N}^* - \\
&\quad N^2 \frac{[\rho_{F1}^* t_{F1}\beta_1 + 2AR_{F1/N}^*\gamma_1 + \rho_{F2}^* t_{F2}\beta_2 + 2AR_{F2/N}^*\gamma_2]^2}{2AR_{S/F} + 2N\rho_N t_N + N\rho_{F1}^* t_{F1} + 2NAR_{F1/N}^* + N\rho_{F2}^* t_{F2} + 2NAR_{F2/N}^*}
\end{aligned} \tag{3.2}$$

$A\Delta R = AR_{AP} - AR_P$ is then given by [92].

$$A\Delta R = 4N^2 \frac{(\rho_{F1}^* t_{F1}\beta_1 + 2AR_{F1/N}^*\gamma_1)(\rho_{F2}^* t_{F2}\beta_2 + 2AR_{F2/N}^*\gamma_2)}{2AR_{S/F} + 2N\rho_N t_N + N\rho_{F1}^* t_{F1} + 2NAR_{F1/N}^* + N\rho_{F2}^* t_{F2} + 2NAR_{F2/N}^*} \tag{3.3}$$

Much of this thesis is built around this equation, which allows the applications potential of a given multilayer to be evaluated by estimating the sizes of its AR_{AP} and $A\Delta R$.

Examining the equation reveals a few important features:

- 1) The only length scales are t_{F1} , t_{F2} and t_N .
- 2) i) The last term in equation 3.1 is very small ($\approx 0.1 \text{ f}\Omega\text{m}^2$ for $[\text{Co}(6)/\text{Cu}(20)/\text{Co}(1)/\text{Cu}(20)]_6$, layer thicknesses in nm) and can be ignored, making AR_{AP} equal to the denominator of equation 3.3 for $A\Delta R$.
ii) Doping the N layer with a dopant that increases the resistivity and leaves the spin-diffusion-length l_{SF}^N unchanged increases AR_{AP} by the difference in resistivity multiplied by the thickness of the normal metal, and decreases $A\Delta R$ accordingly, but does not make any other difference.
- 3) If one of the ferromagnetic metals (or interfaces) has negative asymmetry parameters (both β and δ), and the other has positive ones, $A\Delta R$ becomes negative and the CPP-MR becomes ‘inverse’—i.e., $AR_{AP} < AR_P$. If one metal has positive parameters and the other has one positive and one negative, then whether AR is normal or inverse depends upon the thickness of that metal—i.e., upon the relative magnitudes of $\beta_F \rho_F^* t_F$ and $2\gamma_{F/N} AR_{F/N}^*$ for that F-metal.
- 4) $A\Delta R$ can be enhanced by any of the following:
 - i) Doping F metals with impurities that increase β and/or ρ^* .
 - ii) Creating more interfaces in the multilayer. (This is most efficient in Co/Cu systems where the bulk Co contribution is small).
 - iii) Eliminating terms that contribute to the denominator but not the numerator (e.g. $2AR_{S/F}$).

The 2CSR model assumes no spin flipping anywhere in the multilayer. We now consider a simple $[F/N]_N$ multilayer as in Ch. 1, but when the spin-diffusion lengths in the F-metal, l_{SF}^F , or the N-metal, l_{SF}^N , or both, become comparable to the layer thicknesses t_F or t_N . The equations must then be generalized as described by VF [47]. The VF analysis should apply at low temperatures, where electron-magnon and electron-phonon scattering are both frozen out, so that there is still no mixing of the two-currents. However, spin-flipping due to spin-orbit or spin-spin scattering is now allowed.

VF showed that, in the limit where $l_{SF}^F \gg \lambda_F$ and $l_{SF}^N \gg \lambda_N$, the Boltzmann equation for CPP transport through a multilayer reduces to a pair of macroscopic transport equations (with corrections of order λ/l_{SF} , which are usually expected to be small in metals).

$$\frac{e}{\sigma_s} \frac{\partial J_s}{\partial z} = \frac{\overline{\mu_s} - \overline{\mu_{-s}}}{l_s^2} \quad (3.4)$$

$$J_s = \frac{\sigma_s}{e} \frac{\partial \overline{\mu_s}}{\partial z} \quad (3.5)$$

Here σ_s is the conductance, μ_s the electrochemical potential, l_s the spin-diffusion length, and J_s the current density, all in channel s ($s = \text{up or down}$). Each of the above equations applies locally to every individual layer in the multilayer.

The first equation is a statement of the balance between spin accumulation and spin flipping over the length scale l_s , and the second equation is Ohm's law. The above equations include only macroscopic parameters (i.e. σ_s and l_s) and are, accordingly, called macroscopic equations. Eqs. 3.4 and 3.5 are to be solved in each layer and the solutions matched at the layer interfaces to fix the integration constants involved.

The interfacial boundary conditions are:

$$J_S(z = z_i^+) = J_S(z = z_i^-) \quad (3.6)$$

$$\mu_S(z = z_i^+) - \mu_S(z = z_i^-) = AR_S J_S(z = z_i) \quad (3.7)$$

where z_i is the position of the i^{th} F/N interface.

Equation 3.6 assumes no spin flipping at interfaces (i.e. the components of current in each spin channel are conserved at F/N interfaces) and equation 3.7 expresses the discontinuity of the electrochemical potential due to interface resistance (i.e. the change in electrochemical potential equals current, J times specific resistance, AR , which is just Ohm's law). Solving the coupled equations 3.4 and 3.5 subject to boundary conditions 3.6 and 3.7 in each layer yields complicated expressions for CPP resistance, even for the special cases of P or AP. For infinite multilayers VF derived the following equations:

$$AR_{(P,AP)} = N(AR_0 + 2AR_{(P,AP)}^{\text{SI}}) \quad (3.8)$$

$$\text{where } AR_0 = (1 - \beta^2)\rho_F^* + \rho_N t_N + 2(1 - \gamma^2)AR_{F/N}^*. \quad (3.9)$$

$$AR_P^{\text{SI}} = \frac{\frac{(\beta - \gamma)^2}{\rho_N l_{\text{SF}}^{\text{N}}} \coth\left[\frac{t_N}{2l_{\text{SF}}^{\text{N}}}\right] + \frac{\gamma^2}{\rho_F^* l_{\text{SF}}^{\text{F}}} \coth\left[\frac{t_F}{2l_{\text{SF}}^{\text{F}}}\right] + \frac{\beta^2}{AR_{F/N}^*}}{\frac{1}{\rho_N l_{\text{SF}}^{\text{N}}} \coth\left[\frac{t_N}{2l_{\text{SF}}^{\text{N}}}\right] + \frac{1}{\rho_F^* l_{\text{SF}}^{\text{F}}} \coth\left[\frac{t_F}{2l_{\text{SF}}^{\text{F}}}\right] + \frac{1}{AR_{F/N}^*} \left\{ \frac{1}{\rho_N l_{\text{SF}}^{\text{N}}} \coth\left[\frac{t_N}{2l_{\text{SF}}^{\text{N}}}\right] + \frac{1}{\rho_F^* l_{\text{SF}}^{\text{F}}} \coth\left[\frac{t_F}{2l_{\text{SF}}^{\text{F}}}\right] \right\}} \quad (3.10)$$

$$AR_{AP}^{SI} = \frac{\frac{(\beta - \gamma)^2}{\rho_N l_{SF}^N} \tanh\left[\frac{t_N}{2l_{SF}^N}\right] + \frac{\gamma^2}{\rho_F^* l_{SF}^F} \coth\left[\frac{t_F}{2l_{SF}^F}\right]}{\frac{1}{\rho_N l_{SF}^N} \tanh\left[\frac{t_N}{2l_{SF}^N}\right] + \frac{1}{\rho_F^* l_{SF}^F} \coth\left[\frac{t_F}{2l_{SF}^F}\right] + \frac{1}{AR_{F/N}^*} \left\{ \frac{1}{\rho_N l_{SF}^N} \tanh\left[\frac{t_N}{2l_{SF}^N}\right] + \frac{1}{\rho_F^* l_{SF}^F} \coth\left[\frac{t_F}{2l_{SF}^F}\right] \right\}} \quad (3.11)$$

When $l_{SF} \gg t$ in both ferromagnetic and normal metal layers, these equations reduce to the simple 2CSR model formulae for resistance.

For finite numbers of layers, the VF equations must be solved numerically on a computer. Each layer is characterized by its resistivity (or resistivities for the F-layer) and two lengths, the layer thickness and the layer spin diffusion length l_{SF} . At the layer boundaries, the chemical potentials and currents are matched, taking account of interfacial specific resistances where needed but neglecting any interfacial spin memory loss. For later use, and to try to clarify some significant behaviors, we consider a few cases in which the VF equations simplify.

Limiting Cases

(1) As already noted, when $l_{SF}^F \gg t_F$ and $l_{SF}^N \gg t_N$, the VF equations reduce to the 2CSR model equations 1.1 – 1.3.

(2) When $l_{SF}^F \ll t_F$ in a multilayer, the VF equations reduce to a set of simple resistors in a series-parallel combination, as shown in Fig. 3.2. Each resistor consists of a parallel combination of two entities, each N-layer, the two bounding F/N interfaces, and those portions of the adjacent F-layers within l_{SF}^F of the interface. These parallel combinations are coupled in series by the central $(t_F - 2l_{SF}^F)$ of each F-layer with an ‘unenanced’ F-layer resistivity, ρ_F .

(3) In an F/N/F trilayer with given l_{SF}^{N} , and only t_{N} allowed to vary, $A\Delta R$ decays as

$A\Delta R \sim e^{-\left(\frac{t_{\text{N}}}{l_{\text{SF}}^{\text{N}}}\right)}$. This observation will be used in Ch. 6 to measure l_{SF}^{N} in Ru, and a similar argument for interfaces will be used to measure spin-memory-loss at Cu/Ru interfaces.

(4) In an F/N/F trilayer, or an EBSV, if $l_{\text{SF}}^{\text{F}} \ll t_{\text{F}}$, the VF analysis modifies Eq. 1.2

$$\text{to: } A\Delta R = 4 \frac{(\beta_{\text{F}} \rho_{\text{F}}^* l_{\text{SF}}^{\text{F}} + \gamma_{\text{F/N}} AR_{\text{F/N}}^*)^2}{2\rho_{\text{F}}^* l_{\text{SF}}^{\text{F}} + \rho_{\text{N}} t_{\text{N}} + 2AR_{\text{F/N}}^*} \quad (3.12)$$

Comparing Eq. 3.12 with Eq. 1.2 shows that the ‘MR-active’ region has been reduced to just the central N-layer, its two interfaces with the F-layers, and the portions of the two F-layers within l_{SF}^{F} of the central N-layer. In the numerator, this reduced MR-active region means that t_{F} is replaced by l_{SF}^{F} . In the denominator, everything outside of this MR active region disappears; i.e. $AR_{\text{FeMn/F}}$, $AR_{\text{S/F}}$, and the contributions from the two F-layers beyond l_{SF}^{F} , are all gone. An initially surprising consequence of these changes is that the denominator can decrease more than the numerator increases, thus increasing $A\Delta R$ (i.e., $A\Delta R$ for finite l_{SF}^{F} is larger than $A\Delta R$ for $l_{\text{SF}}^{\text{F}} = \infty$). We caution, however, that AR_{AP} does not similarly decrease, but retains exactly the same form as in Eq. 1.1.

(5) Finally, by analogy to item (4), $A\Delta R$ can be increased by removing the contributions to the denominator of $A\Delta R$ of large ‘lead resistances’ by judicious insertion of a source of strong spin-memory-loss (SSML). An example of such an SSML would be a 1 nm thick layer of FeMn, which has been shown to produce > 99% ‘spin-memory-loss’ [73]. If the leads are normal-metals, thin FeMn layers can be inserted near to the outer edges of the multilayer, constraining the MR active region to between themselves,

and removing all of the lead resistance ‘outside of themselves’. If the leads are superconducting, then their contribution $2AR_{S/F}$ might be replaced by a smaller $2AR_{F/FeMn}^*$. An example of such a result when FeMn was inserted within a Py-layer was given in [85]. In this thesis we examine what happens when FeMn is inserted into the Cu layers (assumed initially superconducting) separating Nb leads from the outer F-layers of a sample.

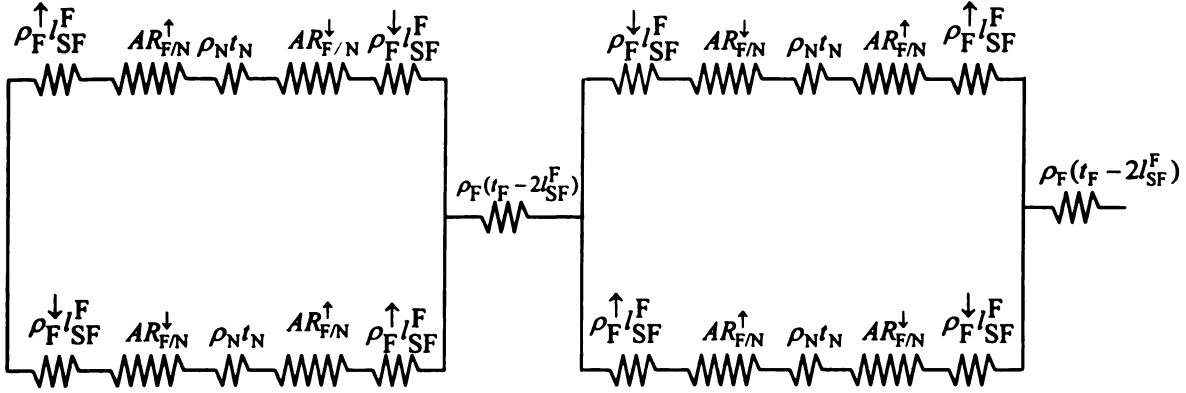


Fig. 3.2. 2CSR model representation of the multilayers when $l_{SF}^F \ll t_F$. The two spin channels mix completely in the middle of each ferromagnetic layer then split at around l_{SF}^F from the F/N interface. So the two spin channels are no longer independent.

Spin-Flip Scattering at Interfaces

As noted above, the original V-F model neglected spin-flipping at F/N interfaces. Including spin flip scattering at interfaces requires modification of either the equations or the analysis procedure. Fert and Lee [93] generalized the VF model to allow for interfacial spin-memory loss by replacing equations 3.6 and 3.7 by:

$$[J_S(z_i^+) - J_S(z_i^-)] - [J_{-S}(z_i^+) - J_{-S}(z_i^-)] = \frac{1}{AR_b^{SF}} \overline{(\mu_{-S} - \mu_S)_{z_i}} \quad (3.13)$$

$$\mu_S(z_i^+) - \mu_S(z_i^-) = r_S \overline{J_S(z_i)} \quad (3.14)$$

where

$$\overline{J_S(z_i)} = \frac{J_S(z_i^+) + J_S(z_i^-)}{2} \quad (3.15)$$

and $\overline{(\mu_{+S} - \mu_{-S})_{z_i}}$ is also the mean value of $\mu_{+S} - \mu_{-S}$ at z_i

AR_b^{SF} is a boundary specific resistance associated with spin-flip scattering at the interface

$$(\text{no spin flipping} \Rightarrow \frac{1}{AR_b^{SF}} \rightarrow 0).$$

In Eq. (3.13), the current in each spin channel is no longer conserved at interfaces. The discontinuity in current is due to spin flipping, which causes relaxation of spin accumulation at interfaces. Of course the total current, J , is still conserved and uniform over the multilayer (i.e. $J_+ + J_- = J$).

We at MSU developed a different approach to treat spin flipping at interfaces [73]. In studies of spin-memory-loss at N1/N2 interfaces (i.e. the interfaces between two different normal metals) the interface was treated as a homogeneous slab of N1N2 alloy of finite thickness, t_I , resistivity, ρ_I , and spin-diffusion-length, l_{SF}^I . This extra interfacial ‘layer’ is subject to the constraint:

$$\rho_I t_I = AR_{N1/N2} \quad (3.16)$$

The strength of spin flipping at N1/N2 interface is measured by a quantity δ defined as

$$\delta = \frac{t_I}{l_{SF}^I}. \quad (3.17)$$

The spin-flip probability at N1/N2 = $e^{-\delta}$. This additional ‘layer’ is then treated as an extra layer in the multilayer, except that the ‘interfaces’ N1/N1N2 and N1N2/N2 are assumed ‘transparent’ (i.e. have zero AR). Because the thickness t_I can be factored out of the

constraint equations 3.15 and 3.16, it has no effect on the outcome of this analysis and can be chosen arbitrarily.

In the present thesis, we have adapted this model to include F/N interfaces. Since the F/N interface has a spin-direction dependent specific resistance, we simply assume that the interfacial FN alloy has a bulk anisotropy parameter β_I , chosen equal to γ , and apply numerical analysis similar to that used for the N1/N2 interfaces. For simplicity of presentation, we describe all of the effects of our inclusion of interface spin-flipping in VF theory in Ch. 4. There we not only use it to analyze data on ‘interleaved’ and ‘separated’ hybrid multilayers, but also show that adding a modest spin-memory-loss at F/N interfaces ($\delta_I \sim 0.25$) does not strongly perturb our prior analyses of $[\text{Co/Cu}]_N$ and similar ‘simple’ multilayers in which we neglected any such loss, but does more significantly perturb the analysis of Co/Cu EBSVs.

3.2 REAL FERMI SURFACE EFFECTS

Bauer and coworkers [4,94,95] have argued that the first issue to be considered concerning real Fermi surface effects is whether the scattering from adjacent interfaces is coherent or incoherent. If it is incoherent, then the specific resistances of neighboring interfaces are independent of each other and simply additive. In the absence of spin flipping, one then ends up with a 2CSR model, with only the parameters changed from their free electron values. In support of such a picture for real multilayers, Stiles [96] and Xia et al. [95] showed that no-free-parameters calculations of AR for ‘single interfaces’ in Ag/Au and Co/Cu agree with the reported experimental values [5] to within mutual uncertainties.

If, however, scattering from adjacent interfaces is at least partly coherent, then the contributions to AR from these interfaces will not be simply additive. The total specific resistance, AR_T , will then, in general, depend upon the separations between interfaces, more specifically upon the ratios of those separations to the mean-free-paths in the N- and F-layers. If, to simplify, one assumes that the thickness t_F of the F-layer is longer than its mean-free-paths, but that the thickness t_N of the N-layer can be varied from shorter than to longer than its mean-free-path, then AR_T should vary with t_N . Because the specific resistance of two interfaces, $2AR_{F/N}$, is usually much larger than the specific resistance ($\rho_N t_N$) of the N-layer, this change in AR_T can be viewed as a change in the interface resistance. Various aspects of such phenomenon have been discussed by several authors [4, 97-99]. For convenience, we follow [89] in calling such effects ‘mean-free-path’ effects. In Ch. 4 we will test a claim in [89] of having observed such effects.

3.3 HIGH CURRENT DENSITY EFFECTS ON MAGNETIZATION

In a pioneering work, Slonczewski [15] and Berger [16] predicted that a spin polarized current can generate magnons or completely reverse (switch) the magnetization direction. Tsoi et. al. [17,18] soon observed magnon generation, and then the Cornell group [19] observed the magnetization reversal. The large current densities needed for both phenomena prohibit observing them in samples with superconducting contacts.

As discussed in Ch.1, two different processes can cause magnetization switching in pillar-shaped samples with submicron areas (nanopillars). The first is the helical magnetic field, or self field, induced by the current, and the second is associated with spin transfer. Both the self field and the spin transfer effects compete and can be observed in the same

current range or different ranges depending on the magnetic parameters of the materials and the diameter of the nanopillar. The dominating process in a given sample can be determined experimentally (see Ch. 1) from the shape of the $R(I)$ curve, which is symmetric around zero for self-field switching and asymmetric for spin-transfer.

3.3.1 Spin-Transfer Switching

When Slonczewski predicted the spin transfer switching of magnetization, he attributed it to spin transfer from the polarized current to the local magnetization, which exerts a torque on both of the ferromagnetic layers. He assumed ballistic transport, that the minority electrons will get totally reflected from the Co layer, and that the majority electrons will go through it without scattering (perfect spin filters). The component of electron spin perpendicular to the magnetization gets reflected at the Co/Cu interface and is responsible for the spin transfer to the local magnetization; thus if the magnetizations of both layers are collinear there will be no spin-transfer switching. Slonczewski used a trilayer of thick Co/spacer Cu layer/thin Co layer. The advantage of having the thick layer is that it needs a very large current density to switch and can thus be considered fixed. When electrons are flowing from the thick Co layer to the thin, the majority electrons emerging out of the thick Co will exert a torque on the thin layer to switch it to the parallel alignment with the thick layer. When the current direction is reversed, the minority electrons that get reflected at the Co/Cu interface between the thick Co layer and the Cu spacer layer will go back to the thin Co layer and switch it in the direction opposite to the thick layer's magnetization. This way, one magnetization state is

stabilized for each polarized current flow direction. The equation of motion of the magnetization of the thin Co layer in the Slonczewski model is:

$$\frac{d\hat{S}}{dt} = \hat{S} \times \left\{ \gamma [H_{eff} \hat{C} - 4\pi M (\hat{S} \cdot \hat{b}) \hat{b}] - \alpha \frac{d\hat{S}}{dt} - \frac{Ig(\theta)}{e|\hat{S}|} \hat{C} \times \hat{S} \right\} \quad (3.18)$$

In this equation, \hat{S} is the spin direction of the F layer, M is the magnetization, \hat{C} is the easy axis of magnetization, I is the current, α is damping coefficient, γ is the gyromagnetic ratio, \hat{b} is the direction perpendicular to thin film, and $g(\theta)$ is a coefficient that depends on the current polarization. In the absence of damping ($\alpha = 0$) and if $Ig(\theta) = 0$ the solution of the above equation is steady elliptic precession of spin around C axis, with time-independent amplitude, A . Magnetic damping, the second term in the above equation, damps A as time passes. On the other hand, the spin-transfer term, the last term, can amplify or damp A , depending on the current direction. The critical currents for switching are:

$$I_C^{AP} = I_C^+ = \alpha \gamma e |\hat{S}| [H_{eff}(0) + 2\pi M] / g(0) \quad (3.19)$$

$$I_C^P = I_C^- = \alpha \gamma e |\hat{S}| [H_{eff}(\pi) - 2\pi M] / g(\pi) \quad (3.20)$$

An applied magnetic field will favor the parallel alignment, making it harder to switch the magnetizations by spin transfer. This causes both I_C^+ and I_C^- to shift in the same direction (i.e. towards more positive values, according to our convention of current direction). When the external field is large enough, it is no longer possible to switch the magnetization completely. Rather, the current will excite steady spin waves in the magnetic layer. The excitation of spin waves shows up as a spike in the dV/dI curve

because the spin waves reduce the parallel component of magnetization, making AR intermediate between that of parallel and antiparallel.

Weintal and coworkers [88] generalized the Slonczewski approach to include both the ballistic and diffuse scattering regimes.

Heide [86] argued that spin induced switching occurs due to the exchange interaction between the spin accumulation and the F (Co) metal. This interaction, according to Heide, creates an effective field that favors either the ferromagnetic or antiferromagnetic coupling between the two Co layers, depending on the current flow direction, and is called nonequilibrium exchange interaction (NEXI). This effective field interaction is very similar to the RKKY interaction, but is not oscillatory—i.e. only one magnetization state is energetically favored for each current direction. Heide argued that the length scale for the spin accumulation-induced effective field is the spin-diffusion-length and that the second Co layer was not needed for the switching of the first, provided that the current is spin polarized.

Recently, Zhang, Levi, and Fert [87] argued that both the spin transfer (spin torque) and the effective field mechanisms occur on equal footing in the exchange interaction. They included the exchange interaction between local moments and spin accumulation of conduction electrons to study the current induced switching in the diffuse transport regime. Another significant finding of Zhang et al. was that the component of spin accumulation perpendicular to the magnetization was the important one and that the length scale over which it relaxes is $\sim 1\text{-}2$ nm. The Zhang et al. model requires two ferromagnetic layers, which have to be noncollinear to produce spin induced switching. Those findings are at odds with the Heide argument that the longitudinal component of

spin accumulation matters and that the appropriate length scale is the spin-diffusion-length, $l_{\text{SF}}^{\text{Co}} \sim 60 \text{ nm}$.

Thus, it remains for experiments to sort out what actual processes dominate the polarized current switching of the magnetization, and what length scales are relevant to those processes. Since we do not yet have a set of systematic samples to do so, we will not go into details of those theories any further.

Chapter 4

SEARCH FOR MEAN-FREE-PATH EFFECTS IN THE CPP-MR

4.1 INTRODUCTION

In the CIP-MR, the mean-free-paths in the N-metal, λ_N , and those for electrons with moments along, λ_F^\uparrow , or opposite to, λ_F^\downarrow , the F-layer magnetization are characteristic lengths [3]. In contrast, in the CPP-MR, according to the theory of Valet and Fert (VF) [47, Ch. 3] the only scaling lengths are the spin-diffusion lengths (spin-flip lengths) in the N- and F-metals, l_{SF}^N and l_{SF}^F . The mean-free-paths appear only indirectly through the layer resistivities, which are parameters in the CPP analysis. Since scattering events with spin-flips are usually only a fraction of all scattering events, l_{SF} is normally expected to be longer than λ . When these lengths are much longer than their respective layer thicknesses, $l_{SF}^N \gg t_N$, and $l_{SF}^F \gg t_F$, they drop out of the CPP-MR, yielding a simple two-current series resistor (2CSR) model. In the 2CSR model, the only lengths are the layer thicknesses t_N and t_F , which appear only algebraically. As described in Ch. 1, this dependence only on t_N and t_F was tested early on by comparing data in the square root form of Eq. 1.3 for samples with the same F-metal, Co, but different N-metals, Cu vs Cu(4%Ge) or Ag vs Ag(4%Sn), that changed λ_N by up to a factor of 20, but left l_{SF}^N and l_{SF}^F long enough so that the 2CSR model should still apply. Agreement of those data with the 2CSR model predictions implied that the model represented a good

approximation to the physics underlying the CPP-MR of these metals, and seemed to show that λ_N , λ_F^\uparrow , and λ_F^\downarrow were not CPP-MR scaling lengths.

Recently, however, the applicability of the 2CSR and VF models was challenged [89], based upon a combination of theoretical analysis with observation of qualitatively different CPP-MRs for two different geometries of samples composed of Co layers with thicknesses $t_{Co} = 6$ nm or 1 nm alternated with Cu layers thick enough ($t_{Cu} = 20$ nm) to eliminate exchange coupling between the Co layers. The geometries are called ‘interleaved’ $[Co(6)/Cu(20)/Co(1)/Cu(20)]_N$ or ‘separated’ $[Co(6)/Cu(20)]_M[Co(1)/Cu(20)]_N$, where italic N indicates the number of repeats. Because the saturation magnetic field H_s of Co layers of macroscopic area increases with decreasing t_{Co} , the use of two very different values of t_{Co} should allow for anti-parallel (AP) alignment of the magnetic moments of thin and thick Co layers over a limited field range. Analysis of experimental data should thus be straightforward. Because the only lengths in the 2CSR CPP-MR equations are t_{Co} and t_{Cu} , those equations predict that the MRs of ‘separated’ and ‘interleaved’ samples should be identical. In contrast to this expectation, [89] found the maximum CPP-MRs of separated samples to be only about half as large as those for interleaved ones and $A\Delta R(H) = AR(H) - AR_P$ for the separated samples to have a more complex shape.

We began our study of mean-free-path effects by trying to reproduce the data of [89]. The filled circles and solid curves in Fig. 4.1 for interleaved and separated samples with $N = 4, 6$, and 8, confirm the qualitative differences in $A\Delta R(H)$ that they found. To allow direct visual comparison of the forms and magnitudes of data for interleaved and

separated samples, in all figures showing $AR(H)$, the scale divisions for interleaved and separated samples are the same.

Because the data for separated and interleaved samples differ, we must be careful in defining the experimental quantities to be discussed in this chapter. $AR(H)$ and $A\Delta R(H) = AR(H) - AR_P$ represent the measured quantities as in Fig. 4.1. Their values will usually differ for interleaved and separated samples with the same numbers of layers N . The symbols $A\Delta R$ and $CPP-MR = A\Delta R/AR_P$ will be reserved for cases where $AR(H)$ equals AR_{AP} for the *state with magnetizations of adjacent layers aligned AP*. We'll see in section 4.2 that, defined this way, $A\Delta R$ and AR_{AP} are essentially independent of whether the sample is separated or interleaved.

The data in [89] were taken on samples with layers sputtered in the order $[Co(1)/Cu(20)/Co(6)/Cu(20)]_N$, whereas the data in Fig. 4.1 and most of our other samples below are on samples sputtered in the order $[Co(6)/Cu(20)/Co(1)/Cu(20)]_N$. Fig. 4.2 shows that we get the same differences if we use instead the order of [89].

We focus first on the filled circles and solid curves, representing $AR(H)$ after the samples were taken to above their saturation fields, H_s . The open squares and dashed curves, showing how $AR(H)$ varied when the samples were first taken to saturation, will be discussed in section 4.2. The solid curves of $AR(H)$ for the 'interleaved' samples consist of a single broad peak, symmetric about $H = 0$. This is the qualitative behavior expected from the series resistor model as the magnetic order of the layer magnetizations in the sample reorients from P at high H to AP for values of H between the saturation fields of the $t_{Co} = 6$ nm and 1 nm layers. The solid curves of $AR(H)$ for the 'separated' samples, in contrast, have more complex shapes, with maximum values of $A\Delta R(H)$ only

about half those for the ‘interleaved’ samples. The smallest N shown ($N = 4$), gives a sharp peak followed by a broad plateau. The largest ($N = 8$), gives two separate peaks, almost equal to the sum of separate contributions from the 6 nm and 1 nm Co layers.

As noted in Ch. 1, differences in $A\Delta R(H)$ for interleaved and separated samples similar to those in the solid curves in Fig. 4.1 were reported previously in samples of Co and Py with Ag, or Co and Fe with Cu. In the first case, the difference was attributed to short l_{SF}^{Py} . In the second, short l_{SF}^{Fe} was taken as part of the explanation, but possible spin-memory-loss at F/N interfaces was also proposed. In contrast, the authors of [89] argued that $l_{SF}^{Co} \sim 60$ nm [76] and $l_{SF}^{Cu} \sim 500$ nm [73] were too long for spin-memory-loss within the Co and Cu to be important. They argued that the series resistor and VF models break down when the mean-free-paths become larger than the layer thicknesses—that ‘mean-free-path effects’ then appear. Their argument is not simply one of changing magnitude of $AR(H)$ as the resistivities ρ_F and ρ_N of the F and N layers change. (We’ll see in section 4.4 that the series resistor and VF models can approximately account for the observed changes in magnitude of $AR(H)$ due simply to changes in ρ_N and/or ρ_F .) Rather they argued that ratios t/λ appear explicitly in equations that differ from those of both the series resistor and VF models. If they are correct, then the differences in behavior in Fig. 4.1 should gradually disappear as the ratio t/λ is increased.

In this Chapter, we test this claim in three ways. First, we replace Cu by a dilute Cu(2%Ge) alloy (hereafter just CuGe) with a short mean-free-path, $\lambda_{CuGe} \sim 8$ nm, but a long spin-diffusion length, $l_{SF}^{CuGe} \sim 130$ nm [68]. Such alloying should mainly reduce λ_{Cu} . For samples identical to those in Fig. 4.1, except with Cu replaced by CuGe, increasing the ratio t_{Cu}/λ_{Cu} by up to a factor of 25 (from $\sim 1/5$ for our sputtered pure Cu to ~ 5 for

the thickest CuGe layers) produces no significant change from Fig. 4.1 in either the forms or relative magnitudes of interleaved and separated samples. Second, in addition to replacing Cu by CuGe, we also replace the 6 nm Co layers by 15 or 30 nm thick layers of Co(2%Zr) (hereafter just CoZr) and the 1 nm Co layers by 30 nm thick layers of Py, both of which have mean-free-paths much shorter than these layer thicknesses. If anything, the differences increase. Such behavior is opposite to that expected from mean-free-path effects, but is expected if the CPP-MR is dominated by short spin-diffusion lengths in CoZr and Py. Lastly, we insert a 1 nm thick layer of FeMn into the middle of the central layer of a separated Co/Cu sample. The total AR contributed by the FeMn layer and its interfaces with Cu is comparable to that contributed by alloying the 20 nm thick Cu layer with Ge. From ‘mean-free-path’ effects, we would thus expect the separated data to move slightly toward the interleaved data. In contradiction, the separated data move away from the interleaved data, in just the way expected for a strong increase in ‘spin-memory-loss’ due to the FeMn layer.

The rest of this chapter is organized as follows. In section 4.2 we discuss the significance of the open circles and dashed lines in Fig. 4.1, representing the behavior of $AR(H)$ while the samples are first taken from their as-prepared state to saturation. We infer that the magnetic structures of the samples in their as-prepared states must in some way be closely similar to the structures in their AP state. In section 4.3 we use magnetization (M), and polarized neutron scattering measurements both to confirm this inference and to show that the magnetic structures in interleaved and separated samples do not differ in spurious ways. The absence of any significant spurious difference in magnetic structures is essential to any simple analysis of the data. With confidence in

such absence, we turn in Section 4.4 to the three tests of mean-free-path effects listed above. We shall see that all three tests strongly suggest that the differences between the data for interleaved and separated samples are due not to mean-free-path effects, but rather to spin-flipping in the multilayers. In section 4.5 we first examine whether the data can be explained by the best available spin-diffusion lengths in the bulk Co and Cu. We conclude that these lengths can only partially explain the data. We propose an explanation based upon spin-flipping at the Co/Cu interfaces. In section 4.6 we summarize and conclude.

4.2 $AR(H)$ FROM THE INITIAL STATE TO FIRST SATURATION

Fig. 4.1 shows that, once the samples have been taken to saturation, the differences between $A\Delta R(H)$ for interleaved and separated samples are large. In contrast, in the as-prepared states of the samples, the differences in $A\Delta R(H)$ are much smaller. If we define $A\Delta R(0) = AR(\text{as-prepared}) - AR_p$ for both interleaved and separated samples, and $A\Delta R(\text{peak}) = AR(\text{peak}) - AR_p$ for interleaved samples, then we find that $A\Delta R(0)$ for separated samples is essentially the same as $A\Delta R(\text{peak})$ for interleaved ones, and that $A\Delta R(0)$ for interleaved samples is about 85% of $A\Delta R(\text{peak})$ for interleaved ones. Because of the differences in H_s for 1 nm and 6 nm thick layers of Co, we expect the magnetizations of adjacent layers in interleaved samples to be oriented nearly AP at the ‘peak’ of $AR(H)$ after the samples have been taken to saturation. Separated samples also have $A\Delta R(0) \approx A\Delta R$, simultaneously arguing that adjacent layers in the as-prepared states of separated samples are also ordered AP, and that $A\Delta R$ is experimentally well-defined,

independent of whether the thicknesses of adjacent layers are the same or different. In contrast, for interleaved samples $A\Delta R(0) \approx 0.85A\Delta R$, indicating that, in the as-prepared state, adjacent layers are not fully AP ordered.

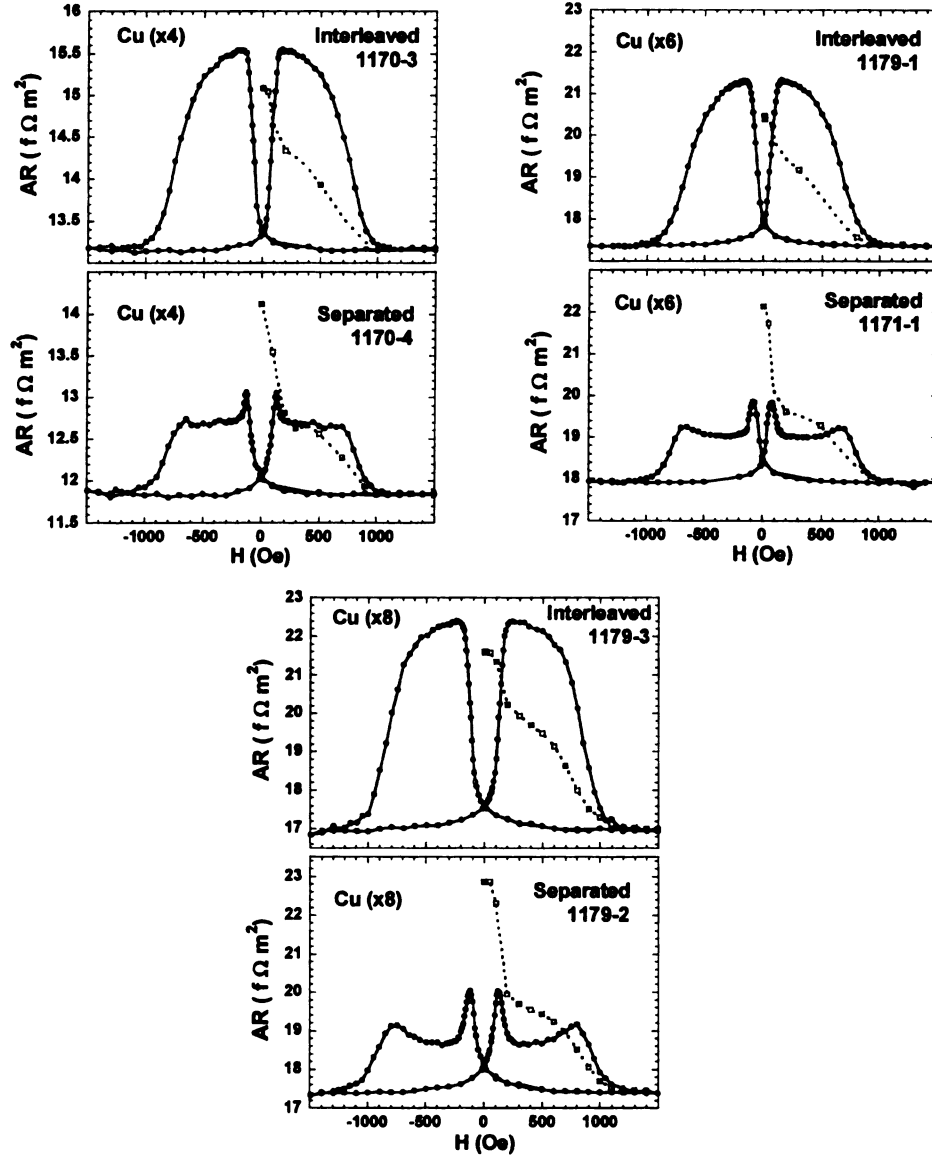


Fig. 4.1. $AR(H)$ vs H at 4.2K for interleaved (top of each pair) and separated (bottom of each pair) multilayers of Co/Cu with $N=4, 6$, and 8 . The unit scales for each coupled pair are identical. The open squares and dashed curves show how $AR(H)$ varied when first taken from the as-prepared state to the saturated state. The filled circles and solid curves show how it varied after having been taken to saturation.

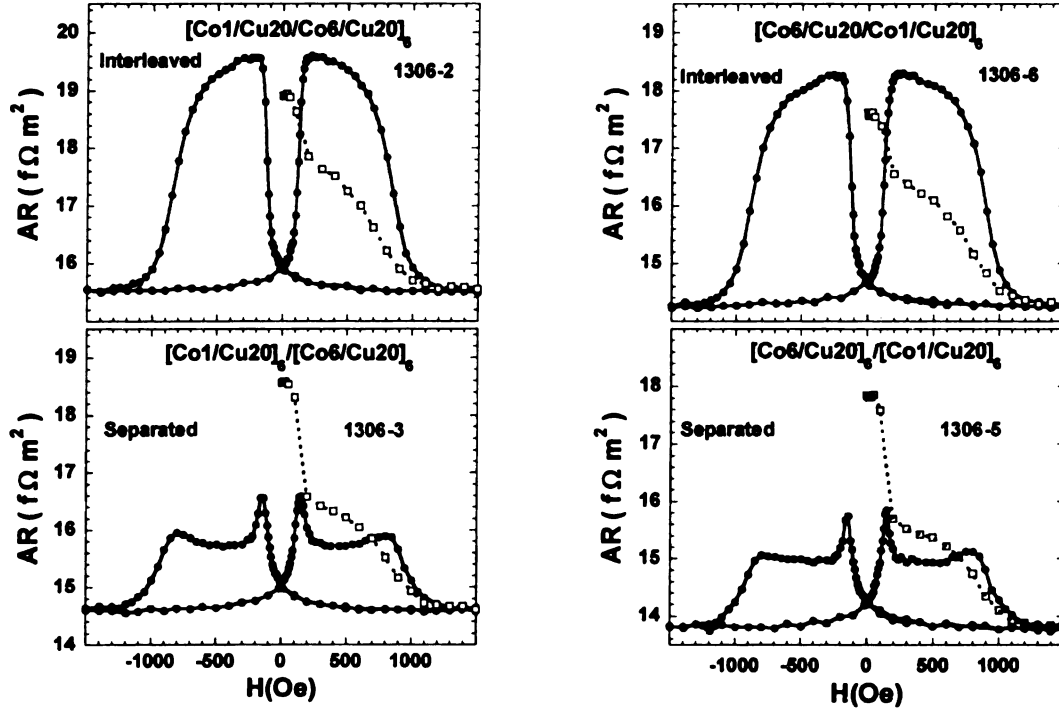


Fig. 4.2. $AR(H)$ vs. H curves for interleaved (top) and separated (bottom) samples. Both samples on the left have the thinner Co layer with $t_{Co} = 1\text{ nm}$ sputtered before the layer with $t_{Co} = 6\text{ nm}$. The two samples on the right have the opposite order.

We interpret these AR results as follows. As just noted, the close agreement between $A\Delta R(\text{Peak}) \approx A\Delta R$ for interleaved samples and $AR(0)$ for separated ones shows that both the peak states of interleaved samples, and the as-prepared states of separated samples, are close to the ideal AP state with magnetizations of adjacent Co layers reversed. The slightly smaller values of $AR(0)$ for the interleaved samples indicate that their magnetic orders deviate slightly from such AP states, a discrepancy we discuss below. For the interleaved samples, oppositely directed magnetizations for thick and thin layers in as-prepared and peak states would lead to $M \neq 0$ if the layers were single domain. In Section 4.3 we will show that $M(H_{\text{initial}} = 0) \approx 0$, and evidence that the domains in as-prepared samples are micron-sized is given in [100]. Based upon these two results, we argue that the as-prepared states of both interleaved and separated samples consist mostly

of micron-sized AP ordered domains that extend from the top to the bottom of the sample, but with the magnetizations of either the thicker or thinner Co layers oriented randomly ‘positive or negative’ in the layer planes. As discussed in [100], such ordering is likely due to the fringe fields from the ends of magnetic domains. To simplify, if the bottom Co-layer consists of small magnetic domains pointing only in opposite directions, such as those shown on the left sides of both drawings in Fig. 4.3, then the fringe fields from these domains will act on the newly growing Co layer above to orient its domains anti-parallel to those in the bottom layer. If the layer thicknesses are all the same, this process could yield the ‘ideal’ as-prepared anti-parallel order in vertical domain structures shown in Fig. 4.3. In separated samples, the thicknesses of adjacent layers are also all the same, except at the one boundary between thick and thin layers. In the as-prepared state, we, thus, expect almost as ideal AP domain structures as in simple $[F/N]_N$ multilayers. In interleaved samples, in contrast, adjacent layers always have different thicknesses. If the first layer is thick, its fringing fields will not be fully ‘taken up’ by the thinner second layer, letting some field lines extend up to the third layer and compete against the smaller fringing fields from the second layer. This difference is compatible with a less ideal AP order of the as-prepared states of interleaved samples and the smaller values of $AR(0)$ in Fig. 4.1. Fig. 4.3 shows the ideal pictures of the differences between as-prepared samples of interleaved and separated samples, and the same samples after being taken to H_s and then having the field reversed only enough to flip the thicker layers. In the as-prepared states, half of both thicker and thinner Co layers would already be oriented along any given field direction. Thus, as each different layer thickness flips, the changes in magnetizations should be only about half as large as when the same layers

flip after the sample has been taken to saturation. These are the behaviors seen in magnetization measurements that we postpone to Fig. 4.5 below. In section 4.3, we will see that magnetization and neutron scattering measurements both support this picture. In section 4.4 we will see that similar behaviors are seen also in Co/CuGe multilayers. Thus the picture seems to apply generally to interleaved and separated multilayers based upon Co and Cu or CuGe.

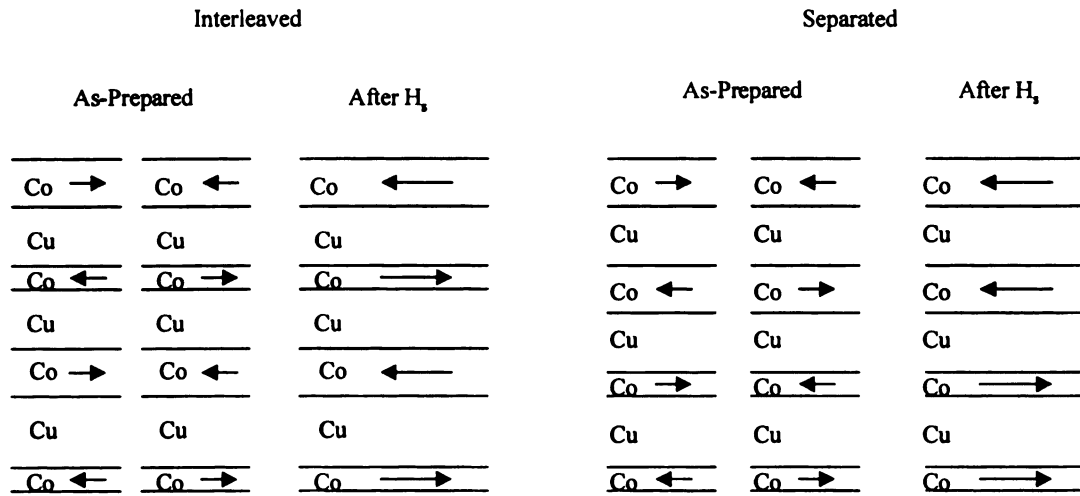


Fig. 4.3. Schematic, approximate pictures of inferred magnetic ordering for interleaved and separated samples in their 'as-prepared' state and after they have been taken to saturation and then the field reversed only enough to flip the thicker Co layers.

4.3 MAGNETIC ORDER

In this section we look for evidence of any unwanted differences in magnetic order between interleaved and separated samples. We do this in two ways. (1) By directly comparing total magnetizations M for interleaved and separated samples. (2) By scattering polarized neutrons from interleaved and separated samples.

(1) Comparison of M for interleaved and separated samples

To avoid the strong diamagnetism of a superconductor, magnetizations M were measured at 12K, above the superconducting transition temperature ($\sim 9\text{K}$) of our sputtered Nb. M was measured both on entire samples—allowing comparison of absolute magnitudes for interleaved and separated samples, and also on the $A \sim 1.2 \text{ mm}^2$ ‘central pieces’ through which the CPP current flows. Similar results were obtained for both.

Fig. 4.4 compares the values of M for whole interleaved and separated samples with both Cu and CuGe non-magnetic metals. In both cases, the two M s are practically identical. Importantly, the fields at which the AP states occur are the same to within our measuring uncertainties. Fig 4.5 shows similar behaviors for pieces of samples involving just the areas through which CPP current flowed. In both the top and bottom figures, the ratios of changes in magnetization as thick and thin layers flip are about the expected 6 to 1. The peaks in $AR(H)$ for the separated samples in Fig. 4.1 after saturation occur about where the average layer magnetizations pass through zero for the thick layers ($\sim 100 \text{ Oe}$) and the thin layers ($\sim 725 \text{ Oe}$), respectively. Fig. 4.5 contains the variations when the samples were first taken from their as-prepared states to above H_S , in addition to those when they were cycled to below $-H_S$ and back to above H_S . In the as-prepared states, both magnetizations in Fig. 4.5 are close to zero. As H is increased from zero, M initially increases rapidly up to $H \sim 200 \text{ Oe}$, then more slowly to above H_S . Both changes are only about half as large as those over the same field range after the samples have been taken to above H_S . These differences in magnetization changes before and after saturation mean that the magnetic structures of the samples differ before and after the samples are taken above H_S .

(2) Polarized neutron reflectivity (These studies were done by J.A. Borchers and K.V. O'Donovan of NIST)

The magnetic structures in these samples were also characterized using polarized neutron reflectivity (PNR), which is sensitive to the interaction between the sample's magnetization and the magnetic moment of the neutron. PNR measurements were performed at the NIST Center for Neutron Research on multilayers prepared in the same way as those for the CPP-MR studies, except that the samples were squares, 1.27 cm on a side, and sputtered directly onto the Si substrates instead of onto Nb. All PNR measurements were made at 17 – 18 K after cooling in zero field in a closed-cycle refrigerator. An electromagnet provided a maximum field of 0.2 T. Using neutrons of wavelength $\lambda = 0.475$ nm on the NG-1 reflectometer, Borchers and O'Donovan measured the non- spin-flip (NSF) reflectivities, R^{++} and R^{--} , as well as the spin-flip (SF) reflectivities, R^{+-} and R^{-+} . (The + and - signs in the superscript describe the polarization state of the incident and scattered neutron spins. These spins are aligned either parallel, +, or antiparallel, -, to the applied field.) The selection and detection of the neutron spin state is described elsewhere [101]. The NSF reflectivities sense the chemical structure of the multilayer and the component of the in-plane magnetization parallel to the applied field. The SF reflectivities are primarily sensitive to the projection of the in-plane magnetization that is perpendicular to the applied field. They measured both the specular and diffuse (i.e., off-specular) reflectivity as a function of the wavevector $Q_z = 4\pi \sin \theta / \lambda$, where θ is the angle of the incident and scattered neutrons relative to the sample surface. We obtained the diffuse data by offsetting the sample normal by 0.1° relative to the specular scattering

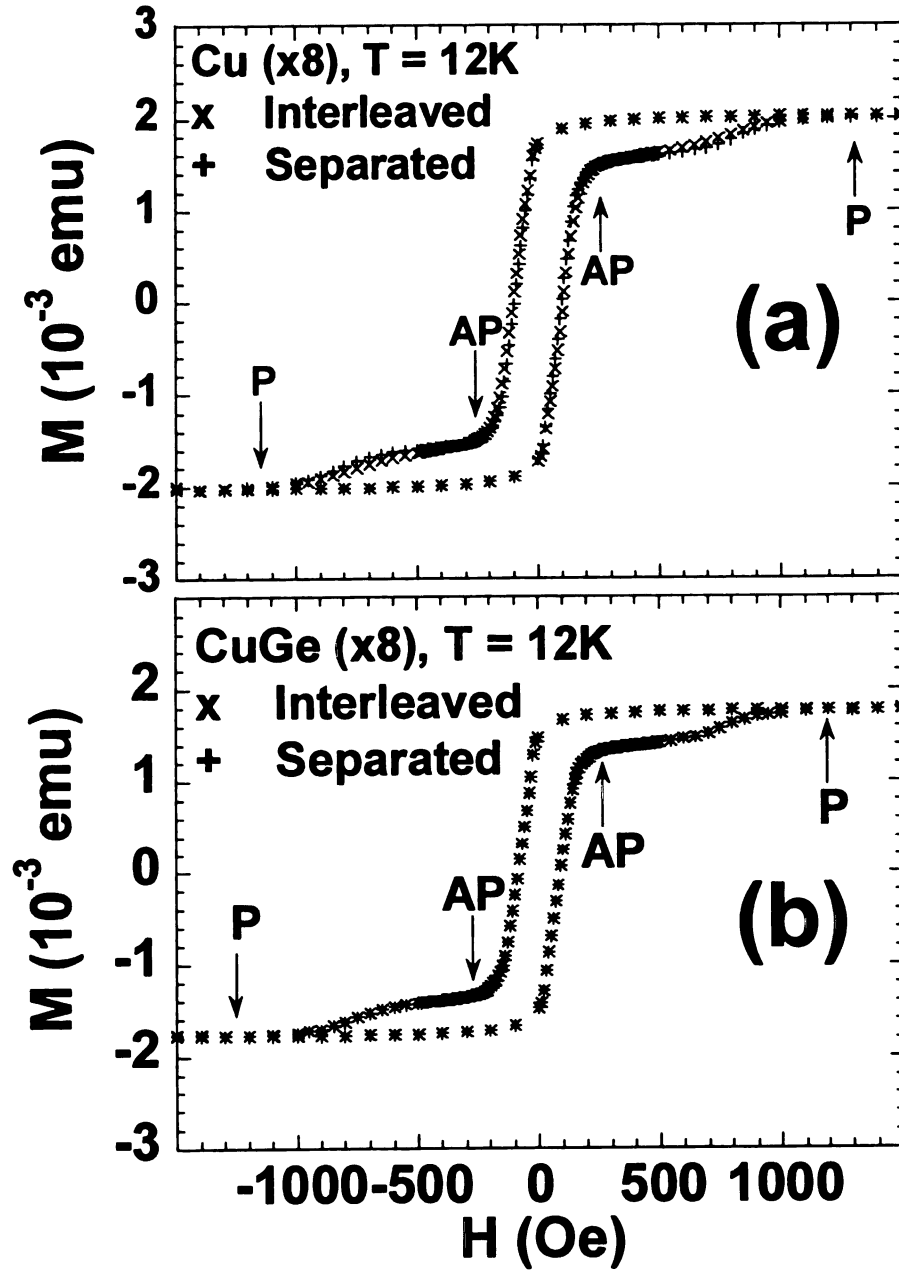


Fig. 4.4. M vs H at 12K for interleaved (x) and separated (+) samples with Cu and CuGe with $N = 8$ for $t_{\text{Cu}} = t_{\text{CuGe}} = 20$ nm. P and AP states are indicated.

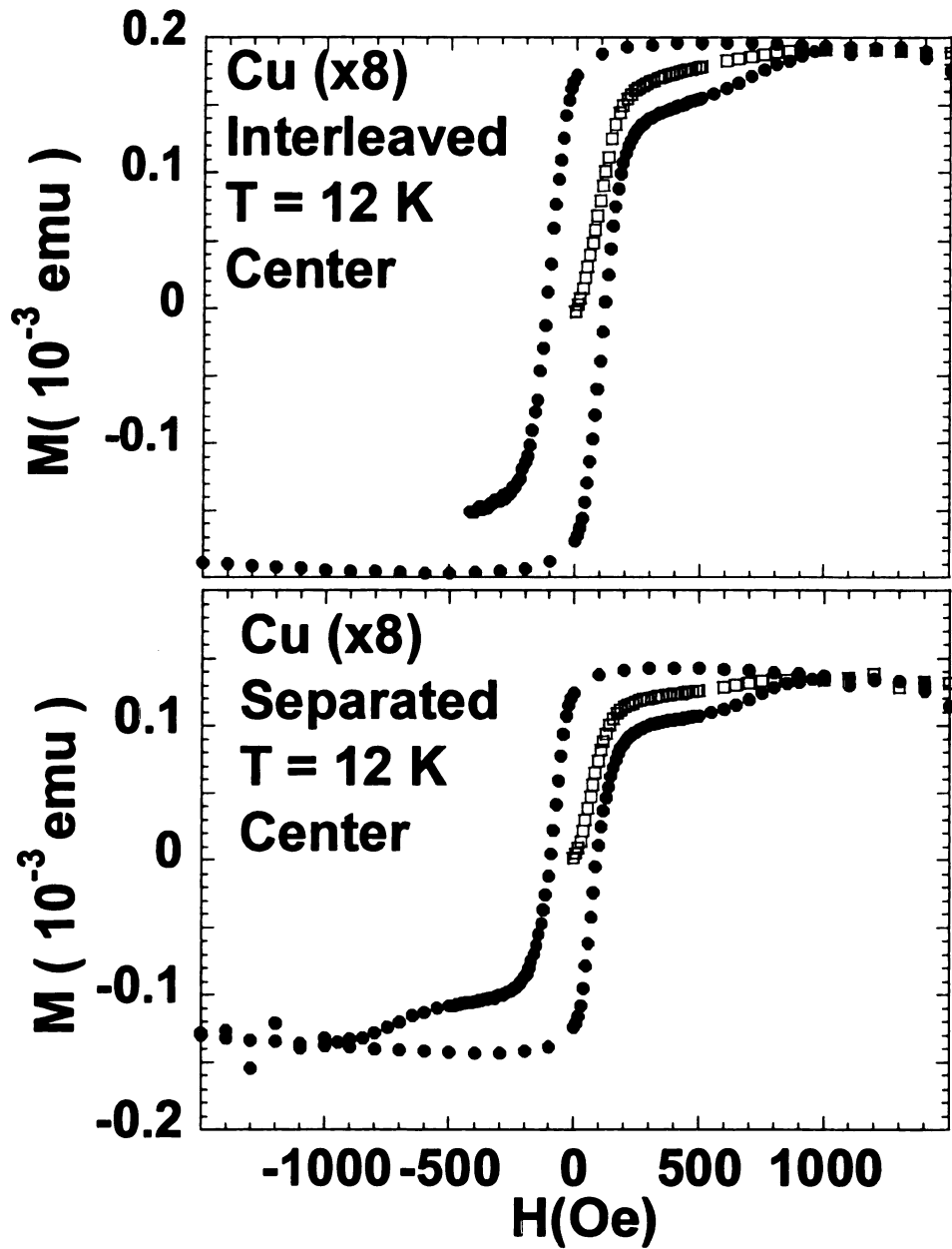


Fig. 4.5. M vs H at 12K for center-cut pieces of Cu interleaved (top) and separated (lower) samples including both data from the as-prepared state to saturation and then from positive saturation to negative saturation and back again.

condition and then scanning Q_z . These diffuse measurements provide general information about growth-axis correlations among in-plane ferromagnetic domains with dimensions less than $100 \mu\text{m}$ [100] and were also subtracted from the total reflectivity to give the specular reflectivity. After correcting the specular data for the efficiencies of the

polarizing elements (ranging from 92% - 100%), the fits give a profile of the vector magnetization as a function of depth for regions of the multilayer with ferromagnetic domains larger than about 100 μm within the sample plane [102-104].

PNR data generally support this picture of randomly oriented, micron-sized domains within the sample plane that become single domains in a saturating field. We examined an interleaved sample $[\text{Co}(6)/\text{Cu}(20)/\text{Co}(1)/\text{Cu}(20)]_8$ and a separated sample $[\text{Co}(6)/\text{Cu}(20)]_8[\text{Co}(1)/\text{Cu}(20)]_8$ with magnetoresistance and magnetization behaviors similar to those shown in Fig. 4.1 and 4.4, respectively. After cooling in zero field and saturating in a field of 2000 G, we obtained the reflectivity of both samples in a field of 250 G (which coincides with the peak in the magnetoresistance of the interleaved sample), and in fields of 74 G, 114 G, and 725 G (the latter two of which are near the two peaks in the magnetoresistance of the separated sample). These results were compared to the reflectivity data measured in a saturating field > 1600 G. The data obtained at all of these fields were characterized by the absence of specular spin-flip (SF) scattering. This result indicates that after saturation the Co moments are aligned either parallel or antiparallel to the applied field direction at *all* fields. Upon field cycling, the reversal of the Co moment directions for the thick and thin layers thus occurs via domain formation, rather than moment rotation within the sample plane.

Figures 4.6 and 4.7 show the NSF specular reflectivity data and corresponding fits for the interleaved and separated samples, respectively, in a field of 250 G. In Fig. 4.6 the data for the interleaved sample are dominated by superlattice peaks above the critical angle at $Q = 0.21, 0.32, 0.44, 0.58, 0.71, 0.85 \text{ nm}^{-1} \approx 2 \pi n / D$, where $D = 45.4 \text{ nm}$ is the multilayer repeat length and n is an integer. (Note that this approximation does not

explicitly hold for the peaks at low Q due to dynamical effects.) In contrast, the R^{--} data for the separated sample in Fig. 4.7 show superlattice peaks at $Q = 0.29, 0.52, 0.76 \text{ nm}^{-1} \approx 2 \pi n / D_1$ where $D_1 = 24.6 \text{ nm}$, and the R^{++} data have superlattice peaks at $Q = 0.35, 0.64, 0.95 \text{ nm}^{-1} \approx 2 \pi n / D_2$ where $D_2 = 19.6 \text{ nm}$. D_1 and D_2 correspond to the repeat lengths of the thick- and thin-layer parts of the multilayers, respectively, within the separated sample. The superlattice peaks for each multilayer appear in different reflectivity cross sections because the thin Co layers are antialigned relative to the 250 G field while the moments in the thick Co layers are aligned parallel to the field. (In a saturating field, both sets of superlattice peaks are evident only in the R^{--} data.) In general, the relative intensities of the superlattice peaks in the R^{++} and R^{--} data are sensitive to the magnitude and orientation of the moments in the thin and thick Co layers averaged across the sample plane. The magnetization profiles at the bottom of Figs. 4.6 and 4.7 were generated from the fits to the corresponding PNR data. (Note that the moments in the thin Co layers appear to be substantially smaller than those in the thick Co layers, even though the moments in both the thick and thin layers saturate in $H = 200 \text{ O}$ to almost 100% of the bulk Co value.) This illusion occurs because the fits are sensitive to the structural interfacial roughness averaged across the sample plane, which exceeds the 1 nm thickness of the thin layers along the growth direction.) Consistent with the magnetization results (Fig. 4.4 & 4.5), our fits reveal that the Co moments in the thin and thick layers are aligned AP to each other for both samples at 250 G, as shown schematically in Fig. 4.3 (“After H_s ”). The magnetizations of the thin Co layers are, however, slightly reduced from their saturation values in both cases, suggesting that small in-plane domains form within these layers as the field approaches the coercive field.

Specular reflectivity data at 73, 114 and 725 G confirm that the thin and thick Co layer moments reverse directions, as expected, at different coercive fields. After saturation in -2000 G, the moments in the thick Co layers in both the interleaved and separated samples flip when the field is increased to approximately 90 G, while the moments in the thin Co layers remain parallel to the original field direction. This behavior is evidenced, in part, by a large reduction of the fitted moments for the thick Co layers compared to their saturation value, as well as by an increase in the diffuse scattering [103]. As stated previously, this moment reversal occurs via the formation of small, in-plane domains. Upon increasing the field to 725 G, the moments in the thin Co layers then reorient parallel to the applied field. Fits to the 725 G reflectivity data for both samples indicate that the thin Co moments, averaged across the sample plane, are reduced from their saturation value. The data suggest that the reversal of the thin Co layer moments also proceeds via formation of small, in-plane domains. The reflectivity data thus confirm that the peak/plateau in the magnetoresistance of the interleaved/separated sample near 250 G (Fig. 4.1) is associated with an anti-parallel alignment of the moments in the thin Co layers relative to those in the thick Co layers. The peaks in the magnetoresistance of the separated sample near 100 G and 725 G (Fig. 4.1) are associated with the *reversal* of the magnetization direction of the Co moments in the thick and thin layers respectively. The orientation and magnitude of the thin and thick Co layer moments thus have a similar field dependence for both the interleaved and separated samples. Any differences in magnetic structures between interleaved or separated samples in their nominal AP or P states appear too small to explain the different magnetoresistances in Fig. 4.1.

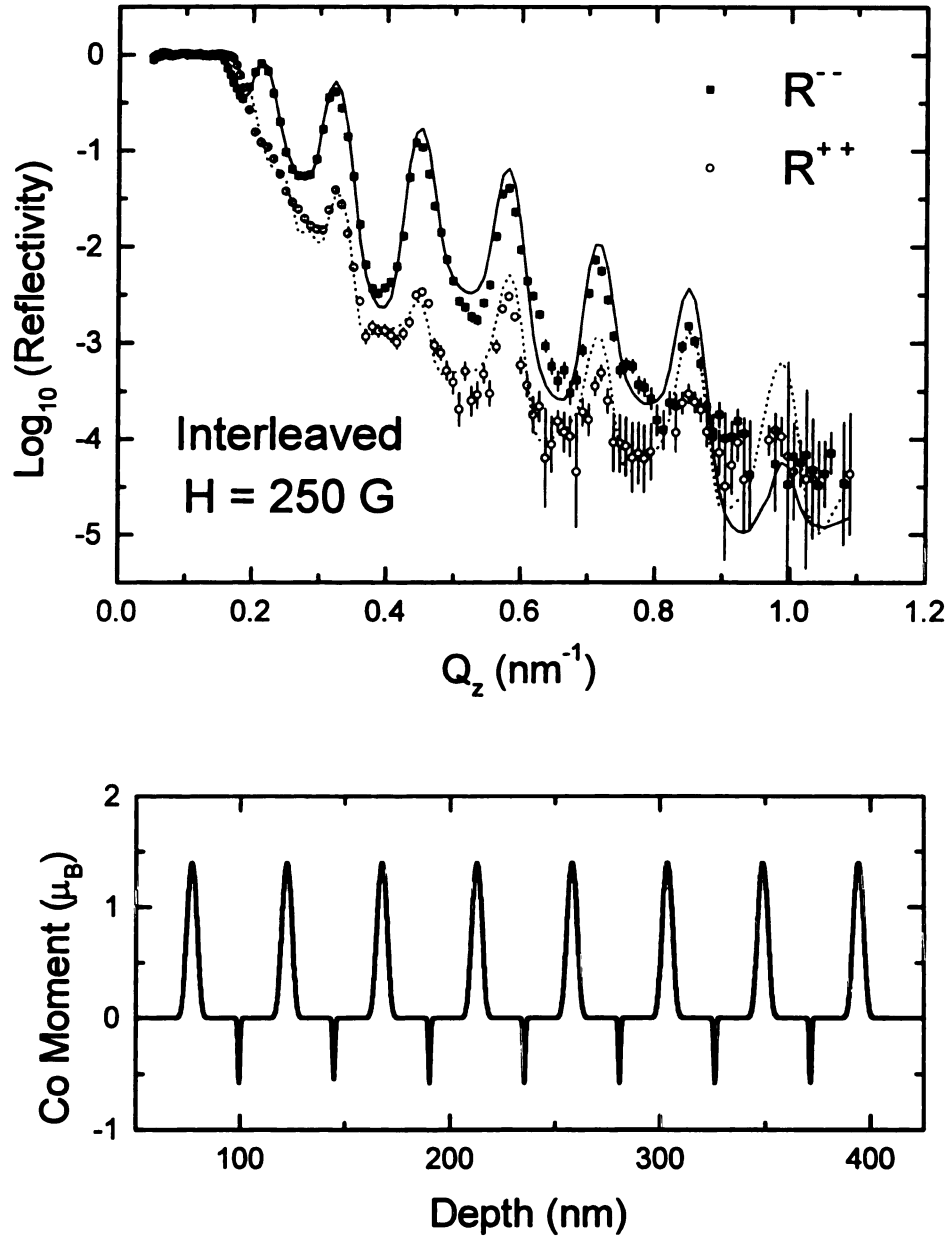


Fig. 4.6. Specular neutron reflectivity data and fits plotted as a function of the wavevector Q_z of an interleaved sample $[\text{Co}(6)/\text{Cu}(20)/\text{Co}(1)/\text{Cu}(20)]_8$ at 18 K in a 250 G field. Only the R^- (dark squares) and R^+ (open circles) reflectivities are shown. (The SF reflectivities are effectively at the background level). The magnetization profile for the Co layers that is shown in the bottom graph was obtained from the fit. The apparent differences in moments in the thin and thick layers are artifacts (see text).

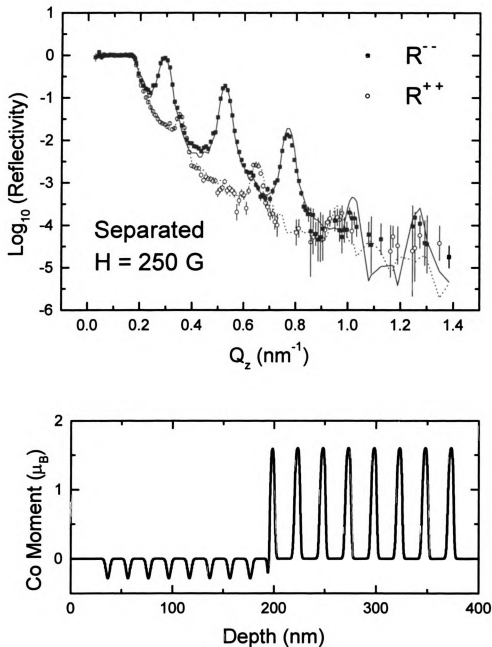


Fig. 4.7. Specular neutron reflectivity data and fits plotted as a function of the wavevector Q_z of a separated sample $[\text{Co}(6)/\text{Cu}(20)]_8[\text{Co}(1)/\text{Cu}(20)]_8$ at 18 K in a 250 G field. Only the R^{--} (dark squares) and R^{++} (open circles) reflectivities are shown. (The SF reflectivities are effectively at the background level). The magnetization profile for the Co layers that is shown in the bottom graph was obtained from the fit. The apparent differences in moments in the thin and thick layers are artifacts (see text).

The PNR data also provide information about the magnetic structures of the samples in their as-prepared states. Fig. 4.8 shows the specular and diffuse reflectivity data for the separated sample. Magnetic SF scattering is evident, and the NSF data show broad features near the structural superlattice reflections. Preliminary fits to the specular data indicate that some fraction of the sample with in-plane domain sizes larger than $100\text{ }\mu\text{m}$ is ordered with the moments in the thick Co layers aligned antiparallel to those in the thin Co layers, and some fraction is ordered with alternating moments of adjacent layers. The situation is not as simple as the ideal case of Fig. 4.3. However, the as-prepared data also show substantial magnetic diffuse scattering (Fig. 4.8b) indicative of magnetic ordering with in-plane ferromagnetic domain sizes smaller than $100\text{ }\mu\text{m}$ [102,103]. Distinct peaks are apparent at $Q = 0.22, 0.42, 0.65\text{ nm}^{-1}$. These magnetic peaks lie halfway between the structural superlattice peaks in the NSF data at $Q \approx 2\pi n/D_I$. ($D_I = 24.6\text{ nm}$ is the repeat distance of the part of the multilayer with thick Co layers in the separated sample.) The presence of these peaks indicates that the repeat length of the magnetic structure within the bottom multilayer is twice that of the multilayer itself. Thus the as-prepared state of the thick layer part of the multilayer is ordered (partially) in small, ferromagnetic in-plane domains that are oriented antiparallel relative to each other across the 20 nm Cu layers, as depicted in Fig. 4.3 (“As-Prepared”). The in-plane direction of these domains is apparently random since the diffuse magnetic intensity is evenly distributed in the NSF and SF reflectivities. Unfortunately the diffuse data do not provide any direct information about the magnetic ordering of the thin-layer part of the separated multilayers.

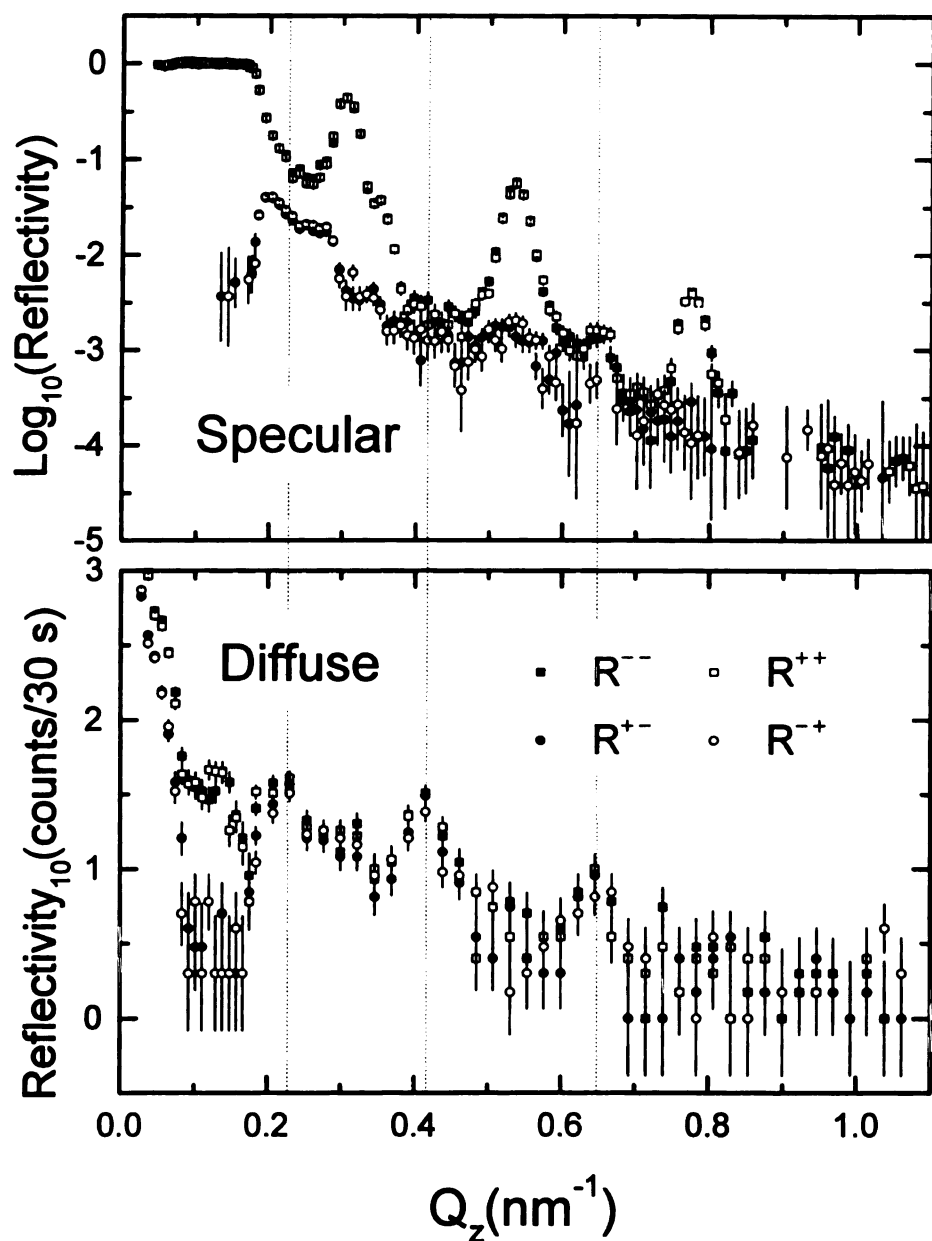


Fig. 4.8. Specular and diffuse reflectivity data for the separated sample $[\text{Co}(6)/\text{Cu}(20)]_8[\text{Co}(1)/\text{Cu}(20)]_8$ at 18 K in the as-prepared state. The data were taken in a 3 G guide field. The R^{--} (dark squares), R^{++} (open squares), R^{+-} (dark circles), and R^{-+} (open circles) reflectivities are all shown. The diffuse data have not been corrected for polarization efficiencies. The dotted lines mark the superlattice peaks in the diffuse data.

4.4 MAGNETORESISTANCE TESTS OF MEAN-FREE-PATH EFFECTS

In this section, we examine differences in $AR(H)$ between interleaved and separated multilayers with various constituents. If t/λ is the controlling parameter in the differences between interleaved and separated samples in Fig. 4.1, then greatly increasing it in either the F or N metal should cause the data for separated samples to approach those for interleaved ones, provided that l_{SF} remains long enough.

As a first test of this expectation, we replaced Cu by Cu(2%Ge)—hereafter just CuGe—which from $\rho = 8.0 \pm 0.5 \mu\Omega\text{cm}$ (see Ch. 2) we estimate a short $\lambda_{\text{CuGe}} \sim 8 \text{ nm}$ [91], but long $l_{\text{SF}}^{\text{CuGe}} \sim 130 \text{ nm}$ [71]. For $t_{\text{CuGe}} = 20 \text{ nm}$ and 40 nm (Figs. 4.9 - 4.11), the ratios $t_{\text{CuGe}}/\lambda_{\text{CuGe}}$ are 2.5 and 5. For $t_{\text{CuGe}} = 20 \text{ nm}$ and $N = 2$ (Fig. 4.10), the ratio $t_T/l_{\text{SF}}^{\text{CuGe}} < 1$, where $t_T = 60 \text{ nm}$ is the total CuGe thickness between outer Co layers. For $t_{\text{CuGe}} = 10 \text{ nm}$ and $N = 3$ (Fig. 4.11), $t_T/l_{\text{SF}}^{\text{CuGe}} < 0.4$ is even smaller. Our data thus cover the range of mean-free-paths in the N-layer from ~ 5 times the layer thickness to $\sim 1/5$ of the layer thickness, while in some of our data the spin-diffusion length in the N-layer exceeds the sum of the thicknesses of those layers. Comparing Figs. 4.1 and 4.9 shows that replacing Cu by CuGe did not reduce the differences between $AR(H)$ for interleaved and separated samples, independent of the number of layers, N , or the thicknesses of the Cu or CuGe layers. We conclude this part of the discussion by noting that the differences in absolute magnitudes of the Cu and CuGe data in Figs. 4.1 and 4.9 are not an issue in the analysis of mean-free-path effects, as they can be explained straightforwardly within the 2CSR model. According to Eqs.1.1-1.3 of the 2CSR model in Ch. 1, replacing Cu by CuGe should increase AR_{AP} and AR_P by simply the increase in specific resistance,

$2N(\rho_{\text{CuGe}}t_{\text{CuGe}} - \rho_{\text{Cu}}t_{\text{Cu}})$, due to this replacement, and should decrease $A\Delta R$ by the ratio of the total anti-parallel specific resistances, $AR_{\text{AP}}^{\text{Cu}}/AR_{\text{AP}}^{\text{CuGe}}$. Comparison of the data of Figs. 4.1 and 4.9 shows that this simple picture properly accounts for most of the differences observed. Small residual deviations can reasonably be attributed to a combination of data fluctuations plus corrections due to the actual finite (but relatively long) spin-diffusion lengths, which require the theory of Valet and Fert.

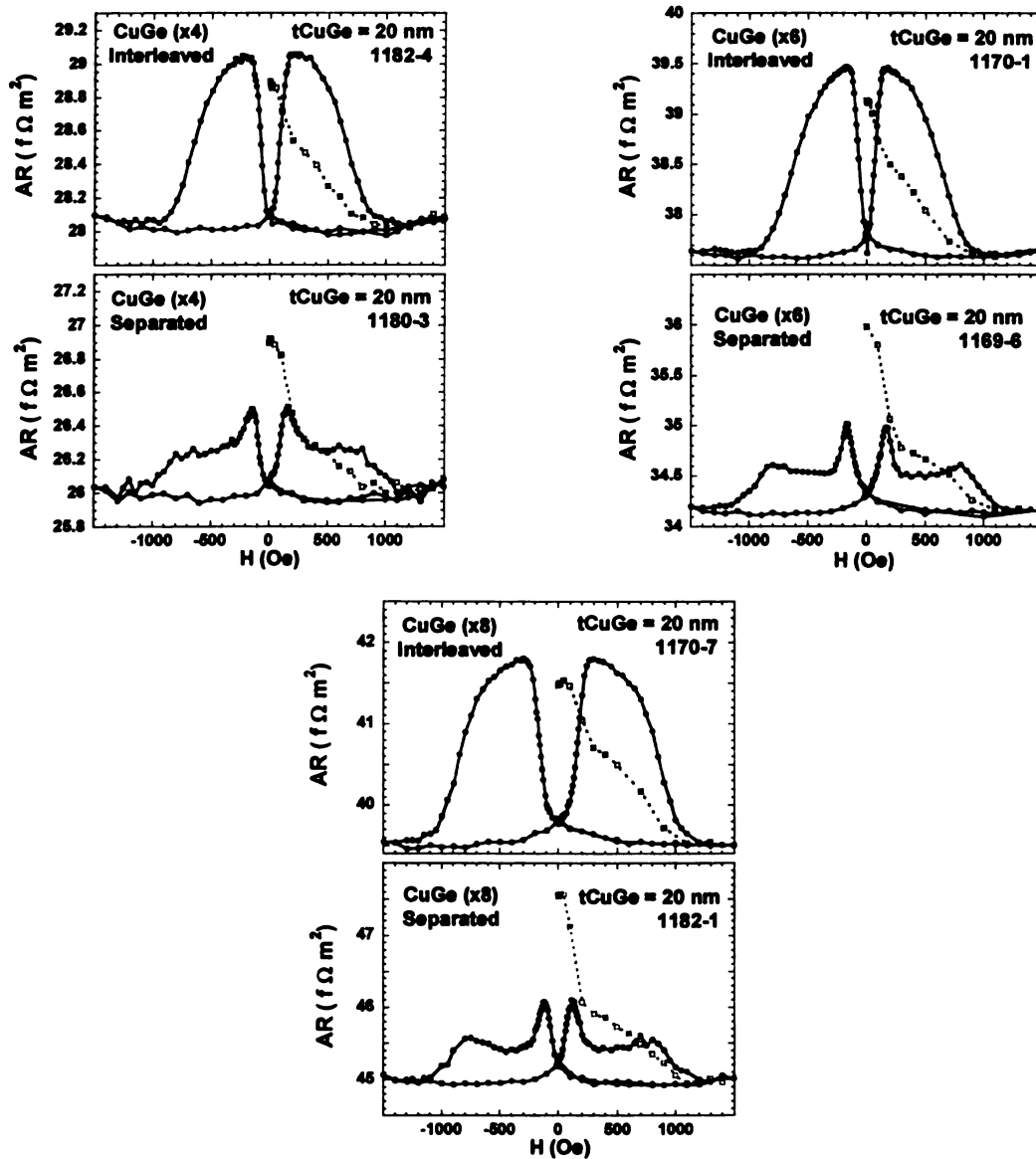


Fig.4.9. AR of interleaved and separated samples identical to samples in Fig. 4.1 except that CuGe replaces Cu. Symbols and curves have the same meaning as in Fig. 4.1.

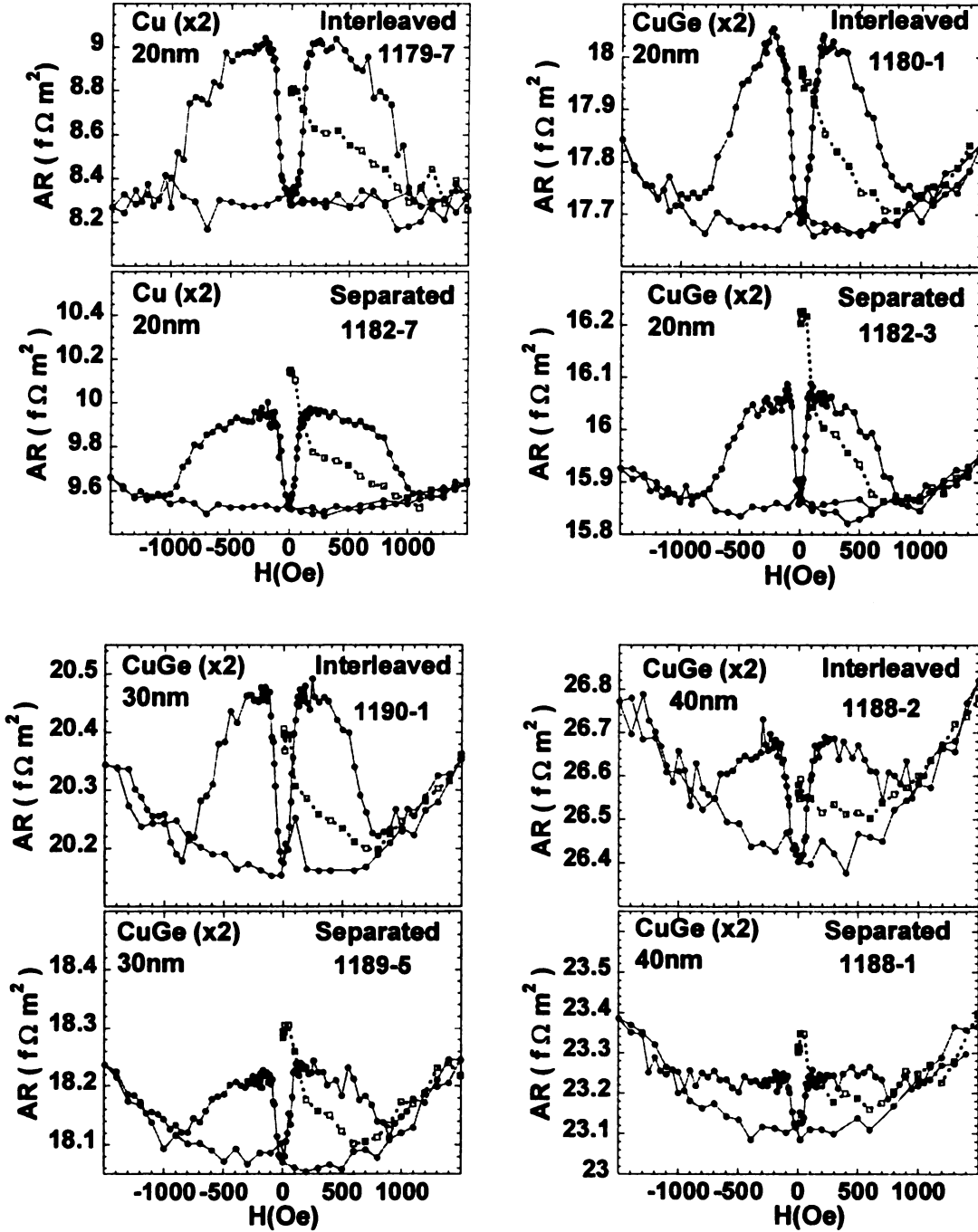


Fig.4.10. Effect of further increasing CuGe thickness on AR of interleaved and separated samples. The convention for symbols is the same as in the previous figures.

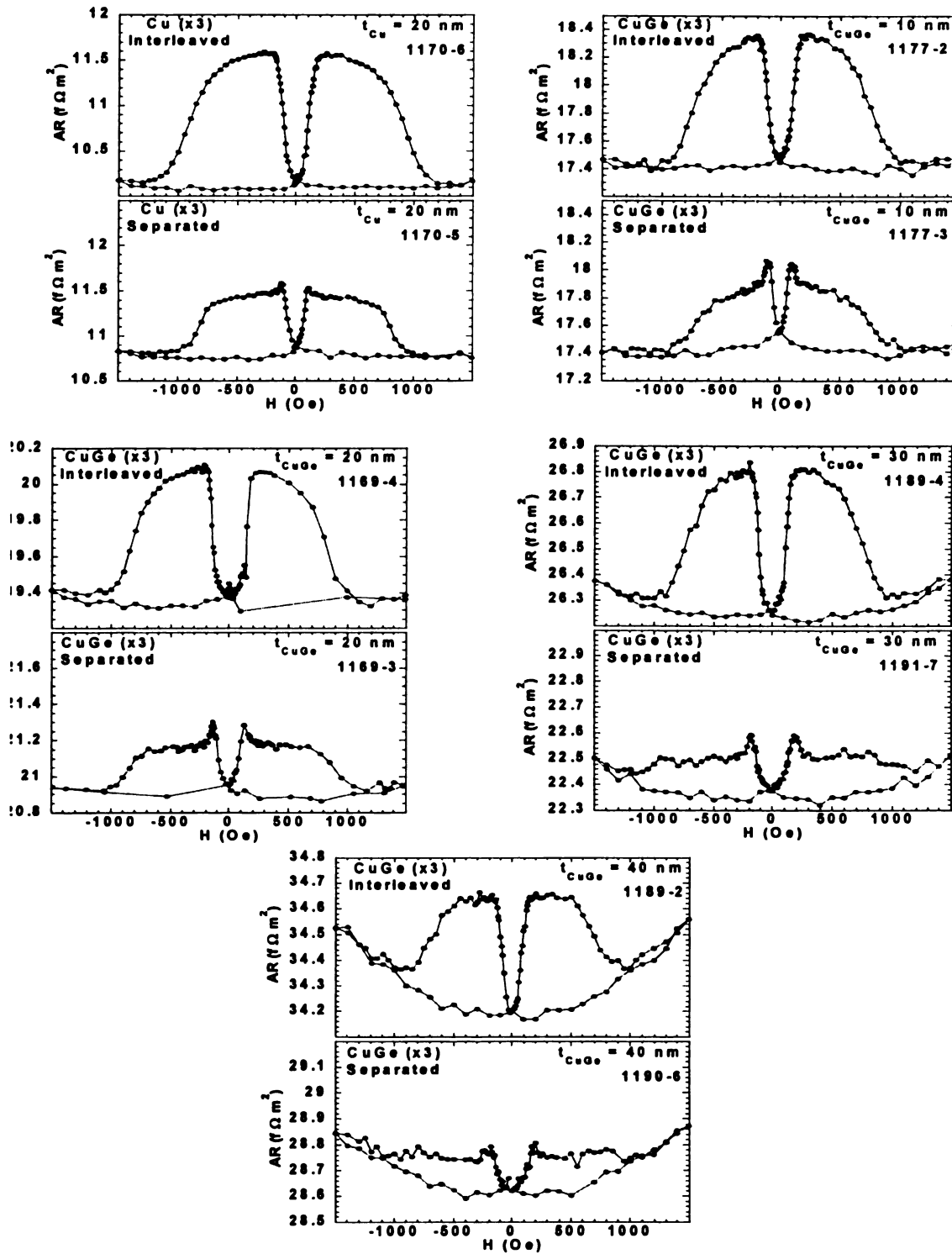


Fig.4.11. AR vs H for Cu, CuGe with $t_{CuGe} = 10, 20, 30,$ and 40 nm. The number of repeats is 3 for all samples. The specific resistance AR_P increases with CuGe thickness, and ΔAR decreases, but the difference between separated and interleaved samples persists. Data shown are after samples were taken to saturation.

In addition to the claim of mean-free-path effects in Co/Cu multilayers in [89], one of the authors of that paper subsequently argued [99] that the differences between interleaved and separated multilayers seen earlier in [83] and [84] might also arise from mean-free-path effects instead of finite spin-diffusion lengths. To test this possibility, we replaced the 6 nm and 1 nm thick layers of Co in interleaved multilayers with much thicker layers of alloys that have much higher resistivities and thus much shorter mean-free-paths, but also short spin-diffusion lengths. Based on prior studies, we chose 30 nm thick layers of Py (a well studied ‘low H_S ’ alloy) to replace the 6 nm thick Co layers, and 15 and 30 nm thick layers of CoZr (an alloy with a large resistivity per atomic percent impurity [91]) to replace the 1 nm thick Co layers. Independent measurements of the resistivities of our sputtered Py and CoZr give $\rho_{Py} = 110 \text{ n}\Omega\text{m}$ (Ch. 1) and $\rho_{CoZr} = 195 \text{ n}\Omega\text{m}$ (Ch. 1 and 5). Such values reduce the ratios λ/t by factors of ~ 10 -20 between $t_{Co} = 6 \text{ nm}$ and $t_{CoZr} = 15 \text{ and } 30 \text{ nm}$ and by ~ 60 between $t_{Co} = 1 \text{ nm}$ and $t_{Py} = 30 \text{ nm}$. Contradicting expectation if the ratios t/λ are important, Fig. 4.12 shows that these large increases of the ratio in every layer did not decrease the difference between interleaved and separated data. Rather, the differences are larger than those in Fig. 4.1. Increased differences are expected if finite spin-diffusion lengths in the Py [74] and CoZr (Ch. 5) layers partly ‘decouple’ the Py and CoZr layers in the separated multilayers.

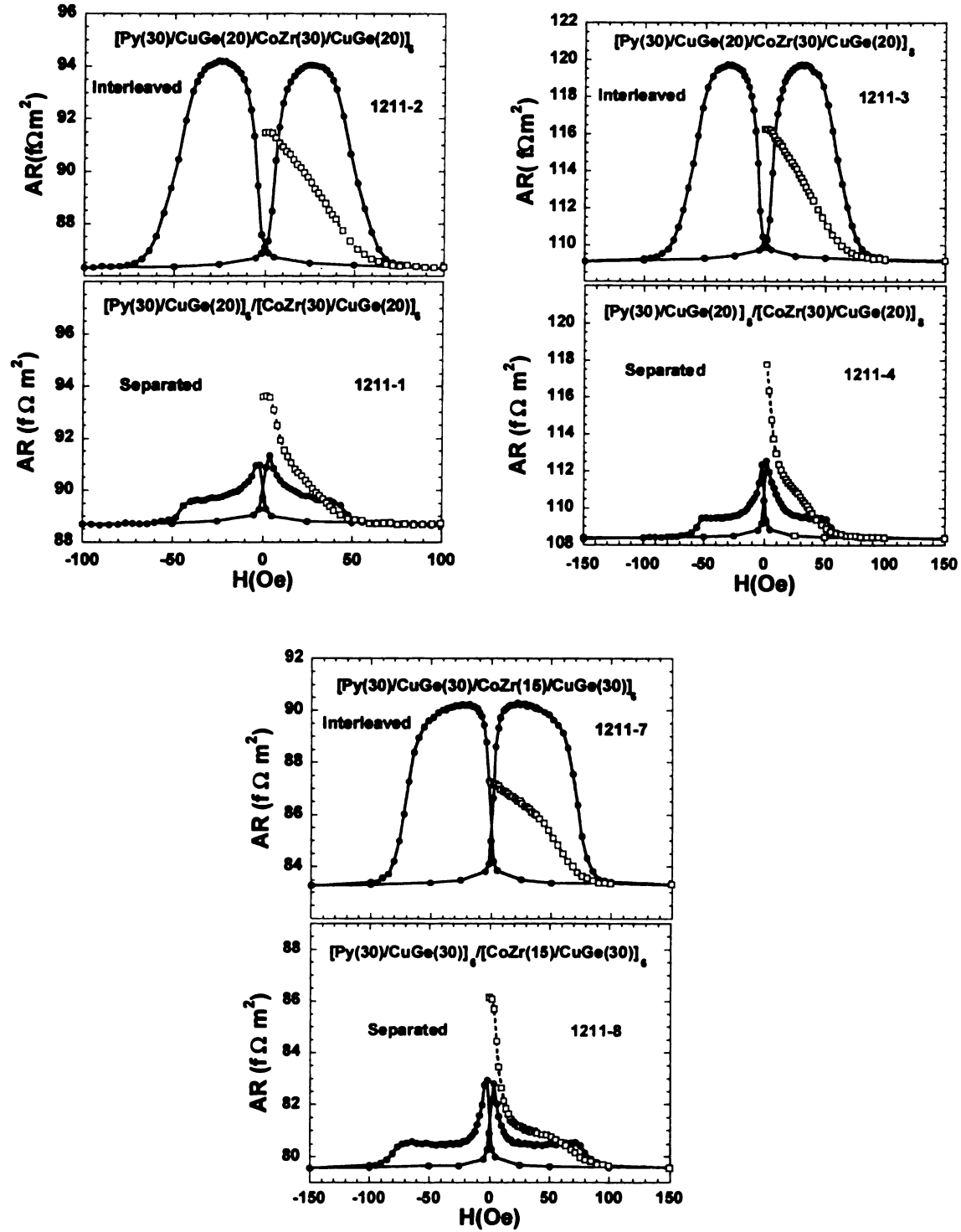


Fig. 4.12. AR vs H for multilayers with short λ/t in all layers. The difference between separated and interleaved samples has grown, disagreeing with mean-free-path effects.

Lastly, we placed a 1 nm thick layer of FeMn in the middle of the central Cu layer of a separated Co/Cu sample to see if it would bring the separated data closer to the interleaved data, as expected for ‘mean-free-path effects’. In [73] we showed that 1 nm of FeMn causes > 99% spin-memory loss. If this loss is dominant, inserting the FeMn layer should completely isolate the contributions from thick and thin Co layers, producing exactly the opposite effect expected from ‘mean-free-path effects’. Fig. 4.13 shows that the data support the dominance of spin-memory-loss. Inserting the FeMn gives two separate peaks, with $A\Delta R(H)$ almost zero in between.

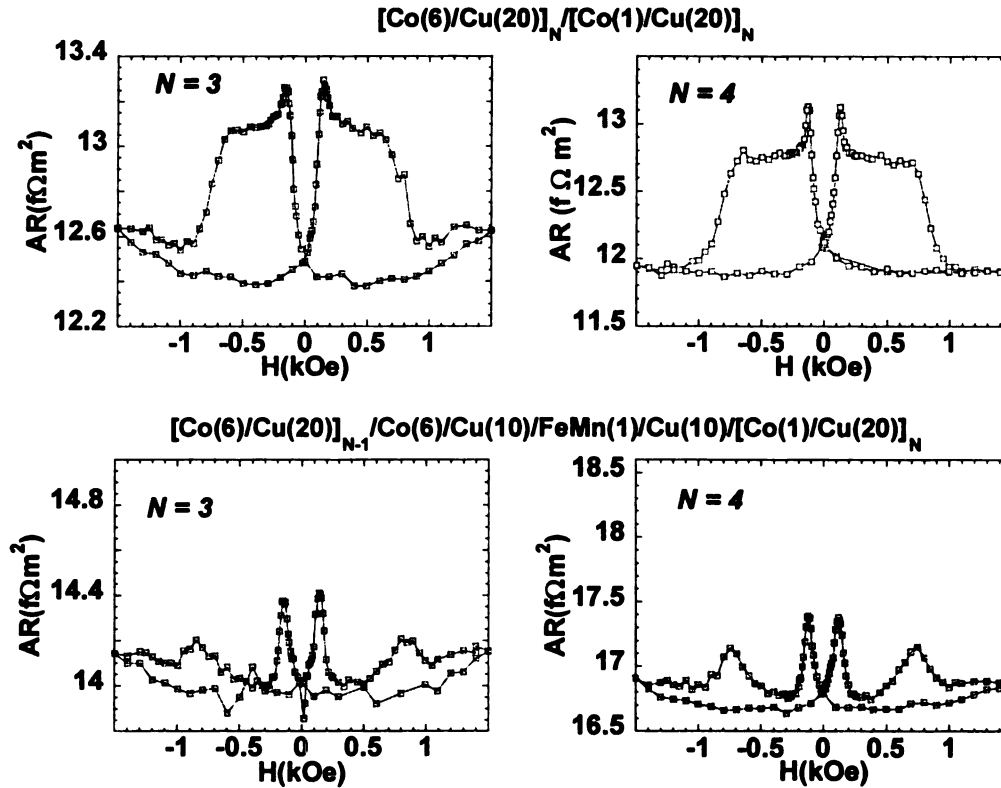


Fig. 4.13. AR vs H curves. All samples are of the separated type. The bottom two have a 1 nm FeMn layer in the middle of the Cu layer that separates the Co(6) layers from the Co(1). Strong spin-flipping by FeMn decouples the two sides of the multilayers giving two separate peaks on each side of $H = 0$.

4.5 EFFECTS OF SPIN-MEMORY-LOSS

From the data in section 4.4, we conclude that the ratio λ/t is not driving the differences between interleaved and separated data—there are no ‘mean-free-path effects’ of the kind described in [89]. In this section we first ask what contribution to the data of Figs. 4.1 and 4.9 can come from VF theory taking the best available values for the bulk spin-diffusion lengths, l_{SF} , in Co, Cu, and CuGe. We will see that these finite spin-diffusion lengths can explain between 20% and 50% of the observed behaviors for samples with different values of N . We then show that the remainder can be consistently explained by spin-memory-loss at the Co/Cu interfaces.

A. Spin-Memory-Loss in bulk Co, Cu, and CuGe.

Published estimates of $l_{\text{SF}}^{\text{Co}}$ lie in the range 60 ± 20 nm [76,77]. For Cu, we estimated $l_{\text{SF}}^{\text{Cu}} \sim 500$ nm [73], with uncertainty from 400 nm to 1 μm . For CuGe, we estimate $l_{\text{SF}}^{\text{CuGe}} = 130 \pm 30$ nm from the data in [68]. For quantitative comparison of separated (Sep) and interleaved (Int) samples, we examine the ratio $(A\Delta R)_{\text{Sep}}/(A\Delta R)_{\text{Int}}$. Experimentally, we take $(A\Delta R)_{\text{Int}}$ at the peak of the interleaved data, and $(A\Delta R)_{\text{Sep}}$ at the plateau just beyond the first peak of the separated data. The results for $t_N = 20$ nm are shown as a function of N in Fig. 4.14 for samples with both Cu and CuGe. The predictions of VF theory for this ratio, assuming $l_{\text{SF}}^{\text{Co}} = 60$ nm, $l_{\text{SF}}^{\text{Cu}} = 500$ nm, and $l_{\text{SF}}^{\text{CuGe}} = 130$ nm are the dotted and long-dashed curves, with error bars showing the ranges of uncertainties due to the uncertainties in l_{SF} listed above. These two curves account for 20% to 50% of the observed differences between interleaved and separated samples. We, thus, disagree with [89] that finite

values of l_{SF} are irrelevant to the differences in Fig. 4.1, but we agree that a further mechanism is needed to fully explain those differences. To account for them by $l_{\text{SF}}^{\text{Co}}$ alone would require $l_{\text{SF}}^{\text{Co}} \sim 10$ nm, a value that seems too short.

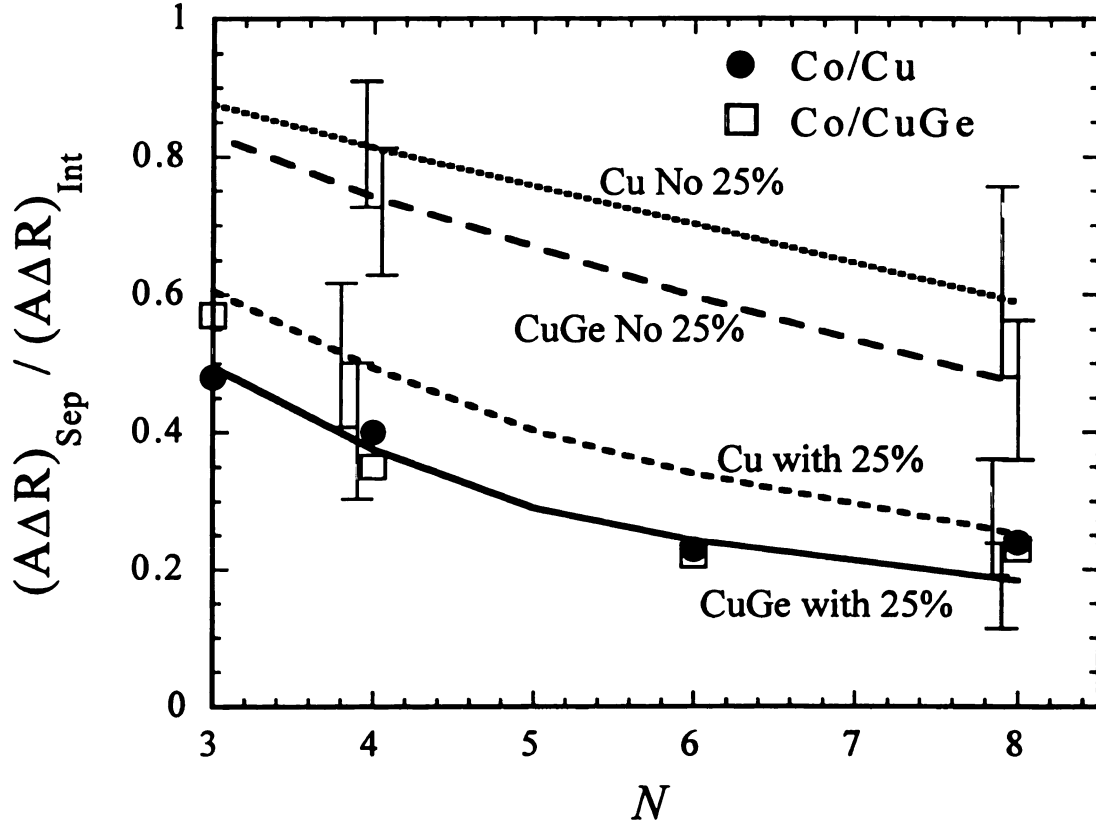


Fig. 4.14. $(A\Delta R)_{\text{Sep}}/(A\Delta R)_{\text{Int}}$ vs N . The dotted and long-dashed curves are predictions using VF theory with the parameters for Co/Cu of [25] plus $l_{\text{SF}}^{\text{Co}} = 60$ nm, $l_{\text{SF}}^{\text{Cu}} = 500$ nm, and $l_{\text{SF}}^{\text{CuGe}} = 130$ nm. The vertical bars indicate the ranges of uncertainties due to uncertainties in these values of l_{SF} . The short-dashed curve for Co/Cu and the solid curve for Cu/CuGe add $\delta_l = 0.25$ to the prior calculations. Now the error bars indicate the ranges of predictions for $\delta_l = 0.25 \pm 0.1$. For these curves, the error bars due to uncertainties in l_{SF} are smaller than the symbols for the data. $(A\Delta R)_{\text{Sep}}/(A\Delta R)_{\text{Int}}$ should be equal to 1 for all N , according to the 2CSR model. The uncertainties in the data are comparable to the symbol sizes.

B. Possible Spin-Memory-Loss at Co/Cu interfaces.

An intriguing possibility is spin-memory-loss (spin-flipping) at F/N interfaces [74,84]. With no direct evidence for such loss, our analysis must be indirect. We recently showed that spin-memory-loss can be large at N1/N2 interfaces; values for V/Cu, Nb/Cu, and W/Cu ranged from $\sim 6\%$ /interface for V/Cu up to $\sim 60\%$ /interface for W/Cu [73]. We attributed these losses to spin-orbit-induced spin-flipping in high-resistivity interfacial alloys. Adding additional flipping due to magnetic disorder in alloyed regions at F/N interfaces could well enhance interfacial spin-memory-loss.

In this section we first show that modest spin-memory-loss at F/N interfaces wouldn't destroy the agreement of published data with 2CSR and VF models. We then show that modest spin-memory-loss at the Co/Cu interface can 'explain' our data for Co/Cu and Co/CuGe.

The model we use to treat spin-memory-loss at interfaces was outlined in Ch.3. VF theory treats spin-polarized transport through a multilayer in terms of spin-dependent, spatially varying, electrochemical potentials and currents. Each layer is characterized by two lengths, the layer thickness and the layer spin diffusion length l_{SF} . At the layer boundaries, the chemical potentials and currents are matched, taking account of interfacial specific resistances where needed but neglecting any interfacial spin memory loss. Fert and Lee [93] included interfacial spin memory loss by defining a 'spin-flip' interface resistance. We use an alternative procedure for F/N interfacial spin flips that builds upon our treatment of spin-memory-loss at interfaces between nonmagnetic metals [73]. We represent the F/N interface by an additional 'layer' (I), taken to be a

homogeneous slab of thickness t_I , resistivity ρ_I^* , ‘bulk’ scattering anisotropy β_I (chosen equal to the interfacial $\gamma_{F/N}$) and spin diffusion length l_{SF}^I , subject to the constraint $AR_{F/N}^* = \rho_I^* t_I$. VF theory then involves matching electrochemical potentials and currents at the boundaries of this I -layer with the F and N-metals. Such matching depends only on two parameters, the interfacial spin-memory-loss parameter $\delta_I \equiv t_I / l_{SF}^I$, and the product $\rho_I^* l_{SF}^I$. However, the constraint $AR_{F/N}^* = \rho_I^* t_I$ lets us write $\rho_I^* l_{SF}^I = AR_{F/N}^* / \delta_I$, leaving only a single independent parameter, δ_I , to control the process, independent of any particular choice of t_I —i.e. t_I turns out to be arbitrary.

We have written programs to solve the VF equations for interleaved and separated samples up to $N = 8$ (equivalent to a standard $[F/N]_N$ multilayer up to $N = 16$). As an example of a solution, we show in Fig. 4.15 the calculated dependences of $A\Delta R$ upon δ_I for interleaved and separated Co/Cu samples with $N=6$, taking the Co and Cu parameters in [5] and assuming, for simplicity, $l_{SF}^{Co} = l_{SF}^{Cu} = \infty$. The only unknown in the problem is then δ_I . The solid curves include the Nb/Co interface resistance, $AR_{Co/Nb} = 3 \text{ f}\Omega\text{m}^2$, at each end of the sample. For the interleaved sample, $A\Delta R$ passes through a weak maximum with increasing δ_I . Over the range from $\delta_I = 0$ to $\delta_I = 1$, $A\Delta R$ varies by little more than 10%. In contrast, for the separated sample, $A\Delta R$ decreases monotonically and rapidly; by $\delta_I = 1$ it has dropped by $\sim 75\%$. To clarify the source of the weak maximum in Fig. 4.15 we also display as dashed curves the same calculation, but now taking $AR_{Nb/Co} = 0$; i.e., neglecting any contact resistance. For $\delta_I = 0$, the larger $A\Delta R$ for the interleaved and separated samples follows from Eq. 3.3 in Ch.3 simply by setting

$AR_{\text{Nb/Co}} = 0$ in the denominator AR_{AP} . Both dashed curves now decrease monotonically with increasing δ_I (increasing interfacial spin memory loss), and join nicely onto the solid curves for large δ_I . By large δ_I , the two Co/Nb interface resistances have dropped out of the problem—in this limit, $AR_{\text{Nb/Co}}$ can be set to zero. The initial rise in $A\Delta R$ in the solid curve for the interleaved sample is a consequence of $AR_{\text{Nb/Co}}$ gradually dropping out of the denominator of Eq. 3.3 as δ_I increases. This rise is an example of a counterintuitive behavior of CPP transport in the presence of a large contact resistance—increasing spin memory loss can initially cause the CPP-MR to *increase* [26].

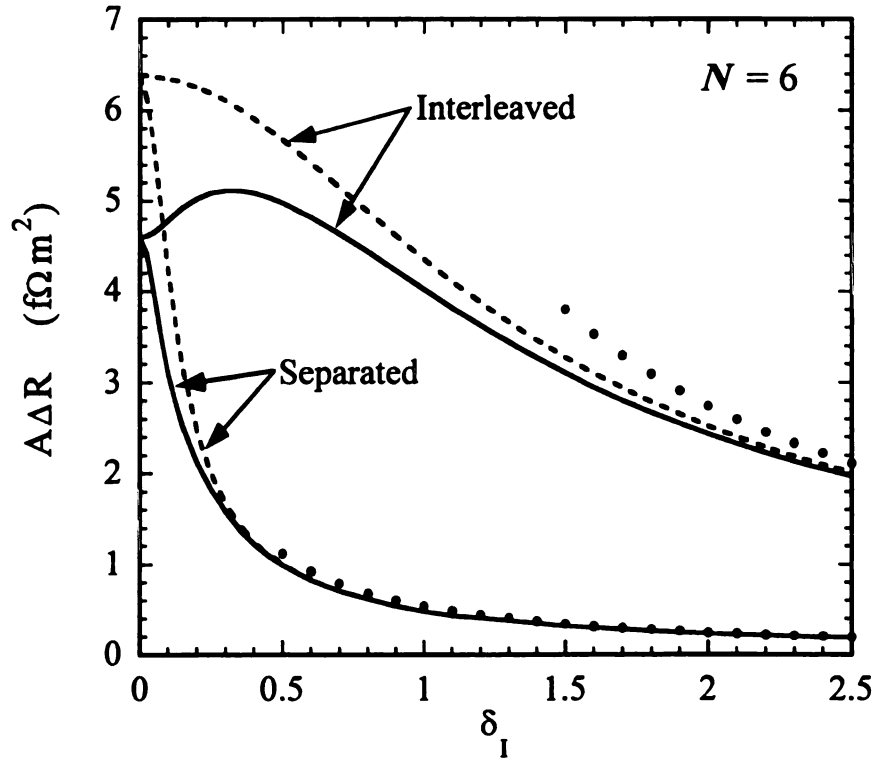


Fig. 4.15. Calculated values of $A\Delta R$ vs δ_I for interleaved and separated multilayers with $N = 6$. The solid curves include the Co/Nb contacts; the dashed curves are the same calculations but without those contacts. The filled circles correspond to Eq. 4.1 with $n = 5$ for the interleaved case and $n = 1$ for the separated one.

In the limit $\delta_l \gg 1$, the samples reduce to a linear combination of units consisting of the Cu interlayers bounded by two thin slices of Co/Cu interfaces (of thickness l_{SF}^I). $A\Delta R$ can then be described by Eq. 4.1, which is a simple extension of Eq. 3.3 to this limit.

$$A\Delta R = \frac{4n(\beta_I \rho_I^* l_{\text{SF}}^I)^2}{2\rho_I^* l_{\text{SF}}^I + \rho_{\text{Cu}} t_{\text{Cu}}}, \quad (4.1)$$

where for separated samples $n = 1$ and for interleaved samples $n = (2N-1)$. As expected, the solutions of Eq. 4.1 (solid circles in Fig. 4.15) agree with the numerical solutions (curves) in the large δ_l limit. These two limits of Eq. 3.3 are equivalent to the results of the ‘non-local’ model of [89]. $A\Delta R$ for the interleaved samples is the sum of contributions from $2N-1$ sandwiches composed of two Co/Cu thin slices on opposite sides of each Cu layer, because the magnetizations reverse from each Co layer to the next. Importantly, as shown by the open boxes and dotted curves in Figs. 4.1 and 4.9, the same value of $A\Delta R$ is seen in the as-prepared state of separated samples, and almost the same value is seen in the as-prepared state of interleaved ones. We saw in section 4.2 that the magnetizations of adjacent layers also reversed from Co layer to Co layer in the as prepared state of the separated samples and approximately also in the as-prepared state of the interleaved ones. In contrast, after the separated samples have been taken to saturation (solid symbols in Figs. 4.1 and 4.9), the magnetizations of adjacent Co layers at the intermediate field corresponding to the ‘AP’ state are all parallel to each other, except at the boundary between the two different Co thicknesses. $A\Delta R$ then contains a contribution from only the one pair of Co layers for which the adjacent layer magnetizations are opposite to each other (i.e. now $n = 1$ in Eq. 4.1).

We now consider what effect finite interfacial spin memory loss with $\delta_I = 0.25$ would have on the Co/Cu parameters that were previously derived assuming no spin-memory-loss [5]. Those parameters were derived using $[F/N]_N$ multilayers in which all of the F- and N-layers were identical, i.e. samples effectively ‘interleaved’. The solid or dashed curves for interleaved samples in Fig. 4.15 show that $A\Delta R$ is not sensitive to the presence of δ_I , until δ_I becomes larger than about 1. More generally, a non-zero $\delta_I \leq 0.25$ makes little change in the linear variations with the thicknesses t_F and t_N of the quantities AR_{AP} and $\sqrt{AR_{AP} \cdot A\Delta R}$ used to determine 2CSR model parameters for multilayers of the form $[Co/Cu]_N$ [6,7]. To show this behavior quantitatively, Fig. 4.16 uses the parameters for Co and Cu given in ref. [5] to calculate AR_{AP} and $\sqrt{AR_{AP} \cdot A\Delta R}$ for fixed $t_{Co} = 6$ nm and for $t_{Co} = t_{Cu}$ as functions of N . The filled circles are calculations with the 2CSR model assuming no spin-memory-loss anywhere. The solid curves are the VF model including spin-memory loss both in the bulk Co and Cu and at the Co/Cu interfaces— $l_{SF}^{Cu} = 500$ nm, $l_{SF}^{Co} = 60$ nm, and $\delta_I = 0.25$. The differences between the filled circles and solid lines are small, and the forms of the two sets of data are very similar. Recalculating the solid curves assuming, instead, $l_{SF}^{Cu} = l_{SF}^{Co} = \infty$ makes almost no change. A similar analysis for an infinite multilayer also produces little change. We conclude that adding interfacial spin-flipping with $\delta_I \leq 0.25$ has little effect on the previous 2CSR model analysis of data for $[Co/Cu]_N$ [5] and $[Co/Ag]_N$ [28] multilayers with equal Co layer thicknesses, only requiring renormalization of the model parameters by amounts small enough to lie within the previously specified uncertainties.

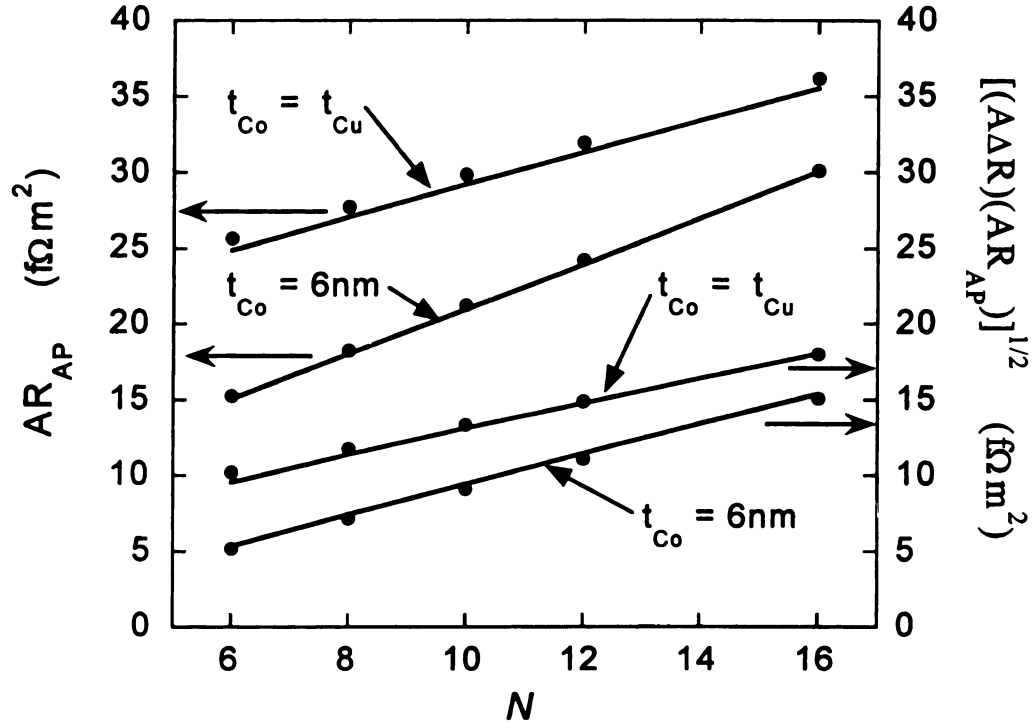


Fig. 4.16. Calculated values of AR_{AP} (left scale) and $\sqrt{AR_{AP} \cdot A\Delta R}$ (right scale) for multilayers with total thickness = 360 nm and either fixed $t_{Co} = 6$ nm or $t_{Co} = t_{Cu}$. Filled circles are for the 2CSR model. Solid curves are VF calculations with $l_{SF}^{Cu} = 500$ nm, $l_{SF}^{Co} = 60$ nm, and $\delta_I = 0.25$.

In contrast to having little effect on both interleaved samples and simple $[Co/Cu]_N$ multilayers, Fig. 4.15 shows that including interfacial spin-flips with $\delta_I = 0.25$ has a large effect on separated samples, and we'll see in Fig. 4.17 that it can also cause larger changes in Co-Cu based exchange-biased spin-valves.

In Fig. 4.14, the short-dashed curve for Co/Cu and the solid curve for Co/CuGe in Fig. 4.14 show our calculations of $(A\Delta R)_{Sep}/(A\Delta R)_{Int}$ adding $\delta_I = 0.25$ to the spin-diffusion lengths listed above. The uncertainties in these curves due to those in l_{SF} are no larger than the sizes of the symbols for the data. The error bars shown for these curves are for $\delta_I = 0.25 \pm 0.1$. This value of δ_I can “explain” our data.

In two initial papers [105,106], we referred to the value of $\delta_I = 0.25$ as corresponding to 25% spin-memory-loss at an F/N interface. For spin-memory-loss at N1/N2 interfaces, the ratio $\delta_2 = t/l_{\text{SF}}$ appears in $A\Delta R$ as a simple exponential, $\exp(-\delta)$, and $\exp(-0.25) \approx 0.78$ corresponds to a 22% reduction in $A\Delta R$. When δ is not too large, it thus approximates the percentage spin-memory-loss. In contrast, Fig. 4.15 illustrates that the situation for F/N interfaces is more complex—e.g., in interleaved or simple $[\text{F/N}]_N$ multilayers, $\delta_I = 0.25$ can produce little change in $A\Delta R$. So in this thesis we simply describe the results produced by $\delta_I = 0.25$, and never refer to a consequent percentage spin-memory-loss.

We conclude this discussion of spin-memory-loss at Co/Cu interfaces by: (a) arguing that the loss observed is plausible if the interface is viewed as a random alloy of Co and Cu, and (b) showing that some previously published data provide indirect support for such loss.

- (a) We estimate $\delta_I = t_I/l_{\text{SF}}^I$ for an assumed Co-Cu 50-50 alloy with thickness t_I assuming that spin-flips are due to spin-orbit scattering. Since the spin-flip cross-section of Co in Cu is rather uncertain [71], and we don't have reliable information about the 'size-effect' parameter $\rho_I\lambda_I$ [91] for the interfacial alloy, we must make assumptions. We assume that $\rho_I\lambda_I$ has the typical value $\rho_I\lambda_I = 1 \text{ f}\Omega\text{m}^2$ [91], and that $\rho_I t_I = AR_{\text{Co/Cu}}^*$, where $AR_{\text{Co/Cu}}^* = 0.5 \text{ f}\Omega\text{m}^2$ is the measured Co/Cu interfacial resistance [5]. Dividing the second relation by the first, we find $t_I/\lambda_I \approx 0.5$. To calculate δ_I , we must relate λ_I to l_{SF}^I . To do so, we assume that the minority and majority mean-free-paths in the interface have the ratio set by our measured γ for Co/Cu interfaces—i.e. that λ_I^\uparrow and

λ_I^\downarrow , are related by $\lambda_I^\uparrow/\lambda_I^\downarrow = AR_{\text{Co/Cu}}^\downarrow/AR_{\text{Co/Cu}}^\uparrow = (1+\gamma)/(1-\gamma) \approx 7$ [6]. Since the transport mean-free-path is the sum of the spin-dependent mean-free-paths, the effective mean-free-path related to the interface resistivity ρ_I , is essentially just the long one, λ_I^\uparrow . In contrast, from Fert et al. [72], l_{SF}^I is related to the short mean-free-path λ_I^\downarrow and the mean-free-path for spin-orbit scattering, λ_{SF} by $l_{\text{SF}}^I = \sqrt{(\lambda_I^\downarrow \lambda_{\text{SF}})/3}$, because the λ_I under the square root is determined by the equation $1/\lambda_I = (1/\lambda_I^\uparrow) + (1/\lambda_I^\downarrow)$. If, from ref. [71] we take $\lambda_{\text{SF}} \sim 20 \lambda_I^\uparrow$ (20 times the transport mean-free-path), we obtain $l_{\text{SF}}^I \approx \sqrt{(\lambda_I^\uparrow \lambda_I^\uparrow)[20/(7 \times 3)]} \approx \lambda_I^\uparrow$. Our estimate then becomes $\delta_I = t_I/l_{\text{SF}}^I = t_I/\lambda_I^\uparrow = 0.2$, large enough to ‘justify’ our experimental estimate $\delta_I \sim 0.25$.

- (b) As noted above, adding an interfacial $\delta_I = 0.25$ has minimal effect on $A\Delta R$ for simple F/N multilayers with identical F layers, or for interleaved multilayers. Such an addition can, however, affect $A\Delta R$ in exchange-biased spin-valves (SVs). In an earlier paper [107] we reported that data for both symmetric (equal Co layer thicknesses) and asymmetric (one Co layer thickness fixed and one variable) Co/Cu exchange-biased SVs fell below the values predicted using non-adjustable, independently determined, CPP-MR parameters for Co, Cu, and Co/Cu interfaces. Fig. 4.17 shows those data and those fits (dashed curves). We also noted [107] that most of the discrepancies could be removed by a combination of modest variations in the assumed parameters plus corrections for failure to reach a fully AP state in the symmetric SVs with thick Co layers. The solid curves in Fig. 4.17 show that an interfacial spin-memory loss of $\delta_I = 0.25$ provides an alternative possible explanation.

These curves (and the uncertainty bars shown) were calculated using exactly the same parameters as for the dashed curves, but simply adding interfacial spin-memory loss of $\delta_I = 0.25 \pm 0.1$. This completely non-adjustable procedure fits both sets of data surprisingly well.

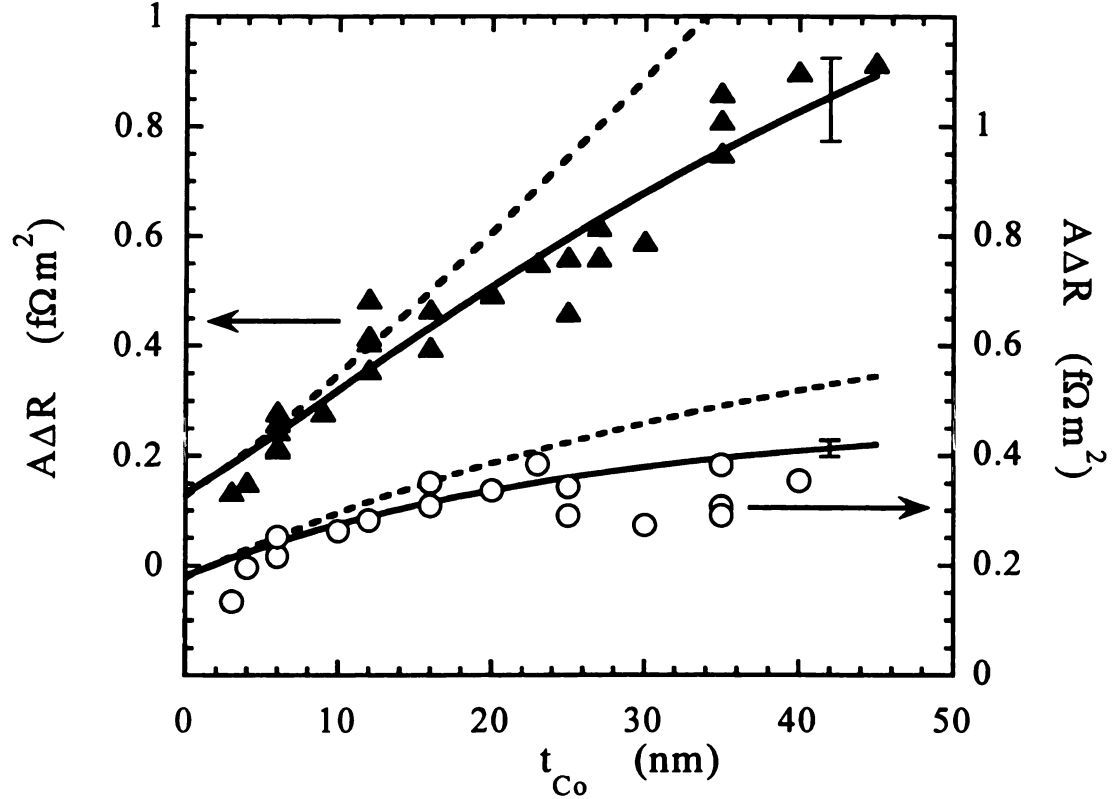


Fig. 4.17. $A\Delta R$ vs t_{Co} for symmetric (filled triangles) and asymmetric (open circles) Co/Cu exchange-biased spin-valves. The dashed curves are prior fits [25] assuming no spin-memory-loss at the Co/Cu interfaces. The solid curves just add an interfacial spin-memory-loss of $\delta_I = 0.25$.

4.6 STUDIES OF CIP-MR IN Co/Cu BASED MULTILAYERS AND CPP-MR IN Co/Ag BASED MULTILAYERS.

For completeness, we also measured the CIP-MRs of interleaved and separated Co/Cu multilayers. If mean-free-paths are the dominant lengths scales in both the CIP- and

CPP-MRs, the two might be expected to show similar differences between interleaved and separated samples. Indeed, we previously reported similar differences for [Py/Ag/Co/Ag] multilayers [83], but attributed them to different underlying physics, mean-free-path limitations for CIP, as noted in the introduction above, and spin-diffusion length limitations, mostly in the Py, for CPP. Fig. 4.18 shows that we find similar differences in the CIP-MRs and CPP-MRs for Co/Cu multilayers. Again, we attribute them to different physics—the CIP-MRs to expected mean-free-path effects there, and now the CPP-MRs to a combination of spin-memory-loss in the bulk materials and at the interfaces as argued above.

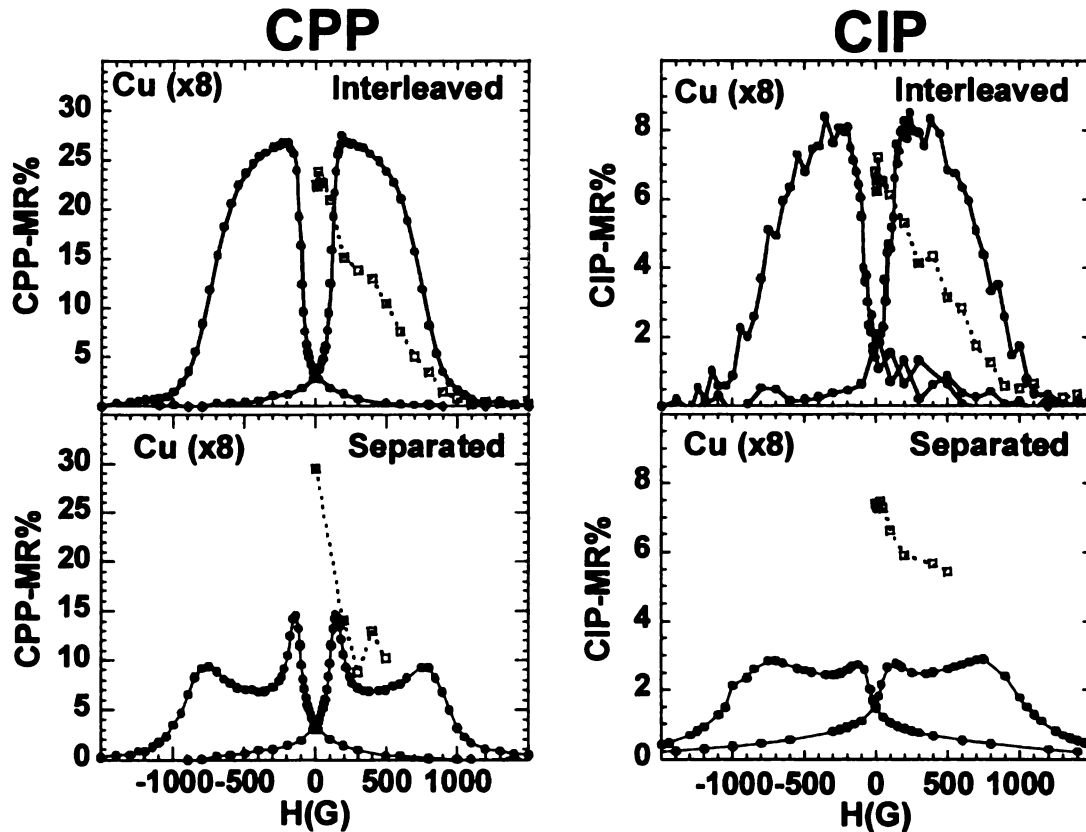


Fig. 4.18. Comparison of CPP-MR and CIP-MR for separated and interleaved Co/Cu multilayers. Symbols and curves have the same meanings as in Fig. 4.1. The open squares for the separated CPP-MR were noisy, as shown by the fluctuations in the points for $H = 200$ -500 Oe. To reduce uncertainty at $H \approx 0$, that square is the average of six very low field measurements. All other points are single measurements.

Lastly, to see if the results of Fig. 4.1 are highly sensitive to details of the mutual solubilities and band structures of the F- and N-metals, we checked the differences between interleaved and separated samples with Cu replaced by Ag, which is insoluble in Co. Fig. 4.19 shows data for $N = 8$ similar to those in Fig. 4.1.

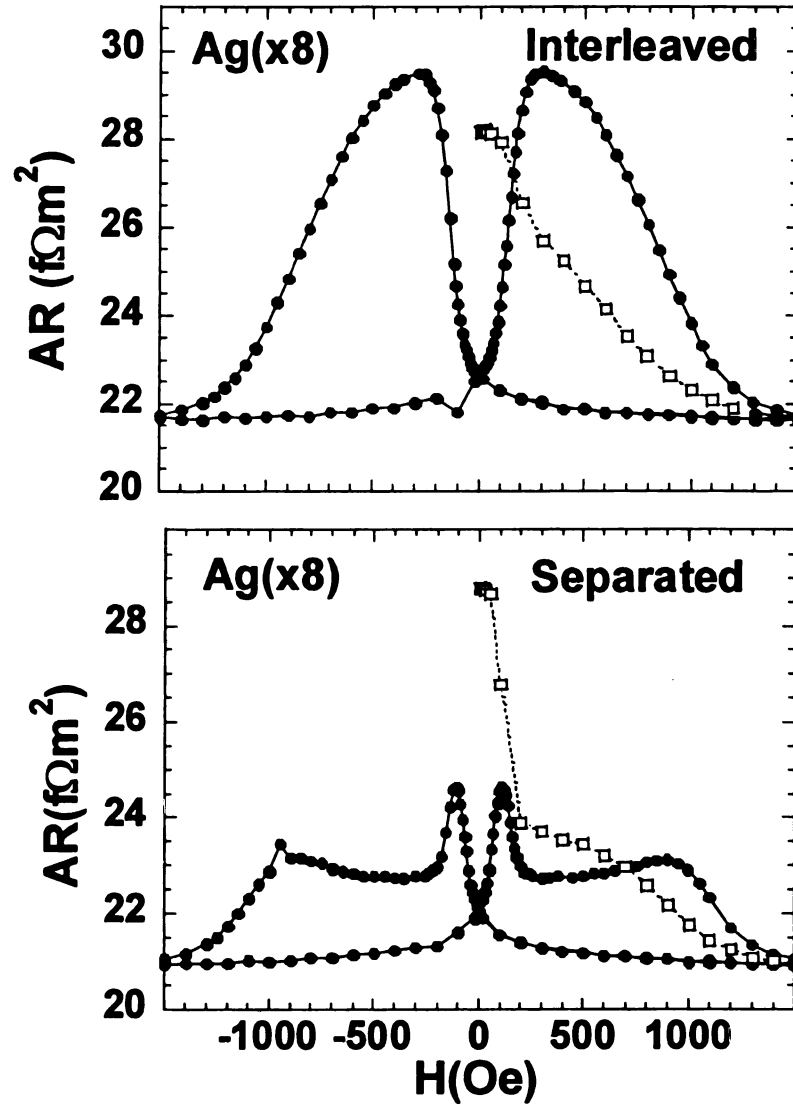


Fig. 4.19. $AR(H)$ vs H at 4.2K for interleaved (top) and separated (bottom) multilayers of Co/Ag with $N = 8$. The scale units for each coupled pair are identical. The open squares and dashed curves are for the initial state and the filled circles and solid lines are after samples were taken to saturation.

4.7 SUMMARY AND CONCLUSIONS

In this chapter we have done the following:

- (1) Confirmed the differences in CPP-MR reported in [89] for interleaved $[\text{Co}(6)/\text{Cu}(20)/\text{Co}(1)/\text{Cu}(20)]_N$ and separated $[\text{Co}(6)/\text{Cu}(20)]_M[\text{Co}(1)/\text{Cu}(20)]_N$ multilayers after they are taken to above their saturation fields, and shown that the differences persist in samples with repeat numbers as small as $N = 2$.
- (2) Showed that the CPP-MRs in the as-prepared states of separated samples are as large as those at the peaks of interleaved samples. We attribute this result to magnetic structures of the separated samples in the as-prepared state in which magnetizations of adjacent layers are reversed, as distinct from the state where the magnetizations of thick and thin layers are reversed. This result confirms the argument in [89] that the magnetic order of adjacent layers in separated samples is crucial.
- (3) Used both magnetization and polarized neutron reflectivity measurements to show that: (a) our samples do reach closely anti-parallel (AP) states and at the same fields for interleaved and separated samples, and (b) any unwanted differences between the magnetic structures of interleaved and separated samples are small.
- (4) Showed that the differences in CPP-MR remain essentially unchanged when Cu is replaced by Cu(2%Ge) with thicknesses that increase the ratio $t_{\text{Cu}}/\lambda_{\text{Cu}}$ of mean-free-path to layer thickness in the Cu from about 1/5 to 5, while still leaving the spin-diffusion length long. We infer that mean-free-paths are not scaling lengths in the CPP-MR of present day samples.

- (5) Showed that the differences remain unchanged, or even increase, when the Co layers are replaced by Py and CoZr layers for which t/λ increases by more than factors of 10. This result is evidence that the CPP-MR scaling lengths are spin-diffusion lengths, not mean-free-paths.
- (6) Showed that insertion of a thin ($t = 1\text{nm}$) FeMn layer into the middle of the central Cu layer of a separated Co/Cu multilayer produced changes in $A\Delta R(H)$ of just the kind expected for a strong increase in ‘spin-memory-loss’ due to the FeMn layer. Because the total AR contributed by the FeMn layer and its two interfaces with Cu was only comparable to the total AR contributed by alloying the 20 nm thick Cu layer with Ge, any mean-free-path effects due to the FeMn can be ruled out.
- (7) Confirmed the claim in [89] that the best available spin-diffusion lengths in Co and Cu are too long to fully explain the observed differences in CPP-MR between interleaved and separated samples, but showed that these lengths are short enough to account for part of those differences.
- (8) Argued that the rest of the differences can plausibly be attributed to spin-flipping at Co/Cu interfaces with spin-flipping parameter $\delta_I \equiv t_I / l_{\text{SF}}^I \approx 0.25$, and showed that the same amount of flipping: (a) can resolve discrepancies between predictions and previously obtained data on Co-Cu exchange-biased spin-valves, and (b) is consistent with a simple estimate of effects of spin-orbit scattering in an interfacial layer composed of a Co-Cu alloy.
- (9) Showed that the differences between interleaved and separated states are similar in the CIP- and CPP-MRs, although we interpreted the two cases differently.

(10) Showed that similar differences between interleaved and separated states persist when the Cu is replaced by Ag, which we take as evidence that the differences between separated and interleaved samples aren't sensitively dependent on details of mutual solubility or band structures.

We conclude that the use of the 2CSR and VF models in most published work on the CPP-MR still seems justified, although if interfacial spin-flipping at F/N interfaces is eventually confirmed, some parameters may need to be slightly modified. The results of this chapter are published in refs. [105,106,108].

Chapter 5

METHODS FOR ENHANCING THE CPP-MR

5.1 INTRODUCTION

For applications of the CPP-MR in devices, one wants to maximize $A\Delta R$ and/or AR_{AP} for a sample of fixed total thickness. According to Eq. 1.2, $A\Delta R$ can be increased by increasing β , increasing ρ_F , increasing $\gamma_{F/N} AR_{F/N}^*$, increasing the number of interfaces, or eliminating the contribution of the lead or contact resistance to the denominator of $A\Delta R$, provided that increasing one parameter does not cause offsetting decreases in others. In this chapter we describe controlled studies involving one or more of these changes.

In 5.2, we describe an attempt to increase both AR_{AP} and $A\Delta R$ in Co/Cu multilayers by alloying the Co with Zr. Zr was chosen based upon the tables of resistivity per atomic percent impurity in Bass [91] and of β in Campbell and Fert [46]. The former shows that Zr produces a relatively large increase in resistivity in Co, and the latter that Zr is one of only a few impurities expected to produce a β equal to or larger than that in nominally pure Co ($\beta_{Co} = 0.46$ [5]).

In 5.3, we describe a successful attempt to increase both $A\Delta R$ and AR_{AP} in Co/Cu and Co/Ag multilayers by adding ‘internal interfaces’ within the Co layers. The procedure is to divide each Co layer into a series of thinner layers by inserting Cu or Ag ‘inserts’ so thin ($t \sim 0.5$ nm) that they add little to the total sample thickness and (probably via pinholes) couple the thin Co layers ferromagnetically so that they continue to behave as a single ‘large layer’.

In 5.4, we describe a successful attempt to increase $A\Delta R$ of a Co/Cu multilayer by inserting thin ($t_{\text{FeMn}} = 1$ nm) layers of FeMn into the Cu portion of its superconducting Cu/Nb contacts. As explained in Ch. 3, VF theory predicts that inserting a source of strong spin-flipping into either magnetic or non-magnetic layers of a CPP-MR structure should eliminate from the denominator of Eq.1.2 anything outside of the source of strong spin-flipping. What will happen upon inserting the source into part of the supposedly superconducting contact layer was unclear before the present measurements.

5.2 ENHANCE THE CPP-MR BY ALLOYING Co WITH Zr

Alloying F-layers is well-known as a way to enhance GMR. As examples, $\text{Ni}_{0.8}\text{Fe}_{0.2}$ (Permalloy = Py) and $\text{Co}_{0.9}\text{Fe}_{0.1}$ are used in CIP-MR devices and both also enhance the CPP-MR over the values for the nominally pure metals Ni or Co [5]. Fig. 5.1 shows how $\text{Co}_{0.91}\text{Fe}_{0.09}$ enhances $A\Delta R$ in symmetric EBSVs of Co with Cu. The primary source of this enhancement is an increase in β from ~ 0.46 for Co [68] to ~ 0.65 for CoFe [82]. Because adding Fe increases the Co resistivity only weakly [82], AR_{AP} for CoFe is only slightly larger than for Co alone, as shown in Fig. 5.2.

We anticipated that CoZr would increase both $A\Delta R$ and AR_{AP} more than is done by Fe in Figs. 5.1 and 5.2. Zr produces a relatively large increase in the resistivity of Co per atomic percent impurity [46,91], but was not expected to reduce β from the value for Co [46]. We chose 2.5% Zr as large enough to dominate the scattering, and thus to produce the β of CoZr, but small enough, hopefully, to leave the interfacial parameters those of Co and the spin-diffusion-length $l_{\text{SF}}^{\text{CoZr}}$ long enough to not excessively truncate $A\Delta R$ for the thickness of CoZr to be studied. We hoped, thereby, to determine the CPP-MR

parameters of dilute CoZr alloys. At the end of this section we will present some data for $\text{Co}_{95}\text{Zr}_5$ and $\text{Co}_{80}\text{Zr}_{20}$, the latter above the concentration ($\sim 5\text{-}7\%$ Zr) at which CoZr is expected to become amorphous [109,110]. As explained in Ch. 2, the Zr alloys were sputtered from targets into which cylinders of Zr were embedded, the number determining the Zr concentration.

To show what we hoped to achieve, the solid lines in Figs. 5.1 and 5.2 compare 2CSR and VF predictions for $A\Delta R$ and AR_{AP} for a $\text{Co}_{97.5}\text{Zr}_{2.5}$ alloy with the measured values for CoFe and Co. As most of our data are for the 2.5 atomic % Zr alloy, hereafter we designate it by CoZr, and use subscripts only for other Zr concentrations. Our CoZr predictions use the V-F model, assuming a resistivity $\rho_{\text{CoZr}} = 19.5 \mu\Omega\text{cm}$ (corresponding to our measured resistivity for 2.5%Zr—see Ch. 2), $\beta_{\text{CoZr}} = 0.5$ from Campbell and Fert [46], and the interface parameters of Co, i.e. $\gamma_{\text{CoFe}} = \gamma_{\text{Co}} = 0.77$ and $AR_{\text{CoZr/Cu}}^* = AR_{\text{Co/Cu}}^* = 0.5 \text{ f}\Omega\text{m}^2$ [5]. The other parameters for CoFe-based EBSVs are taken from ref. [82].

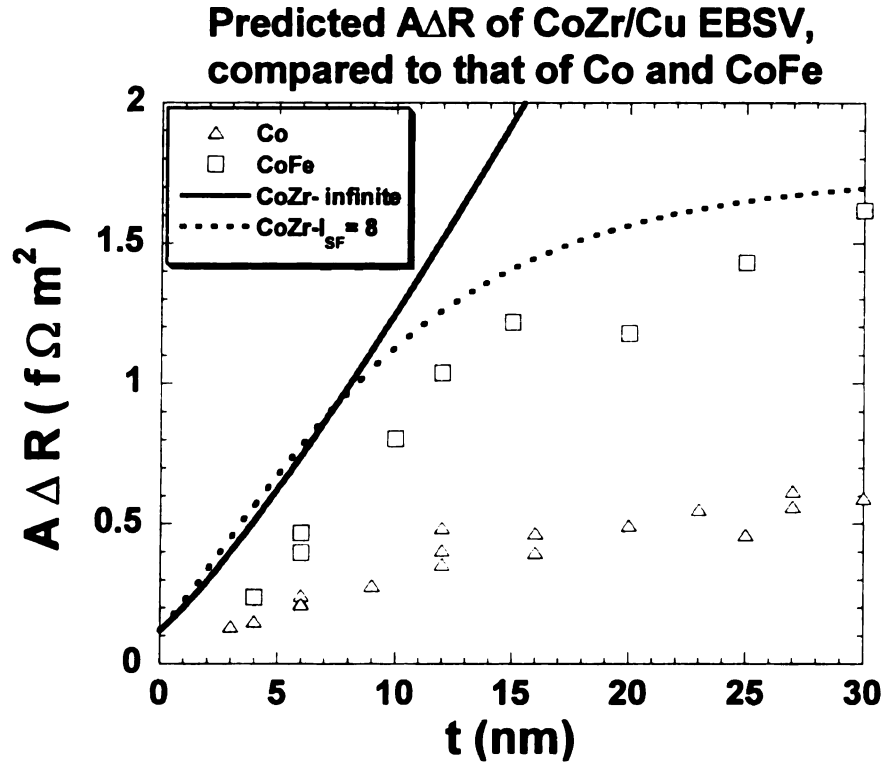


Fig.5.1. Predicted $A\Delta R$ of CoZr/Cu symmetric EBSVs using parameters given in the text and assuming infinite spin-diffusion-length, l_{SF}^{CoZr} , (solid line) or $l_{SF}^{CoZr} = 8$ nm (dotted line). The predictions are compared to data for Co/Cu and CoFe/Cu EBSVs.

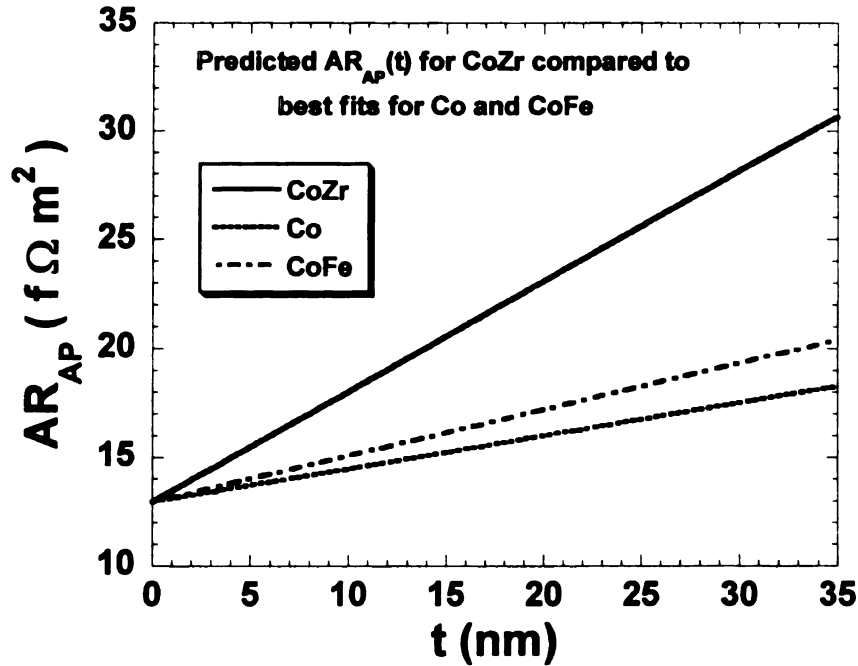


Fig. 5.2 AR_{AP} for CoFe and Co EBSVs as functions of layer thickness along with the predicted AR_P for CoZr using the parameters given in the text.

To show the effect of a finite spin-diffusion length, the $A\Delta R$ predictions assume spin-diffusion lengths of infinity (solid curve) or 8 nm (dashed curve) (less than the value for CoFe [82]). The predictions in both figures are much larger than those for Co/Cu and larger than those for CoFe.

The large resistivity of Zr in Co, coupled with the expected large β , earlier spurred a search for a large CIP-MR with CoZr alloys. However, Bouziane and coworkers [111-113] found a lower CIP-MR for $\text{Co}_{98}\text{Zr}_2/\text{Cu}$ multilayers than for Co/Cu. They concluded [112,113] that the reduced CIP-MR for CoZr was due to poor CoZr/Cu interface quality. Dusting the CoZr/Cu interfaces with thin layers of Co recovered the CIP-MR of Co/Cu multilayers, and dusting Co/Cu interfaces with thin layers of CoZr reduced the CIP-MR. We still decided to try CoZr in the CPP geometry, on the basis that the dominant electrons impact the interfaces differently in the CPP-MR and CIP-MR. The dominant electrons for the CIP-MR are those moving parallel to the interfaces, whereas the dominant ones for the CPP-MR are those moving perpendicular to the interfaces.

5.2.1 Giant Magnetoresistance of CoZr/Cu Systems

Here, we present a systematic study of the CPP-MR in a variety of CoZr based multilayers, along with detailed analyses of the scattering parameters of CoZr and CoZr interfaces with the normal metals Cu and Ag. We began with symmetric CoZr/Cu EBSVs. When the results did not agree with our expectations, we added asymmetric CoZr/Cu/Py EBSVs and later CoZr/Cu/Py/Cu hybrid spin-valves to try to pin down the parameters and clarify the source(s) of the deviations from expectations. To further explore those sources we later examined similar samples with Ag replacing the Cu. To simplify the discussion, we will describe all of these latter results in groups.

We begin with the data for our symmetric EBSVs of the form Nb(250)/Cu(20)/FeMn(8)/CoZr(t)/Cu(20)/CoZr(t)/Cu(20)/Nb(250), with all thicknesses in nm. Figs. 5.3 and 5.4 compare the measured values of AR_{AP} and $A\Delta R$ for symmetric CoZr spin-valves with the equivalent values for CoFe and Co. The 2CSR model predictions were already described for Figs. 5.1 and 5.2 above. The zero on the ordinate axis of Fig. 5.3 is suppressed to eliminate most of the contributions of the FeMn and superconducting contacts, allowing more direct comparisons between the contributions of CoZr, Co, and CoFe to AR_{AP} . We see that the AR_{AP} data for CoZr fall near the simple 2CSR model predictions; i.e., adding CoZr increases the total specific resistance almost as much as predicted. In contrast, the $A\Delta R$ data fall well below the predictions. This latter behavior is similar to that found for the CIP-MR [108-110]. Obvious possibilities for contributors to the small values of $A\Delta R$ are: (a) weaker than expected interfacial scattering anisotropy γ and/or interface resistance $2AR^*$; (b) weaker than expected bulk anisotropy, β ; or (c) a short spin-diffusion length, l_{SF}^{CoZr} . The low ordinate intercept suggests a low interfacial contribution to the CPP-MR. The relative flatness of the data at high t_{CoZr} suggests a short l_{SF} . The low values of $A\Delta R$ suggest a small β .

We began to try to understand these data by extending our analysis to the Valet-Fert (VF) model using most of the same parameters as for the 2CSR model analysis above, but now leaving three parameters adjustable: the spin-diffusion length in CoZr, l_{SF}^{CoZr} , the bulk spin-asymmetry parameter in CoZr, β_{CoZr} , and the interfacial spin-asymmetry parameter for CoZr/Cu, $\gamma_{CoZr/Cu}$. Because the numerator of $A\Delta R$ is dominated by the product $\gamma_{CoZr/Cu} AR_{CoZr/Cu}^*$ (see Eq.1.2), fixing $AR_{CoZr/Cu}^*$ and leaving only $\gamma_{CoZr/Cu}$

adjustable is sufficient to let us characterize the data. However, this procedure leads to uncertainty in the ‘true’ separate values for parameters $\gamma_{\text{CoZr/Cu}}$ and $AR_{\text{CoZr/Cu}}^*$. Moreover, the scattered data of Fig. 5.4 alone were not sufficient to pin down the values of all three parameters very well. In particular, as EBSVs have only two active F/N interfaces, EBSV data are only moderately sensitive to interfacial contributions to the CPP-MR.

For these reasons, we also measured several additional sets of samples.

First, to try to achieve better AP states, we made asymmetric EBSVs combining pinned CoZr layers with free layers of Py, which has a lower switching field than CoZr. We started with Py thickness $t_{\text{Py}} = 6$ nm, about equal to the Py spin-diffusion length ($l_{\text{SF}}^{\text{Py}} \sim 6$ nm [74]), to keep the Py contribution to the total AAR down, but not make the Py switching field too large (in large area samples, the switching field decreases with increasing layer thickness). Finding that samples with large t_{CoZr} didn’t seem to reach good AP states (see the appendix), we tried thicker $t_{\text{Py}} = 24$ nm, much larger than $l_{\text{SF}}^{\text{Py}}$.

Second, to enhance the importance of the CoZr/Cu interfaces, and to give larger signals overall, we made multilayer hybrid SVs combining layers of CoZr and Py. Again we started with $t_{\text{Py}} = 6$ nm, and then extended measurements to $t_{\text{Py}} = 24$ nm.

Detailed analyses showed that the best-fit parameters to AAR for different sets of samples were not identical. Rather than describe separate fits to each different set of data, for simplicity we show fits to just two groups of data: (a) the EBSV AAR data and (b) the hybrid SV AAR data, and then, for comparison, also a ‘common’ fit to all of the AAR data together. The separate fits are shown as dashed curves and the common fit as solid curves. These three fits illustrate the uncertainties in the derived parameters.

Fig. 5.5 compares these two best fits with the $A\Delta R$ data for the symmetric CoZr EBSVs already shown in Fig. 5.4. For the dashed curve, the best-fit parameters are: $\beta_{\text{CoZr}} = 0.4$, $\gamma_{\text{CoZr/Cu}} = 0.35$, and $l_{\text{SF}}^{\text{CoZr}} = 8\text{nm}$. For the solid curve, the parameters are: $\beta_{\text{CoZr}} = 0.34$, $\gamma_{\text{CoZr/Cu}} = 0.52$, and $l_{\text{SF}}^{\text{CoZr}} = 8\text{nm}$. These best fit parameters were determined using only data for $A\Delta R$. It is therefore important to check how well they describe the AR_{AP} data for these same samples. Fig. 5.6 shows that they both predict the values of AR_{AP} quite well, certainly much better than the 2CSR model did with the original ‘guessed parameters’ for CoZr and CoZr/Cu listed above. We end the discussion of symmetric EBSVs by showing in Fig. 5.7 that the magnetoresistance hysteresis curves indicate that we achieved good AP states for both thin and thick CoZr layers.

To continue our analysis, Fig. 5.8 compares these same two fits with our data for the three different sets of EBSVs. For the samples containing Py, the parameters for Py and the Py-based interfaces are taken from earlier papers and are non-adjustable. These parameters are: $\rho_{\text{Py}} = 110 \text{ n}\Omega\text{m}$, $\beta_{\text{Py}} = 0.75$, $\gamma_{\text{Py/Cu}} = 0.7$, $AR_{\text{Py/Cu}} = 0.51 \text{ f}\Omega\text{m}^2$, $l_{\text{SF}}^{\text{Py}} = 5.5\text{nm}$, and $2AR_{\text{Py/Nb}} = 6.1 \text{ f}\Omega\text{m}^2$. Surprisingly, despite the lower reversing fields for the Py layers, the hysteresis curves for the EBSVs with Py were not as good as for those with just CoZr. Hysteresis curves given in the appendix imply good AP states for thinner CoZr layers, but not so good for thicker ones. The thick CoZr data points in Fig. 5.8B and C should, thus, probably be viewed as only lower bounds. Indeed, the thick CoZr data points for $t_{\text{Py}} = 6 \text{ nm}$ actually decrease with increasing t_{CoZr} . As shown in the appendix (Fig. A.5), the agreement between the ‘predictions’ for AR_{AP} and the data are also not as good in the asymmetric EBSVs as they were in the symmetric ones, with the

‘predictions’ now lying a bit above the data and growing with increasing t_{CoZr} a bit too fast. At least part of the problem may lie with the Py parameters, which are not the focus of the present work.

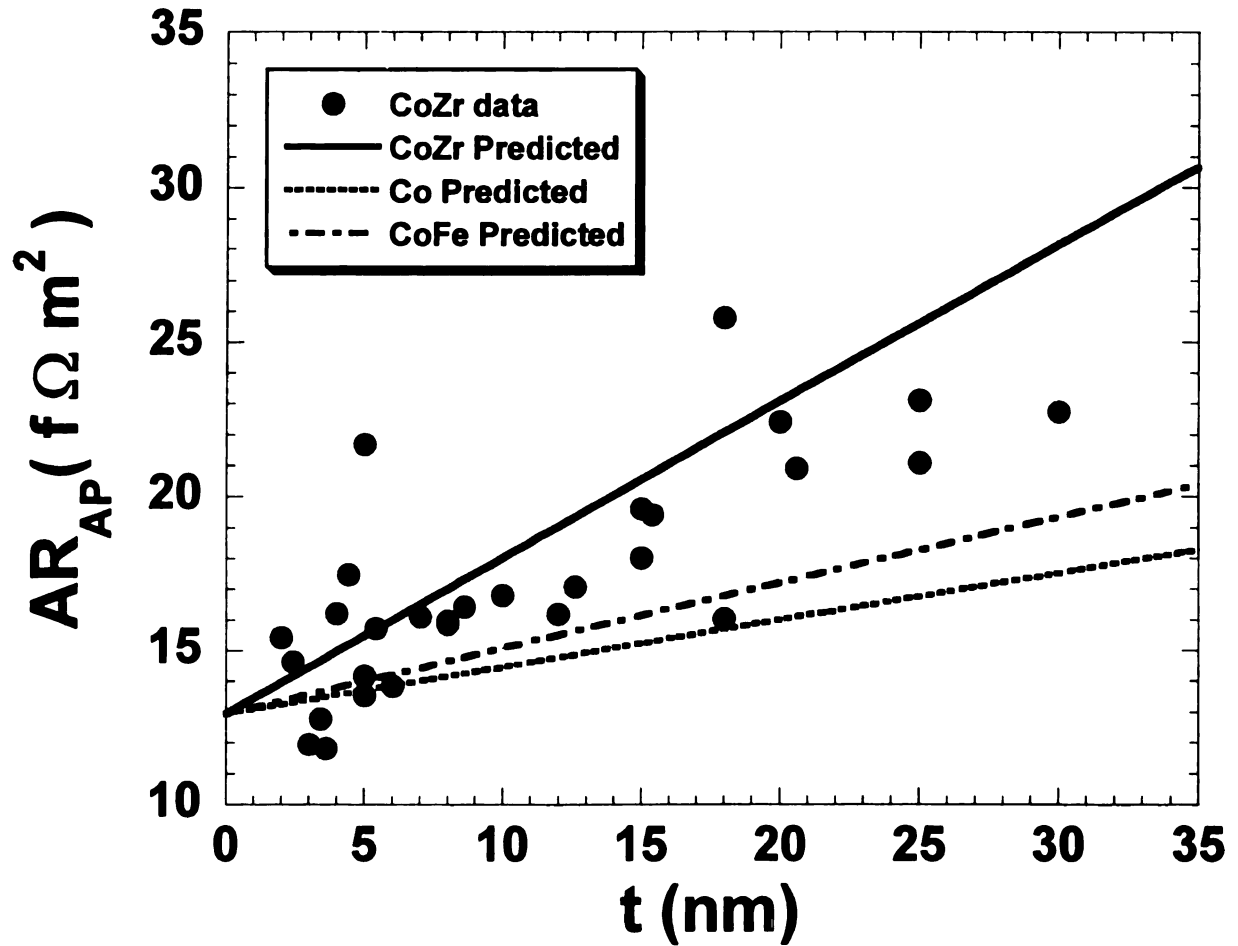


Fig. 5.3. AR_{AP} vs t for CoZr/Cu EBSV data, compared with ‘best fit lines’ for CoFe/Cu EBSVs (broken curve), Co/Cu EBSVs (dotted curve), and the 2CSR model for CoZr/Cu described in the text above.

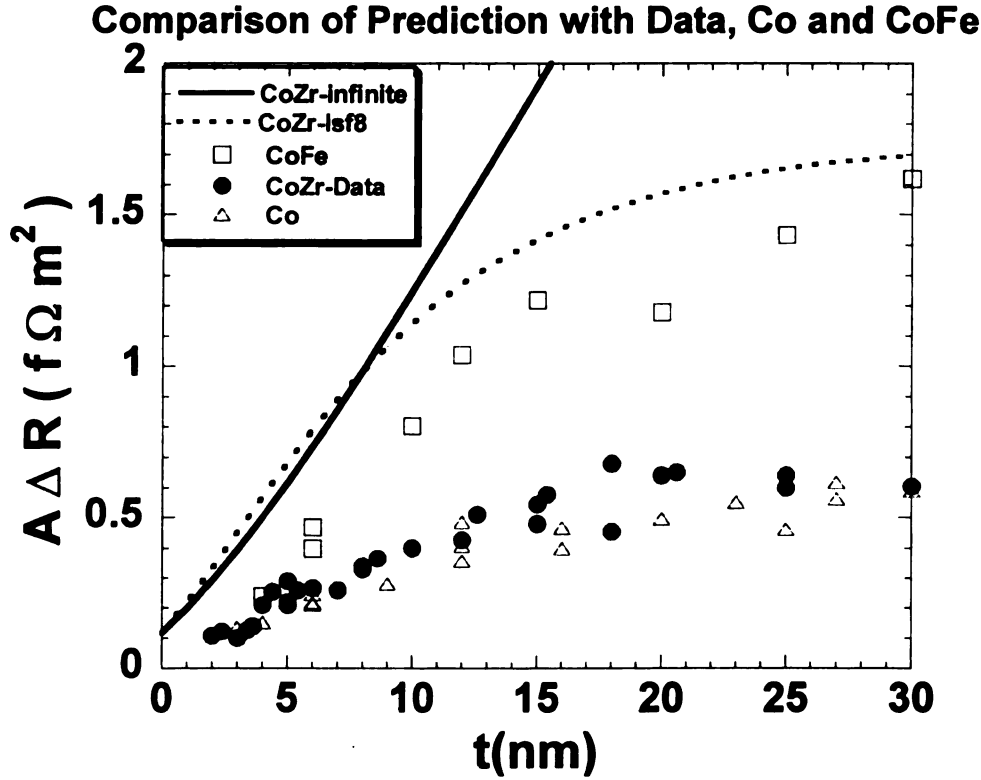


Fig. 5.4. $A\Delta R$ vs t for Co, CoFe, and CoZr symmetric EBSVs. This figure is a replot of Fig. 5.1 with the addition of our CoZr symmetric EBSV data.

Finally, we turn to the hybrid data, for which the $A\Delta R$ data are collected together in Fig. 5.9. Hybrid SVs have the advantage that both AR_{AP} and $A\Delta R$ are larger than for the EBSVs, and thus easier to measure. Fig. 5.9 contains the best fit curves for both the hybrid data alone (dashed curves with parameters $\beta_{CoZr} = 0.3$, $\gamma_{CoZr/Cu} = 0.6$, and $l_{SF}^{CoZr} = 6nm$) and the ‘best common’ fit (solid curves with the parameters already given). The lower l_{SF}^{CoZr} in the hybrid multilayers could be partly due to the lack of AP state at moderate CoZr thicknesses (see Appendix for examples of magnetoresistance hysteresis curves). As for the asymmetric EBSVs, the AR_{AP} predictions are systematically a bit too large, and the hysteresis curves suggest possible problems with AP states for thick CoZr layers (see Appendix).

Table 5.1 summarizes the parameters from the three sets of fits given above. Two of these parameters are unexpected.

First, the small value of $\gamma_{\text{CoZr/Cu}} = (0.3 - 0.5)$ relative to $\gamma_{\text{Co/Cu}} = 0.77$. Because 2.5% Zr is such a small impurity content, we had expected the Zr atoms to be largely irrelevant to the interfacial properties. However, the CPP-MR analyses of the data in Figs. 5.5 and 5.8 agree with the conclusions of the CIP-MR studies that the CoZr/Cu interface is less effective in producing MR than the Co/Cu interface. We will see below, however, that interfacial dusting of CoZr/Cu interfaces with Co, or Co/Cu interfaces with CoZr, gives less clearcut results than those reported for the CIP-MR.

Second, $\beta_{\text{CoZr}} \sim (0.34)$ is smaller than the value 0.5 listed by Campbell and Fert [46]. Here, however, the uncertainty of the Campbell-Fert value is unknown.

Table 5.1. CoZr parameters found from the fits to our data.

Sample Set	β_{CoZr}	γ_{CoZr}	$l_{\text{SF}}^{\text{CoZr}}$ (nm)
Expected	0.5	0.77	?
EBSV fits	0.4	0.35	8
Hybrid fits	0.3	0.6	6
Common fit	0.34	0.52	8

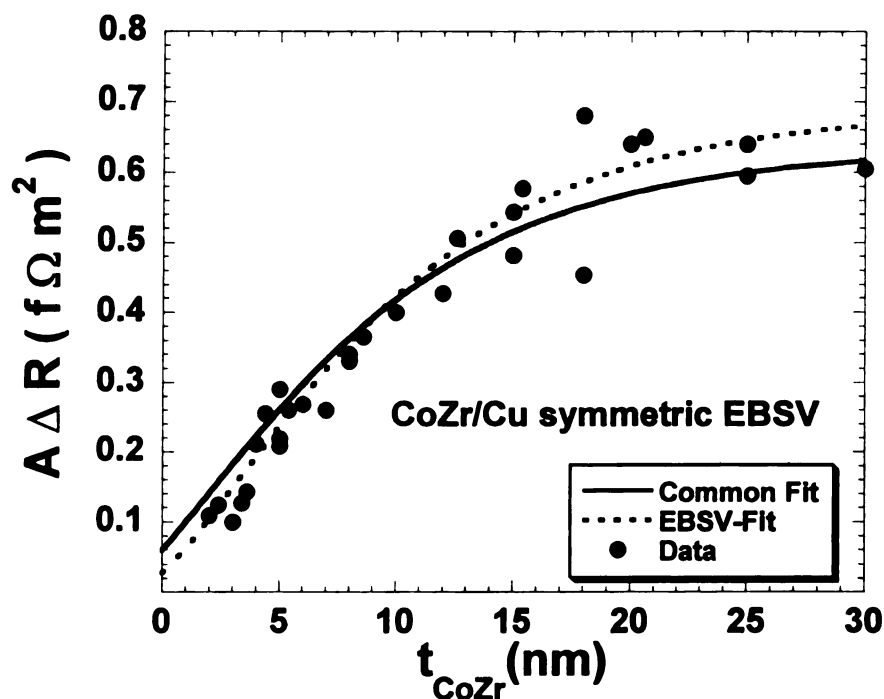


Fig. 5.5. $A\Delta R$ vs t_{CoZr} for symmetric EBSVs. The dotted curve is a best to just the three EBSV data sets for $A\Delta R$. The solid curve is the best 'common fit' to all of the samples, exchange biased and hybrid.

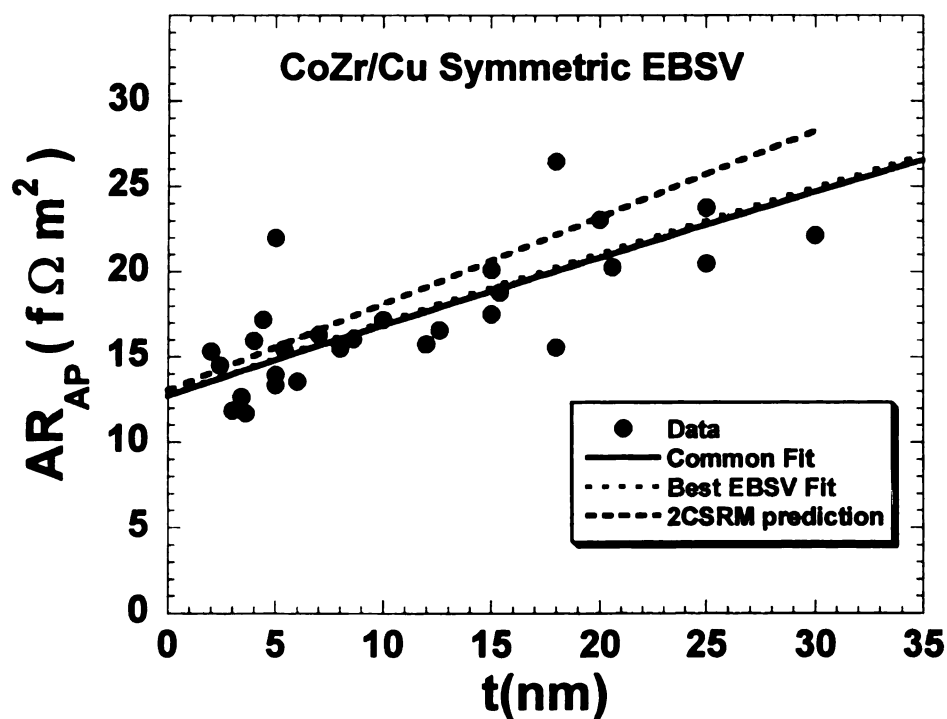


Fig. 5.6. Using the parameters from the fits to $A\Delta R$ fits the data for AR_{AP} quite well. The dashed curve is the 2CSR model fit described in the text above. The best fits are closer to the data than the 2CSR model prediction.

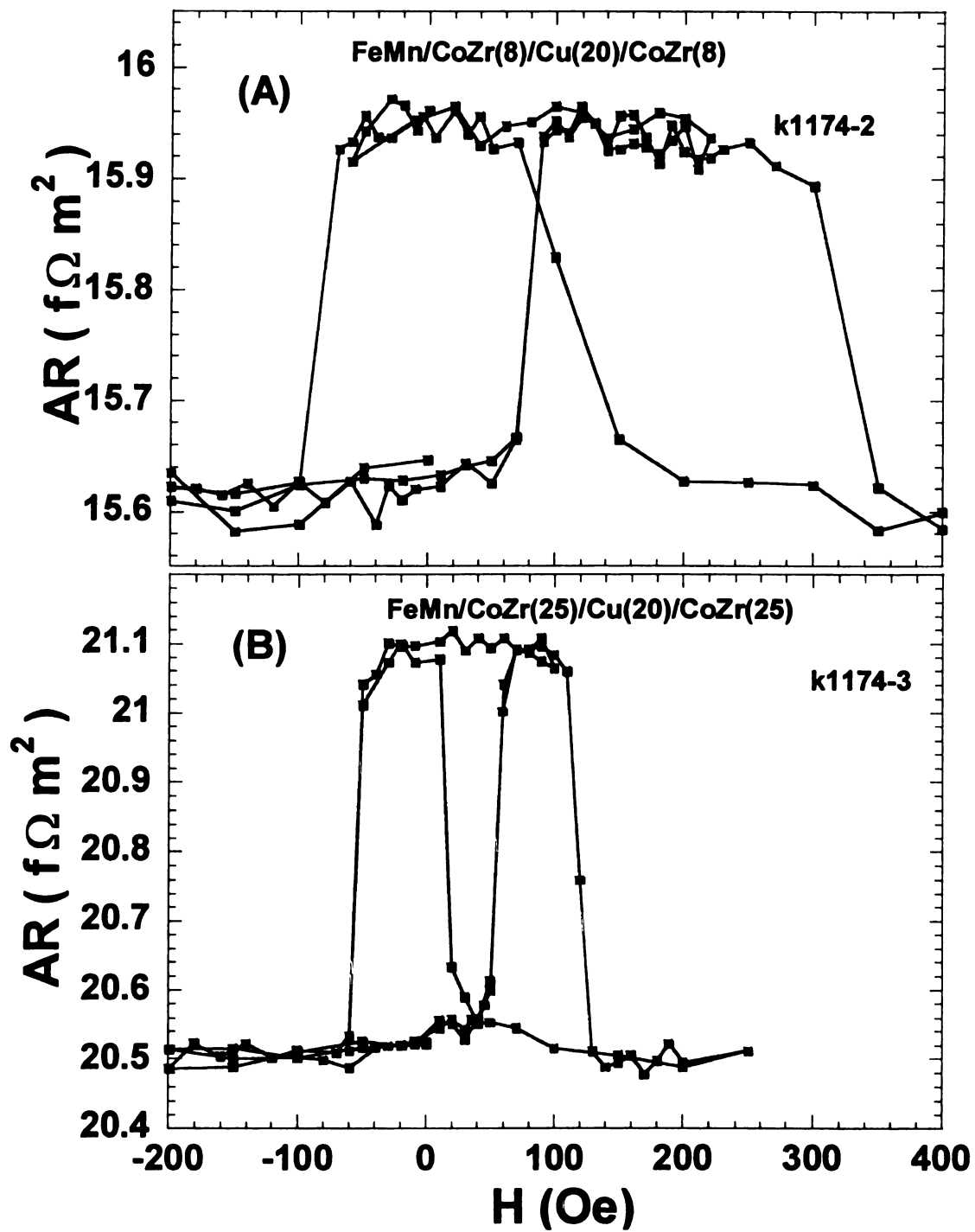


Fig. 5.7. AR vs H for symmetric EBSVs with $t_{CoZr} = 8$ nm (A) and 25 nm (B). In both cases, the hysteresis curves are nicely square, indicating well-formed AP states.

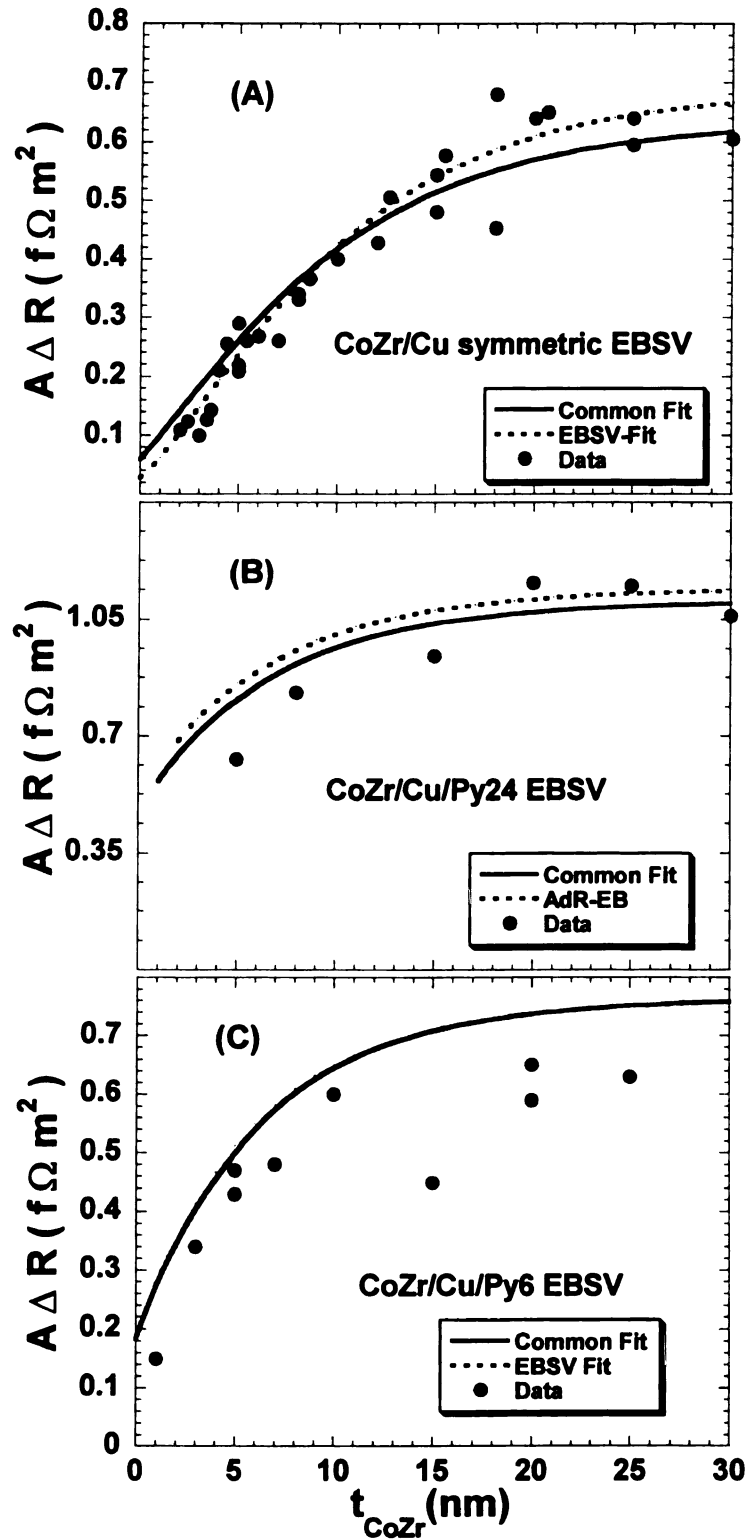


Fig. 5.8. $A\Delta R$ vs t_{CoZr} for EBSVs. (A) Symmetric EBSVs; (B) Asymmetric EBSVs with $t_{\text{Py}} = 24$ nm; (C) Asymmetric EBSVs with $t_{\text{Py}} = 6$ nm. The dashed curves represent a fit to just these three sets of data. The solid curves represent a 'common fit' to all of the exchange biased and hybrid samples with CoZr/Cu. In C, the two fits fall on top of each other.

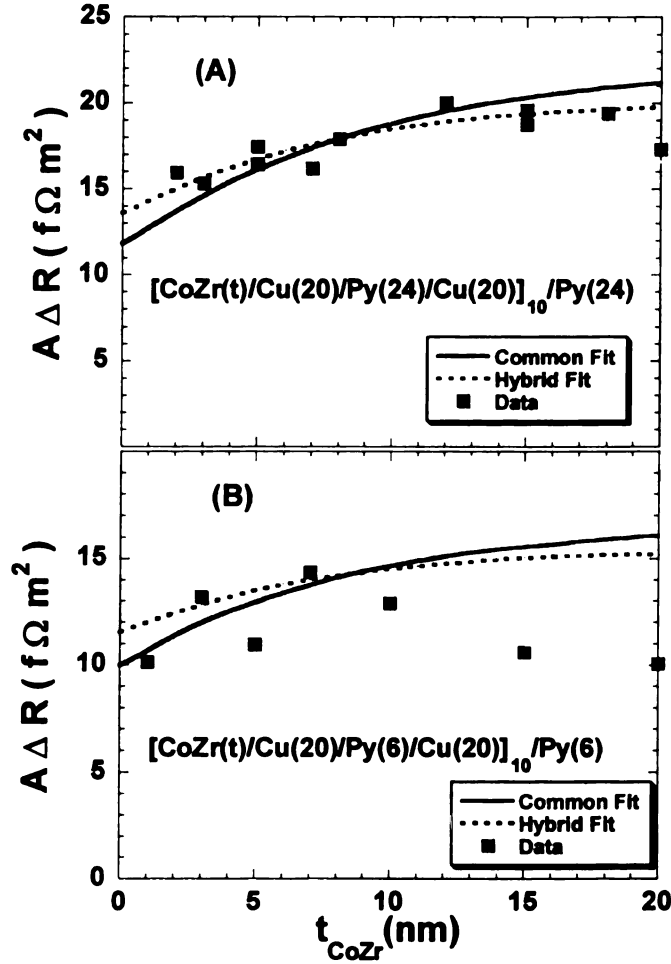


Fig. 5.9. $A\Delta R$ vs t_{CoZr} for hybrid SVs with $t_{\text{Py}} = 24$ nm (A) or 6 nm (B). The dashed curves represent a fit to just these two sets of data. The solid curves represent a 'common fit' to all of the CoZr/Cu data in Figs. 5.8 and 5.9.

5.2.2 Dusting CoZr/Cu Interface With Co:

To see if some property of the CoZr/Cu interface is causing the apparent low $\gamma_{\text{CoZr/Cu}}$ of Table II, we 'dusted' the CoZr/Cu interfaces with 1 nm of Co to create Co/Cu interfaces. The structure of those samples is $\text{FeMn}/\text{CoZr}(t)/\text{Co}(1)/\text{Cu}(20)/\text{Co}(1)/\text{CoZr}(t)$. If Zr impurities reduce γ , dusting with Co should increase $A\Delta R$. Fig. 5.10 shows that Co dusting did not significantly change $A\Delta R$.

To look at the effect of dusting more carefully, we prepared a set of symmetric EBSV samples with the following structures:

- A) [FeMn/CoZr(12)/Cu(20)/CoZr(12)]
- B) [FeMn/CoZr(10)/Co(2)/Cu(20)/Co(2)/CoZr(10)]
- C) [FeMn/Co(12)/Cu(20)/Co(12)]
- D) [FeMn/Co(10)/CoZr(2)/Cu(20)/CoZr(2)/Co(10)]

We chose the thickness to be 12 nm total for each ferromagnetic layer because our fits are most sensitive to the value of $\chi_{\text{CoZr/Cu}}$ at this thickness. Fig. 5.11 shows data for the above samples, where we made a pair of each structure to check reproducibility. All eight samples were prepared in a single sputtering run. The numbers in Fig. 5.11 show the order in which each of the samples was sputtered. First, there is a systematic decrease in $A\Delta R$ with the order in which each sample was sputtered. That is, comparing pairs of samples with the same structure (samples 1 and 6 (having structure C), 2 and 5, 3 and 8, and 4 and 7) shows that the earlier the sample was sputtered, the larger is $A\Delta R$. The issue of more relevance here is to compare samples with different structures. Comparing samples with structure (C) Co/Cu/Co, with samples of structure (D), Co/CoZr/Cu/CoZr/Co, shows that introducing CoZr slightly reduces the $A\Delta R$ compared to a 'bare' Co/Cu interface. Comparing samples A and B shows the same effect, but less pronounced. This experiment suggests that CoZr/Cu interface is at least partly responsible for the reduced MR effect in CoZr-based spin valves, since dusting Co/Cu interfaces with CoZr thin layers reduces $A\Delta R$ and dusting CoZr/Cu interfaces with Co increases $A\Delta R$.

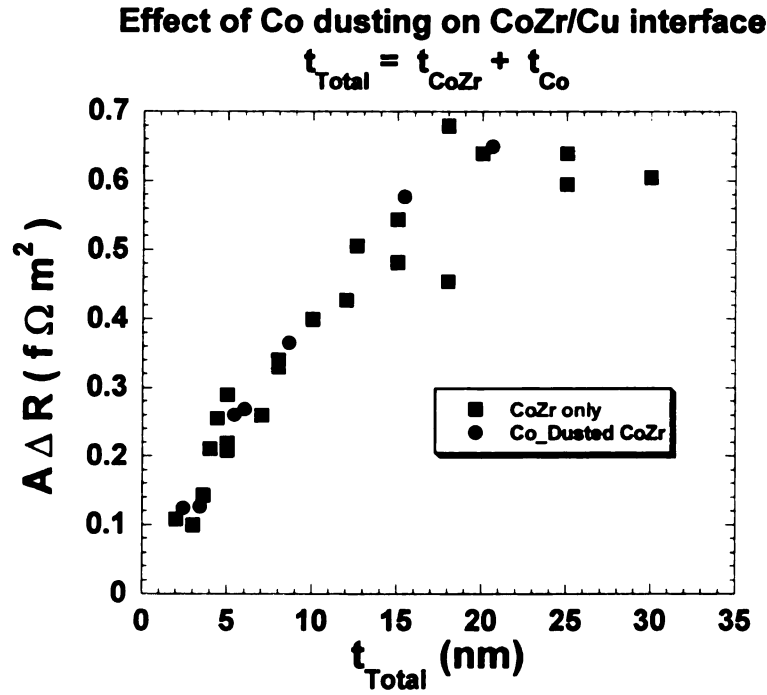


Fig.5.10. Co dusting of CoZr/Cu symmetric EBSVs. Sputtering a 1 nm thick layer of Co at each CoZr/Cu interface does not increase $A\Delta R$.

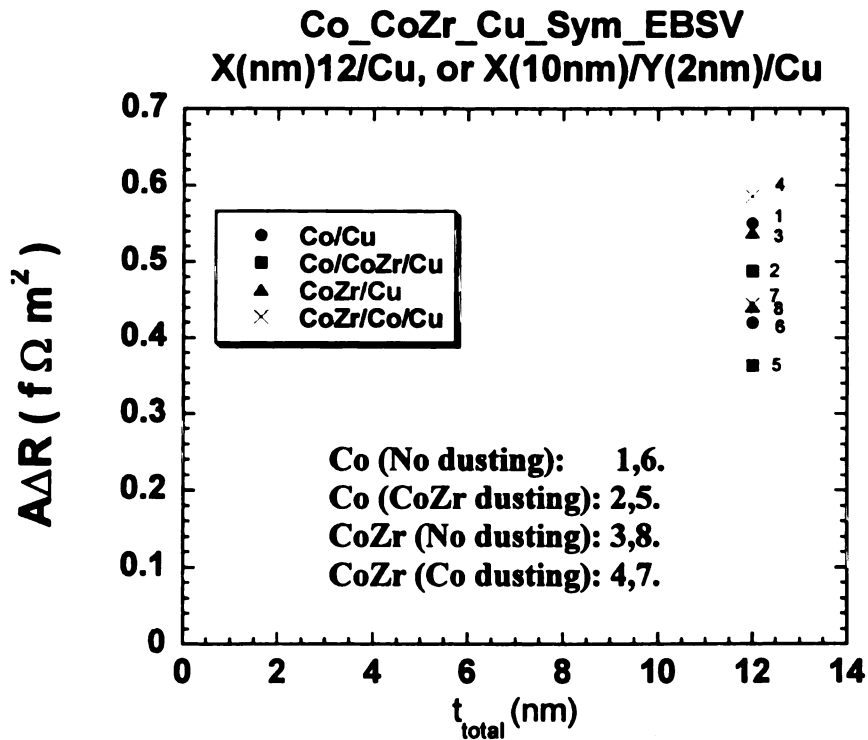


Fig.5.11. Comparing $A\Delta R$ for dusting CoZr/Cu interfaces by Co, dusting Co/Cu interfaces by CoZr, and no dusting. There is a systematic reduction in $A\Delta R$ with the order of preparing the sample (indicated by numbers) in the sputtering run. Dusting a Co/Cu interface with CoZr reduces $A\Delta R$, and dusting a CoZr/Cu interface with Co increases it.

5.2.3 GMR in CoZr/Ag:

To see if the unexpectedly small CPP-MR seen in CoZr/Cu multilayers is unique to Cu, we also tried CoZr/Ag multilayers. We found that $A\Delta R$ is systematically larger for CoZr/Ag, and the increase seems to be associated mainly with the CoZr/Ag interface. But there are complications, in that there is a significant increase in AR_{AP} in going from Cu to Ag that is too large to be explained in terms of the difference in resistivities or interface AR s for Cu and Ag. The difference may be due to problems with the FeMn layers in the CoZr/Ag. The quality of FeMn seems to change when grown on Ag instead of Cu. Fig.5.12 compares $AR(H)$ for a Cu sample (A) and a Ag sample (B), plus the same Ag sample (C) after reannealing to a higher temperature. We see that FeMn grown on Cu has better pinning properties than that grown on Ag (i.e. pinning persists to a higher field), and also gives smaller total resistivity (AR_{AP}). The total specific resistance in the sample of Fig. 5.12B is larger than that of Fig. 5.12A. This higher AR_{AP} persists in all Ag-based samples. We take this higher AR_{AP} and different details of $AR(H)$ curve of Ag based samples as an indication that the FeMn grown on top of Ag has higher resistivity and poorer pinning properties than FeMn grown on Cu. Fig.5.12C displays the $AR(H)$ curve for the same sample of Fig. 5.12B reannealed at a higher temperature. After the second annealing the total specific resistance rose a bit, and a 'flatter top' to the $AR(H)$ curve suggests a closer approach to antiparallel alignment.

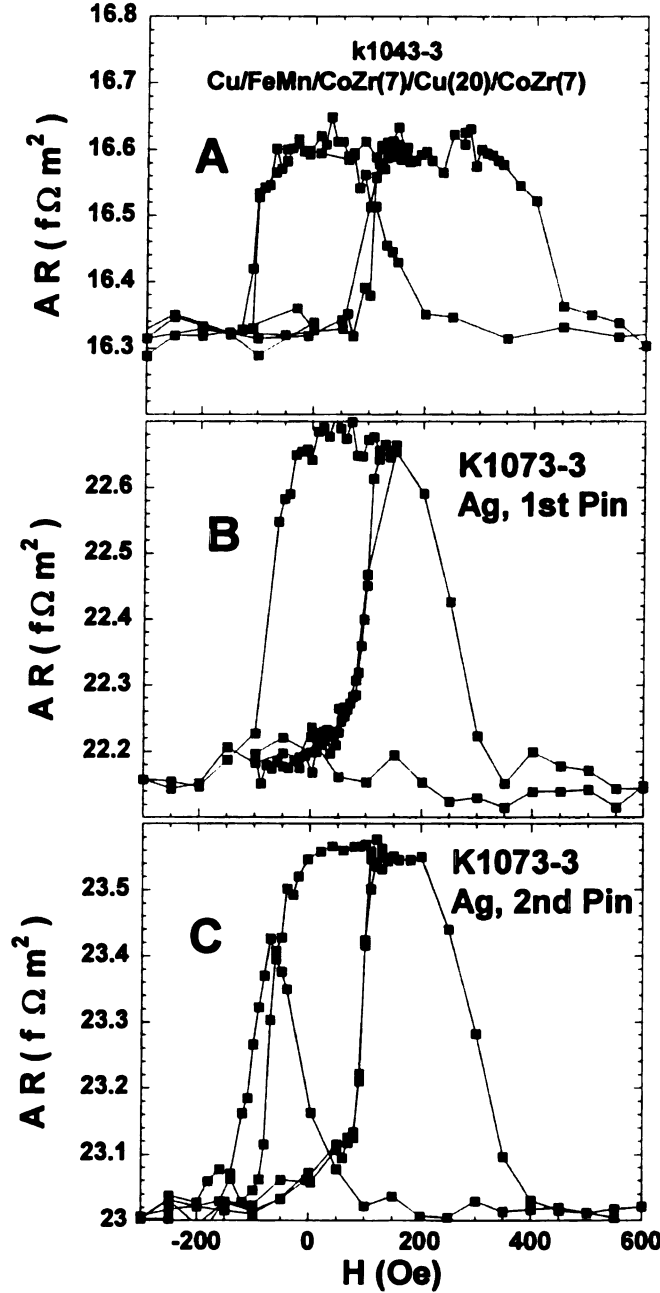


Fig.5.12. $AR(H)$ curves for EBSVs with Cu spacer layers (A), and Ag spacer layers (B and C). The pinning is strongest for the Cu sample A and the total specific resistance, AR_P , is lowest. Pinning the Ag sample at a higher temperature (C) gave a slightly better result than at the usual pinning temperature (B). $t_{\text{CoZr}} = 7$ nm in both samples.

Fig.5.13 compares $A\Delta R$ versus CoZr thickness for symmetric EBSVs with structure $[\text{Ag}/\text{FeMn}/\text{CoZr}(t)/\text{Ag}(20)/\text{CoZr}(t)]$ with $A\Delta R$ for Cu based EBSVs (from Fig. 5.5). The Ag-based samples give larger $A\Delta R$ s. The higher extrapolated 'ordinate intercept' for Ag,

combined with similar modest rises with increasing t_{CoZr} for both Ag and Cu, suggest that the larger $A\Delta R$ s are mainly the result of $\gamma_{\text{CoZr/Ag}}$ being larger than CoZr/Cu. The fits shown use the ‘common fit’ parameters given in table 5.1, except that for Ag, $\gamma_{\text{CoZr/Ag}} = 0.8$ [28] replaces $\gamma_{\text{CoZr/Cu}} = 0.52$. With this larger $\gamma_{\text{CoZr/Ag}}$, the fit to the CoZr/Ag data is reasonable, suggesting similar contributions from CoZr whether CoZr is grown on Ag or on Cu.

The same behavior also occurs in hybrid samples, where slightly higher values of $\gamma_{\text{CoZr/Ag}}$ are needed to better fit the CoZr/Ag data. Fig.5.14 shows $A\Delta R$ of hybrid samples with structure $[\text{CoZr}(t)/\text{Ag}(20)/\text{Py}(24)/\text{Ag}(20)]_{10}/\text{Py}(24)$. Using the same ‘common fit’ parameters but with $\gamma_{\text{Py/Ag}} = 0.8$ roughly fits the data, within its rather large scatter.

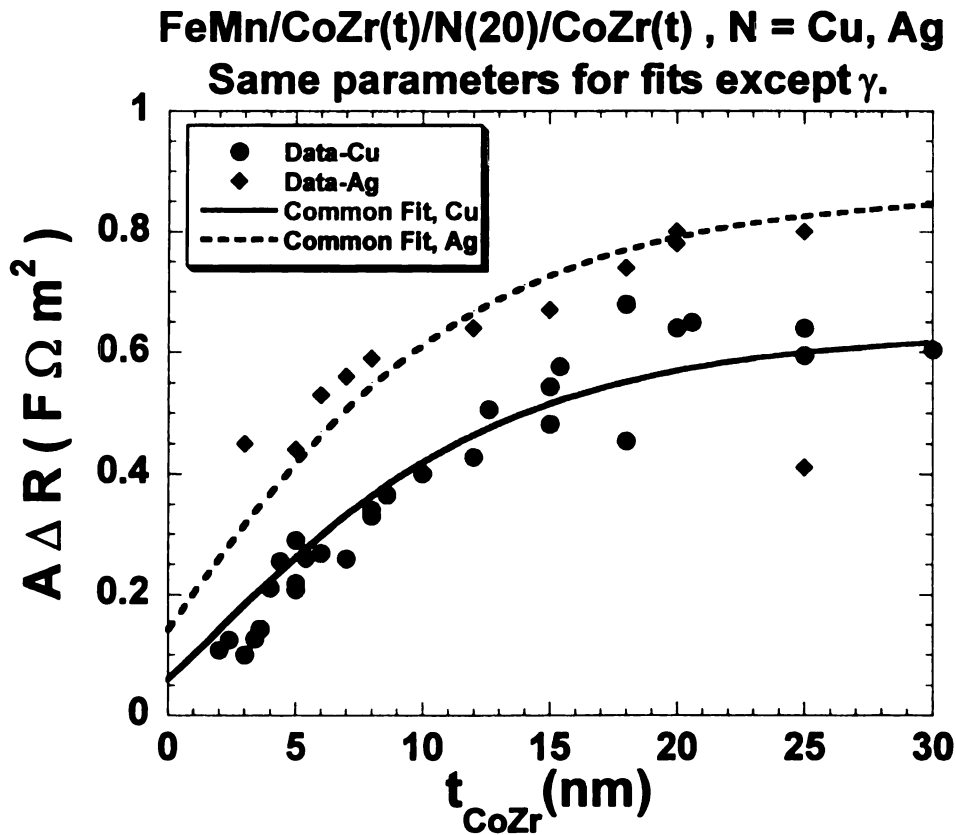


Fig. 5.13 $A\Delta R$ of CoZr/Ag based symmetric EBSVs and a comparison with Cu. Ag gives larger $A\Delta R$ values, especially at small thicknesses, indicating the CoZr/Ag interface gives a larger contribution to MR than the CoZr/Cu interface.

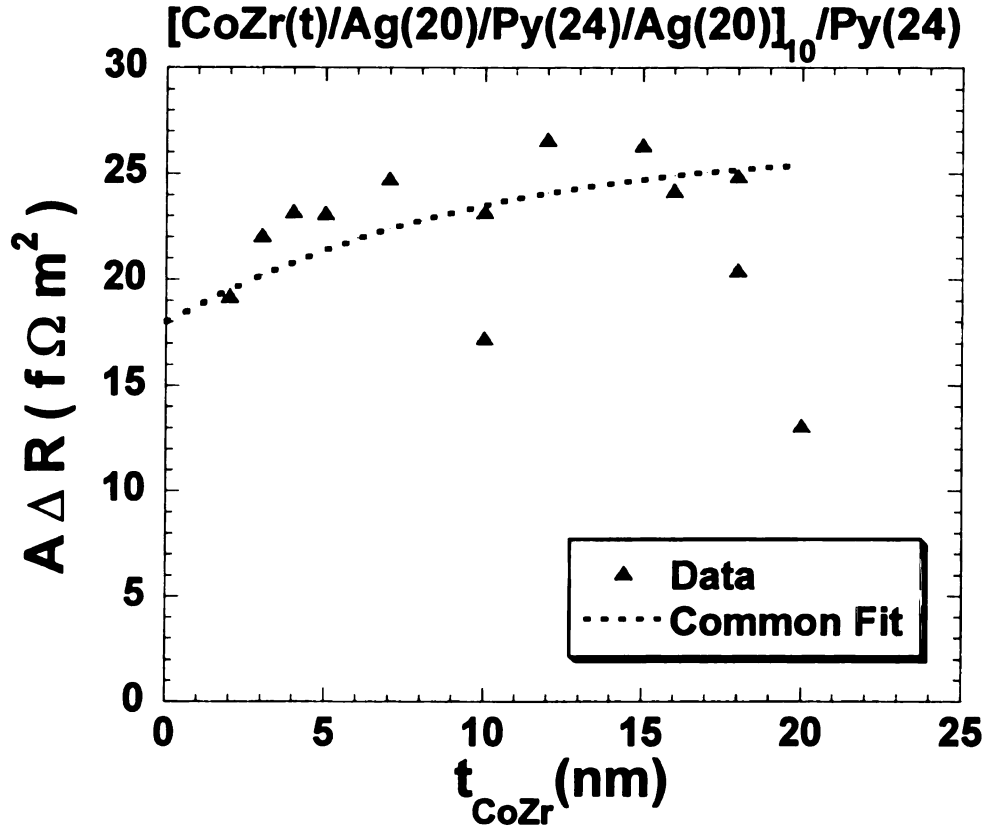


Fig. 5.14. $A\Delta R$ vs t_{CoZr} in CoZr/Ag/Py hybrid samples. The fit uses the same parameters as in Fig.5.13 plus $\gamma = 0.8$ for the CoZr/Py interface. As in the Cu-based samples the fit is below data, requiring a slightly larger value of γ .

5.2.4 Effect of FeMn Growth on MR

As mentioned above, Fig.5.12 shows a difference in the CPP-MR “hysteresis” curves depending on the type of nonmagnetic spacer layer. The Cu-based sample has a lower total specific resistance, AR , and a stronger pinning of the CoZr layer in contact with FeMn. The relatively large difference in AR_{AP} between samples with Cu and Ag suggest that the change is coming from the FeMn, since the resistivities of the rest of the layers are too small to account for the difference. Since the pinning is also weaker in the Ag samples, we suspected that FeMn grown on top of Ag behaves differently from FeMn grown on Cu. Antiferromagnetism in FeMn is known to depend on the crystal structure of the FeMn [116], which in turn depends on the growth. FeMn is antiferromagnetic in

the FCC (or γ phase), and nonmagnetic in the BCC structure (β phase). The presence of pinning in our samples indicates the FeMn is antiferromagnetic when grown on Cu and may be partly so on Ag. We made a systematic set of samples to study the effect on the CPP-MR of EBSVs of growing FeMn on Cu, Ag, or CoZr. This section is limited to the symmetric EBSVs and we will show that FeMn is most likely the source of the differences in Fig. 5.12. The samples used in this search for FeMn growth effects had the following structures:

- A) Cu(20)/FeMn(8)/CoZr(t)/Cu(20)/CoZr(t)
- B) Ag(20)/FeMn(8)/CoZr(t)/Ag(20)/CoZr(t)
- C) Cu(2)/FeMn(8)/CoZr(t)/Ag(20)/CoZr(t)
- D) Cu(20)/CoZr(t)/Cu(20)/CoZr(t)/FeMn(8)

Fig. 5.15 shows $A\Delta R$ versus t_{CoZr} for all four structures. Sample B has the highest $A\Delta R$ on average, which is surprising since the GMR-active region in B is identical to that in C. We do not yet have an explanation for this difference. Except for structure B, the other three samples give basically the same $A\Delta R$ to within fluctuations.

To test whether the differences in AR_{AP} between the different structures are due to differences at the CoZr/N interface, we plot AR_{AP} as a function of t_{CoZr} for the four samples along with two predictions using the VF model. The differences are even more visible in Fig. 5.16 where samples of structure B have a higher AR_{AP} than the other three. The difference between AR_{AP} of B and C rules out the possibility that the CoZr/N interface is causing the differences in AR_{AP} since the only difference in them is the material on which the FeMn layer is grown. Since there is a small possibility that CoZr itself may change in structures in A through D, we plot in Fig. 5.17 AR_{AP} as a function of

CoZr thickness for both samples A and B, fitting each to a straight line. The slopes of the two lines are the same, which means that the resistivity of CoZr is the same for both types of nonmagnetic spacers, Cu and Ag. The value of the slope also agrees with the CoZr resistivity found earlier (Ch. 2) using the Nb/CoZr(t)/Nb sandwiches and Van der Pauw measurements. Dividing the slope of each line in Fig. 5.17, $360 \pm 50 \text{ n}\Omega\text{m}$, by two gives $\rho_{\text{CoZr}} = 180 \pm 25 \text{ n}\Omega\text{m}$. However, the intercepts on the AR_{AP} axis are different for the two sets of samples; $13 \pm 1 \text{ f}\Omega\text{m}^2$ for Cu and $20 \pm 1 \text{ f}\Omega\text{m}^2$ for Ag. From Fig. 5.17, we ruled out the CoZr/N interfaces as the source of this difference. We, thus, end with only the FeMn layer as the source of the increased AR when grown on Ag.

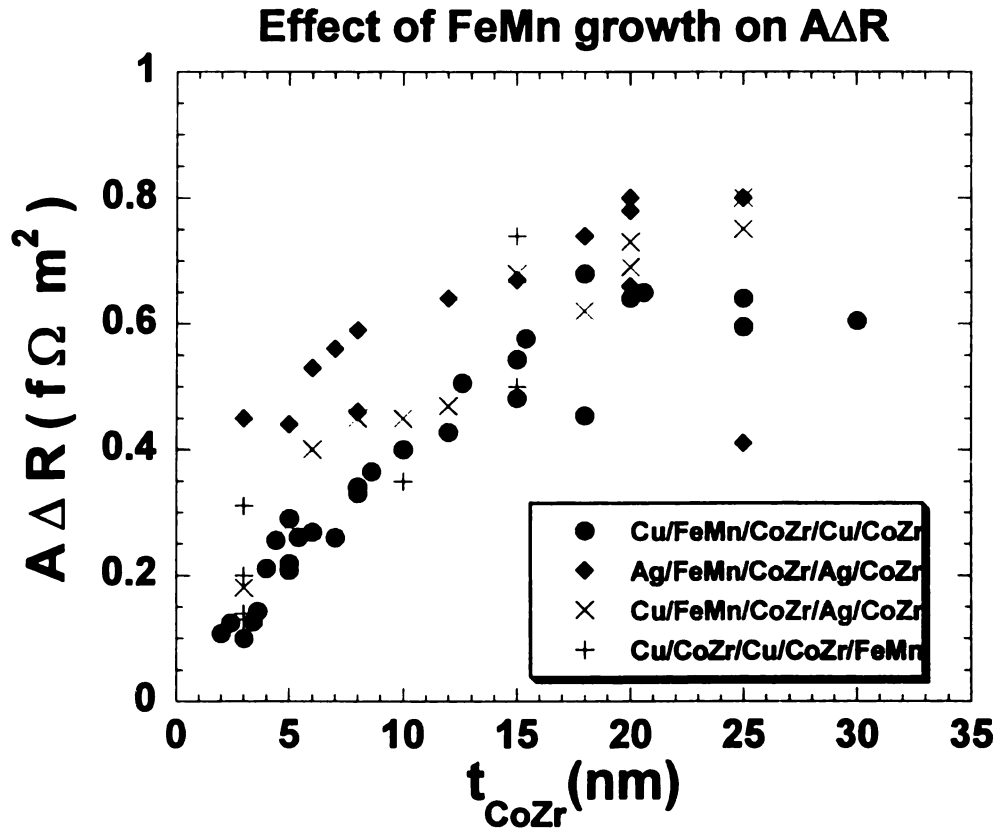


Fig. 5.15. $A\Delta R$ vs t_{CoZr} in symmetric EBSVs. Changing the metal on which FeMn is grown affects $A\Delta R$. Growing FeMn on Ag gives the highest $A\Delta R$.

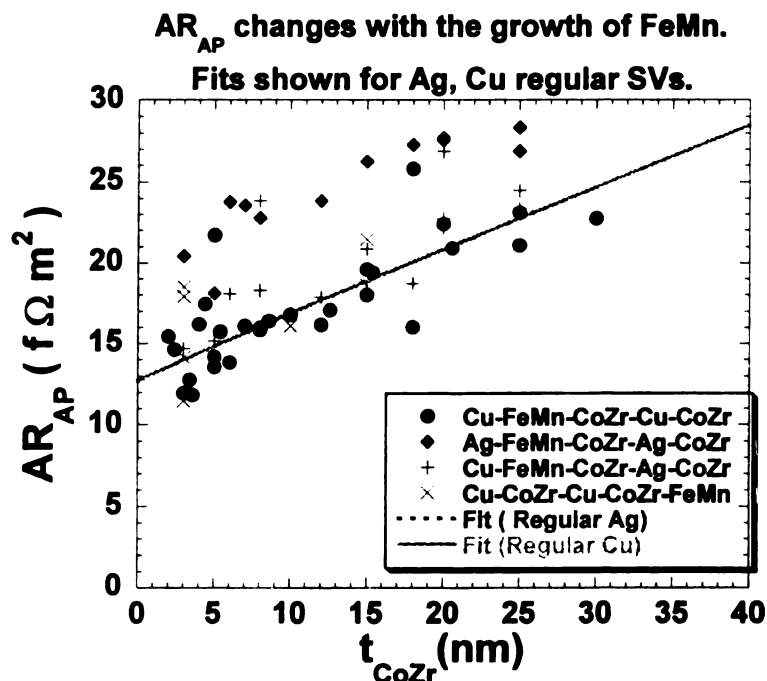


Fig. 5.16. Effect of FeMn growth on AR_{AP} . Growing FeMn on Ag gives a significantly higher AR_{AP} than when growing it on Cu or CoZr. The V-F model predicts only a slight increase in AR_{AP} for the Ag samples over the Cu samples. The fits for Ag and Cu are on top of each other.

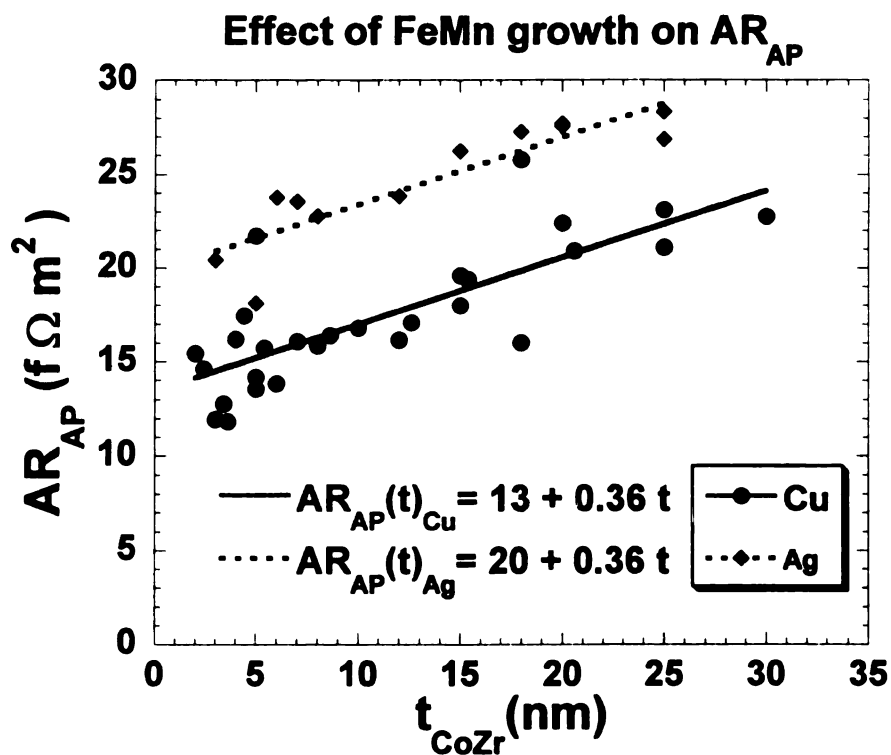


Fig. 5.17. AR_{AP} vs t_{CoZr} . As predicted by the 2CSR model, AR_{AP} grows linearly with t_{CoZr} . The slope is the same for Ag and Cu samples, showing that CoZr has the same resistivity in both. But the intercepts are different, pointing to the FeMn as the source of the larger AR_{AP} for Ag.

5.2.5 Search for Magnetically Dead Layers

The discussion above shows that the CoZr/Cu and CoZr/Ag interfaces are potential sources of complications in the physics of the multilayers. The existence of a magnetically dead layer CoZr layer at these interfaces might influence the CPP-MR. This possibility prompted us to search for dead layers at CoZr/Cu and CoZr/Ag interfaces.

To check for dead layers we prepared multilayered films of structure: $[\text{CoZr}(t/N)/\text{X}(5)]_N$, where N is the usual number of repeats in the multilayers.

The total magnetic moment, μ_t , of the multilayer is given by: $\mu_t = \mu_{\text{Sheet}} \times t$, where μ_{Sheet} is the magnetic moment per unit thickness of CoZr, and t is the total thickness of the magnetic CoZr material. μ_{Sheet} is a constant having no effect on the analysis. For fixed total thickness of CoZr, t_t , number of layers, N , each with thickness t , and a magnetically dead layer of thickness t_0 at each interface, the total magnetic moment of the multilayer should be:

$$\mu_t = \mu_{\text{Sheet}} \times t_t = \mu_{\text{Sheet}} \times (N t - 2 N t_0) \quad (5.1)$$

Plotting μ_t/N versus t should then be a straight line with ordinate intercept at $t = 2 t_0$.

Fig.5.18 shows the magnetization curves of 6 multilayers with fixed $t_{\text{CoZr}} = 48$ nm and variable N . The inset shows only a very slight reduction, if any, in the total saturation magnetic moment of the multilayers as N is increased up to 48. This near constancy indicates that any dead layer at the CoZr/Cu interface must be very thin. Fig.5.19 shows the total magnetic moment divided by the number of repeats, μ_t/N , versus t_{CoZr} . Using Eq. 5.1 gives $2t_0 = 1.06/(0.61) \approx (1.8 \pm 3.6) \text{ \AA}^0 \Rightarrow t_0 \approx (0.9 \pm 2) \text{ \AA}^0$. The best fit is only half a dead layer. Within our errors, we cannot rule out either no dead layer at all, or a single dead monolayer. In the same way we determined from Fig. 5.20, that at CoZr/Ag

interfaces, any dead layer would be: $2t_0 = 1/5.5 \approx (0.2 \pm 0.5) \text{ \AA}^0 \Rightarrow t_0 \approx (0.1 \pm 0.3) \text{ \AA}^0$.

Here, we can rule out a dead layer at the CoZr/Ag interfaces.

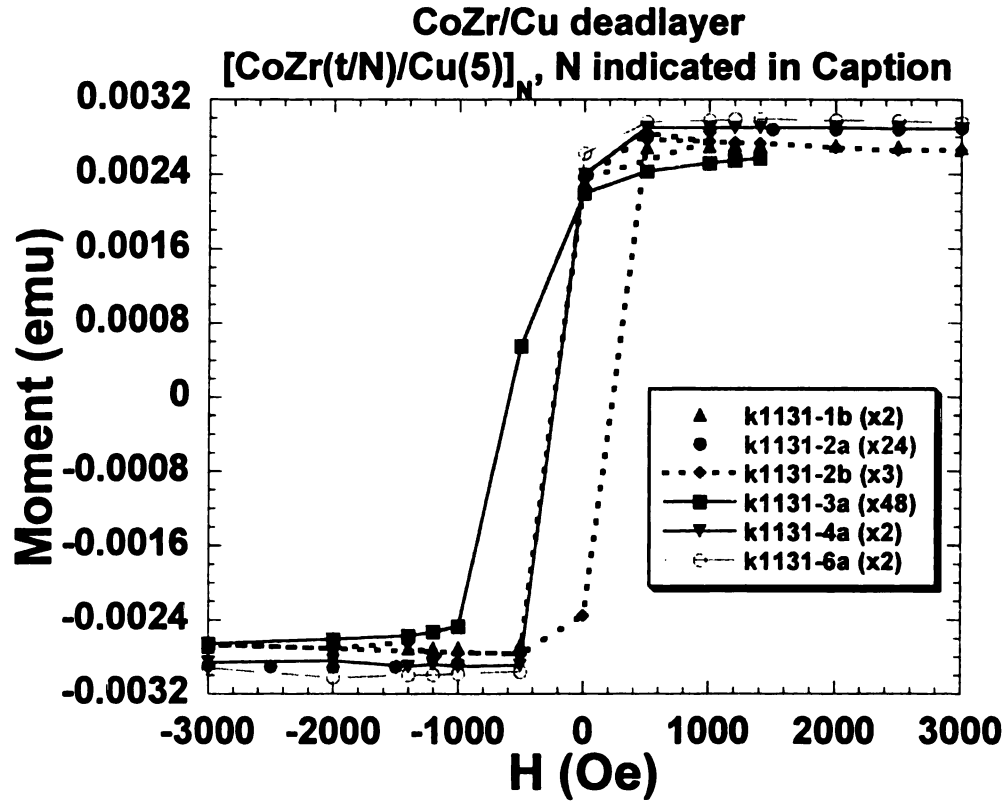


Fig.5.18. Hysteresis loops of [CoZr(*t*)/Cu]_{*N*} multilayers with fixed total CoZr thickness, $t_T = 480 \text{ \AA}^0$. The saturation magnetization is almost the same for all samples, regardless of the individual CoZr layer thicknesses. Any magnetically dead CoZr layer at the CoZr/Cu interface must be thin.

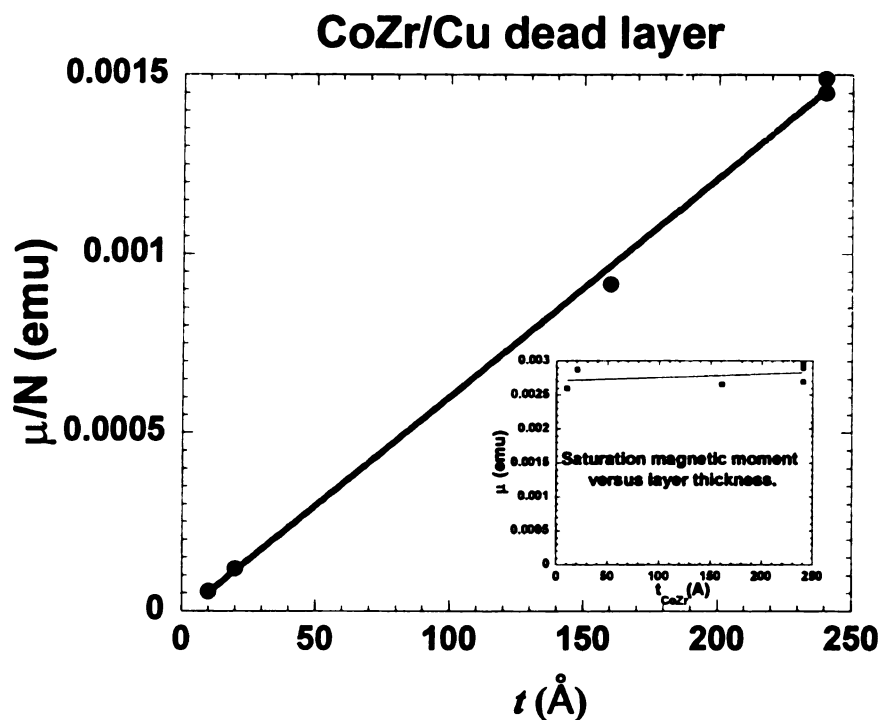


Fig. 5.19. μ/N vs t_{CoZr} thickness for CoZr/Cu multilayers. The ordinate intercept gives the thickness of any dead layer.

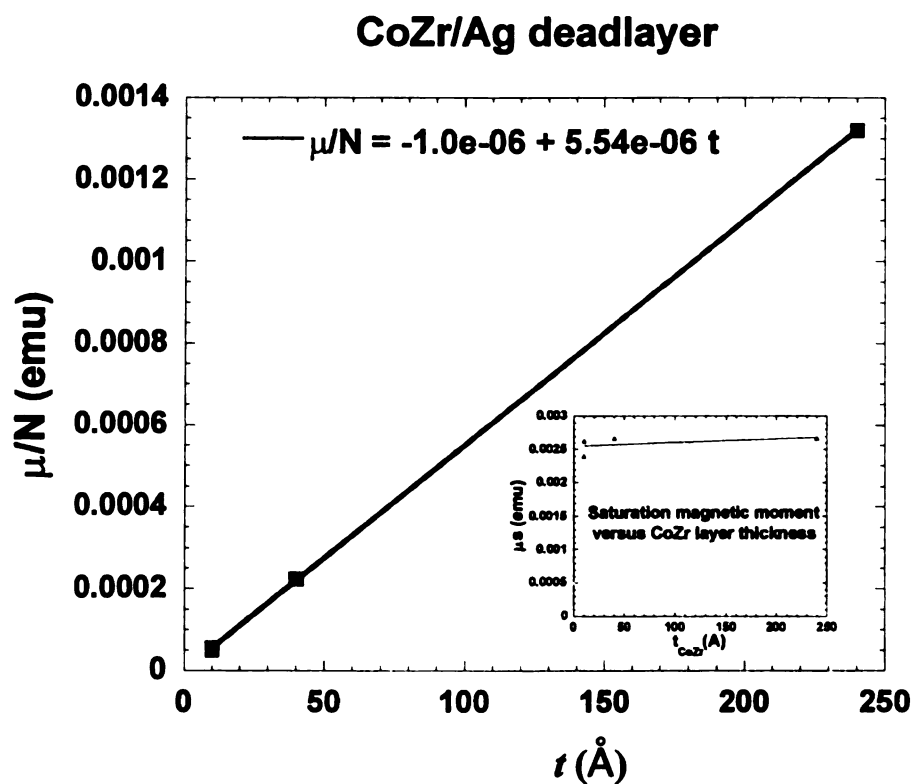


Fig. 5.20. μ/N versus CoZr layer thickness for CoZr/Ag multilayers. The ordinate intercept indicates little or no magnetically dead layer at the CoZr/Ag interface.

5.2.6 Co₉₅Zr₅ and Co₈₀Zr₂₀

In this section we study samples with higher Zr content. The two concentrations of Zr we chose were 5% (still polycrystalline), to see how the CPP-MR behaves with increasing Zr, and 20% (expected to be amorphous), which is a magnetically ultrasoft structure [111,114] with potential for applications if it has a decent CPP-MR. Fig. 5.21 shows $AR(H)$ curves for two Co_{100-x}Zr_x(5)/Cu(20)/Py(6) hybrid samples. Fig. 5.21A is for $x = 2.5$, and B is for $x = 5$ sample. There are three important features of Fig. 5.21. The first is that the switching fields for CoZr are the same and not noticeably small for both Zr contents, indicating that Co(5% Zr) is still polycrystalline (since amorphous CoZr is magnetically ultrasoft [109,114,115]). 5% Zr is probably just below the critical value at which CoZr becomes amorphous. The second feature is that ΔR is smaller for the Co₉₅Zr₅ sample than the Co_{97.5}Zr_{2.5} one. The third feature is that the total AR_P of the sample with $x = 5$ is larger, as expected for higher Zr content that increases the resistivity. Combining the lower ΔR and the higher AR_P makes it clear that increasing the Zr content from 2.5% to 5% reduces the MR significantly, instead of enhancing it. To make sure that the reduction in MR in Fig. 5.21 is not a coincidence we present more data and analysis for samples of Co₉₅Zr₅. To have two different sets of results we investigate two different types of samples. Hybrid multilayers [CoZr(t)/Cu(20)/Py(6)/Cu(20)]₁₀/Py(6), and asymmetric EBSVs [FeMn/CoZr(t)/Cu(20)/CoZr(t)]. Results for the hybrid samples are displayed in Fig. 5.22 along with different V-F model fits. Fig. 5.21B shows that a decent AP state can be established for the 5 nm thick CoZr, yet Fig. 5.22 shows that ΔR of the 5 nm sample has decreased from that of the 3 nm thick CoZr. Production of a good AP state means that the less rapid growth of ΔR is not due to the lack of AP alignment,

but to something else—probably a very small β . To fit the data requires $\beta \approx 0.03$ (short-dashed curve).

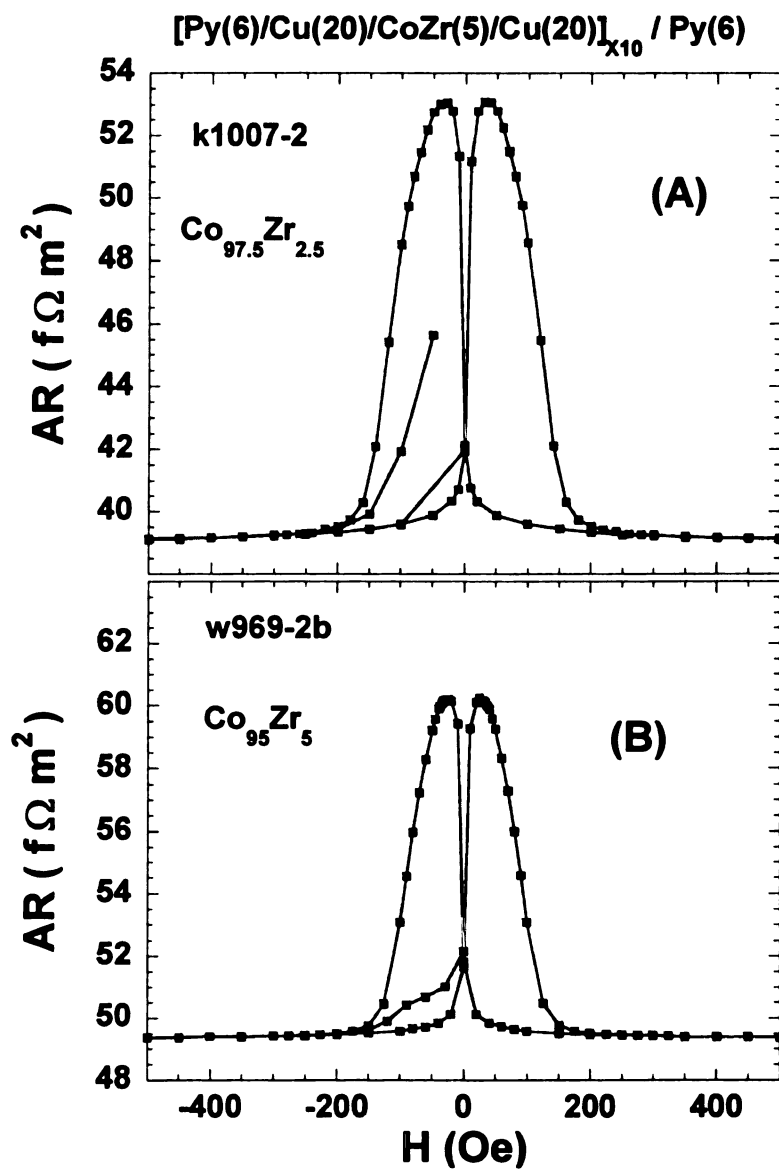


Fig. 5.21. $AR(H)$ versus H , for $[Co_xZr_{100-x}(5)/Cu(20)/Py(6)/Cu(20)]_{10}/Py(6)$. x is 97.5 in A and 95 in B. Vertical and horizontal scales are the same for direct visual comparison.

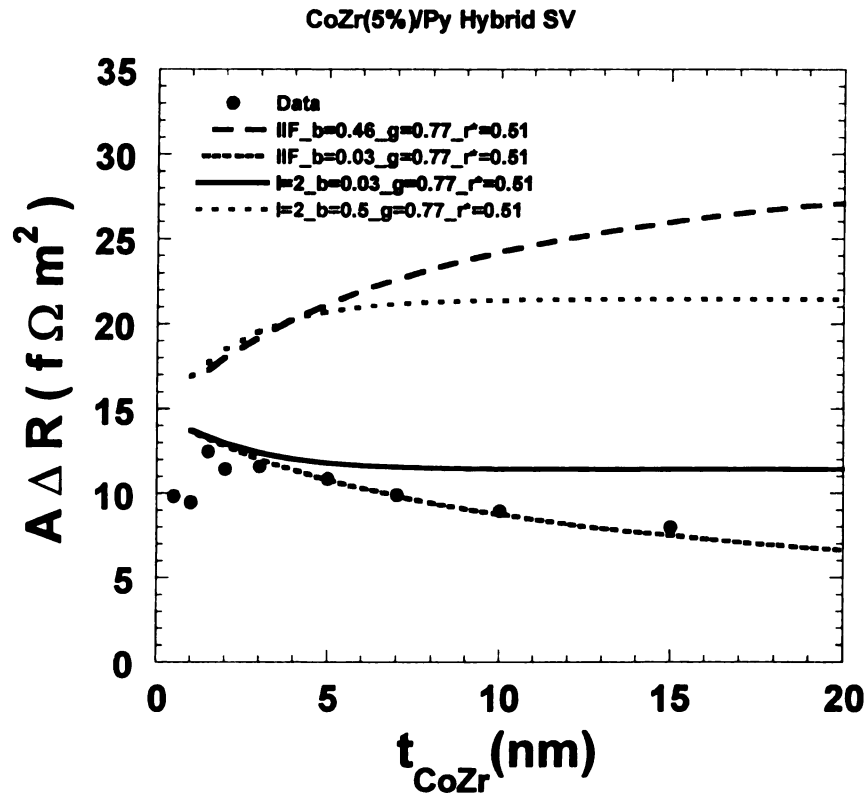


Fig. 5.22. $A\Delta R$ vs t_{CoZr} . Different fits are shown: l_{SF} = infinity or 2 nm, β = 0.5 or 0.03, γ = 0.77, and $AR_{\text{CoZr/Cu}}^* = 0.51$.

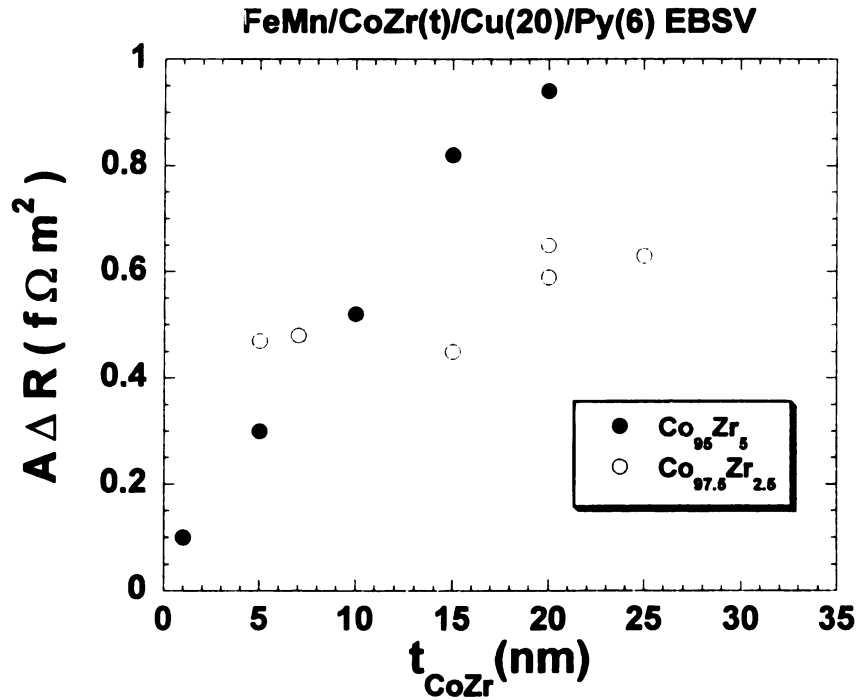


Fig. 5.23. $A\Delta R$ vs t_{CoZr} for CoZr(t)/Cu(20)/Py(6) EBSVs.

Having tested the CPP magnetoresistance of polycrystalline CoZr alloy with two different concentrations, we look for a CPP-MR in $\text{Co}_{80}\text{Zr}_{20}$. A high resistivity ($>100 \mu\Omega \text{ cm}$), which decreases with increasing temperature, suggests an amorphous state. Fig. 5.24 shows that $AR(H)$ curve displays little or no variation with H . This result is not completely surprising, since an amorphous metal should have a very short spin-diffusion-length.

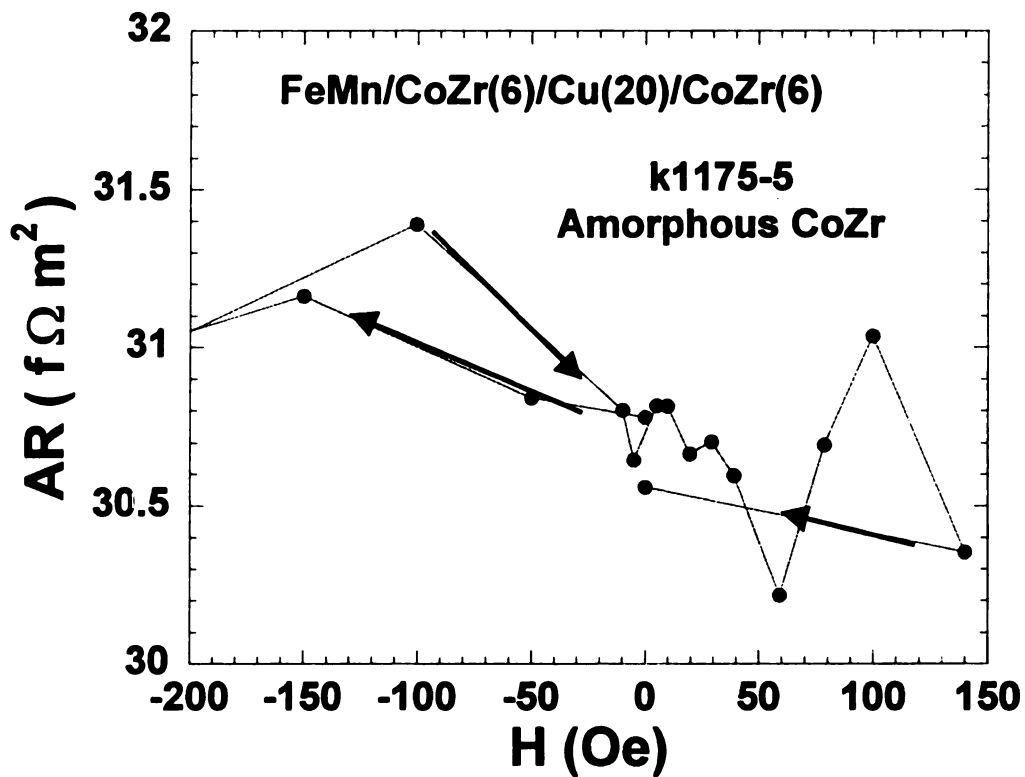


Fig. 5.24. AR vs H for a CoZr/Cu symmetric EBSV. The amorphous CoZr does not give a noticeable ΔAR within the fluctuations of the data.

5.3. INTERNAL INTERFACES.

F/N interfaces typically have specific resistances ($2 AR_{F/N}^* \sim 1 \text{ f}\Omega\text{m}^2$ [5]) much larger than those of a few monolayers of the F-metal. In such a case, it is, in principle, possible to insert additional interfaces into the F-layers of an F/N multilayer and significantly increase both the total specific resistance AR and the change in specific resistance $A\Delta R$, without greatly increasing the total multilayer thickness [53,117]. Inserting 'n -1' thin N-layers into the F-layers divides the latter into 'n' thinner layers, producing $M = (2n-2)$ '*internal interfaces*'. One would like the N-layers to be thick enough to completely separate the interfaces on both sides, leaving some unmixed N-layer in between; we'll call these '*complete interfaces*'. For sputtered multilayers, unavoidable intermixing then will require the N-layers to be at least 2-4 monolayers (ML) thick, equal to 0.4-0.8 nm [118]. But, to maximize $A\Delta R$, the 'F-layers' should behave as single magnetic entities with switching fields similar to those of the unmodified F-layers. To achieve this condition, the N-layers must be thin enough to give ferromagnetic coupling, either by the RKKY interaction or by means of pinholes. They must, thus, be thinner than the $t_N \approx 0.9\text{-}1.0 \text{ nm}$ for the first antiferromagnetic coupling peak [11,12]. It is not clear in advance that both conditions can be satisfied at once for a given F/N multilayer.

For the CIP-MR, the preferred geometry for devices is the EBSV, because its hysteresis curve allows local control of the magnetization [53] and its magnetic structure is stable over many magnetization reversals [54]. For the CPP-MR, the situation is more complex, because a standard EBSV has only two active F/N interfaces, and the AR of the pinning AF layer is in series with the multilayer. A hybrid spin valve may often be competitive, since it can contain more repeats, thereby enhancing both AR and $A\Delta R$. In

the present study, we chose a hybrid spin valve with 3 repeats ($N = 3$) to enhance the signal. We chose Co for the F-layer and Cu (later also Ag) for the inserted N-layer because $l_{SF}^{Co} \sim 60$ nm [5] is long enough to be neglected and because our knowledge of all of the Co/Cu parameters [5,43] lets us predict without adjustment the values of AR_P , $A\Delta R$, and the CPP-MR with which to compare our data. We pair the Co layers with Py layers, for which we also know all of the parameters in advance [74], and which have a much smaller saturation field, thus ensuring a good AP state for the data analysis.

Fig. 5.25 shows the 2CSR model predicted enhancements of AR_P , $A\Delta R$, and CPP-MR = $\Delta R/R$ as a function of M for a multilayer with structure $[Py(6nm)/Cu(4.5)/[Co(t/n)/Cu(0.5)]_n/Cu(4.5)]_3$. We see that all three quantities increase with increasing M , and that adding only 4 internal interfaces should increase $A\Delta R$ by 100%, $AR(P)$ by 20% and $\Delta R/R_P$ by more than 80%, with less than 5% increase in total thickness. The predictions are for continuous Co, Cu layers with well-defined interfaces. They assume the parameters given in section 5.2-- $AR_{Co/Cu}^* = 0.5 f\Omega m^2$, $\rho_{Co}^* = 7.5 \mu\Omega cm$, $\beta_{Co} = 0.46$, and $\gamma_{Co/Cu} = 0.77$, $\rho_{Py}^* = 24 \mu\Omega cm$, $\gamma_{Py/Cu} = 0.7$, etc. We chose the Py thickness of 6nm to roughly equal l_{SF}^{Py} [74], since making it thicker would increase the thickness of the device and AR_P more than it would increase $A\Delta R$ (see Eq. 3.12). We introduce interfaces only into the Co, both to simplify the analysis by eliminating effects of finite l_{SF} in Py and because the effect of internal interfaces is less pronounced in Py due to the larger values of β_{Py} and ρ_{Py}^* compared to $2 AR_{Py/Cu}^*$ [5]. Note that the hybrid spin valve contains two different thicknesses of non-magnetic spacer (Cu or Ag). For Cu, 4 nm thick layers are thick enough to separate Py magnetically from Co, and our initial studies

use 0.5 nm thick Cu to produce the ‘internal interfaces’. For Ag, we found that 4 nm was not enough to decouple the Co and Py, so we use 10 nm of Ag instead.

We begin our discussion with the Cu-based samples, which we have studied in most detail. We then present less complete data on Ag-based samples. In both cases, we initially find substantial enhancements of AR_P and $A\Delta R$ with increasing M . But, then the growth with increasing M becomes less than predicted. These results lead us to examine two possible explanations: ‘incompletely formed interfaces’ and ‘spin-memory-loss at interfaces’. We conclude that both probably contribute, with the case for spin-memory-loss at interfaces the strongest.

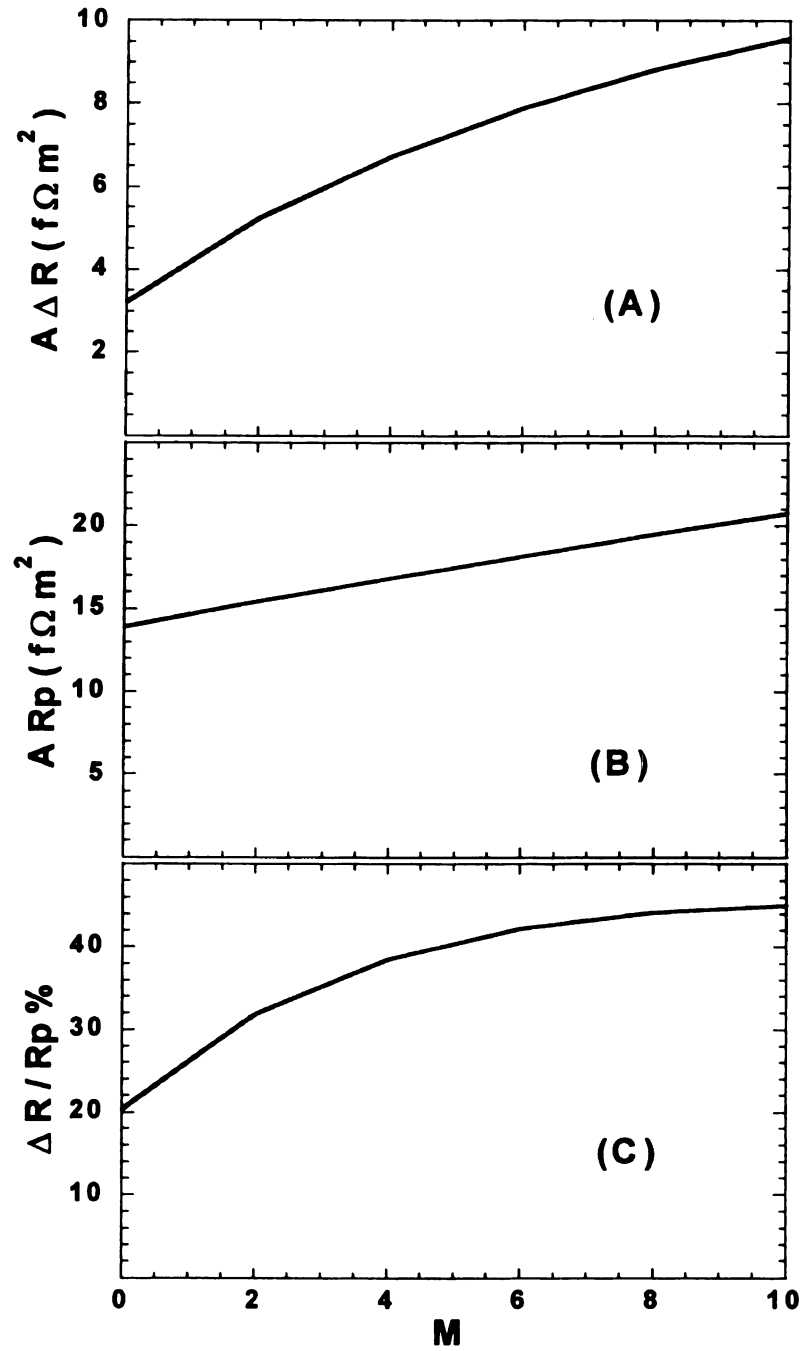


Fig.5.25 Predicted change in $A\Delta R$ (A) and AR_p (B) and $\Delta R/R_p$ (C) with number of inserted internal Co/Cu interfaces.

5.3.1 Data and Analysis

Resistances and Magnetoresistances of Samples with $t_{\text{Cu}} = 0.5 \text{ nm}$

Figs. 5.26A and B compare data on $AR(H)$ vs H for a sample with 4 internal interfaces and a similar sample with no internal interfaces. In both cases, the data round off at their peaks, seeming to indicate a decent AP state. We see that adding the internal interfaces increases the saturation specific resistance AR_p by $\sim 10\%$, ΔAR by $\sim 100\%$, and only modestly increases the switching field of the Co layers.

Fig. 5.27 compares our experimental values of AR_p for Cu based multilayers as a function of M with predictions from the 2CSR model. As predicted, AR_p increases almost linearly with M . But the data lie a bit below the prediction and, more importantly, grow more slowly with M than predicted (see dashed line).

Figure 5.28 compares ΔAR as a function M with the 2CSR model predictions. There is an initially large enhancement of ΔAR , as much as 100% for $M = 4$. Thereafter the data grow more slowly with M .

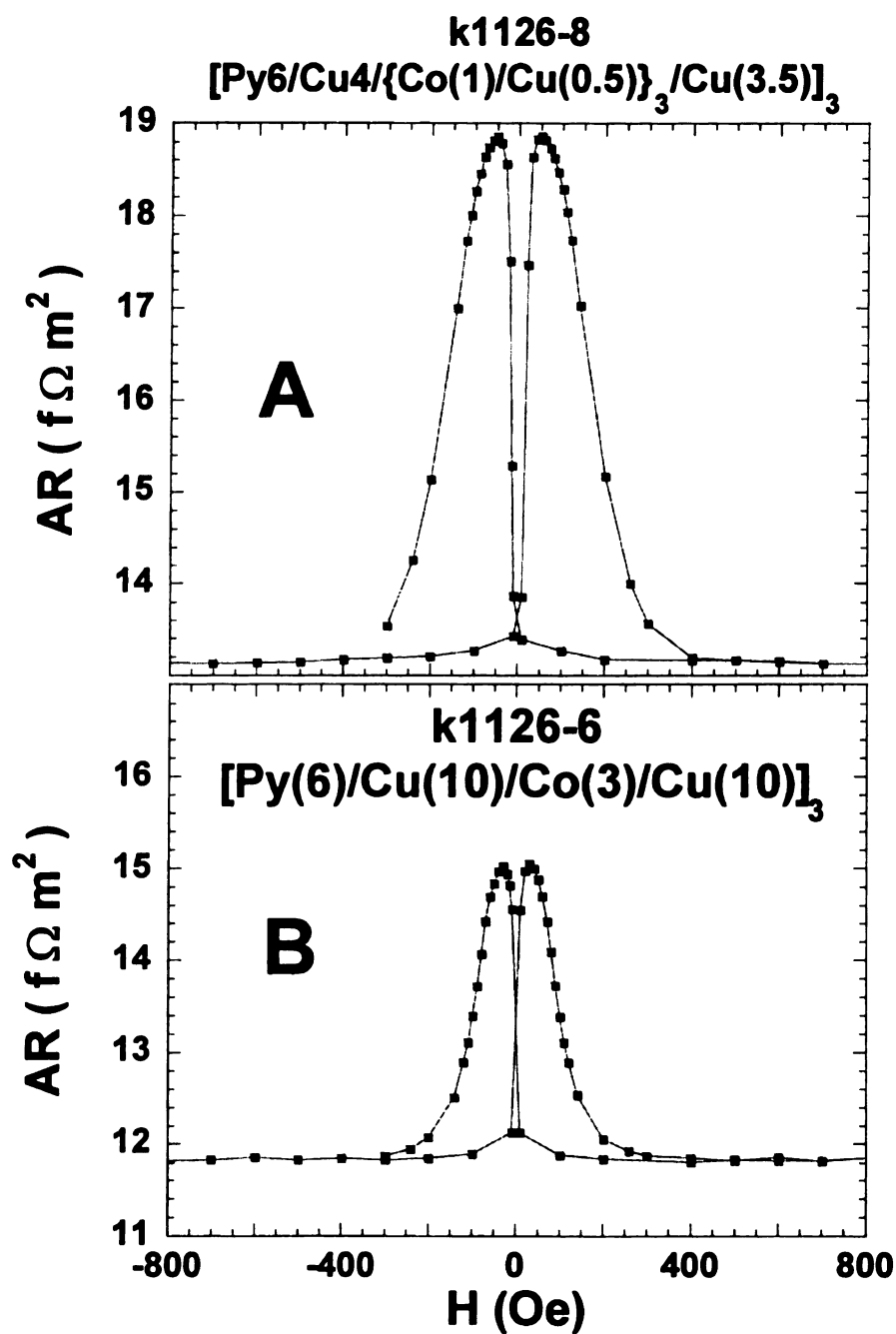


Fig. 5.26. $AR(H)$ curves for samples (A) with 4 internal interfaces and (B) without. To allow direct comparison, both the vertical and horizontal scales are the same for both samples. Introducing the interfaces increases AR , ΔAR , and the H_S for the Co.

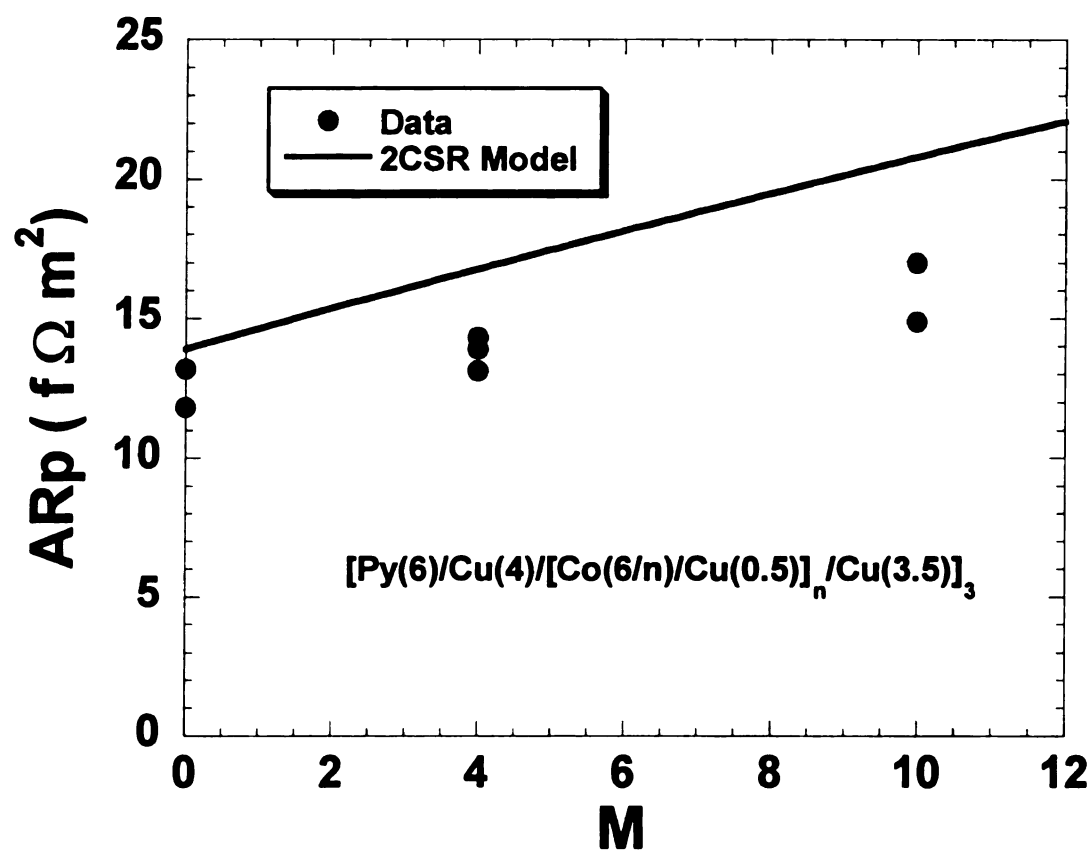


Fig.5.27 Increase of AR_p with M in $[Py(6)/Cu(5)/(Co(t/n)/Cu(0.5))_n/Cu(4.5)]_3$ multilayers versus prediction (solid curve).

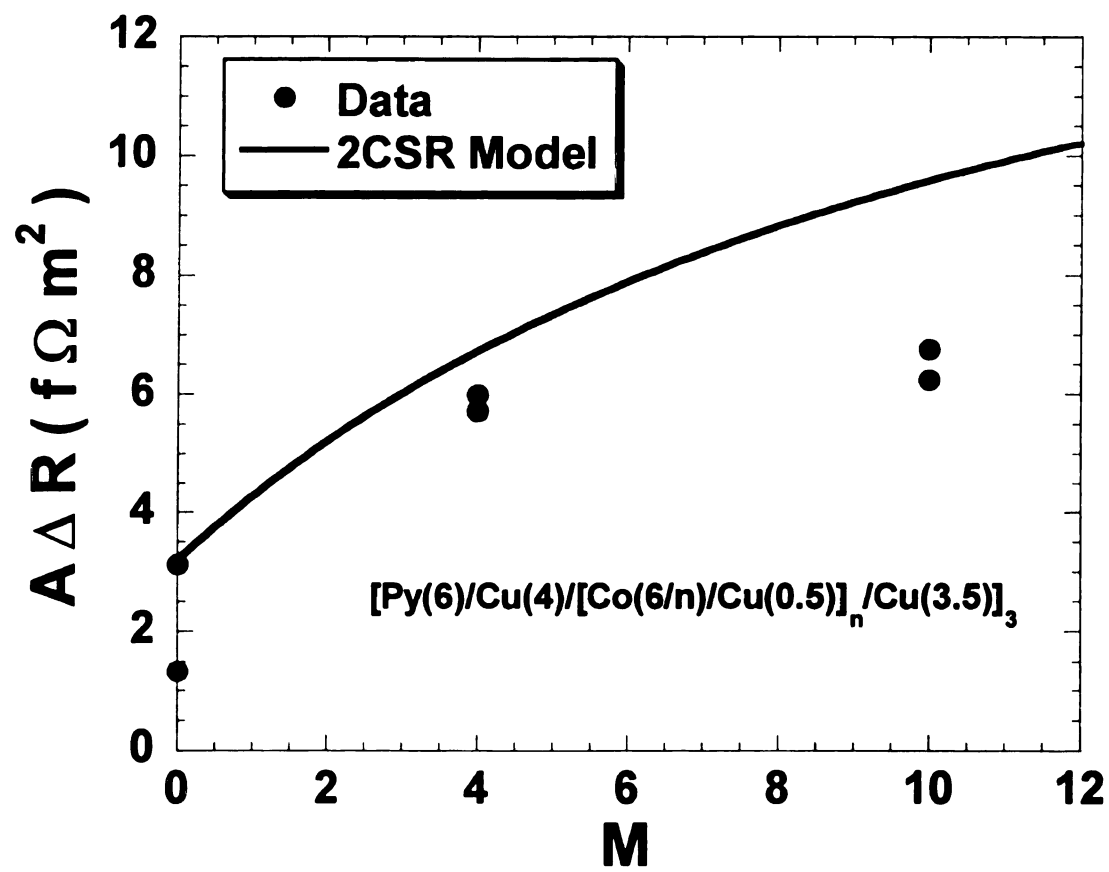


Fig. 5.28. $A\Delta R$ vs M . compared with 2CSR prediction. Data shows a significant increase in $A\Delta R$ at $M = 4$, then $A\Delta R$ levels off faster than predicted.

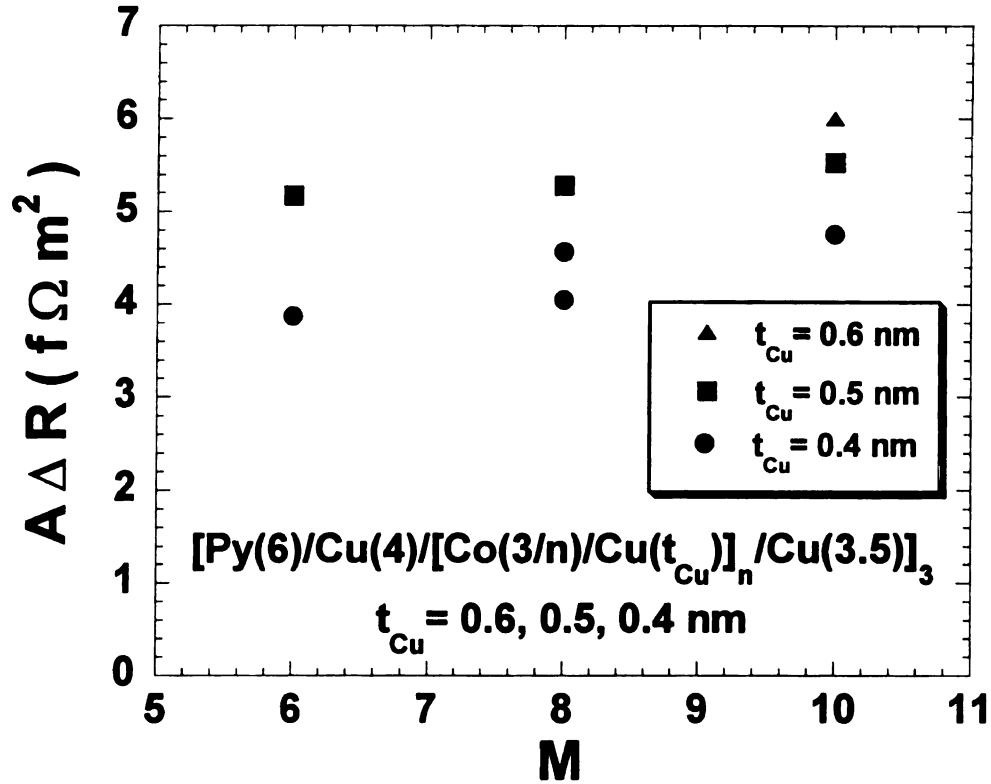


Fig.5.29. Effect of the thin Cu spacer layer thickness on $A\Delta R$. When Cu layer thickness is 0.4 nm (filled boxes) $A\Delta R$ is smaller than when Cu thickness is 5 nm (filled circles). The one sample with $t_{Cu} = 0.6$ nm (filled triangle) is slightly higher than the 0.5 nm.

Lastly, Fig. 5.29 compares values of $A\Delta R$ for Cu thicknesses $t_{Cu} = 0.4$, 0.5, and 0.6 nm (only one point) for $M = 6, 8$, and 10. In all three cases, $A\Delta R$ is smaller for $t_{Cu} = 0.4$ nm than for 0.5 nm. In the only case studied, $A\Delta R$ is slightly larger for $t_{Cu} = 0.6$ nm than for $t_{Cu} = 0.5$ nm, but probably within fluctuations.

Taken together, these data show that $t_{Cu} = 0.5$ nm is certainly the minimum thickness needed to produce two complete Co/Cu interfaces, and suggest that it might not even be quite sufficient to do so. The slower than expected growth of $A\Delta R$ with M in Fig. 5.28 might be due in part to such incomplete interfaces. However, another possibility is spin-memory-loss at Co/Cu interfaces, as inferred from the data and analysis in Ch. 4. Inserting internal interfaces leads to a sample structure similar to that of ‘separated’

samples in Ch. 4. To further examine these two possibilities we prepared additional samples, which we describe in the next section.

5.3.2 Incomplete Interfaces versus Interfacial Spin Memory Loss

To see whether (and if so how) the data of Figs. 5.27-5.28 are affected by incomplete interfaces or interfacial spin-memory-loss, we made a series of Py and Co based hybrid spin valves, all of which have total thicknesses of Py and Co equal to 18 nm, all but one of which have fixed individual ferromagnetic layers with $t_{\text{Co}} = t_{\text{Py}} = 2$ nm and a total of 17 Co/Cu and 17 Py/Cu interfaces, but each of which has a different order of the F-layers and/or different Cu thicknesses. Two of the samples are ‘interleaved’ in the sense defined in Ch. 4, and the other four are composed of combinations of ‘interleaved’ and ‘separated’ portions that we designate ‘mixed’.

In Fig. 5.30 we begin with three samples with t_{Cu} large enough (20 nm) so that all of the interfaces should be ‘complete’. Sample C is an interleaved sample of the form $[\text{Py}(6)/\text{Cu}(20)/\text{Co}(6)/\text{Cu}(20)]_3$ with 5 interfaces each of Co/Cu and Py/Cu. We use it as a reference sample, equivalent to an $M = 0$ sample from Figs. 5.27 and 5.28, except that it has $t_{\text{Cu}} = 20$ nm instead of $t_{\text{Cu}} = 4$. Because of the low resistivity of Cu, this difference should be minor. Interestingly, AR_{P} and $A\Delta R$ for this sample fall nicely on the predicted (solid) curves in Figs. 5.27 and 5.28. Sample A is also a simple interleaved sample, but of the form $[\text{Py}(2)/\text{Cu}(20)/\text{Co}(2)/\text{Cu}(20)]_9$, containing 17 interfaces each of Co/Cu and Py/Cu. It shows the usual behaviors from Ch. 4 for an interleaved sample, a single peaked CPP-MR, with an ‘as-prepared’ value of AR just a bit smaller than the ‘peak’ value. Sample B is a mixed sample of the form $[\{\text{Py}(2)/\text{Cu}(20)\}_3/\{\text{Co}(2)/\text{Cu}(20)\}_3]_3$. As usual for ‘separated samples’, its AR is larger in the ‘as prepared’ state than at the

subsequent ‘peak’ after the sample has been taken to saturation, and $A\Delta R$ between the ‘as prepared’ and parallel (P) states is close to that for the ‘peak’ and P states of the interleaved sample A. However, unlike the more complex structure seen in simple ‘separated samples’ in Ch. 4, this mixed sample has only a single MR-peak on each side of $H = 0$. This difference is a consequence of the ‘mixed’ nature of the sample.

With the data for these samples in hand, we now turn to samples having the same order as sample B in Fig. 5.30, but some Cu layer thicknesses are reduced to $t_{\text{Cu}} = 0.5$ nm to test effects of possible incomplete interfaces. We are especially interested in how the values of AR_P , $A\Delta R$, and H_{switch} for these samples compare with those for sample B.

The structure of sample A in Fig. 5.31 is identical to that of sample B in Fig. 5.30, except that the thickness of the Cu layers between the Co layers is reduced to $t_{\text{Cu}} = 0.5$ nm. The structure of sample B is again the same as B in 5.30, except that now the thickness of the Cu layers between the Py layers is reduced to $t_{\text{Cu}} = 0.5$. In sample C, the Cu layer thicknesses between neighboring Py layers and neighboring Co layers are all reduced to $t_{\text{Cu}} = 0.5$ nm, and the Cu layer thicknesses between the Py and Co layers are fixed at 5 nm to approximate those in the ‘internal interface’ samples in Figs. 5.27 and 5.28.

Comparing the data of the three samples in Fig. 5.31 with those of samples A and B in Fig. 5.30 we see the following.

(1) The similarities in behaviors of the data for samples A and B in Fig. 5.31 with those for interleaved and separated samples in Ch. 4, strongly suggest that the difference between the $A\Delta R \approx 6 \text{ f}\Omega\text{m}^2$ between the peak and saturation states for sample B and the

$A\Delta R \approx 8 \text{ f}\Omega\text{m}^2$ for the same states in Sample A is due to the source ascribed in Ch. 4, which we proposed to be interfacial spin-memory-loss.

(2) The values of $A\Delta R \approx 6 \text{ f}\Omega\text{m}^2$ for the peak to saturation values of all three samples in Fig. 5.31 and of sample B in Fig. 5.30 are all closely the same. This agreement means that this $A\Delta R$ is insensitive to the thickness of the Cu layers, and strongly suggests that the main limitation on $A\Delta R$ in Figs. 5.28 is due to interfacial spin-memory-loss.

(3) The variations in switching fields of Co between sample B in Fig. 5.30 and the three samples in Fig. 5.31 correlate with the ‘effective thickness’ of the Co layer. That is, high switching fields are required for thin, widely separated Co layers, but much lower switching fields are required for thin, closely coupled Co layers.

(4) Considering only sample B from Fig. 5.30 and the three samples from Fig. 5.31, AR_p decreases as the separation between adjacent Co and adjacent Py layers is reduced. That is, AR_p is largest when $t_{\text{Cu}} = 20 \text{ nm}$ between both Py and Co layers and smallest when $t_{\text{Cu}} = 0.5 \text{ nm}$ between both. However, as illustrated by the unpredicted difference between the values of AR_p for samples A and B in Fig. 5.30, this interpretation can only be preliminary, because fluctuations can bias analysis of only a few samples.

(5) Comparing the initial states of sample B in Fig. 5.30 and those of the three samples in Fig. 5.31, we see that the AR for the initial state of B in Fig. 5.30 is higher than that for its peak state, the AR s for the initial states of the two samples in Fig. 5.31 with only one set of thin Cu layers are about the same as for their peak states, and the AR for the sample with both sets of Cu layers being thin is less than that of its peak state. We presume that the magnetizations of widely separated (uncoupled) adjacent Co or Py layers tend to align anti-parallel to each other in the as-prepared state (as for the ‘separated’ samples in Ch 4),

whereas the ferromagnetic coupling between adjacent Co or Py layers separated by only $t_{\text{Cu}} = 0.5$ nm causes them to tend to align parallel, thereby decreasing the value of AR in the as-prepared state.

Table 5.2 The Composition of the samples used to study the effect of incomplete interfaces and separated-like effect (due to the internal interfaces).

Effect Of Internal Interfaces: Thickness and Ordering Dependence						
Sample#	Composition	ARp	AΔRinitial	AΔRstable	Switching Field	Notes
1242-1	[Py(2)/Cu(20)/Co(2)/Cu(20)]x9	24.8	6.4	7	600	Rinitial < Rstable
1242-2	[Py(6)/Cu(20)/Co(6)/Cu(20)]x3	14.5	3	3.35	200	Rinitial < Rstable
1242-4	[(Py(2)/Cu(20))x3/(Co(2)/Cu(20))x3]x3	19.2	7.9	5.5	600	Rinitial > Rstable
1242-5	[(Py(2)/Cu(20))3/(Co(2)/Cu(.5))3/Cu(20)]3	17.7	5.92	5.77	300	Rinitial ~ Rstable
1242-7	[(Py(2)/Cu(.5))3/Cu(20)/(Co(2)/Cu(20))3]3	16.2	5.4	5.5	600	Rinitial ~ Rstable
1242-8	[(Py(2)/Cu(.5))3/Cu(4.5)/(Co(2)/Cu(.5))3/Cu(4.5)]3	13.8	3.2	4.95	250	Rinitial < Rstable

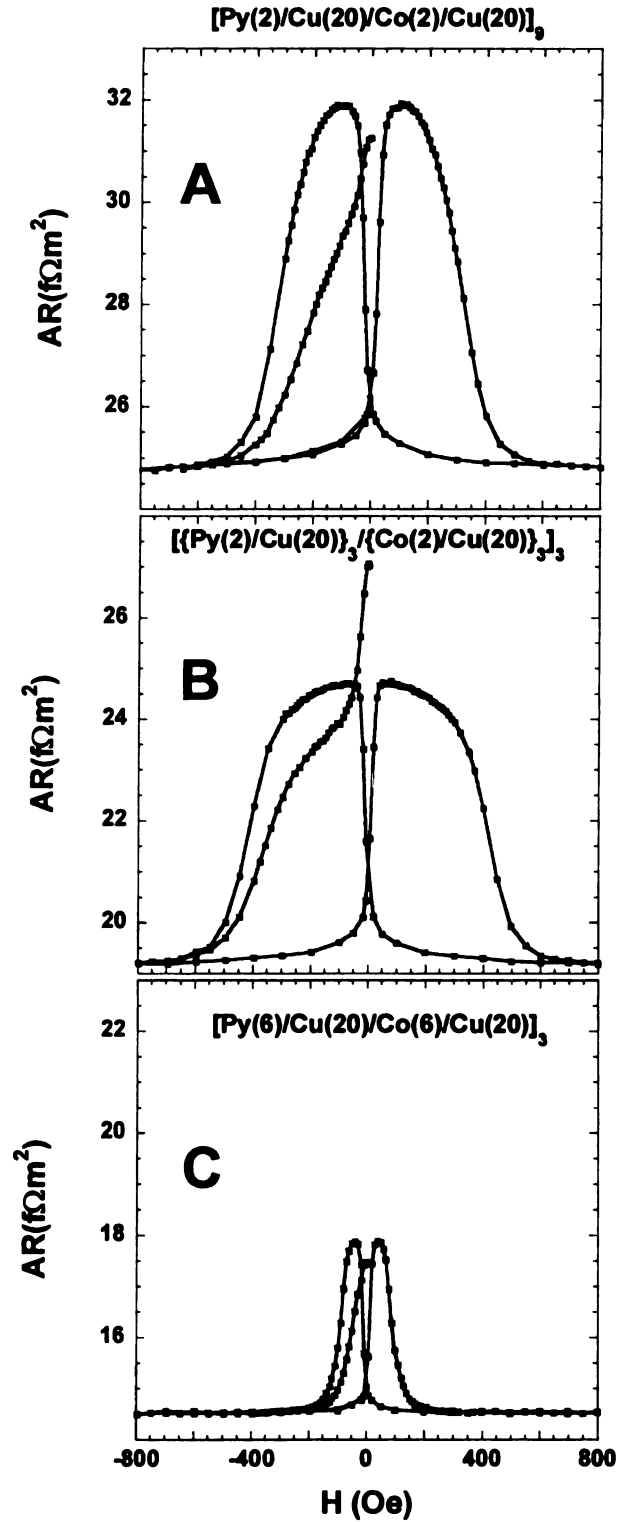


Fig.5.30. $AR(H)$ curves for (A) Interleaved, (B) Separated and (C) Regular samples. Regular means samples without any internal interfaces. The reduction in ΔAR due to the difference in ordering of the layers between A and B was already seen in Ch. 4. Note that samples A and B also have larger AR s than sample C.

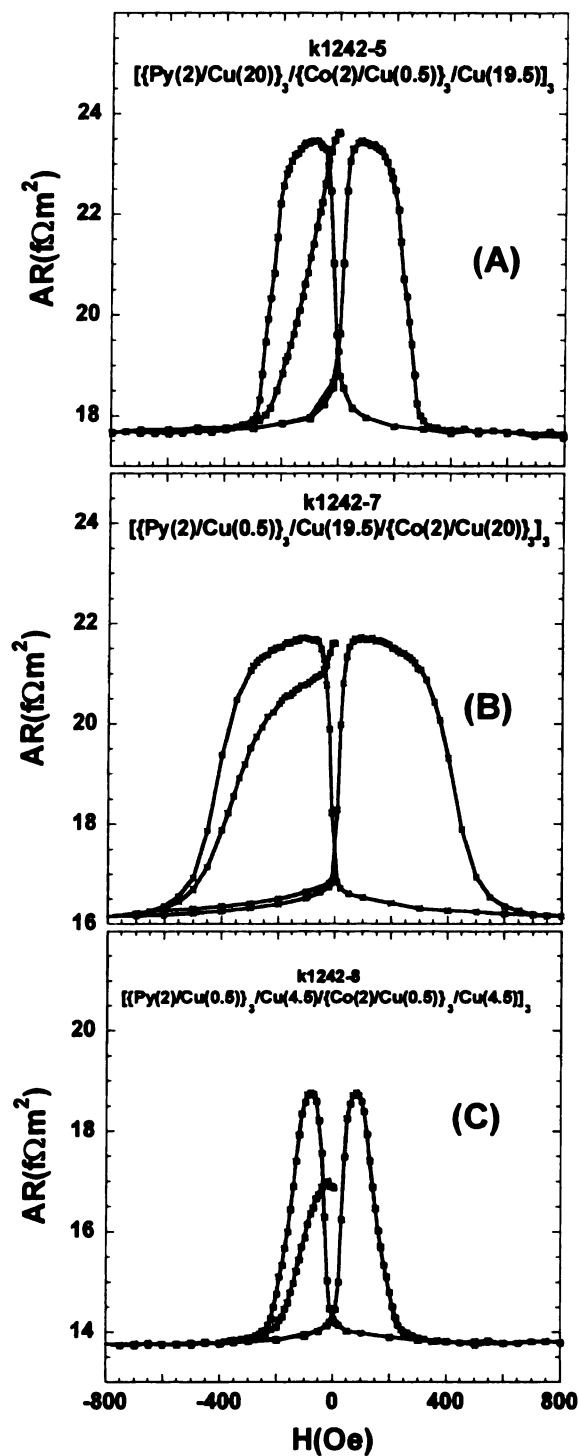


Fig. 5.31. AR vs H for samples identical to the sample in Fig. 5.30 except for the Cu thicknesses. In A the Cu layer between neighboring Co layers is 0.5nm and the rest are 20nm. In B the Cu layer between neighboring Py layers is 0.5 nm and the rest are 20 nm. In C the Cu layer between neighboring Co or neighboring Py layers is 0.5 nm and the Cu layer between Co and Py is 5 nm.

Ag Samples:

We now turn to less extensive studies with Ag as the nonmagnetic spacer layer. Since Ag has a larger lattice parameter mismatch with Co [28], the Co/Ag interfaces may be rougher than Co/Cu. Since Ag and Co are completely immiscible [28], there may also be less chemical mixing at their interfaces.

Fig.5.32 shows $R(H)$ for a $[\text{Py}(6)/\text{Ag}(4)/[\text{Co}(0.6)/\text{Ag}(0.5)]_6/\text{Ag}(3.5)]_3$ multilayer. The sharp peaks in the data mean that a good AP state was not achieved in this multilayer. 4 nm of Ag between Co and Py does not seem to be enough to decouple the ferromagnetic layers from each other. Perhaps larger interfacial roughness enhances ferromagnetic coupling between the Co and Py layers across the 4 nm Ag layer. Figs. 5.33 A and B show that we achieved at least better approximations to AP states by using 10 nm of Ag to separate the Py and Co layers and 0.8 nm of Ag to separate neighboring Co layers. Comparing 5.33A and B shows that introducing 8 interfaces increased $A\Delta R$ by $\sim 40\%$. Note that the magnetic field range is smaller for Ag than it was for Cu. Since the AP states are somewhat uncertain for Ag, our curves should probably be viewed as providing only a lower limit on those states. The use of a slightly thicker (4 nm) Co layer in the Ag samples does not produce a significant change in the MR or switching field compared to the 3 nm in the Cu samples.

Fig.5.34 shows AR_P vs M for samples of the form $[\text{Py}(6)/\text{Ag}(10)/[\text{Co}(4/n)/\text{Ag}(0.8)]_n/\text{Ag}(9.2)]_3$. Here the 2CSR model fits the data better than with the Cu samples. This better agreement might be due to more nearly complete interfaces, both due to less intermixing of Co and Ag and to the thicker 'thin' Ag layers (0.8 nm vs 0.5 nm for Cu).

Fig.5.35 shows that introducing a pair of Co/Ag internal interfaces increases ΔR by $\sim 30\%$, but, as for Co, adding still further ones gives less increase than predicted. Although we haven't performed additional experiments to check for sure, we presume that interfacial spin-flipping (spin-memory-loss) is affecting the Ag data as we argued it did for the Cu data.

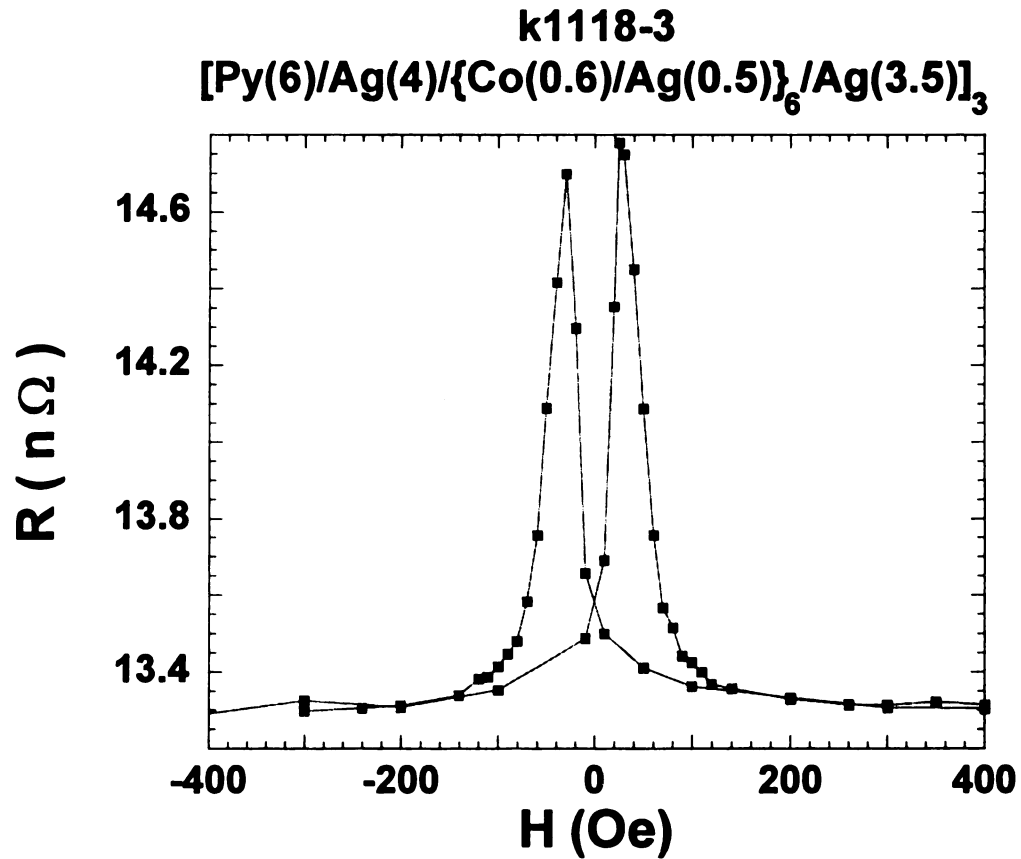


Fig.5.32. $R(H)$ for an Ag based multilayer. Using a 4 nm thick Ag spacer layer is not enough to decouple Py and Co layers and an AP state is not achieved in this sample, giving sharp instead of rounded or flat peaks.

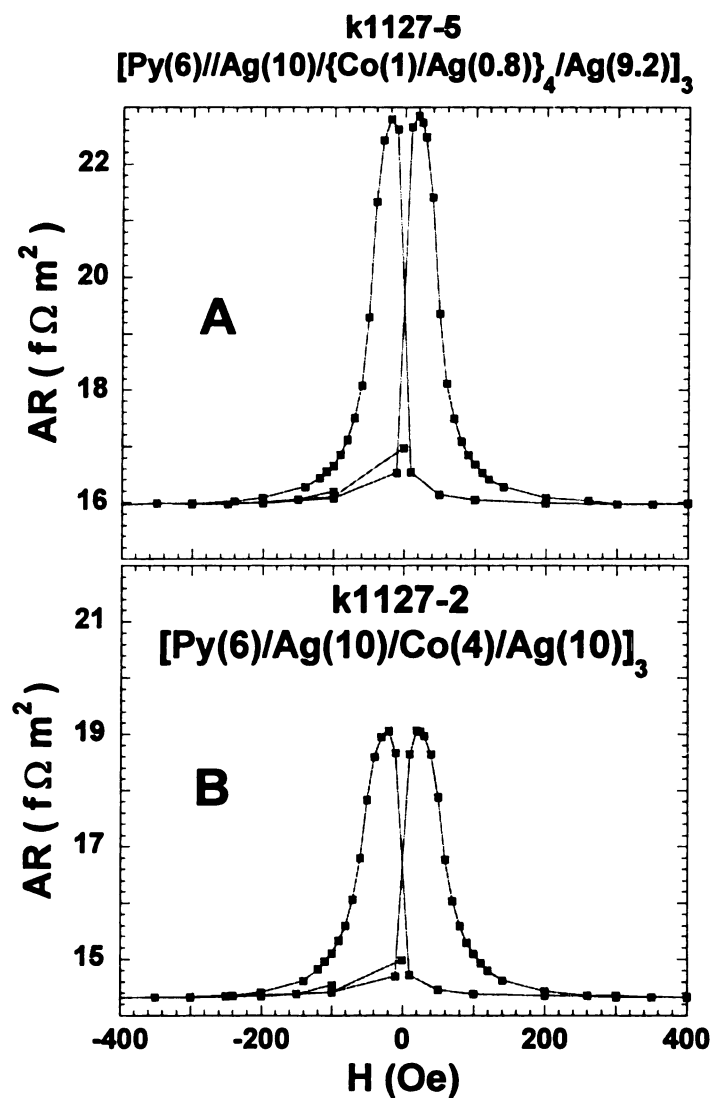


Fig.5.33. Effect of internal interfaces on $AR(H)$ curves for samples with Ag spacer layers. Introducing eight internal interfaces(part A) increases ΔAR and AR_p .

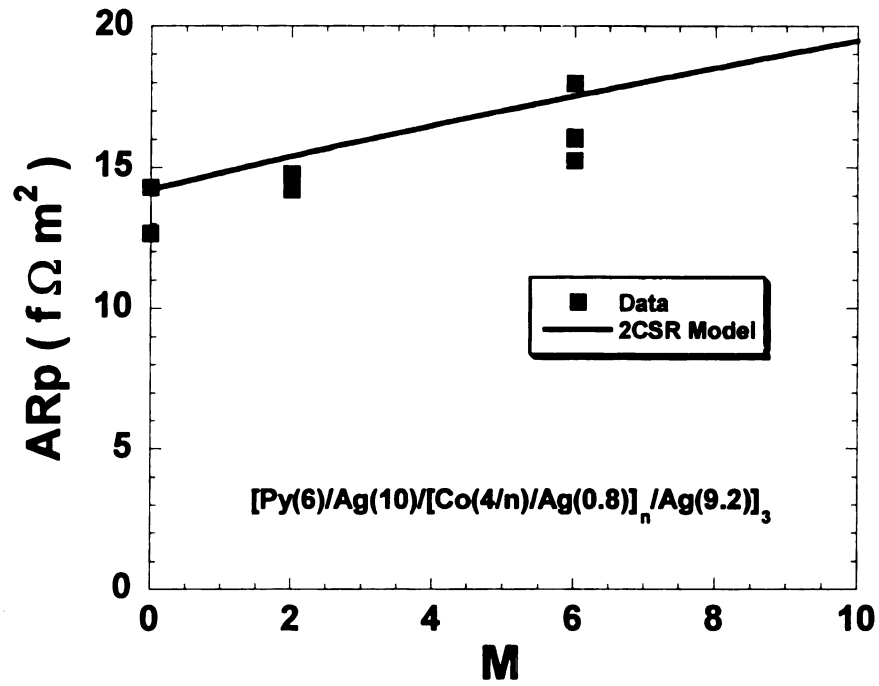


Fig.5.34. Dependence of AR_p on the total number of internal interfaces M . solid boxes are for data and solid line is the 2CSR model prediction. The data agree with prediction within the fluctuations.

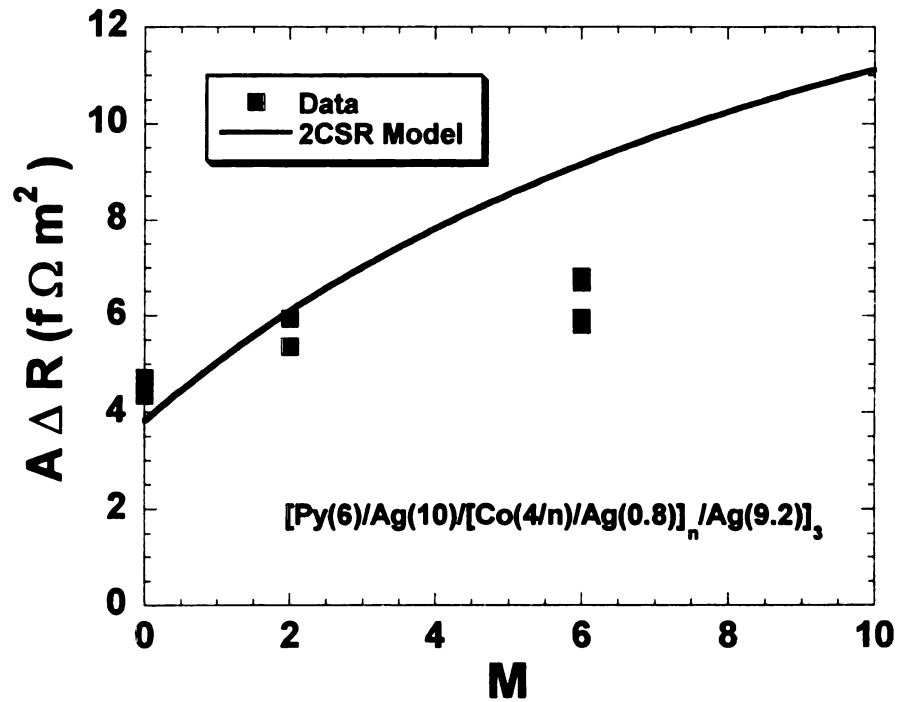


Fig.5.35. $A\Delta R$ dependence on the number of internal interfaces in Co/Ag based multilayer.

5.4 SPIN-MEMORY-LOSS TO ENHANCE GMR

In this section we try to introduce strong spin-memory-loss by inserting a 1 nm FeMn layer in each of the two Cu layers separating Co from Nb in multilayers of structure Nb(100)/Cu(20)/[Co(1)/Cu(20)/Co(6)/Cu(20)]_N/Nb(100). We wish to see if this strong spin flipping increases $A\Delta R$ by eliminating the contact resistance $2AR_{S/F}$ from the denominator of Eq. 1.3.

Our group [85] showed earlier that, introducing a thin ($t_{\text{FeMn}} = 1$ nm) layer of FeMn that produces strong spin flipping [73] into the free Py layer of a Py-based EBSV enhanced $A\Delta R$ monotonically as the spin-flipping layer was moved towards the outside of the Py layer. Our procedure here differs, in that the FeMn layer is placed outside of the multilayer in a Cu layer that otherwise separates the outer F-layer from the superconducting Nb leads.

If we simply assume that the FeMn eliminates the $2AR_{S/F}$ term in the denominator of Eq. 1.2 we obtain:

$$A\Delta R = 4N^2 \frac{(\rho_{F1}^* t_{F1} \beta_1 + 2AR_{F1/N}^* \gamma_1)(\rho_{F2}^* t_{F2} \beta_2 + 2AR_{F2/N}^* \gamma_2)}{2AR_{\text{FeMn/Cu}} + 2N\rho_N t_N + N\rho_{F1}^* t_{F1} + 2NAR_{F1/N}^* + N\rho_{F2}^* t_{F2} + 2NAR_{F2/N}^*} \quad (5.1)$$

Another possible result of introducing the FeMn between Nb and the multilayer might be to make the outermost Co/Cu interface contribute to $A\Delta R$. In the absence of the FeMn, the Cu layer next to Nb becomes superconducting by proximity with the superconducting Nb, perhaps making the Co/Cu(superconducting) interface not MR active. If the resistance of the outer Co/Cu interface becomes active, it would further enhance $A\Delta R$, especially for a small number of layers, the case of most interest for devices. More details of F/S interfaces will be examined in Chapter 6.

5.4.1 Data and Analysis

Fig. 5.36 shows the structure of the multilayers used in this study. We chose $[\text{Co}(6\text{nm})/\text{Cu}(20)/\text{Co}(1)/\text{Cu}(20)]_N$ multilayers for three reasons: First, we have the results of studies of such multilayers without FeMn inserts in Ch. 4. Second, the Co/Cu interface makes a stronger contribution to GMR than bulk Co layers of these thicknesses. Third, Co has a fairly long spin-diffusion length [5], thereby leaving scope for the FeMn to have a significant effect.

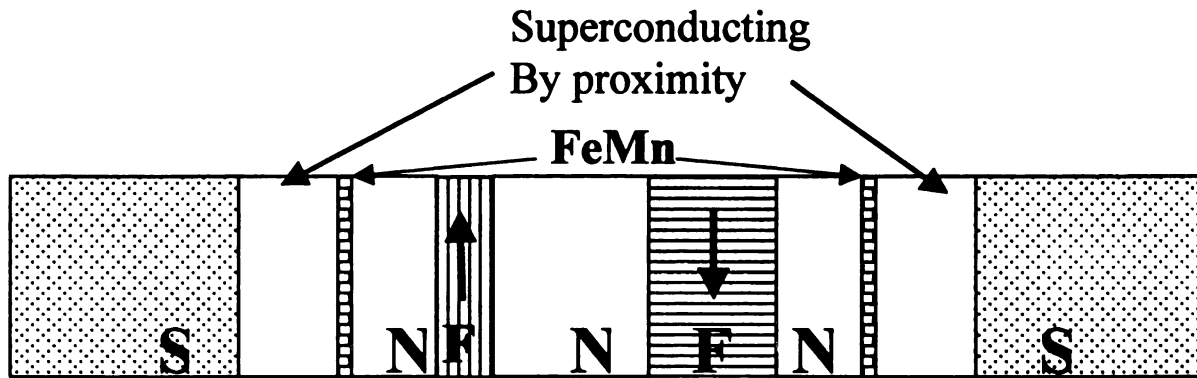


Fig. 5.36. Cartoon of the multilayer (with $N = 1$) with FeMn layers to enhance GMR. A single FeMn layer is inserted in the middle of the Cu layer next to Nb on each side of the multilayer. The Cu layers in direct contact with Nb are assumed to become superconducting by the proximity effect.

Fig. 5.37 shows that the 2CSR model with no adjustable parameters [5] predicts rather well our experimental values for $A\Delta R$ vs N in samples with no FeMn. Fig. 5.38 shows that it also describes well the increase in AR_p with increasing N , but does not get the absolute magnitude correct. The source of this discrepancy might be that the $t_{\text{Co}} = 1\text{nm}$ Co layers are too thin to be fully continuous, and thus do not contribute fully to AR_p .

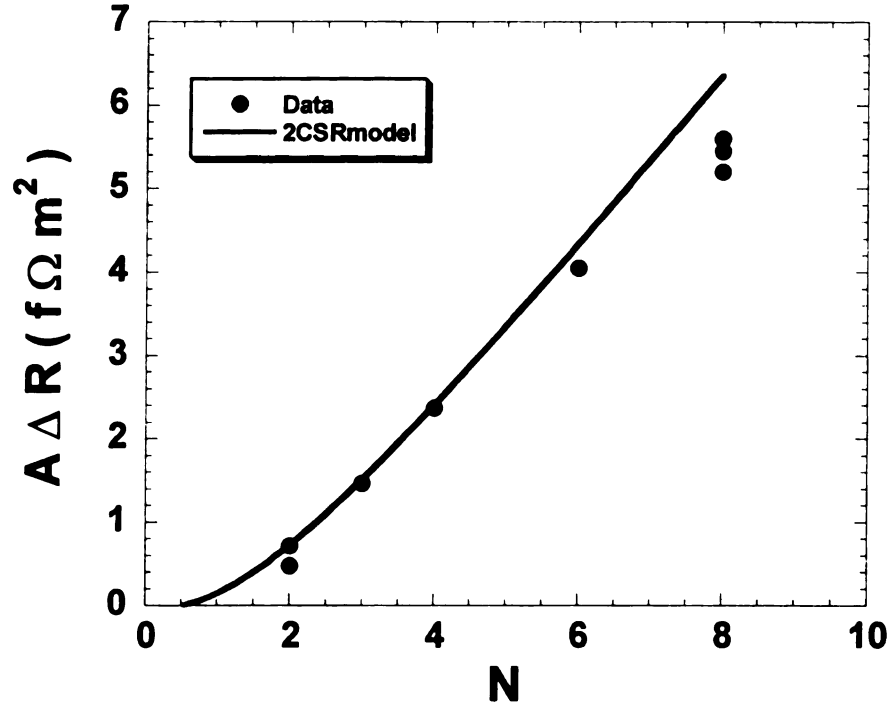


Fig.5.37. $A\Delta R(N)$ in $[\text{Co}(6)/\text{Cu}(20)/\text{Co}(1)/\text{Cu}(20)]_N$ multilayers. The filled circles are data points and the solid line is a no-adjustable-parameters prediction of the 2CSR model. There is a good agreement between the two, especially at small N .

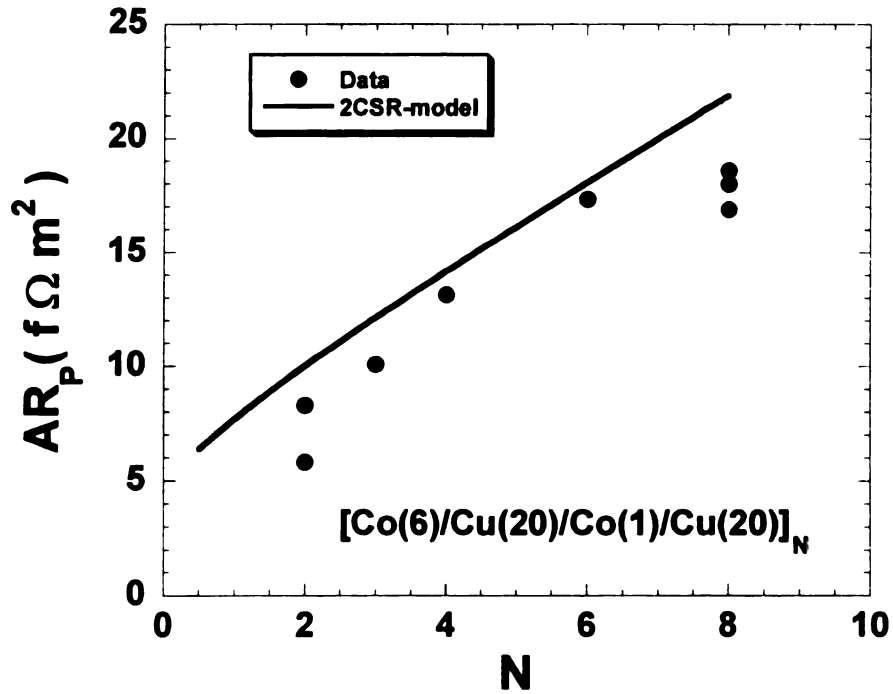


Fig.5.38 Comparison of 2CSR model prediction of $AR_p(N)$ with data for $[\text{Co}(6)/\text{Cu}(20)/\text{Co}(1)/\text{Cu}(20)]_N$ multilayers. The data falls below the predictions, which may be because the Co/Cu interfaces are not fully established in the 1 nm Co layers.

Fig.5.39 compares data for multilayers of the form of Fig. 5.36 with data for multilayers without FeMn. For convenience, we call the samples without FeMn ‘regular samples’. Fig.5.39 shows that introducing FeMn increases $A\Delta R$ significantly, especially for the smaller numbers of layers in the multilayer. For example, $A\Delta R$ increases by about 90% for $N=2$, and by about 46% for $N=3$. The effect gets weaker for larger number of repeats, in part because the effects of the contact resistance, $2AR_{S/F}$, and of the additional Co/Cu interfaces that might become GMR active, get smaller with increasing N .

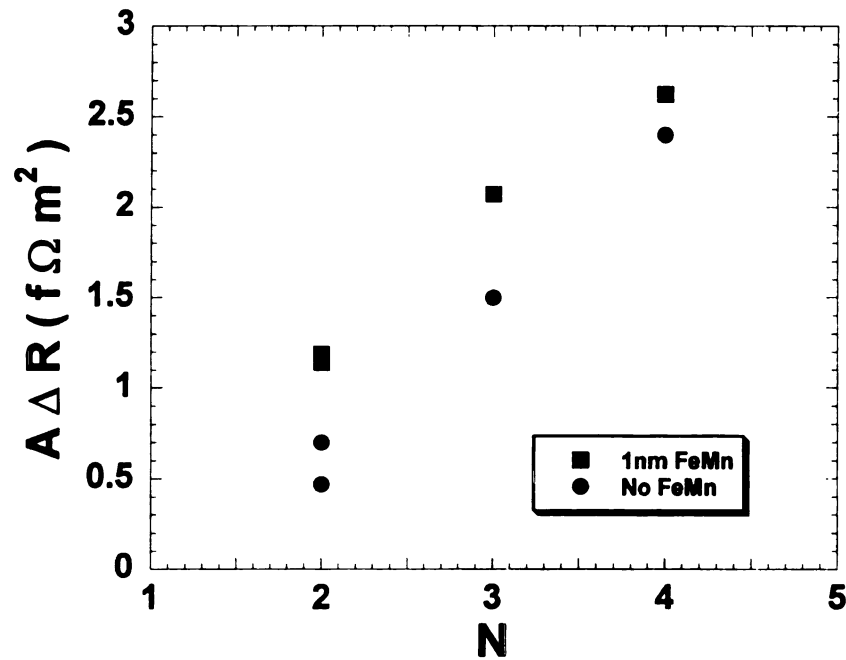


Fig.5.39. $A\Delta R$ vs N for multilayers with (filled boxes) or without (filled circles) FeMn. Structure is $[\text{Cu}(10)/\text{FeMn}(1)/\text{Cu}(10)/[\text{Co}(6)/\text{Cu}(20)/\text{Co}(1)/\text{Cu}(20)]_N/\text{FeMn}(1)/\text{Cu}(5)]$. The ‘regular’ samples are identical, just without the FeMn layers. $A\Delta R$ increases by $\sim 90\%$ for $N=2$ to $\sim 9\%$ for $N=4$.

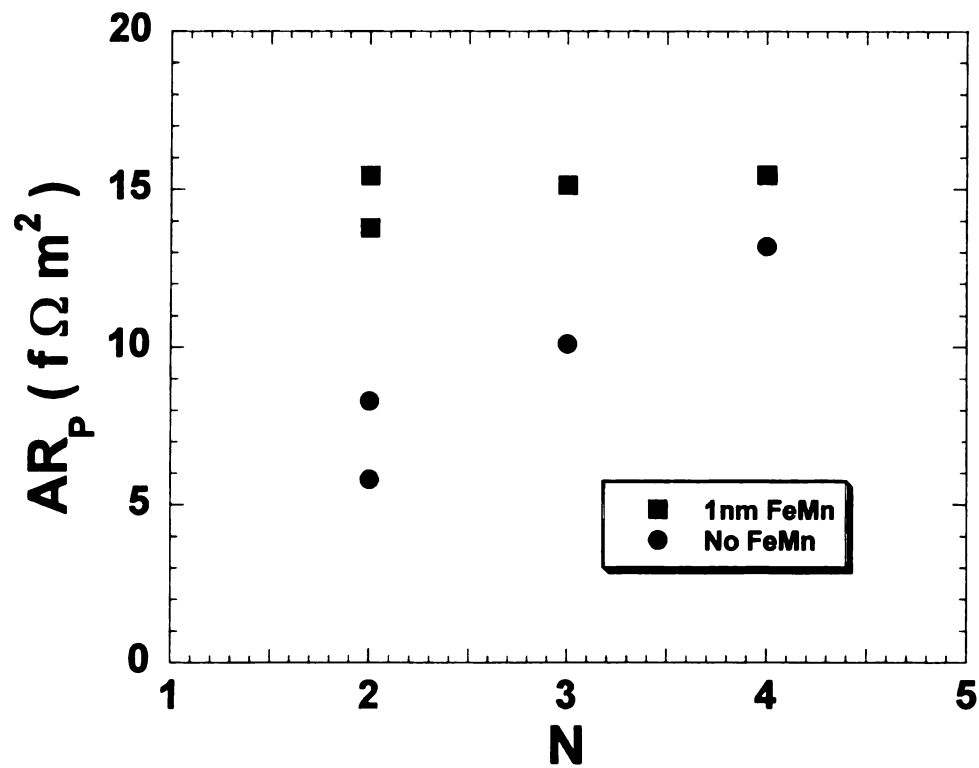


Fig.5.40. AR_p vs N . Effect of the FeMn layers on the total specific resistance, AR_p . Boxes and circles have the same meaning as in the previous figure.

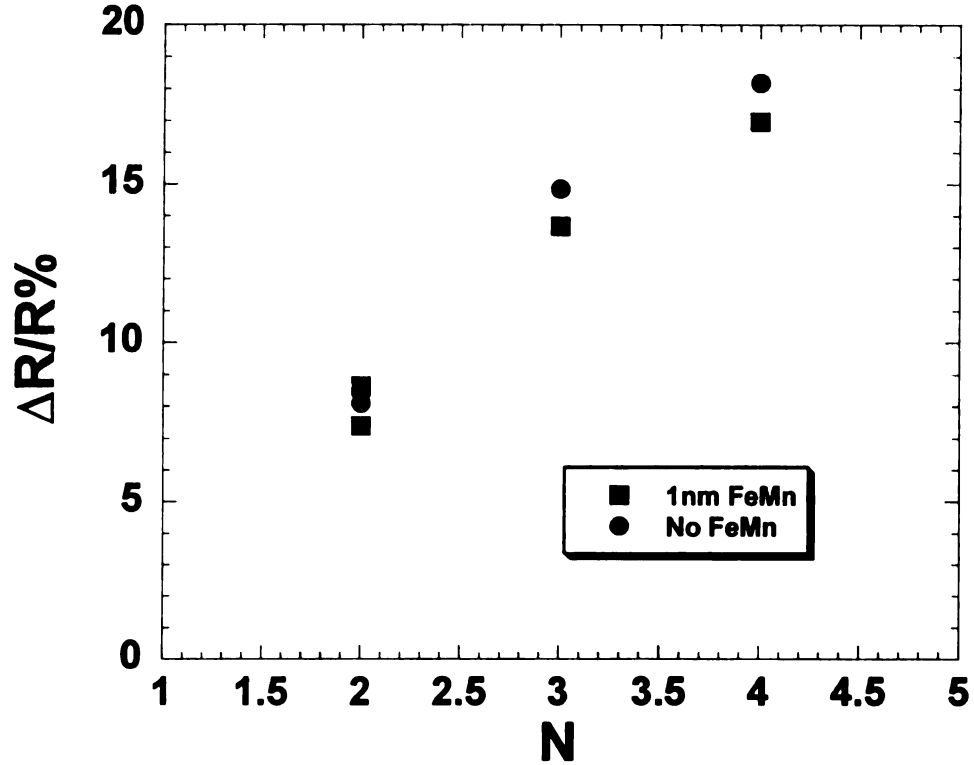


Fig. 5.41. $\Delta R/R$ vs N with (circles) and without (squares) FeMn inserts. Since both $A\Delta R$ and AR_p increase with introducing the FeMn layers, the magnetoresistance, $\Delta R/R$, changes only slightly.

Fig. 5.40 shows that inserting the FeMn layers also increases AR_p . This increase in AR_p is largest at small number of repeats N .

Fig. 5.41 is a combination of the data of Figs. 5.39 and 5.40. Fig. 5.41 shows that inserting the FeMn layers slightly decreases $\Delta R/R$. So inserting thin layers of FeMn to introduce strong spin flipping can significantly increase both AR_p and $A\Delta R$, without greatly reducing $\Delta R/R$. Being able to increase both $A\Delta R$ and AR_p is highly desired for CPP-MR potential applications, especially if $\Delta R/R$ increases with them or stays unchanged.

5.4.2: Fitting Data to the 2CSR Model:

Fitting the data to models helps us better understand how the FeMn enhances $A\Delta R$. As discussed at the beginning of the section, introducing strong spin flipping at the ends of the multilayer can make the VF model for $A\Delta R$ reduce to equation 5.1. The introduction of FeMn might also have two other possible effects. It may destroy the coherence between the current-carrying electrons and the holes created by Andreev reflection, or stop the Cooper pairs completely and limit them to outside the area between the two FeMn layers. Either of these two effects could turn the outside Co/Cu interfaces MR active. For our fits we use parameters found earlier [5,43], including $AR_{\text{FeMn/Nb}} = 0.6 \text{ f}\Omega\text{m}^2$, $\rho_{\text{FeMn}} = 875 \text{ n}\Omega\text{m}$, and $AR_{\text{FeMn/Cu}} = 1 \text{ f}\Omega\text{m}^2$.

Fig. 5.42 compares the data with three 2CSR model curves. The data do fall above the dot-dash line expected without any effects of FeMn. But they fall below both the dashed line 2CSR model prediction assuming equation 5.1, and the top dotted line, which adds to the numerator of equation 5.1 two additional Co/Cu interfaces.

We conclude that introducing $t_{\text{FeMn}} = 1 \text{ nm}$ into the Cu layer next to superconducting Nb does increase $A\Delta R$, but not by as much as would be expected if it were fully inside a non-superconducting metal. To check whether 1 nm of FeMn was enough or not, we tried samples with FeMn layer thickness 2 nm or 3 nm. Fig. 5.43A shows that increasing the FeMn layer thickness does not change AR_p from the samples with 1 nm of FeMn. Fig. 5.43B, however shows that increasing the thickness of the FeMn decreases $A\Delta R$ slightly, which means the magnetoresistance would go down for the thicker FeMn layers. So, Fig. 5.43 shows that 1 nm of FeMn is better than any thicker layers to enhance the CPP-MR.

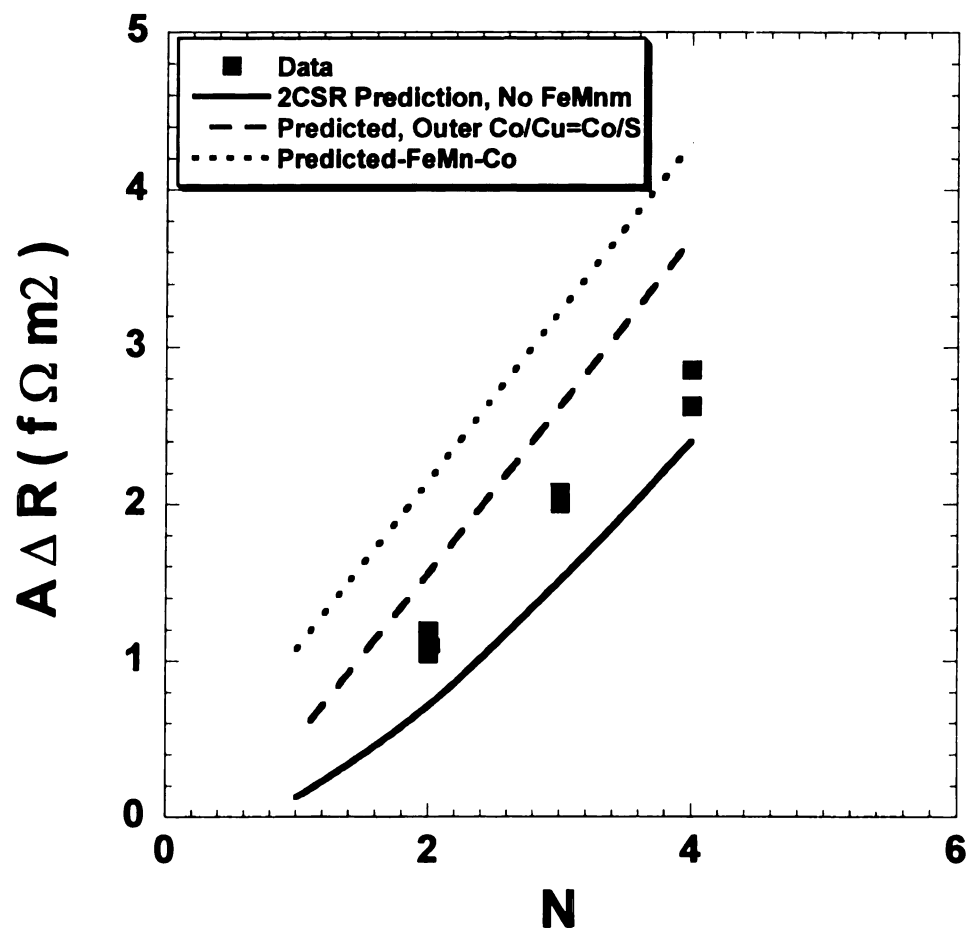


Fig.5.42. $A\Delta R$ versus N . Data (filled boxes) for samples with FeMn thin layers, 2CSR model predictions for the case without FeMn (solid curve), assuming that FeMn just removes $2AR_{S/F}$ (dashed curve), and assuming that FeMn removes $2AR_{S/F}$ and turns on asymmetry at the outer two Co/Cu interfaces (dotted curve).

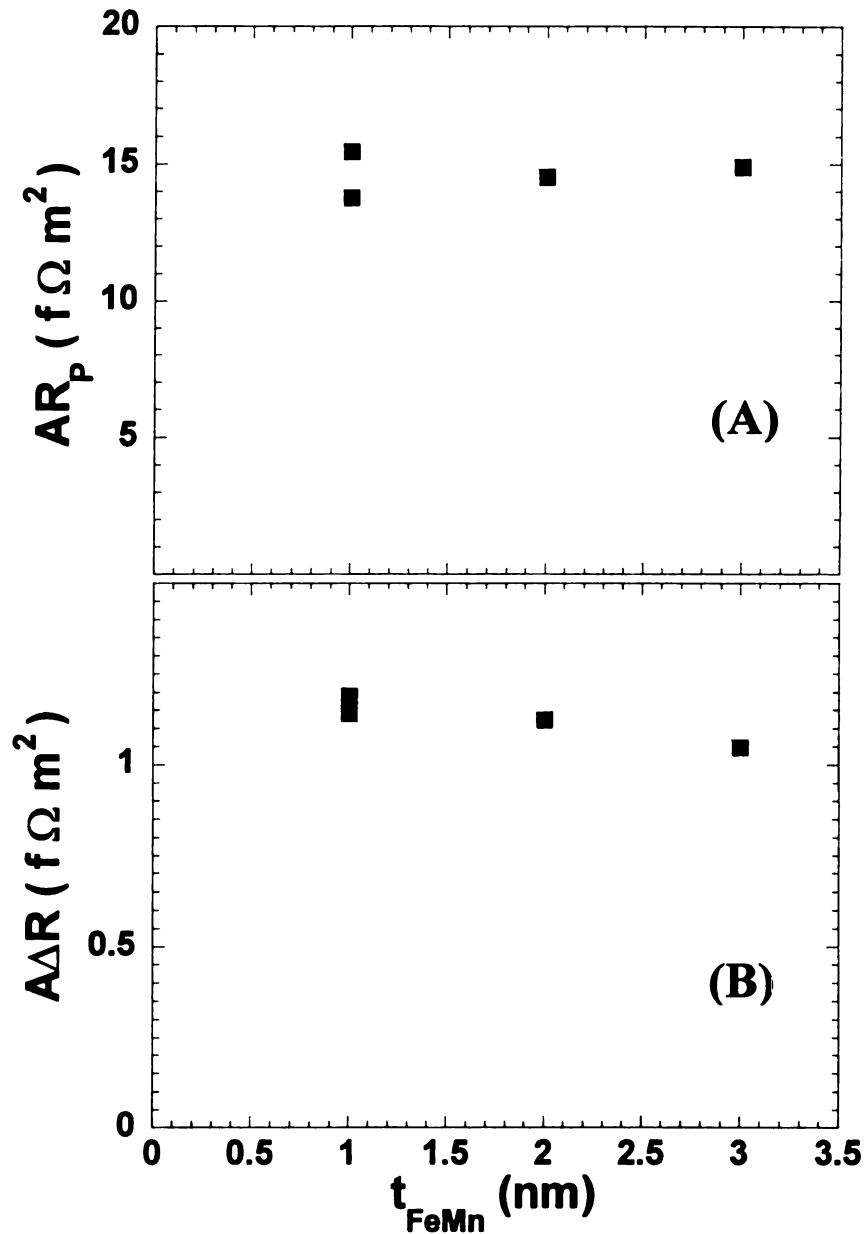


Fig.5.43. Effect of t_{FeMn} on AR_p (top) and $A\Delta R$ (bottom) for Nb/Cu(10)/FeMn(t)/Cu(10)/[Co(6)/Cu(20)/Co(1)/Cu(20)]₂/FeMn(t)/Cu(10)/Nb samples. Increasing t_{FeMn} beyond 1 nm essentially does not change AR_p and reduces $A\Delta R$ slightly.

To further check whether the outer Co/Cu interface contributes to GMR, or still has no asymmetric scattering, we replaced the Cu/FeMn/Cu layers on each side of the multilayer by Cu/FeMn/Cu/Co/Cu. Now the Cooper pairs should stop outside the outer Co layers, and all the volume between the two outer Co layers should be normal. Fig.5.44

shows that adding the Co layers had little effect on $A\Delta R$, while increasing AR_P . This result shows again that 1 nm of FeMn is enough to cause the maximum enhancement attainable in those samples.

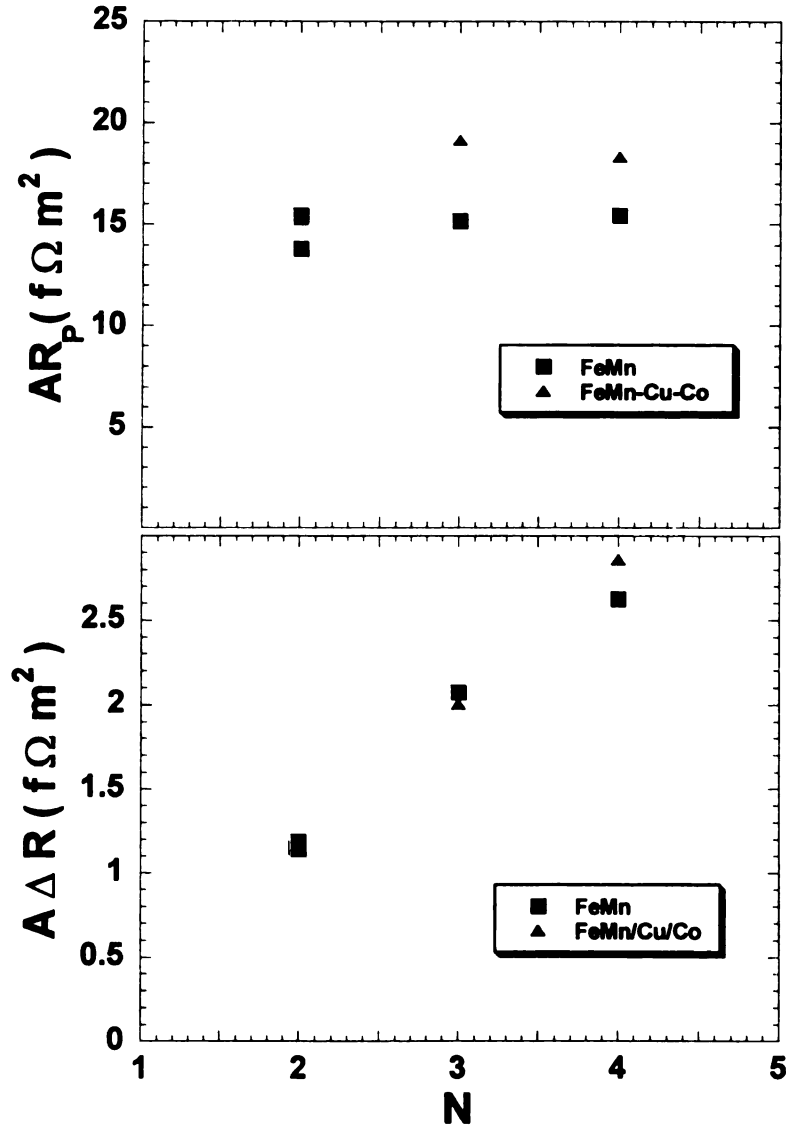


Fig.5.44. AR_P (top) and $A\Delta R$ (bottom) vs N for FeMn inserts with (triangles) or without (squares) additional thin Co layers outside of the FeMn layers. Adding the Co layer gives no gain in $A\Delta R$, but increases AR_P .

Finally, to check for possible structural changes due to introducing FeMn into the multilayers, we looked for the difference in AR_P and $A\Delta R$ when the FeMn is sputtered on

the bottom or top of the multilayer. Fig.5.45 shows that any difference is small. The reasons for the behaviors of FeMn in the superconducting layer are not yet clear. Some further information about such interfaces will be presented in Ch. 6.

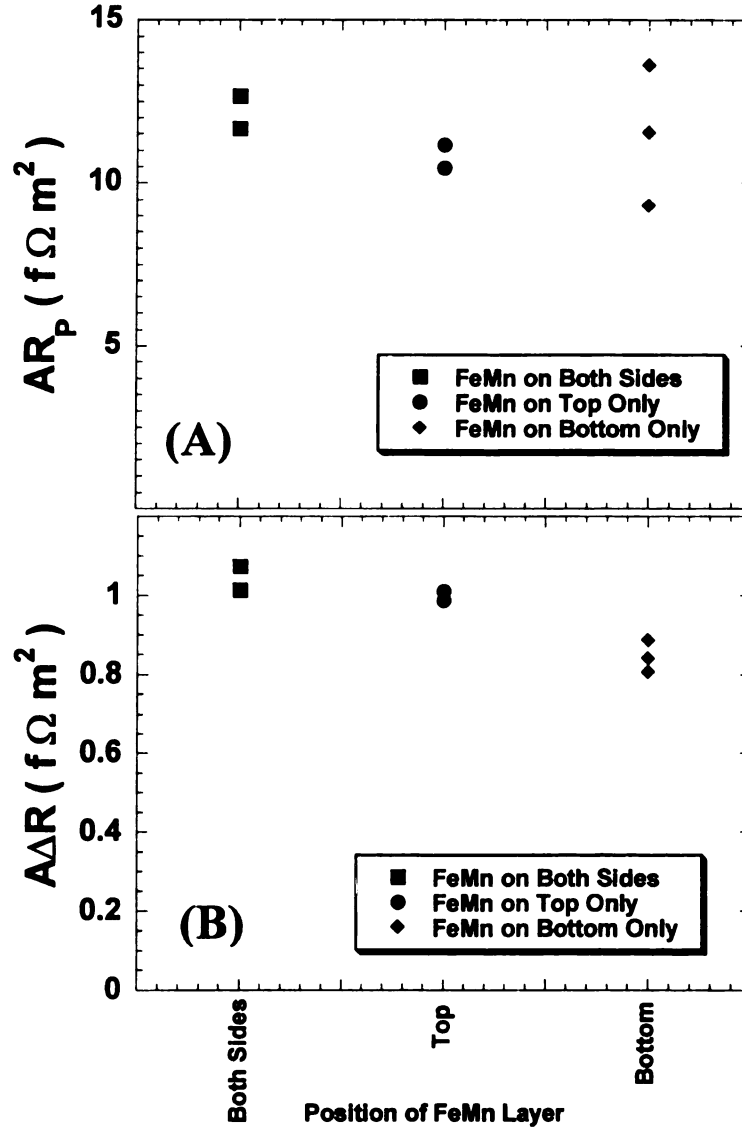


Fig.5.45. Effect of the position of FeMn on (A) AR_p and (B) $A\Delta R$. Growing the FeMn on the top of the multilayer gives a larger $A\Delta R$ and a slightly smaller AR_p than when FeMn is grown before the multilayer.

CHAPTER 6

CPP-MR STUDIES WITH RUTHENIUM (Ru).

There is now great interest in Ruthenium (Ru) for CIP-MR technology as the basis for a Co/Ru/Co ‘synthetic antiferromagnet’ (SAF) [13,14,119-121], in which a very thin ($t_{\text{Ru}} = 0.6 \text{ nm}$) Ru layer strongly couples two Co layers ($t_{\text{Co}} \sim 3 \text{ nm}$) antiferromagnetically. This coupling is used in read heads of structure [AF/Co(3)/Ru(0.6)/Co(3)/Cu/F] [119], where F is a ferromagnetic alloy with high contribution to the GMR and AF is an antiferromagnetic material that pins the Co layer in direct contact with it. SAFs offer better stability over many reading cycles than a normal antiferromagnet alone.

To estimate whether Ru can play a significant role in CPP-MR technology, it is necessary to know its CPP parameters: ρ_{Ru} , $\gamma_{\text{Co/Ru}}$, $AR_{\text{Co/Ru}}$, and $I_{\text{SF}}^{\text{Ru}}$. In addition, CIP-MR measurements on Co/Ru multilayers have been interpreted as yielding a negative interfacial scattering anisotropy parameter [122, 123]. In the CPP-MR this would translate into a negative $\gamma_{\text{Co/Ru}}$.

In the first part of Ch. 6, we determine the CPP properties at 4.2K of sputtered Ru and examine AAR for a variety of different sample structures involving Ru as the N-metal. Among the results obtained is evidence that $\gamma_{\text{Co/Ru}}$ is indeed negative. Some of this work has already been published [124]. In the second part of Ch. 6, we use this negative $\gamma_{\text{Co/Ru}}$ to construct a multilayer structure that lets us investigate in a controlled way the anisotropic scattering properties (specifically η) of various interesting interfaces, I. We

do so by constructing a multilayer that gives $A\Delta R \equiv 0$ for any I that has $\eta = 0$. $A\Delta R$ is then very sensitive to the properties of interfaces I that have non-zero values of η .

6.1 Ru FOR CPP-MR:

The resistivity of Ru was shown in Ch.2 to be $\rho_{\text{Ru}} = 9.5 \pm 0.5 \mu\Omega\text{cm}$. We begin our studies of CPP-MR properties of Ru by determining the spin-diffusion length in Ru, $t_{\text{SF}}^{\text{Ru}}$, and spin-memory-loss at Ru/Cu interfaces. We measure these using a Py-based EBSV, spin-memory-loss detector [73] with structure (Fig. 6.1): $[\text{Nb}(150)/\text{Cu}(20)/\text{FeMn}(8)/\text{Py}(24)/\text{Cu}(10)/\text{X}/\text{Cu}(10)/\text{Py}(24)/\text{Cu}(20)/\text{Nb}(\text{Nb}(150))$. X is the material creating the spin-memory-loss to be measured, in the present case either a single layer of Ru of thickness t_{Ru} or a $[\text{Cu}/\text{Ru}]_N$ multilayer with variable N . We measure how $A\Delta R$ for this EBSV decreases with increasing t_{Ru} or N , and fit the data numerically using the theory of VF and the parameters for Py-based EBSVs as described in Ref. [74].

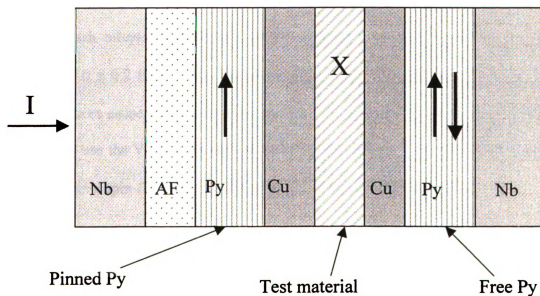


Fig. 6.1. Spin-memory-loss detector. In the experiments to be described, X is either a single layer of Ru or a Cu/Ru multilayer.

Fig. 6.2 shows how $\log A\Delta R$ decreases with increasing t_{Ru} . For no Ru, $A\Delta R$ has the expected value for a Py-based EBSV, $\sim 2.1 \text{ f}\Omega\text{m}^2$ [73]. As t_{Ru} increases, $A\Delta R$ first decreases rather rapidly, and then more slowly. The slower decrease is consistent with a straight line on the log-linear plot, indicating an exponential decay. The initial falloff in the curve is due to the formation of two Cu/Ru interfaces. Those interfaces suppress $A\Delta R$ both by increasing the specific resistance of the sample (see Eq. 3.3) and due to spin-flipping at the Cu/Ru interface. The slower exponential falloff is what is expected from the V-F model ($A\Delta R \sim e^{-(t/l_{\text{SF}}^{\text{Ru}})}$), for finite $l_{\text{SF}}^{\text{Ru}}$ in the Ru. From the slope of this line we estimate $l_{\text{SF}}^{\text{Ru}} = 14 \pm 1 \text{ nm}$ for our sputtered Ru. This spin-diffusion length is much longer than the thickness of Ru layers used in synthetic antiferromagnets. To fully fit all of the data in Fig. 6.2 we must know also $AR_{\text{Cu/Ru}}$ and the spin-memory-loss parameter for Cu/Ru interfaces.

To measure $AR_{\text{Cu/Ru}}$ and the spin-memory-loss parameter $\delta_{\text{Cu/Ru}}$ at Cu/Ru interfaces, we replaced the single Ru layer by a $[\text{Cu}(5)/\text{Ru}(3)]_N$ multilayer. Fig. 6.3 shows AR_{AP} vs N . Since each bilayer contains two Ru/Cu interfaces, a linear fit to the data gives $2AR_{\text{Cu/Ru}} = 2.0 \pm 0.2 \text{ f}\Omega\text{m}^2$. Fig. 6.4 shows $A\Delta R$ vs N . The rapid dropoff means that Cu/Ru interfaces cause strong spin-memory loss. To estimate the spin-memory-loss per interface, we use the V-F model and subtract the spin-memory-loss contribution of bulk Ru. We obtain a spin-flipping probability of $35 \pm 5\%$ per Cu/Ru interface.

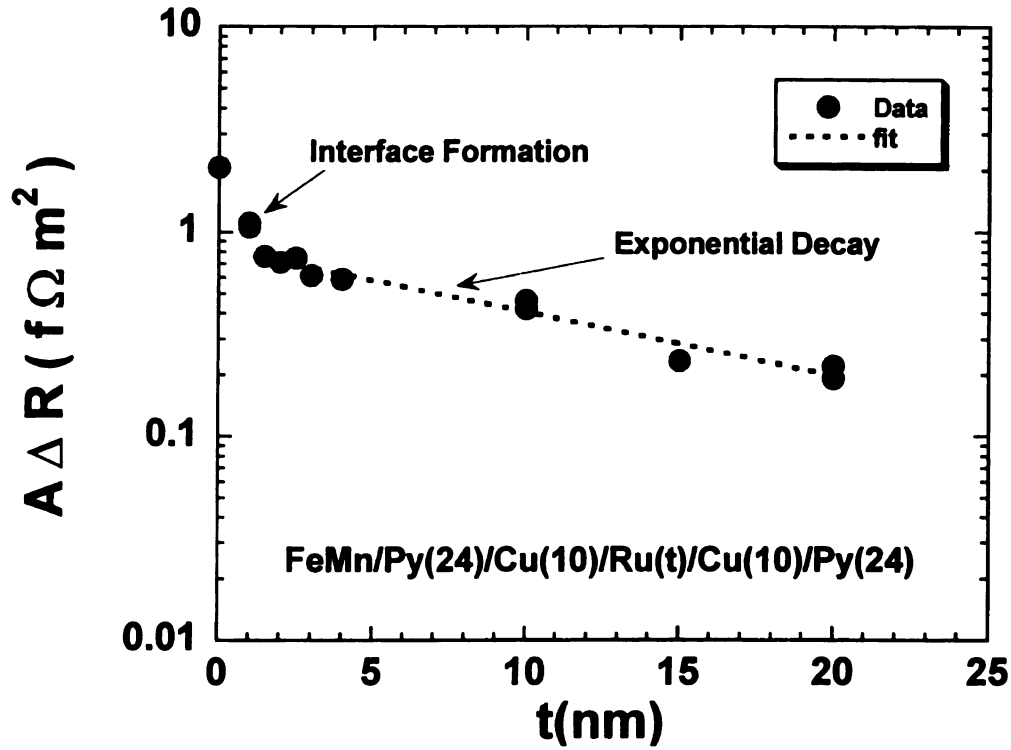


Fig.6.2. $A\Delta R$ on a log scale vs t_{Ru} . The steep drop at small t_{Ru} is due to the formation of two Cu/Ru interfaces. After the two interfaces are established, $A\Delta R$ drops exponentially with t_{Ru} , and the slope of the straight line on this semi-log graph is the inverse of the spin-diffusion-length in Ru $l_{\text{SF}}^{\text{Ru}} = (14 \pm 1)$ nm.

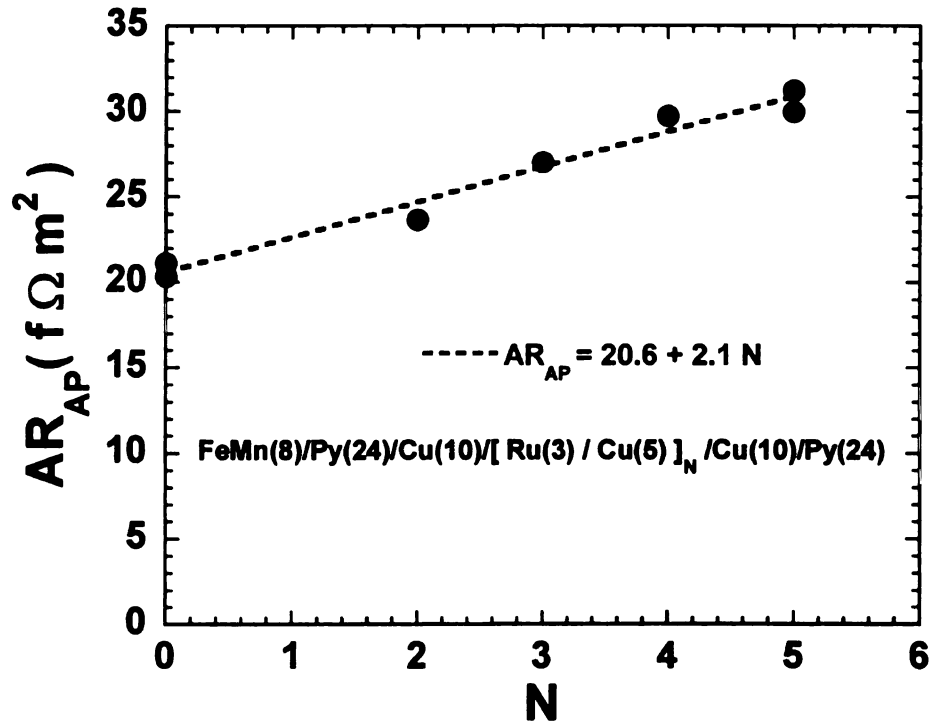


Fig. 6.3. AR_{AP} vs N for a Py-based with EBSV with an $[\text{Cu/Ru}]_N$ insert. The slope of the best fit line gives $2AR_{\text{Cu/Ru}} = 2.0 \pm 0.2 \text{ f}\Omega\text{m}^2$.

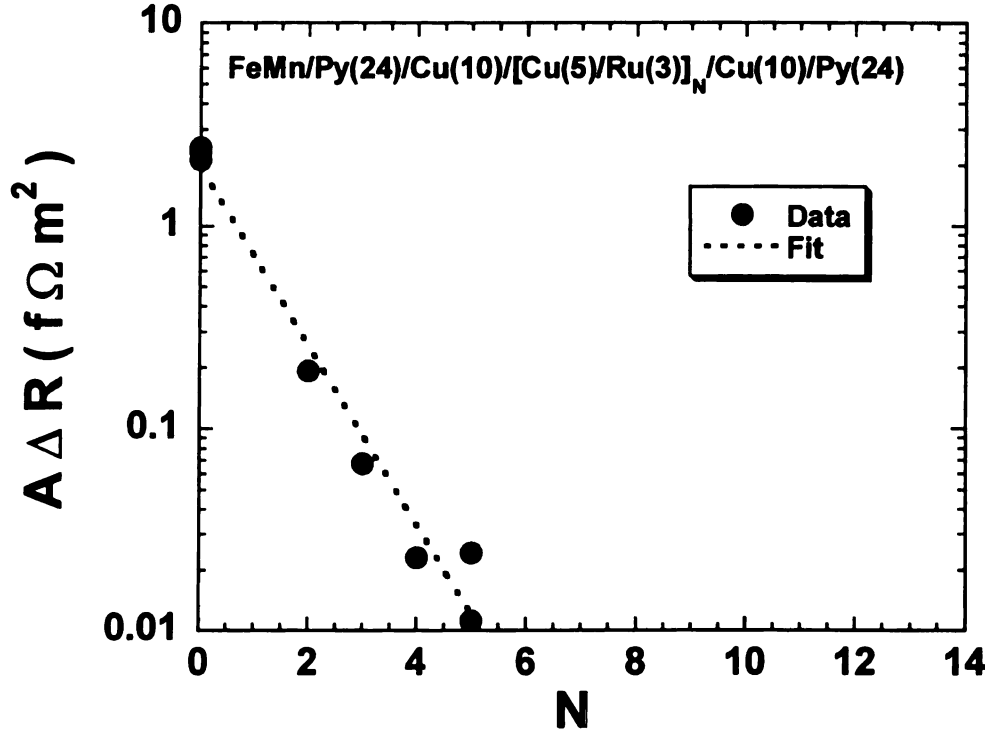


Fig. 6.4. $A\Delta R$ on a log scale vs the number of $[\text{Ru}(3)/\text{Cu}(5)]$ bilayer inserts. This straight line fit (on the log scale) of the data gives a spin-flip probability of electrons at the Cu/Ru interface $\sim 35\%$ per interface.

6.1.1. CPP-MR of Co/Ru.

Motivated by literature evidence [46] of negative anisotropy (i.e. negative β) in CoRu alloys, we decided to examine the contribution of Co/Ru interfaces to the CPP-MR, given that the interfaces of sputtered Co/Ru multilayers can be thought of as a CoRu alloy. In the process, we studied simple $[\text{Co}/\text{Ru}]_N$ multilayers, symmetric Co-based EBSVs with Ru as the N-layer, and $[\text{Py}(6)/\text{Cu}(20)/\text{Ru}(2)/\text{Co}(t)/\text{Ru}(2)/\text{Cu}(20)]_N$ hybrid multilayers with Co/Ru interfaces. We hoped that a negative β for the CoRu alloy would produce a negative γ at the Co/Ru interface. Since bulk Co has a positive β , Co layers having interfaces with Ru would have to be thin for the interface contribution to dominate. As shown in Eq. 3.3, a negative γ for Co/Ru can be inferred from a negative $A\Delta R$ for a

hybrid multilayer in which the other ferromagnetic metal (i.e. Py) has positive parameters. We first used the hybrid multilayers $[\text{Co}(6)/\text{Cu}(20)/\text{Ru}(1)/\text{Co}(1)/\text{Ru}(1)/\text{Cu}(20)]_N$ because we had studied such multilayers thoroughly in Chapter 4 (without the Ru layers). If $\gamma_{\text{Co/Ru}}$ is negative, and two Co/Ru interfaces contribute more to the CPP-MR than does 1nm of Co, then the above multilayer should give an inverse GMR, characterized by $AR(H)$ curves having $AR_{\text{AP}} < AR_{\text{P}}$. Fig. 6.5 shows $AR(H)$ for the above multilayer. Although the curve is noisy, because of the small value of $A\Delta R$ and the need for a relatively large H to switch the magnetization of the Co(6) layer, and despite a gradual rise in the background AR with H , it seems clear that the CPP-MR is inverse.

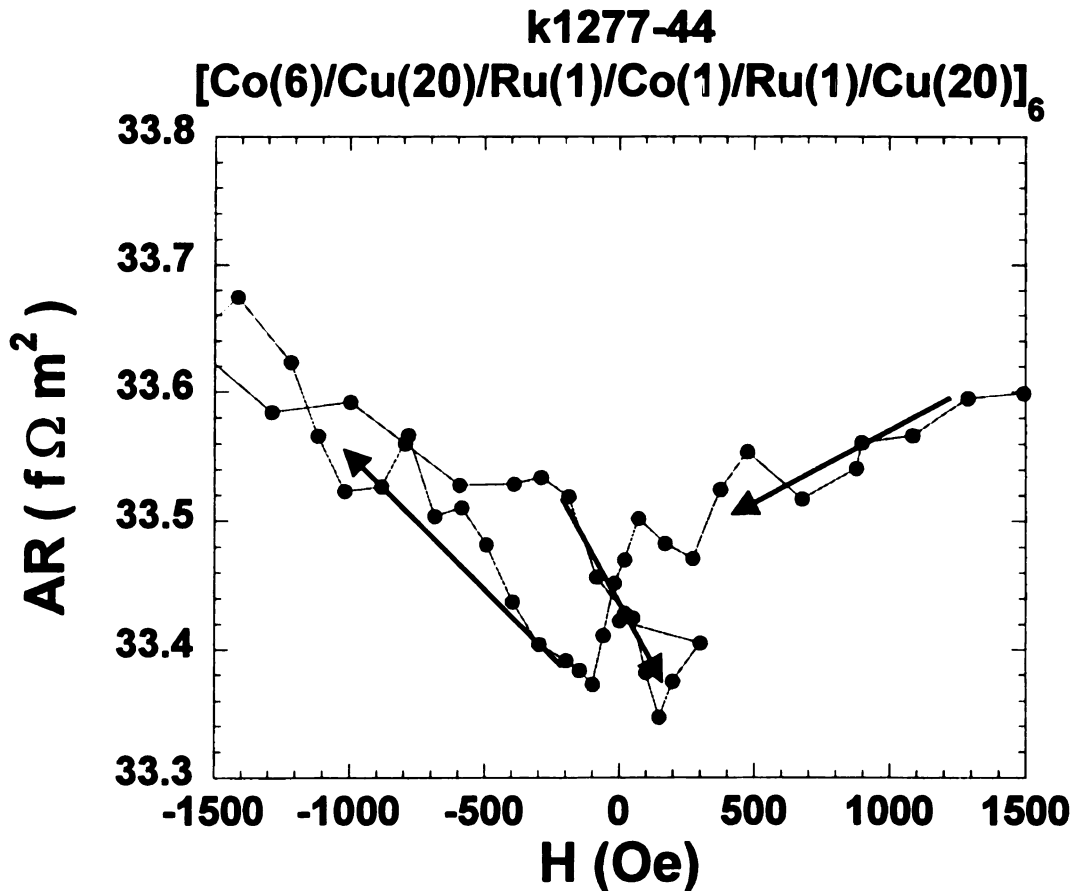


Fig. 6.5. AR vs H curve showing an inverse CPP-MR, i.e., $AR_{\text{AP}} < AR_{\text{P}}$. The small $A\Delta R$ compared to noise, and the background change with H , make it hard to quantify the data.

To get a larger $A\Delta R$ at smaller fields, we replaced the thick Co layer by a 6nm thick Py layer, giving $[\text{Py}(6)/\text{Cu}(20)/\text{Ru}(1)/\text{Co}(1.5)/\text{Ru}(1)/\text{Cu}(20)]_6$. Py gives a larger contribution to $A\Delta R$ than Co (because both β and ρ are larger for Py than for Co), and also needs only a smaller switching field. Fig. 6.6 shows a clear inverse MR. Since the anisotropy parameters for bulk Py, the Py/Cu interface, and bulk Co are all positive, only a negative γ at the Co/Ru interface can create such a negative $A\Delta R$.

Fig. 6.7 shows that the sample of Fig. 6.6 also has an inverse CIP-MR. We presume that this inverse CIP-MR is also due, at least partly, to a negative γ at the Co/Ru interface. If the negative CIP-MR was only due to the AMR of Py, then the switching field should be only that of Py. Comparing Figs. 6.6 and 6.7 we see that the switching fields are the same and have magnitude ≈ 450 Oe, which is the switching field of the Co layer, not the Py one (i.e. the MR depends on both the Co and the Py, which is peculiar to GMR, not to AMR). The sharp peak in the CIP-MR at small fields might be associated with the AMR of Py. As in many other cases, the CIP-MR is much smaller than the CPP-MR.

If our analysis above is correct, then as the Co thickness, t_{Co} , increases, $A\Delta R$ should decrease in magnitude and finally switch sign, becoming positive when Co is thick enough to overcome the negative contribution of the Co/Ru interface to the CPP-MR. Fig. 6.8 shows the progression of $AR(H)$ curves with increasing t_{Co} for three different samples. The Co/Ru interface dominates at low Co thickness giving an inverse MR, whereas bulk Co dominates at higher thickness giving normal MR. The three curves in Fig. 6.8 are plotted on the same scale to allow direct comparison between the signs and magnitudes of $A\Delta R$.

To estimate the value of $\gamma_{\text{Co/Ru}}$ we made a series of samples with varying t_{Co} like those of Fig. 6.8. Fig. 6.9 shows $A\Delta R$ versus t_{Co} . $A\Delta R$ follows an almost straight line with t_{Co} , switching from inverse to normal at $t_{\text{Co}} \approx 5 \text{ nm}$. This straight line can be explained with Eq. 3.3 in Chapter 3, where we see that the ‘bulk’ Co contributes to $A\Delta R$ in two places. First, it adds to the total specific resistance in the denominator. But this addition is small, due to the relatively small resistivity of Co. The more important contribution is through the numerator, where $A\Delta R$ is proportional to t_{Co} , thus explaining the straight line in Fig. 6.9. Using this figure, we estimated the value of $\gamma_{\text{Co/Ru}}$ to be $-(0.15 \pm 0.05)$.

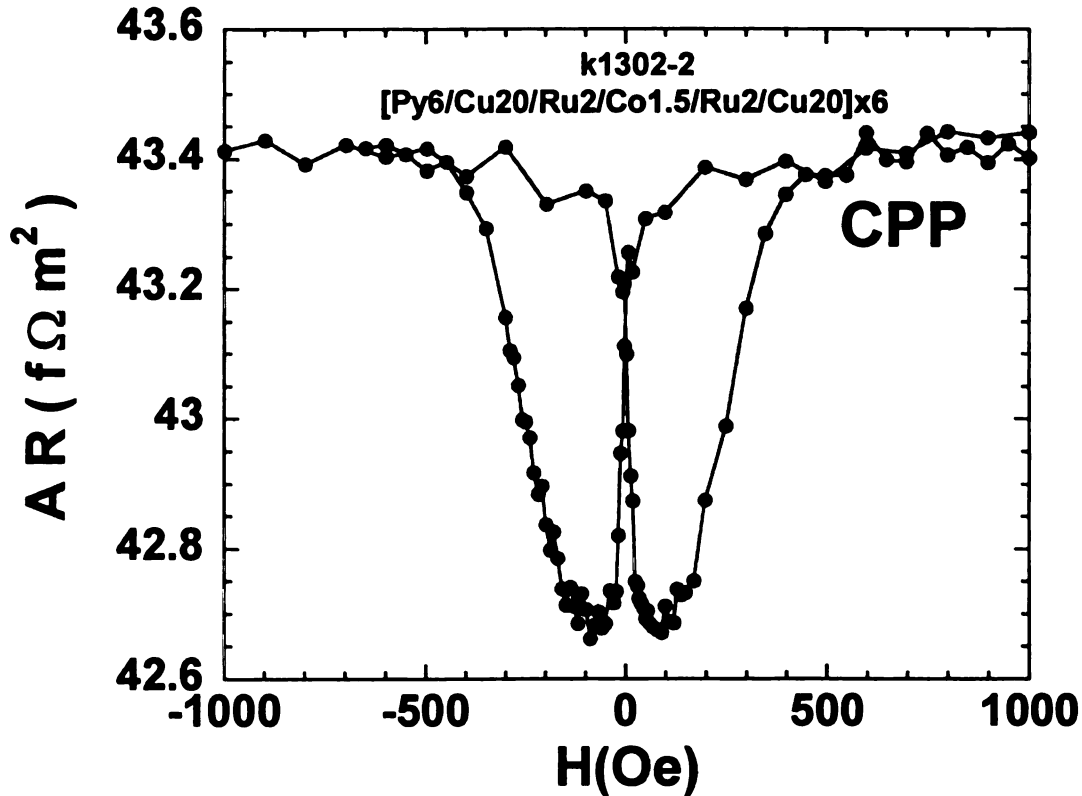


Fig. 6.6. $AR(H)$ for the hybrid sample $[\text{Py}(6)/\text{Cu}(20)/\text{Ru}(2)/\text{Co}(1.5)/\text{Ru}(2)/\text{Cu}(20)]_6$, showing inverse CPP-MR.

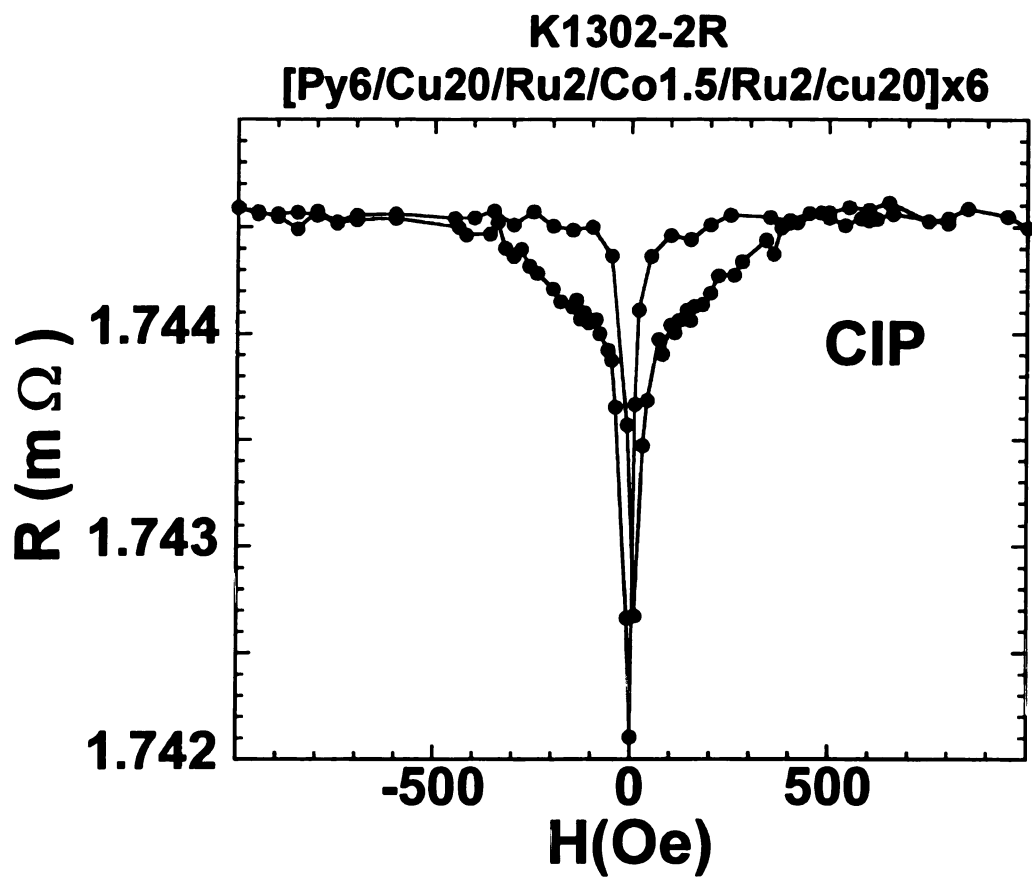


Fig. 6.7. CIP $R(H)$ loop for the sample of Fig. 6.6. The CIP-MR is also inverse.

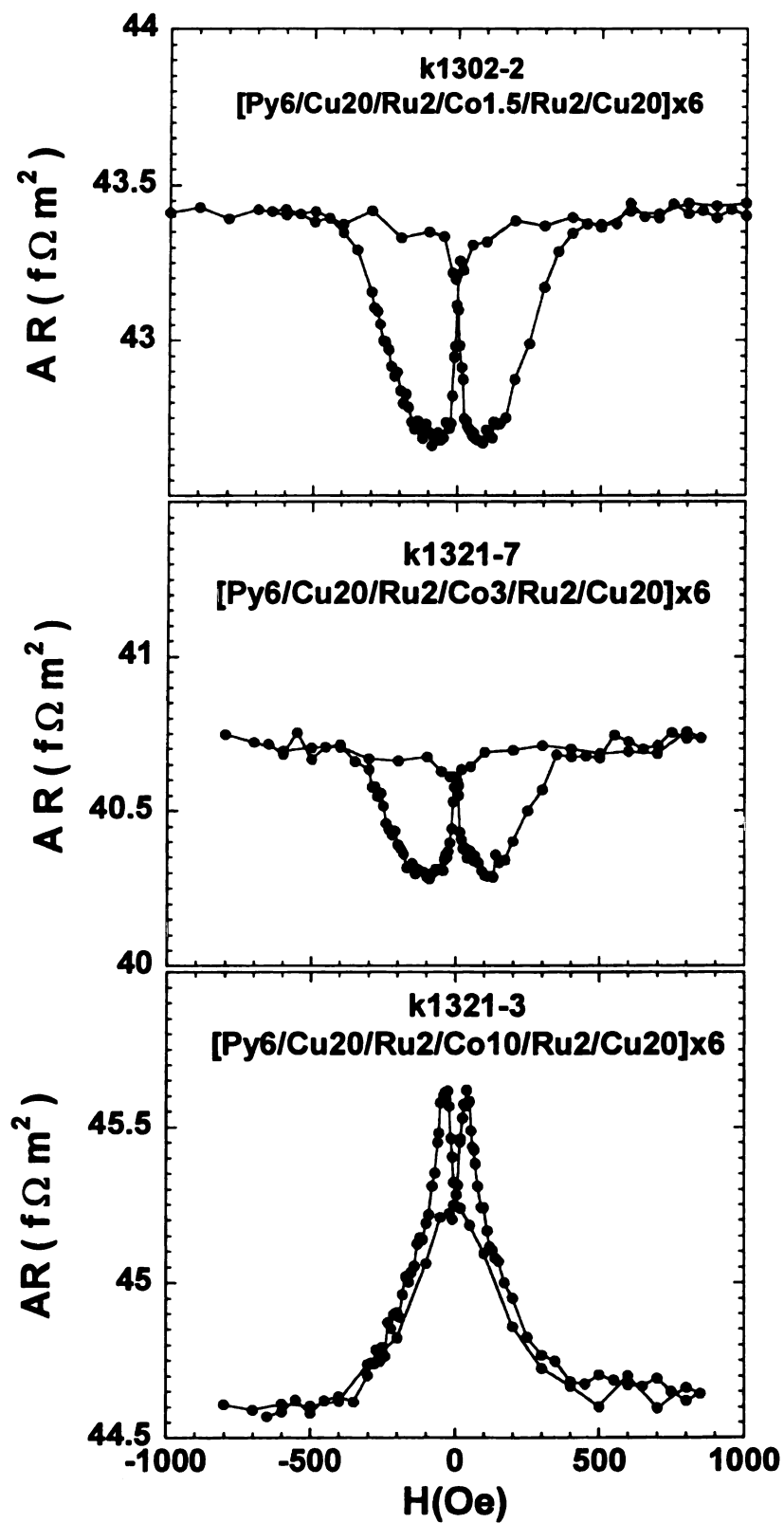


Fig. 6.8. Progression of $AR(H)$ curve with increasing Co layer thickness. MR is inverse for small thicknesses of Co and switches to normal for large Co thickness.

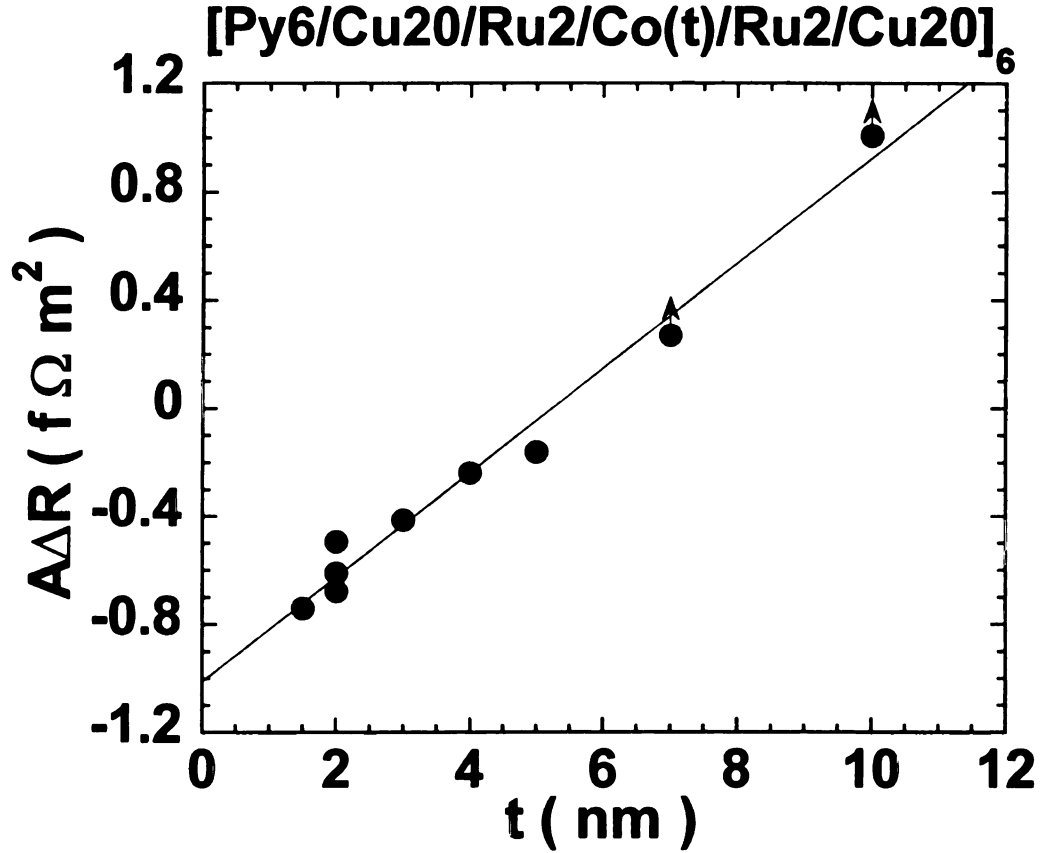


Fig. 6.9. ΔR vs t_{Co} . The data follow a nearly straight line, allowing an estimate of $\gamma_{\text{Co/Ru}} = (-0.15 \pm 0.05)$. Arrows in the plot indicate that those data points involve only a lower bound on the AP state.

To further study the CPP-MR properties of multilayers containing Ru we made samples with structure: Nb/Cu/[Co(3)/Ru(0.6)]_N/Co(3)/Cu/Nb. We chose the Co and Ru thicknesses to give coupling between the Co layers at the first antiferromagnetic peak. This choice should yield a good AP state. Fig. 6.10 shows $AR(H)$ curve for the multilayer: Nb/Cu/[Co(3)/Ru(0.6)]₂₀/Co(3)/Cu/Nb. Even at $H = 8$ kG, we do not get the flat $AR(H)$ evidencing parallel alignment. This behavior agrees with literature results

showing very strong antiferromagnetic coupling in Co/Ru multilayer with Ru layers thickness $t_{\text{Ru}} \sim 0.5\text{-}0.6$ nm [14,119].

To avoid such high fields, we switched to $t_{\text{Ru}} = 1.6$ nm, at the second AP coupling peak. This change allowed us to switch the magnetic state from AP to P within the available field range. Moreover, since the Co/Ru interface is quite broad [125], the thicker Ru should create better interfaces than $t_{\text{Ru}} = 0.6$ nm.

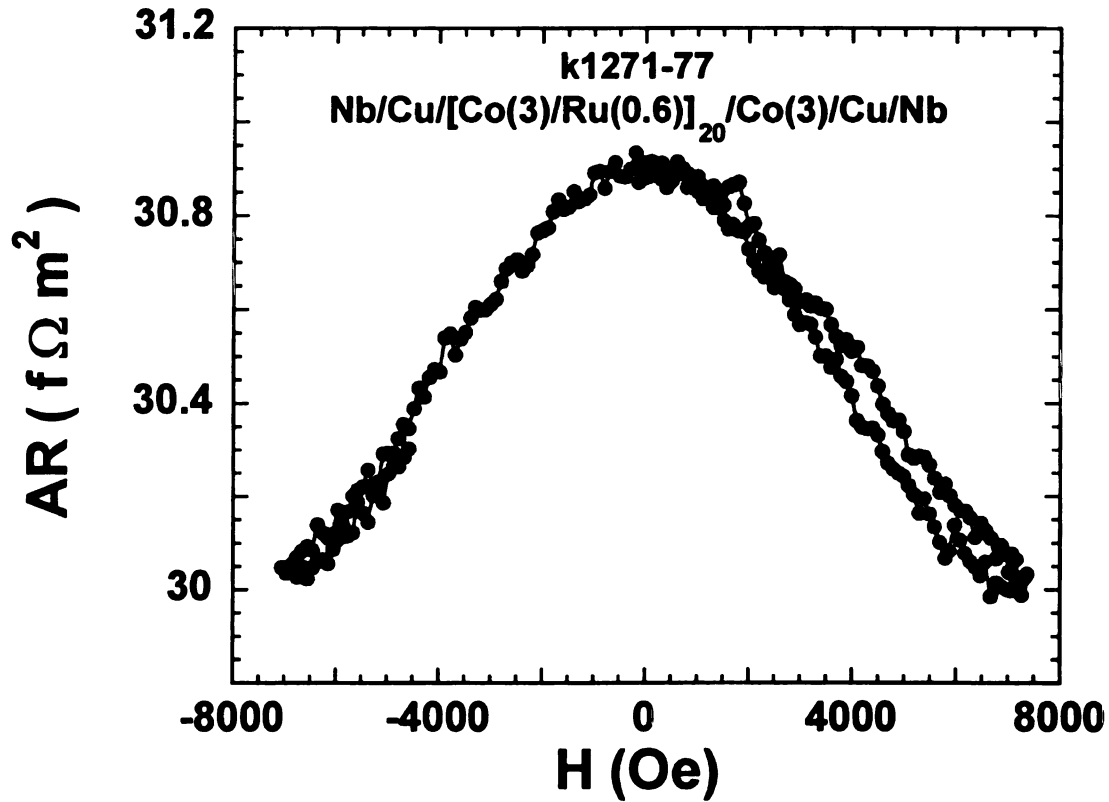


Fig. 6.10. $AR(H)$ of an $[\text{Co/Ru}]_{20}$ multilayer. The antiferromagnetic coupling is too strong to be overcome even at our highest applied field of about 8 kG.

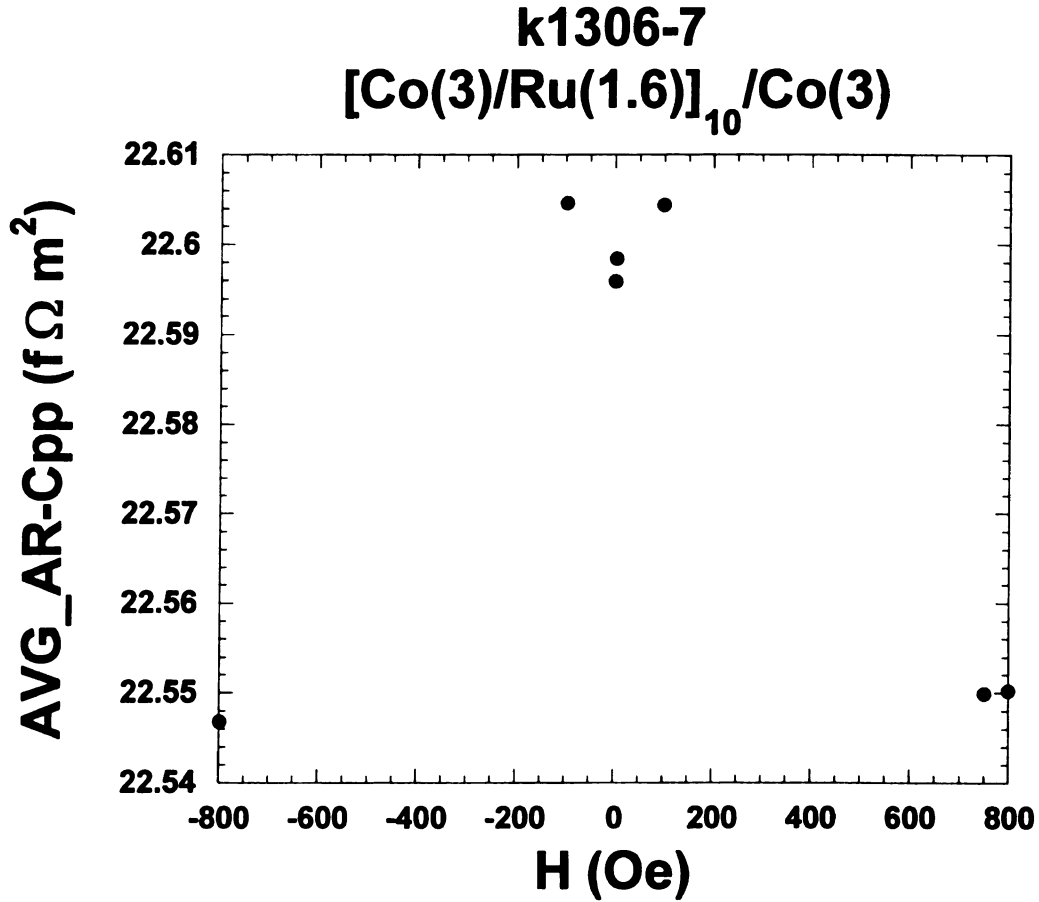


Fig. 6.11. Average $AR(H)$ for a $[Co(3)/Ru(1.6)]_{10}/Co(3)$ multilayer vs H . Each point is repeated 100 times and averaged to get reliable results.

In Fig. 6.11, $A\Delta R$ of the multilayer $[Co(3)/Ru(1.6)]_{10}/Co(3)$ was so small that we needed to measure each point 100 times and take the average value of $AR(H)$ at that point. This extremely small $A\Delta R$ is due to the opposite contributions of bulk Co and the Co/Ru interfaces, which almost cancel each other at this particular Co thickness (See Fig. 6.9). The small CPP-MR in this multilayer agrees with those of the hybrid samples in Fig. 6.9. The larger value of $A\Delta R$ in Fig. 6.10 could be due to CoRu alloying playing a larger role, giving a negative β , and thereby making $A\Delta R$ larger than when the Ru is 1.6 nm thick.

Fig. 6.12 shows AR_{AP} versus N , the number of Co/Ru bilayers, for $t_{Ru} = 1.6$ nm. In principle, the slope of the line gives $2AR_{Co/Ru}$, and the ordinate intercept gives $2AR_{Nb/Co}$. However, each additional bilayer also adds bulk contributions from the Co and Ru layers. Taking the slope as 1.6 ± 0.16 f Ωm^2 , and taking $\rho_{Co}^* = 7 \pm 2$ $\mu\Omega cm$ and $\rho_{Ru} = 9.5 \pm 1$ $\mu\Omega cm$, respectively, we estimate $2AR_{Co/Ru} = 1.20 \pm 0.23$ f Ωm^2 . The value of 7.5 ± 2.3 f Ωm^2 for the ordinate intercept equals $2AR_{S/F} + \rho_{Co}^* t_{Co}$, because we have an extra Co layer on top of the multilayer. This leaves $2AR_{Nb/Co} = 7.3 \pm 2.3$ f Ωm^2 , which is a bit higher than, but overlaps with, our 'standard' value of $2AR_{Nb/Co} = 6 \pm 1$ f Ωm^2 .

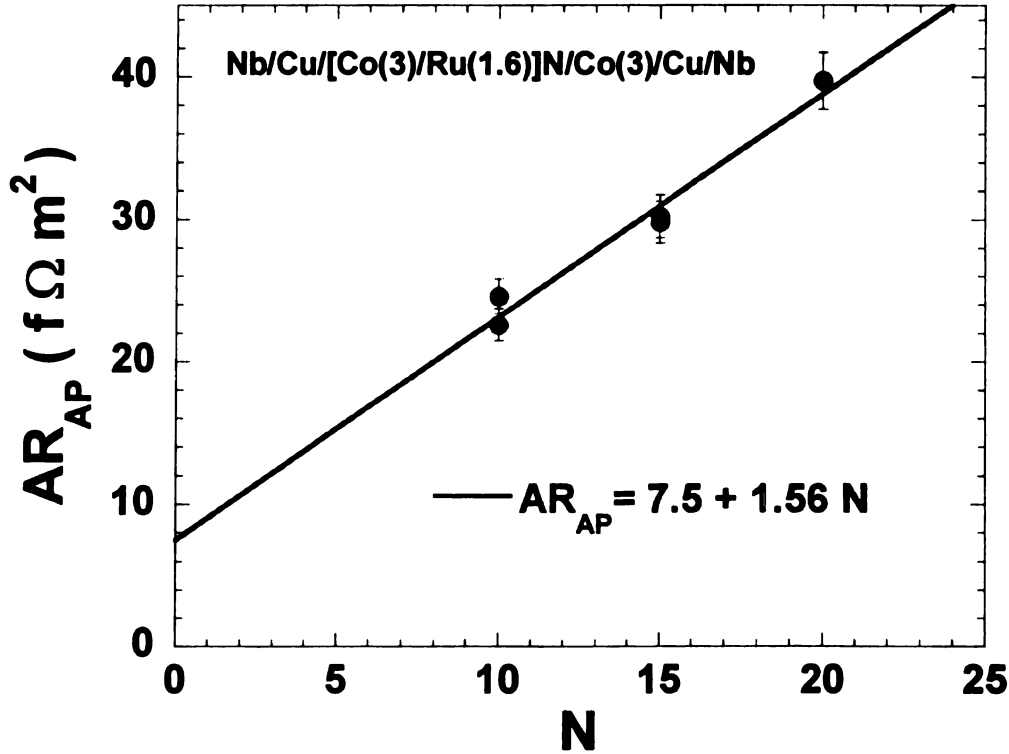


Fig. 6.12. AR_{AP} vs N . Analysis of the slope of the straight-line fit gives $2AR_{Co/Ru} = (1.2 \pm 0.23)$ f Ωm^2 , and analysis of the intercept gives $2AR_{Co/Nb} = (7.3 \pm 2.3)$ f Ωm^2 (see text).

To better control the AP state, and achieve a wider variety of MR data for Co/Ru, we also made EBSVs with structure: Nb/Cu(10)/FeMn(8)/Co(t)/Ru(10)/Co(t)/Cu(10)/Nb. The resulting values of AR could be even smaller than those of multilayers, depending

on the Co layers thickness, limiting our ability to analyze those samples quantitatively. .

Fig. 6.13 shows the 2CSR model based prediction of $A\Delta R(t_{Co})$ for a Co(t)/Ru(10nm)/Co(t) EBSV. The prediction shows how difficult it is experimentally to measure such EBSVs. Fig. 6.14 shows AR(H) for an EBSV of composition: Nb/Cu/FeMn/Co(15)/Ru(10)/Co(15)/Cu/Nb. Each point is the average of 100 points. We took the points at fields where we expected AP or P states based on Co/Cu/Co EBSVs. The change in specific resistance is much smaller than predicted in Fig. 6.13. Either our choice of AP field is incorrect, or some of the parameters used in Fig. 6.13 are a bit off.

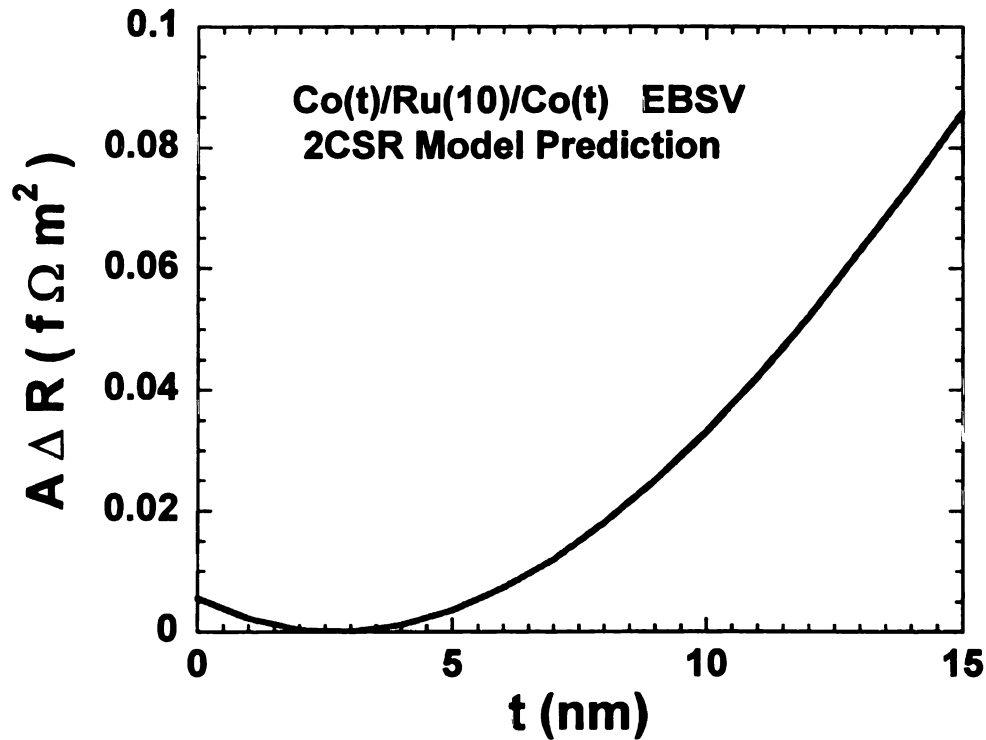


Fig. 6.13. 2CSR Model predicted $A\Delta R$ as a function of t_{Co} for a Co(t)/Ru(10)/Co(t) EBSV. $A\Delta R(t)$ is non-monotonic due to the competition between the contributions from the Co/Ru interfaces and bulk Co.

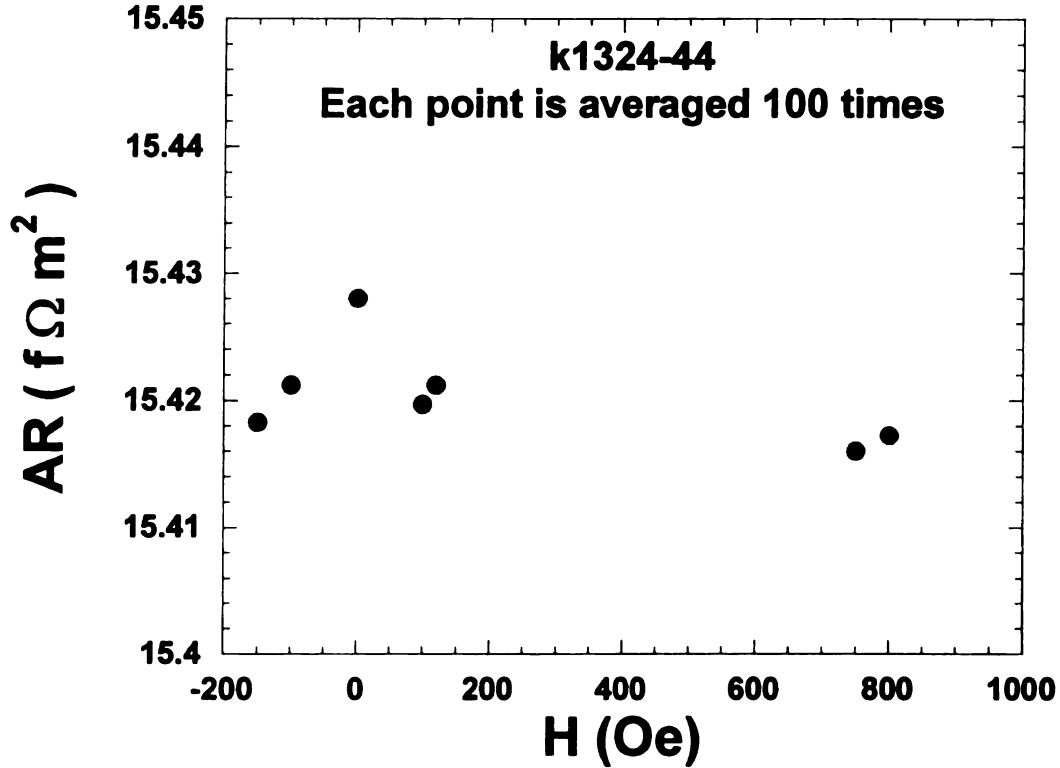


Fig. 6.14. $AR(H)$ for Co(15)/Ru(10)/Co(15). Fields were chosen based on the $AR(H)$ curves of Co(15)/Cu(20)/Co(15) EBSVs. ΔAR is much less than predicted in Fig. 6.13.

6.2 STUDIES OF SPIN-ASYMMETRIES AT INTERFACES USING

Ru.

In this section we describe a way to use Ru in a Py- and Co-based hybrid spin-valve to allow sensitive studies of spin-asymmetric-scattering at certain interfaces. The interfaces we study are Co/S (where S is Cu, initially presumably superconducting by proximity effect with the superconducting Nb), Co/FeMn, Co/Cu, and Co/Ru.

The structures we use have the form Nb/Cu(1)/Py(24)/Cu(20)/Ru(0.6)/Co(2)/X/Nb (Fig. 6.15) where X will be:

- (1) Cu (20)
- (2) FeMn(t)/Cu(20)

- (3) Cu(10)/FeMn(2)/Cu(10)
- (4) Cu(10)/FeMn(2)/Cu(2)/Co(1)/Cu(3)
- (5) Ru(2)/Cu(20)
- (6) Ru(2)/Cu10)/FeMn(2)/Cu(10).

As a reference, to establish the magnitudes of expected deviations of $A\Delta R$ from zero and to choose the magnetic field range needed to achieve AP and P states, we also made a sample with no Ru: Nb/Cu(20)/Py(24)/Cu(20)/Co(2)/Cu(20)/Nb. The AR curve for this sample is shown in Fig. 6.16. The value of $A\Delta R \approx 0.4 \text{ f } \Omega\text{m}^2$ agrees with the 2CSR model predictions. Note that the very different switching fields of the Py layer ($\sim 50 \text{ Oe}$) and the Co layer ($> 400 \text{ Oe}$) give good AP alignment over an extended field range.

As indicated in the introduction to this chapter, the structure above is chosen to give $A\Delta R \cong 0$ in case #1 when X generates no asymmetric scattering. We explain how this occurs using the 2CSR model Eq. 3.3, which we generalize to distinguish between the two different interfaces of the Co layer.

$$A\Delta R = 4 \frac{(\beta_{Py} \rho_{Py}^* t_{Py} + \gamma_{Py/Cu} AR_{Py/Cu}^*)(\beta_{Co} \rho_{Co}^* t_{Co} + \gamma_{Co/Ru} AR_{Co/Ru}^* + \gamma_{Co/X} AR_{Co/X}^*)}{AR_{Nb/Py} + \rho_{Cu} t_{Cu} + \rho_{Py}^* t_{Py} + AR_{Py/Cu}^* + \rho_{Co}^* t_{Co} + AR_{Co/Ru}^* + AR_{Co/X}^* + AR_{Nb/X}}. \quad (6.1)$$

For simplicity, we have assumed that the very thin Ru layer to the left of the Co layer contributes only to the Co/Ru interface (i.e., we neglect any bulk Ru contribution). In practice, this equation has to be modified due to the finite spin-diffusion length in Py and also if X generates spin-memory-loss. But, as such changes do not affect the main point of our argument, which focuses upon the right-hand term in the numerator of Eq. 6.1, we omit them to simplify this discussion. Any quantitative fits to the data can take proper account of all such subtleties.

The numerator of $A\Delta R$ in Eq. 6.1 is the product of two terms. The left-hand term depends only upon the properties of Py and Cu, and is strictly positive because both β_{Py} and $\gamma_{Py/Cu}$ are positive. In the right-hand term, in contrast, $\beta_{Co} \rho_{Co}^* t_{Co}$ is positive, but the interfacial contribution from $\gamma_{Co/Ru} AR_{Co/Ru}^*$ is negative. Using the Ru parameters earlier in Ch. 6, and our standard Co and Co/Cu parameters [5,43], we have chosen the Co thickness, $t_{Co} = 2$ nm, to make $\beta_{Co} \rho_{Co}^* \times (2 \text{ nm}) \approx \gamma_{Co/Ru} AR_{Co/Ru}^*$, thereby making $A\Delta R \cong 0$ for the first two terms on the right. The sign and magnitude of $A\Delta R$ should, thus, be very sensitive to whether γ_A in third term on the right is zero or non-zero.

From prior work [68], we expect this third term to be zero for a simple Co/S interface, where the superconductor S is either Nb alone or Cu turned superconducting by the proximity effect with the neighboring Nb. Said another way, prior studies showed the Co/S interface to be MR inactive ($\gamma_{Co/S} = 0$) [28, 68]. We tested this expectation first.

(1) X = Cu.

If $\gamma_{Co/S} \cong 0$, we expect $A\Delta R \cong 0$ for X = Cu(20), since the Cu should be turned superconducting by proximity effect with the adjacent Nb. Fig.6.17 shows AR for this sample. Because $A\Delta R$ is so small, we no longer took a complete $AR(H)$ hysteresis curve as in Fig. 6.16. Rather we cycled between a few selected fields where we expected to get AP and P states and measured AR at each field 100 times and averaged. Happily, the change in resistance is close to zero ($\leq 0.02 \text{ n}\Omega$). The measuring sequence was as follows. $H = + 700$ Oe (to give a P state), $H = + 200$ Oe expecting the system to remain approximately in the P state, then -60 Oe to give an AP state, -70 Oe to repeat the AP state, -700 to again give the P state, and then a reversed cycle to check for symmetry and

double the data set. The sequence was intended to allow us to correct for the size of any superficial slow parabolic rise of the resistance with magnetic field that occurs for single Nb/F/Nb sandwiches (i.e., that is not GMR related). In the end, the changes in AR were small enough that any such correction is not crucial.

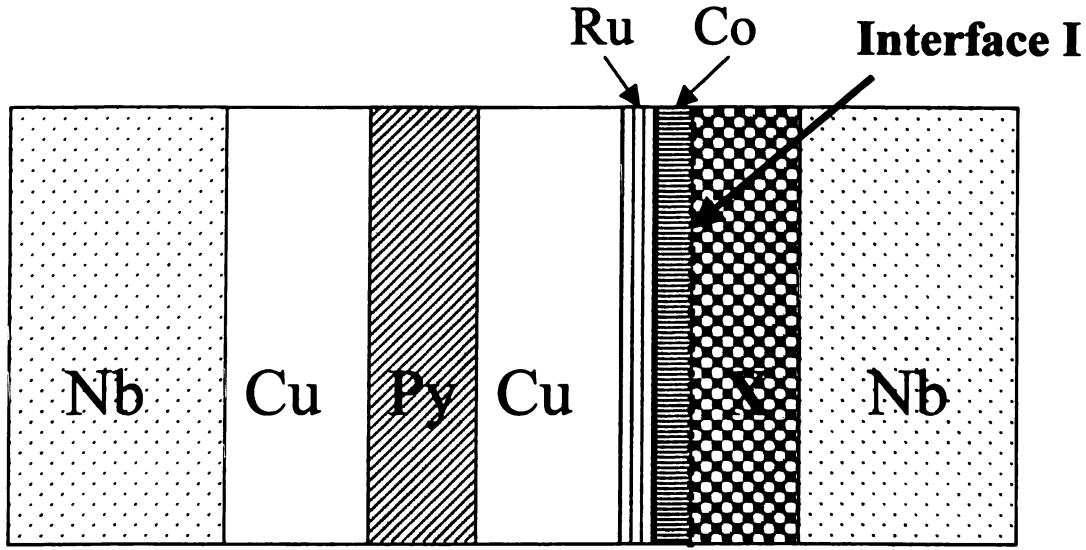


Fig. 6.15. Drawing of the “spin-asymmetry-scattering detector” used to study Co/X interfacial $\chi_{\text{Co/X}}$. If $\chi_{\text{Co/X}} = 0$, then ΔR is also zero. Even small values of $\chi_{\text{Co/X}}$ will give nonzero MR, making the detector quite sensitive.

(2) X = FeMn (1)

We showed elsewhere that 1 nm of FeMn in a non-superconducting environment is enough to almost completely (> 99.9%) ‘quench’ spin-memory. Here we examine what happens if one side of the FeMn is in contact with a ferromagnet (Co) [123,124] and the other is in contact with a superconductor. Fig. 6.18 shows that $\Delta R \cong 0$. The Co/FeMn interface is also not magnetically active (i.e. $\chi_{\text{Co/FeMn}} \cong 0$).

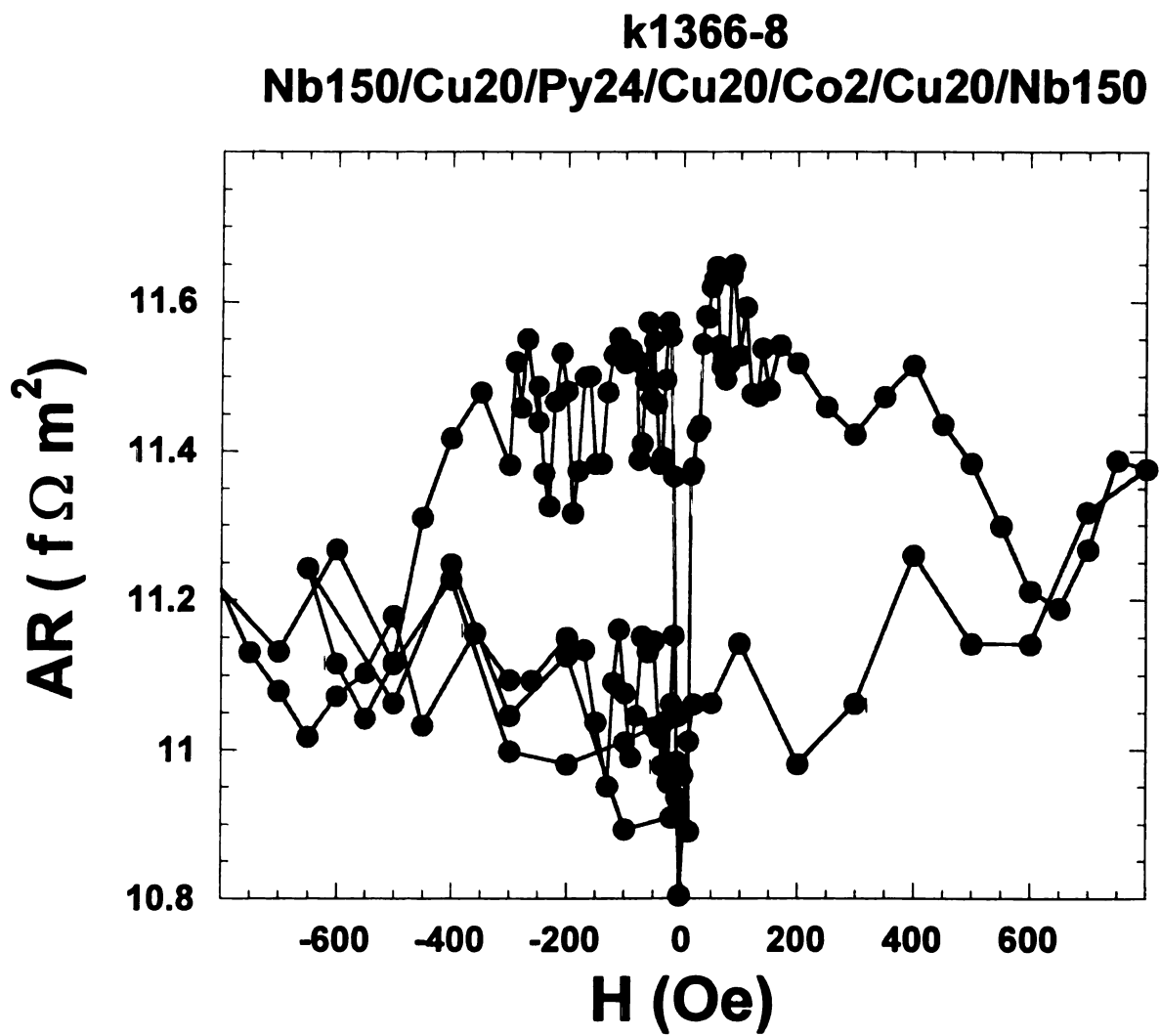


Fig. 6.16. Reference sample: $A\Delta R \approx 0.4 \text{ f}\Omega\text{cm}$, is non-zero when there is no Ru in contact with the Co.

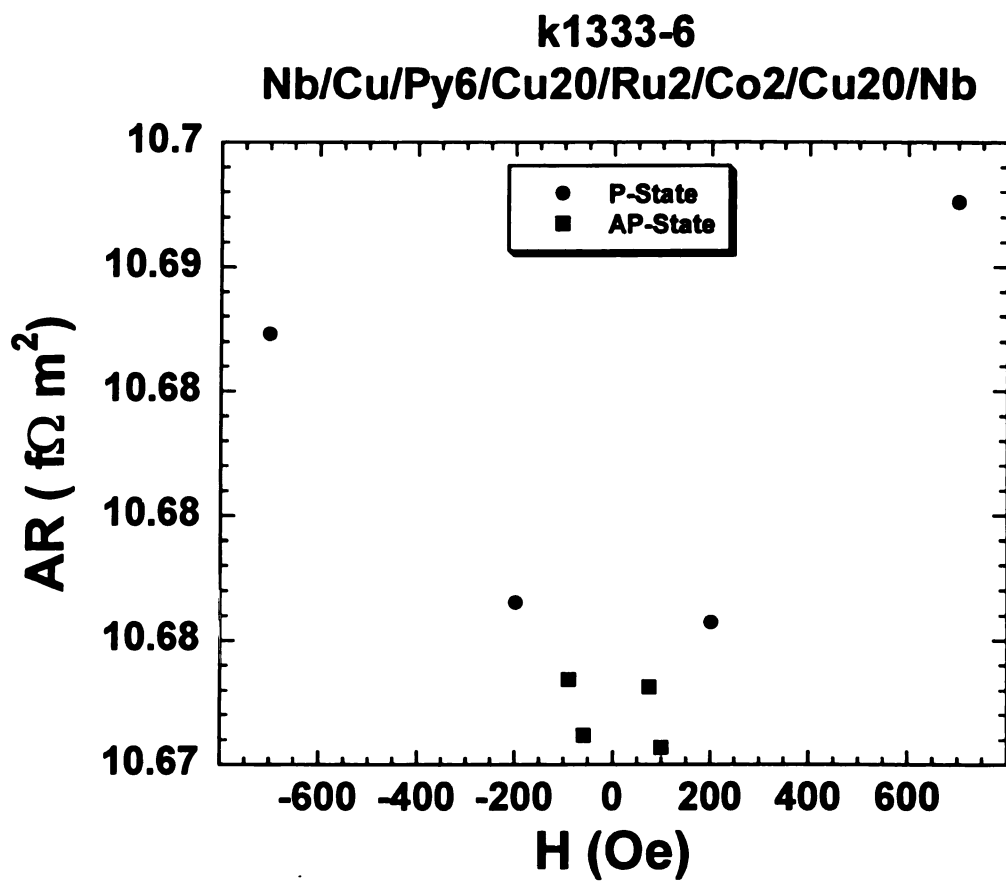


Fig.6.17. $AR(H)$ curve. ΔAR is very small in the curve. Solid boxes are taken for the AP state and solid circle are for the P state.

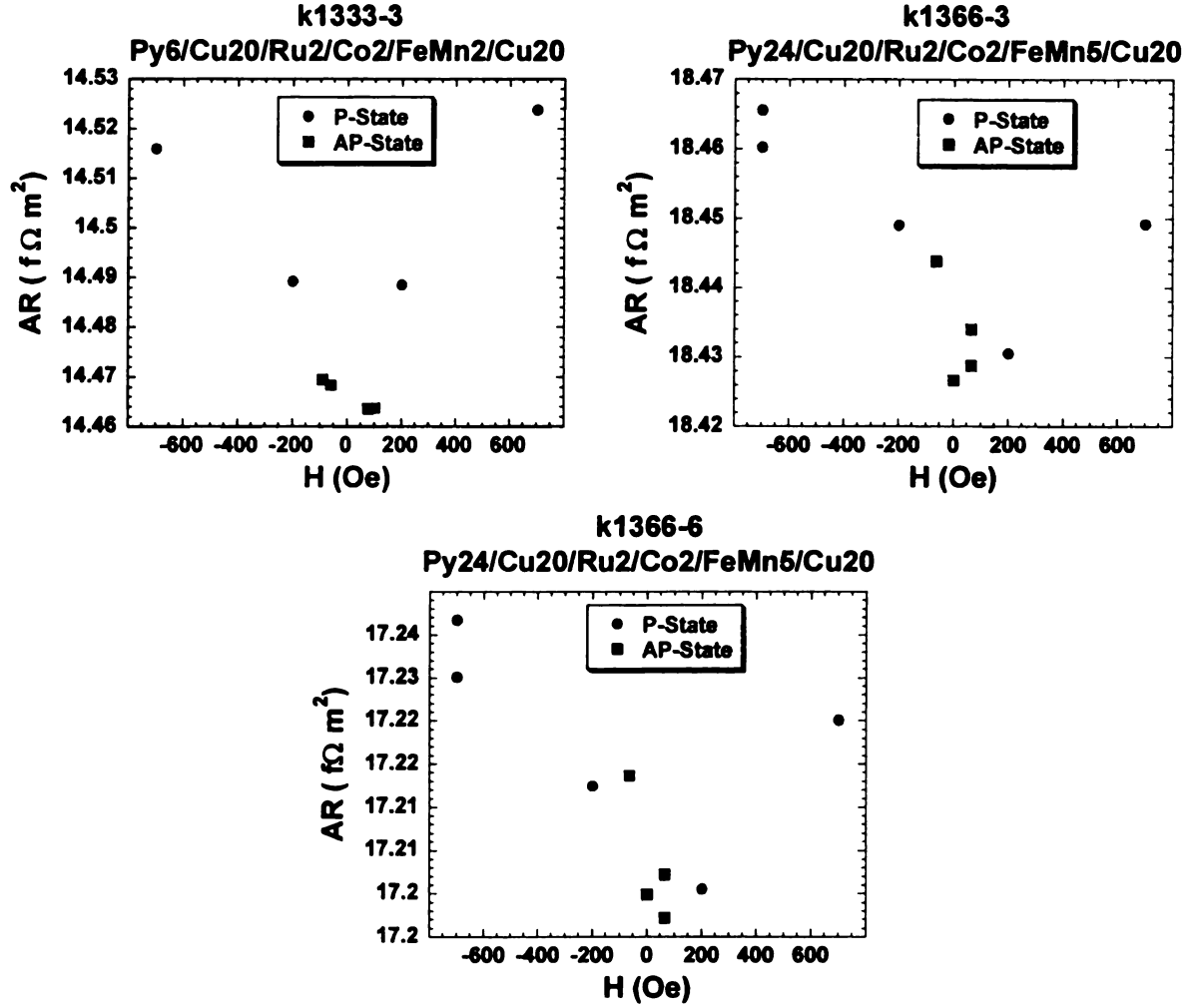


Fig. 6.18. $AR(H)$ for samples with $X = \text{FeMn}(2, 5)$. The values of $A\Delta R$ are very close to zero in this case, just as in Fig. 6.17.

(3) $X = \text{Cu}(10)/\text{FeMn}(2)/\text{Cu}(10)$:

As an antiferromagnet and a strong spin-flipping alloy, FeMn might block Cooper pairs from penetrating to the multilayer (thereby turning the Cu layer between FeMn and Co normal), or destroy the coherence between the electrons and the Andreev reflected holes from the superconductor [128]. In either case, the Co/X interface could become a Co/Cu interface. Fig. 6.19. shows $AR(H)$ for four samples with this structure. Separating the FeMn layer from the Co by Cu changes $A\Delta R$ from being $\cong 0$ to a positive value. Apparently the Co/Cu interface has become GMR active. However, the positive $A\Delta R$ is

much less than predicted by the 2CSR model. This disagreement may be attributed to two different reasons. The spin-memory-loss at the Cu/Ru interface (spin-flip probability $\approx 35\%$), or (even more interesting) possible spin-memory-loss at the Co/Ru interface.

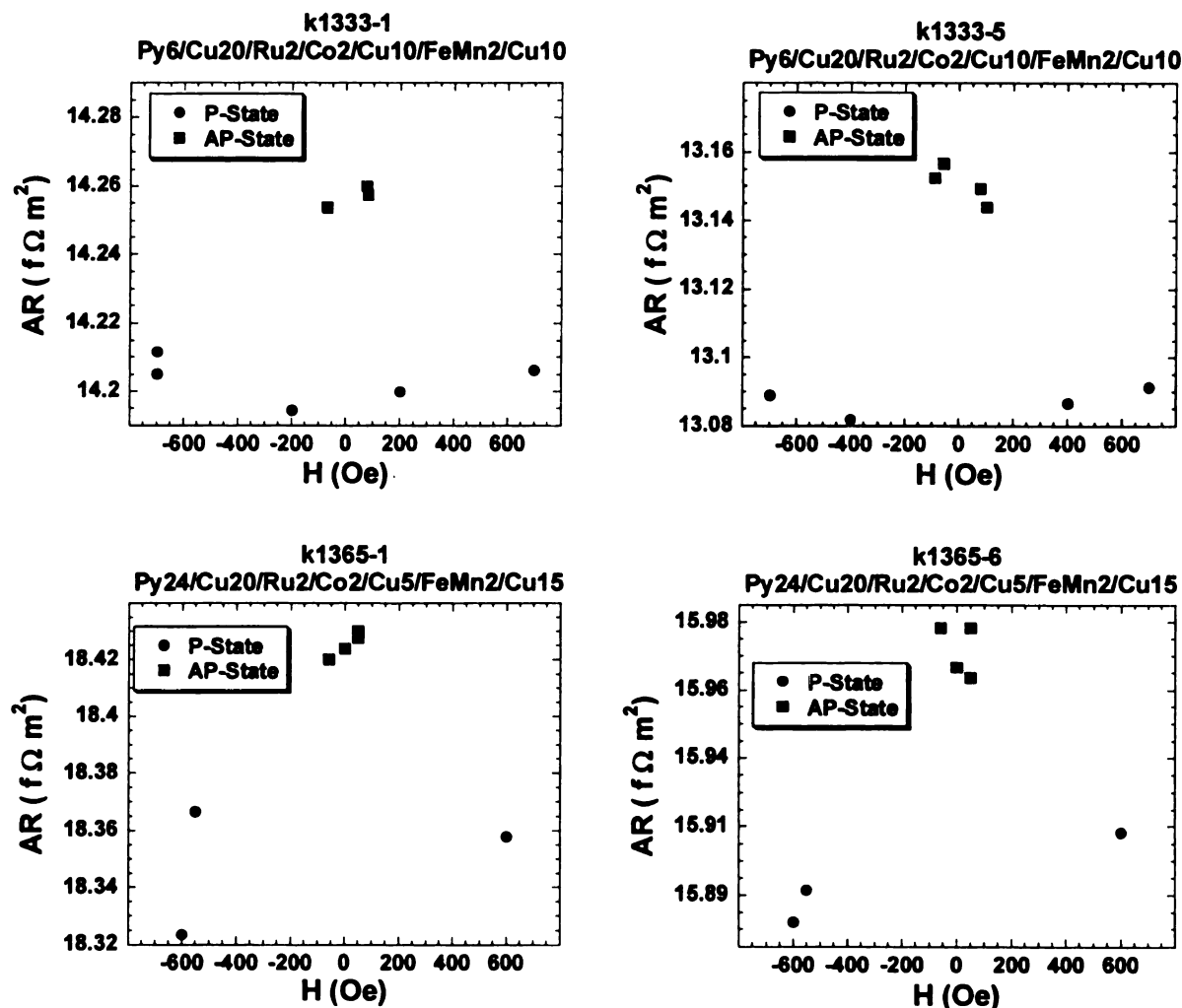


Fig. 6.19. AR for samples with $X = \text{Cu}(10)/\text{FeMn}(1)/\text{Cu}(10)$. $A\Delta R$ is now a non-zero positive value, which indicates that the Co/Cu interface is now contributing to GMR.

(4) $X = \text{Cu}(10)/\text{FeMn}(2)/\text{Cu}(2)/\text{Co}(2)/\text{Cu}(3)$.

We inserted a ferromagnetic Co layer to see if it would enhance the effect of FeMn seen in case (3). The idea was that the Co layer might block the passage of Cooper pairs from the Nb, making everything to its left normal instead of superconducting. As Fig. 6.20 shows, introducing the Co layer added little or nothing to $A\Delta R$ from what had been seen with the FeMn alone.

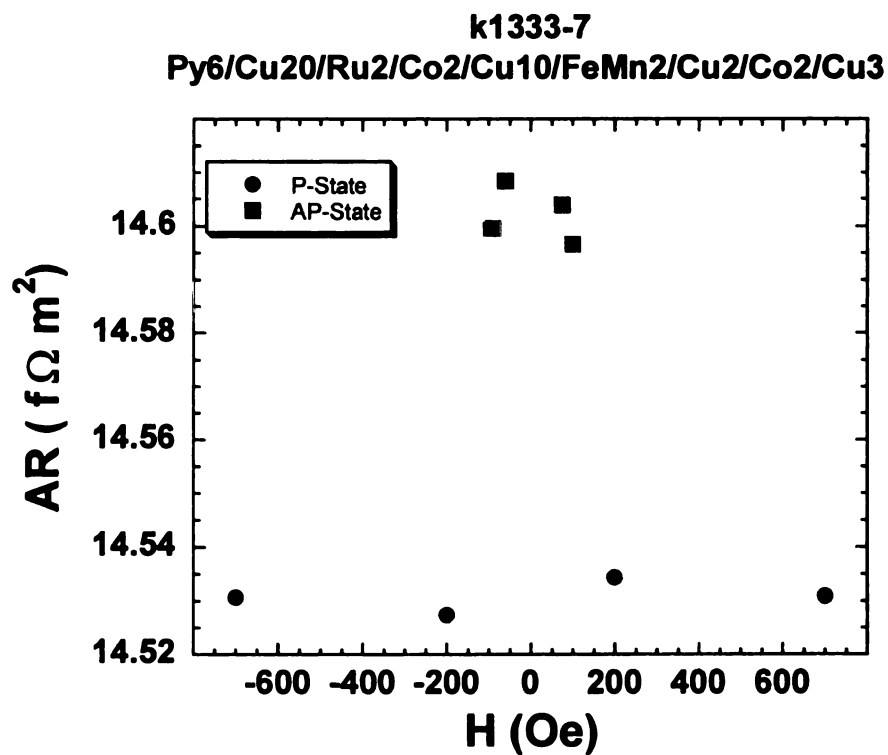
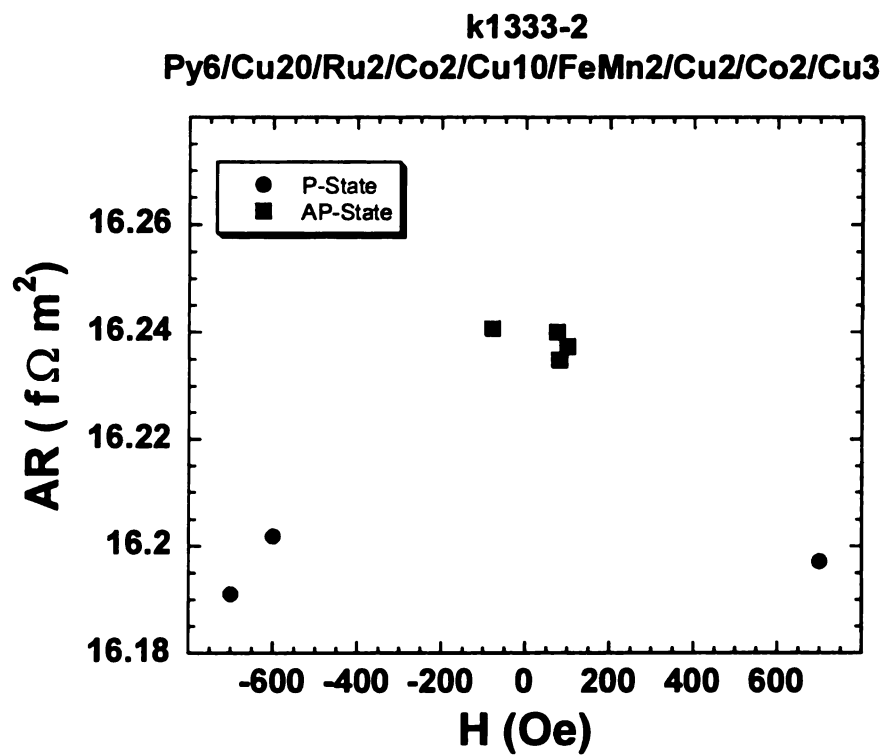


Fig. 6.20. AR for samples with $X = \text{Cu}(10)/\text{FeMn}(2)/\text{Cu}(2)/\text{Co}(2)/\text{Cu}(3)$. The AR values are almost identical to the ones without the Co layer.

(5) $X = \text{Ru}(2)/\text{Cu}(20)$:

If Ru is simply turned superconducting by the proximity effects with the superconducting Nb through the Cu, then this insert should still give $A\Delta R \cong 0$. In contrast, Fig. 6.21 shows a modestly strong negative $A\Delta R$. This behavior seems to contradict our earlier argument that a Co/X interface has no GMR contribution when X is a normal metal in proximity to superconducting Nb. But we saw in Section 6.1 that a Cu/Ru interface causes a significant spin-memory loss $\sim 35\%$. Perhaps the outer Ru/Cu interface could be responsible for making the Co/Ru interface GMR active[129].

(6) $X = \text{Ru}/\text{Cu}/\text{FeMn}/\text{Cu}$

To check the plausibility of our explanation for case 5, we put FeMn into the middle of the Cu outside the Ru layer. Comparing Fig. 6.22 with Fig. 6.21 shows that inserting the FeMn produced almost no change in $A\Delta R$. This suggests that the effect of the Ru layer is similar to the FeMn layer, but with less strength.

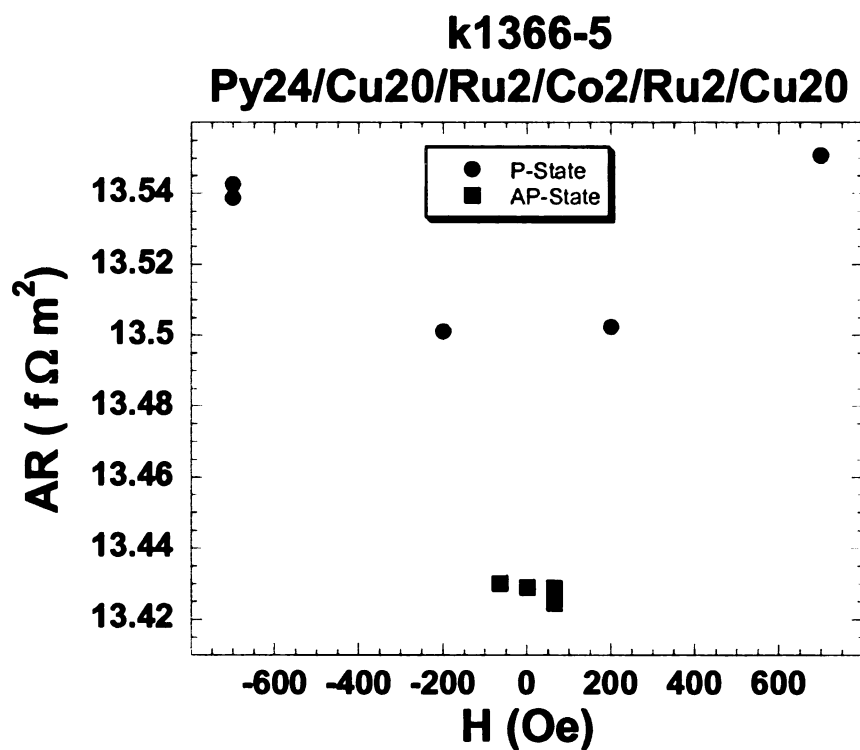
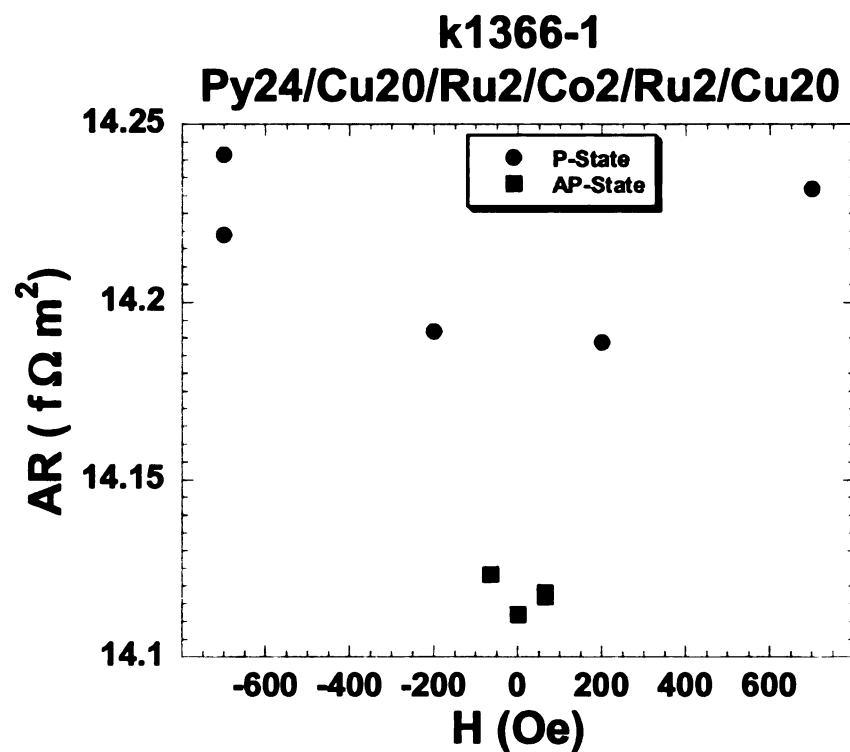


Fig. 6.21. AR for samples with $X = \text{Ru}(2)/\text{Cu}(20)$. Putting the Ru next to Co gives a negative ΔAR indicating that the outer Co/Ru interface is active and contributes to GMR.

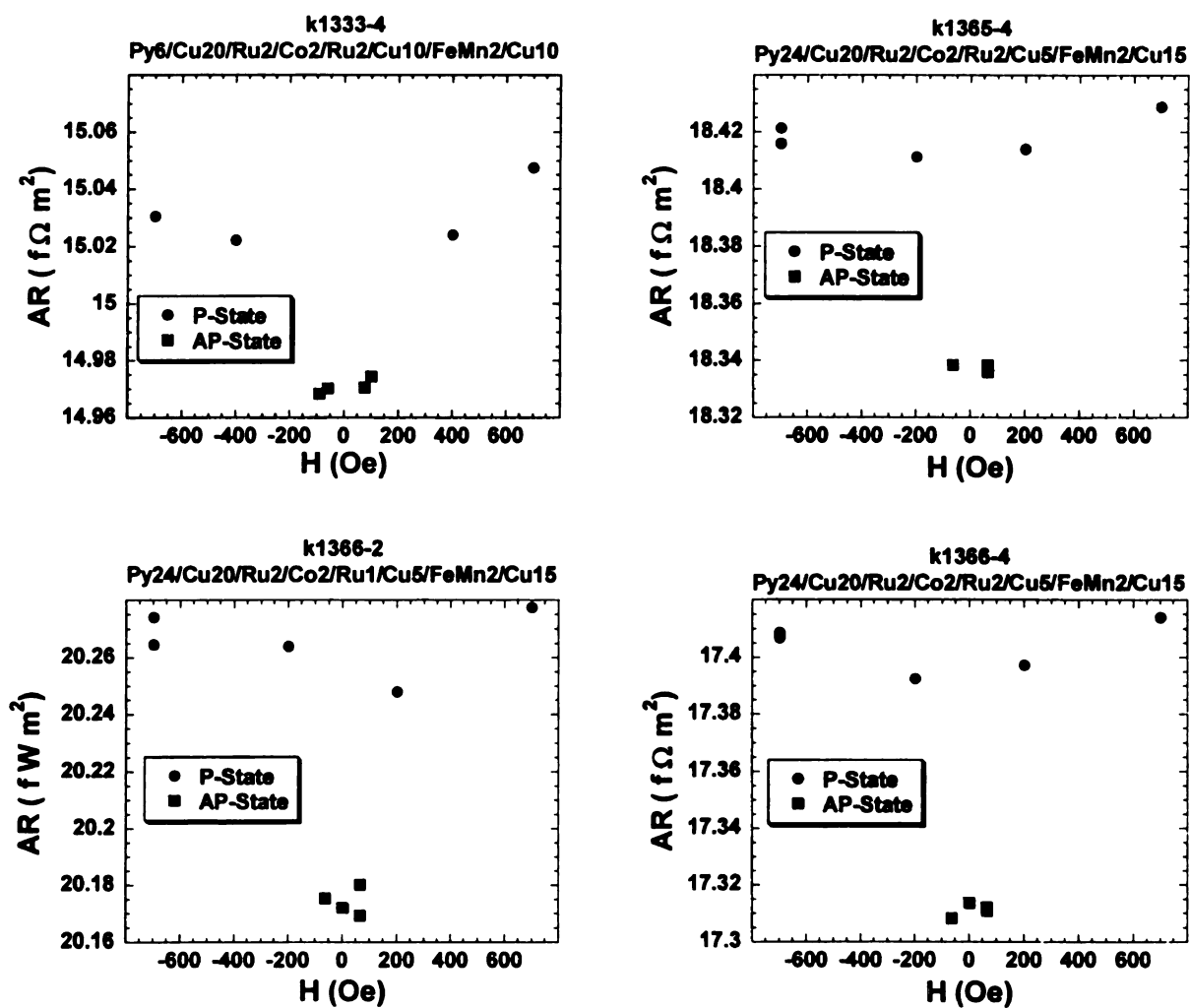


Fig.6.22. AR for samples with $X = Ru(1 \text{ or } 2)/Cu(5 \text{ or } 10)/FeMn(2)/Cu(10 \text{ or } 15)$. Adding the FeMn layer changes AR very slightly from its value without FeMn.

Chapter 7

GMR IN MULTILAYERS WITH SUB-MICRON AREAS

In this short chapter we present some preliminary data on trilayers of Co(30)/Ag(10)/Co(1.5) lithographed into nanopillars. As noted out in Ch. 1, the study of F/N multilayers with diameters ~ 100 nm has attracted attention because of their potential for devices and the new perspectives on physics that they open.

Here we present room temperature (RT) and liquid-helium-temperature measurements of resistance in a few such samples. Only a portion (~ 3 nm) of the ‘thickness’ of bottom Co layer is lithographed to avoid the magnetostatic antiparallel interaction created by free poles when both F-layers are lithographed to the same small area. The pillar has a diamond shape to use shape anisotropy to try to achieve a single magnetic domain in the thin Co layer (See Fig. 2.10). The pillar diameter is ≈ 150 nm. Fig. 7.1 shows the R versus H curve for a Co(30)/Ag(10)/Co(1.5)/Ag(60) sample. The sample resistance of $\sim 1 \Omega$ is measured without the need for the SQUID-based system, enabling measurements at room temperature. Because the peaks are sharp, we can put only a lower bound on the AP state. However, the peaks are reproducible and symmetric. The sharp switching from the AP to the P states at the outer side of each peak indicates that the magnetization of the patterned thin Co layer switches as a single domain (i.e. bulk rotation rather than domain wall formation and motion).

Fig. 7.2 shows the $R(H)$ curve for the same sample at 4.2 K. Note first that the changes in resistance ΔR are almost the same in Figs. 7.1 and 7.2. Second, as expected, the resistance at 4.2 K is less than the room temperature resistance, due to freezing out of the phonon scattering at 4.2K. Third, also as expected, the switching fields are higher at low temperature. Fourth, the $R(H)$ curve at 4.2K is not symmetric around $H = 0$, but is shifted towards negative H values. This asymmetry could be due to exchange bias created by a CoO layer on one or the two of the Co layers. CoO is antiferromagnetic with a Curie temperature less than room temperature, which may be why there is not any exchange bias at room temperature.

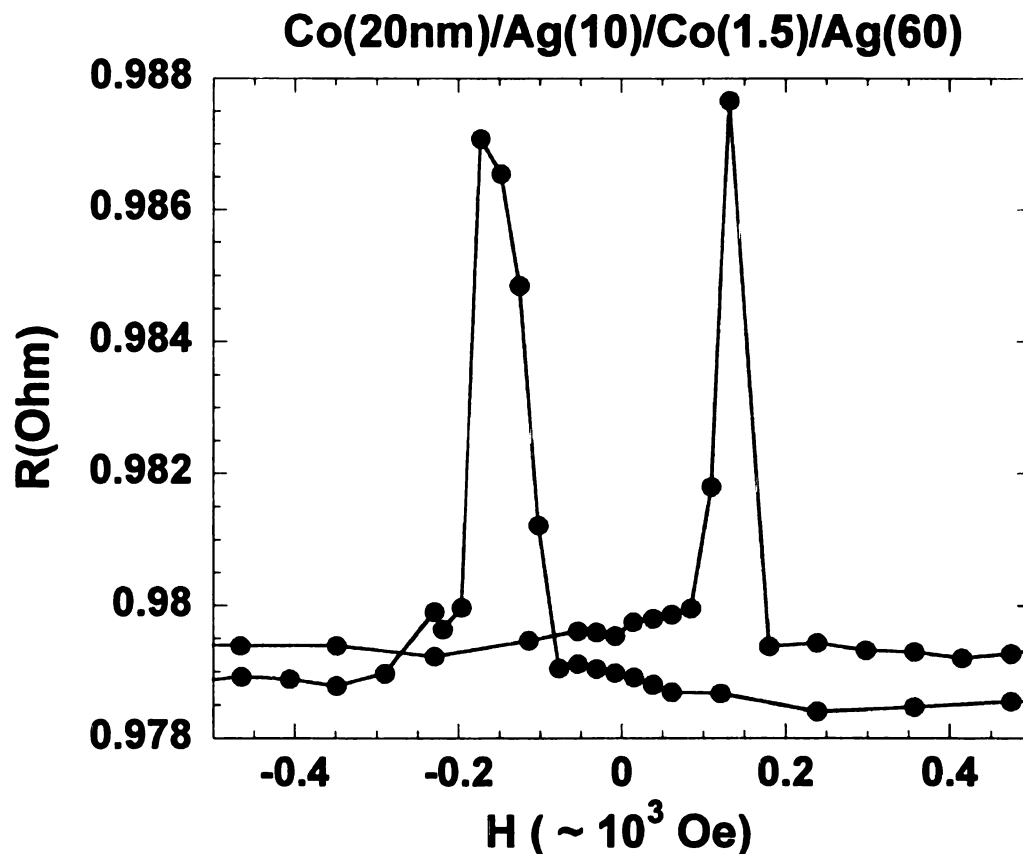


Fig. 7.1. R vs H at room temperature. The sharp drop on the outer side of the two peaks indicates a single-domain magnetization in the lithographed Co layer.

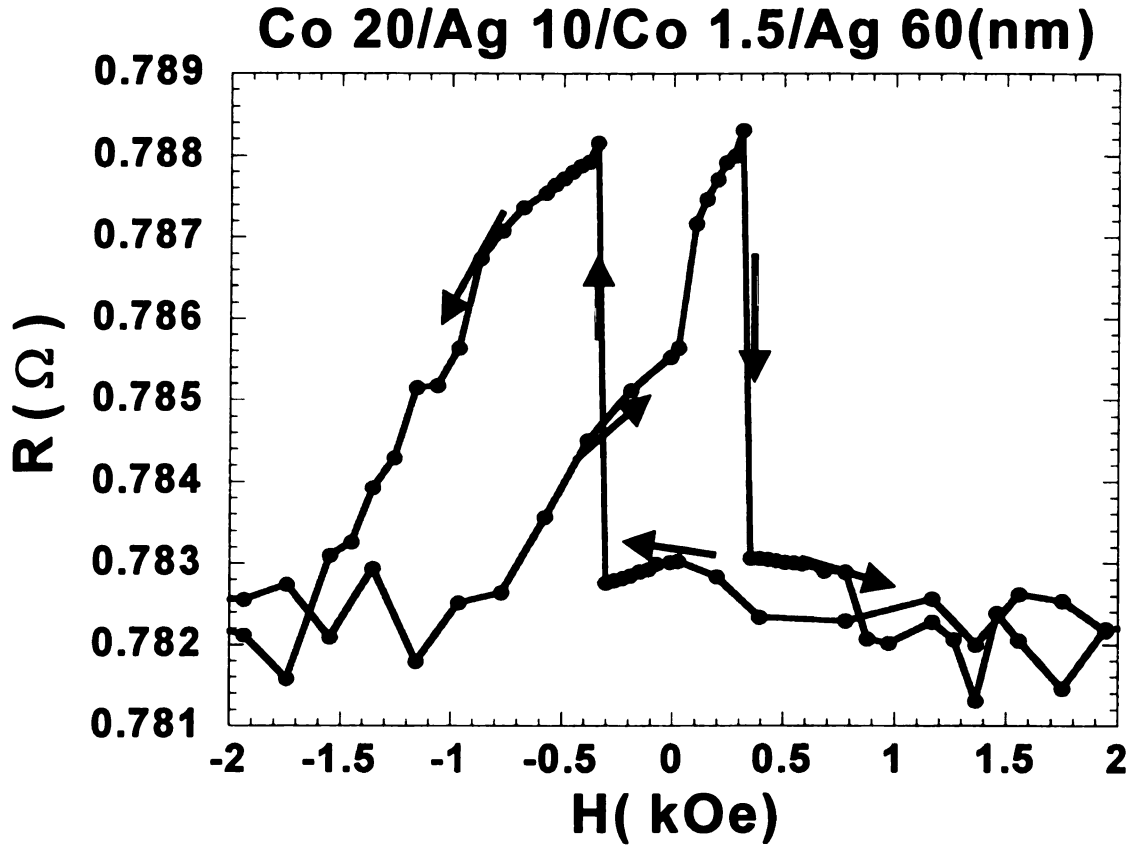


Fig. 7.2. R vs H of the same sample in Fig. 7.1 taken at 4.2 K. The $R(H)$ curve is asymmetric now probably due to the formation of an antiferromagnetic CoO layer on one or both Co layers. Arrows indicate the direction of changing H .

Our current-driven switching data are not as clean as the field-dependent switching shown above. Fig. 7.3 shows the $R(I)$ curve of the same sample at 4.2 K. There is an overall drop in sample resistance with current that we do not yet understand (it might be due to some tunneling through the SiO insulating layer). The most important features of Fig. 7.3 are the two steps on each side of the zero. The jump in resistance, ΔR , in each of those two hysteretic features is equal to the jump in resistance in the $R(H)$ curve. Those equal jumps in R suggest that the source of the changes in R is the same in both cases (i.e. magnetization switching of the thin Co layer). The two hysteretic features are symmetric around zero current, suggesting that the switching is caused by the self-field (induced

magnetic field) of the current as discussed in Ch.1. The two features were reproducible for two different field sweeps.

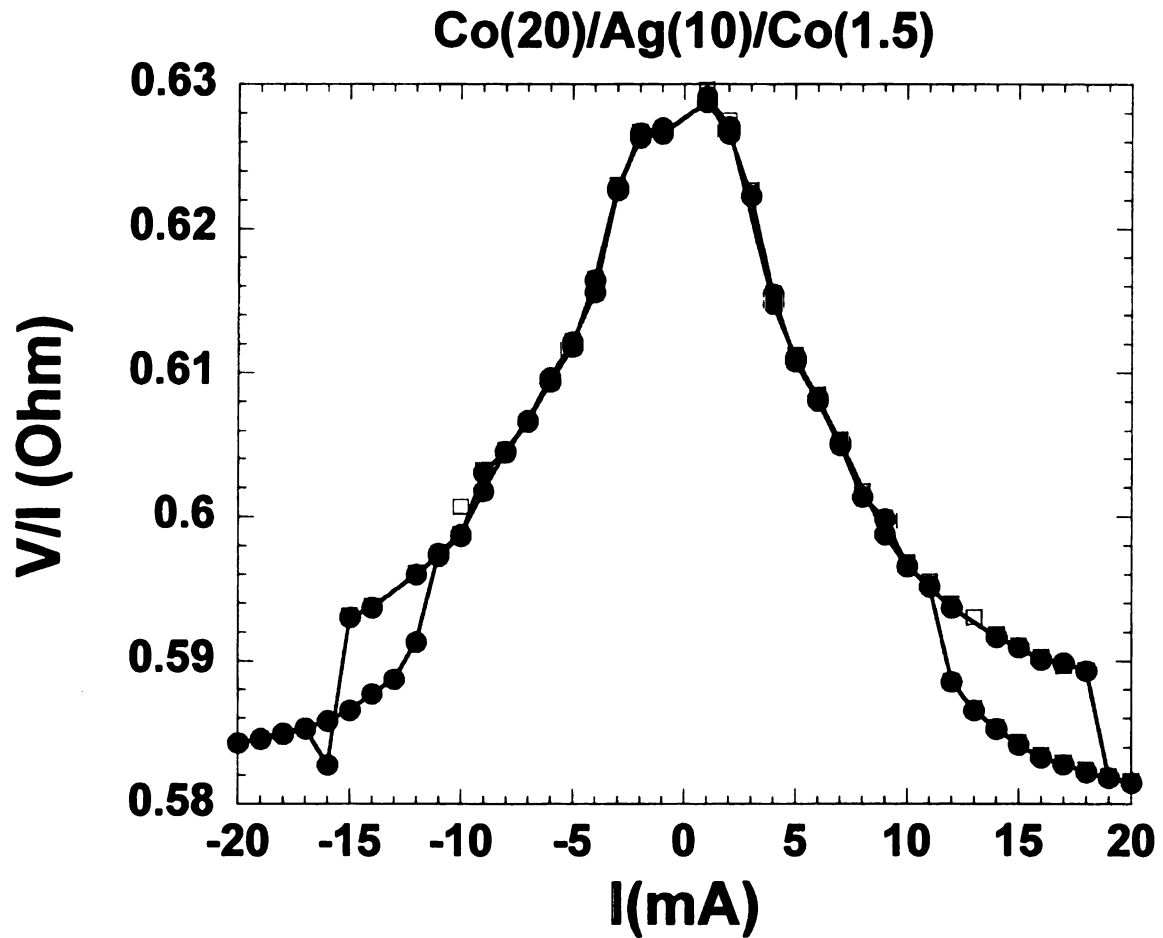


Fig. 7.3. R vs I curve at 4.2 K of the same sample of Figs. 7.1 and 7.2. There is an overall drop of resistance with current. The two hysteretic loops between ± 10 and ± 20 mA are probably due to current-driven switching of the magnetization. Open boxes and filled circles are for two sweeps of current.

Fig. 7.4 shows $R(H)$ at room temperature for a sample with the same structure, but a better AP alignment, which leads to a larger change in resistance. The MR of this sample is about 3%, larger than the value in ref [20] and comparable to the results of [19].

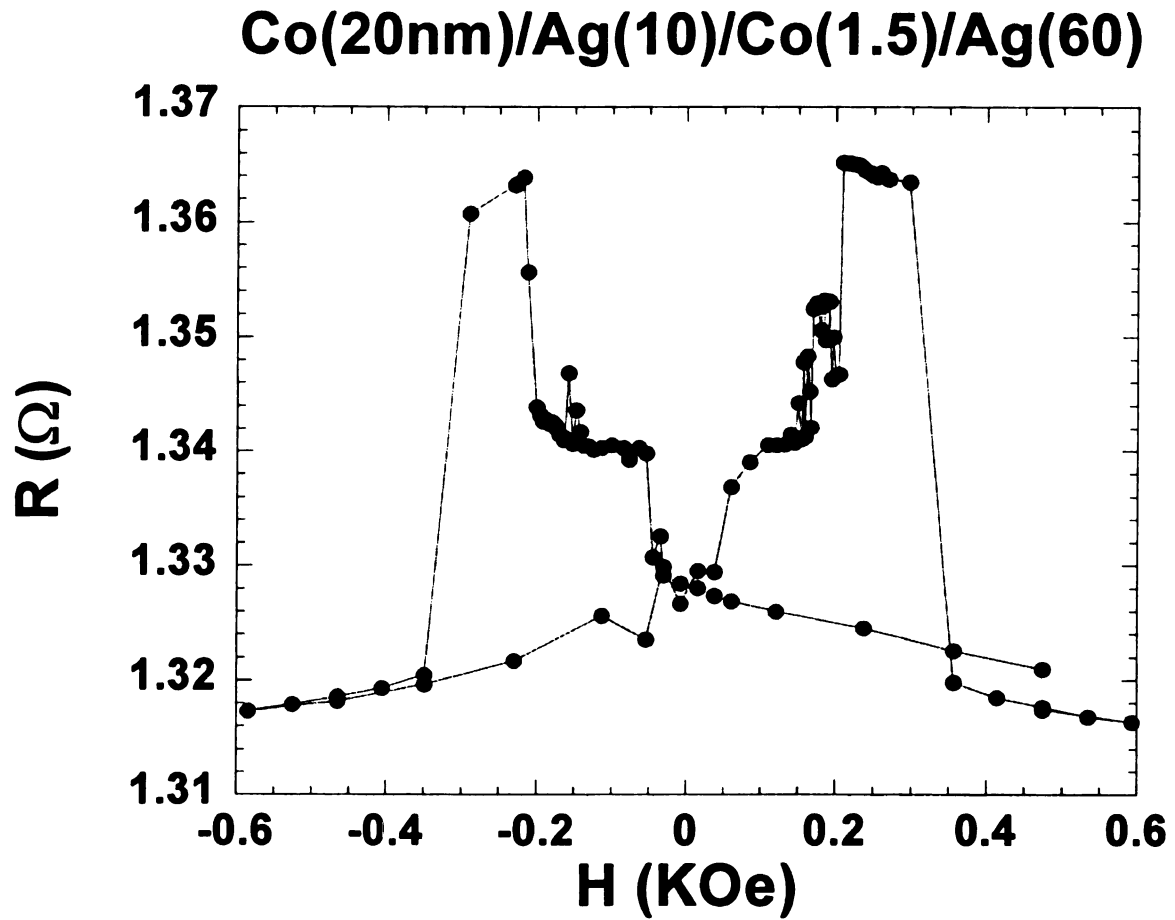


Fig. 7.4 R vs H at room temperature. Relatively flat peaks indicate a good AP alignment. The change in resistance is higher than in Fig. 7.4, and the drop in the resistance after the AP peak is sharp indicating single domain switching of the magnetization.

We conclude that we have successfully prepared a couple of nanopillars with resistances $\sim 1 \Omega$, measured their MRs both at room temperature and 4.2K, and measured $R(I)$ on one sample at 4.2K.

Chapter 8

SUMMARY AND CONCLUSIONS

This dissertation studied several topics in CPP-MR aimed at understanding the physics underlying GMR and trying to improve the CPP-MR to make it more viable for devices. The study included testing of the main theories used in the field, enhancing CPP-MR by three different methods, studying Ru for the CPP-MR, studying spin-asymmetric-scattering at Co interfaces with other metals, and preparing and studying multilayers with submicron dimensions.

First, we made a systematic study searching for mean-free-path effects that were claimed to appear as deviations from the two-current series-resistor (2CSR) or Valet-Fert (VF) models. We have shown in several different ways that the data involved cannot be explained by mean-free-path effects, but are most likely due to spin-memory-loss in the multilayers, especially at ferromagnetic/non-magnetic (F/N) metal interfaces. These results are important both for clarifying the relevant length scales of the CPP-MR and for fundamental understanding of GMR.

Second, we successfully implemented three ideas to enhance the CPP-MR, although none produced effects as large as we had hoped. (A) Alloying of Co with Zr impurities increased the total specific resistance, AR , but not the more important quantity, the change in specific resistance, ΔAR , with magnetic field. (B) Introducing internal interfaces into the Co layers of Co/Cu multilayers significantly increased AR and ΔAR , without substantially increasing the total multilayer thickness. (C) Inserting FeMn inside

the Cu layers separating Co layers from superconducting Nb layers increased AR and $A\Delta R$, especially for multilayers with few repeats.

Third, we determined the CPP-MR parameters of sputtered Ru, an element of present interest for technology. We showed that the Ru spin-diffusion-length is long enough, and its resistivity small enough, that they do not limit the potential of Ru for devices. We also found a negative scattering-anisotropy parameter, γ , at the Co/Ru interface.

Fourth, we presented a new method for high precision measurements of spin-asymmetric-scattering at Co interfaces with other metals, alloys, and superconducting Nb. This method helped us verify some experimental assumptions. The probe also provided some intriguing results about the GMR behavior of Ru in proximity with Nb.

Fifth, we prepared samples with submicron areas and studied the CPP-MRs at both 4.2K and room temperature. Those samples have room temperature resistances $\sim 1\Omega$, and we manipulated their resistances using either an external magnetic field or a direct current.

APPENDIX

MORE MAGNETORESISTANCE DATA ON COZR-BASED MULTILAYERS

This appendix shows additional $AR(H)$ curves for CoZr-based multilayers and two figures comparing AR_{AP} with the best fits to the $A\Delta R$ data. The data presented in the appendix is a completion to data presented in Section 5.2. The $AR(H)$ curves shown here are for CoZr/Ag symmetric EBSVs, FeMn/CoZr/N/Py(t_{Py}) asymmetric EBSVs, and [Py/N/CoZr/N]₁₀/Py hybrid spin valves. Here, N = Cu or Ag and t_{Py} = 6 or 24 nm. Fig. A.1 shows $AR(H)$ curves for Cu/FeMn/CoZr/Cu/Py asymmetric EBSVs. A good AP state is produced for thin CoZr for both Py thicknesses, while the samples with thicker CoZr do not show such a good AP alignment. Based on Fig. A.1 only a lower bound can be put on $A\Delta R$ of the asymmetric samples with thick CoZr.

Figs. A.2 and A.3 show that the AP state is even less controlled in the hybrid samples than in the exchange-biased samples whether using Cu (Fig. A.2) or Ag (Fig. A.3) as the nonmagnetic spacer.

Fig. A.4 shows that the AP state is best produced in the Ag-based symmetric EBSVs . This was also observed in the Cu-based EBSVs (Fig. 5.7). When using Ag however, the pinning is weaker than when using Cu, probably due to changes in the quality of FeMn when grown on Cu from when it is grown on Ag. Finally Fig. A.5 shows the parameters

giving the best fits to the AR data in Ch. 5 give superior estimates to AR_{AP} in [FeMn/CoZr/Cu/Py] asymmetric EBSVs.

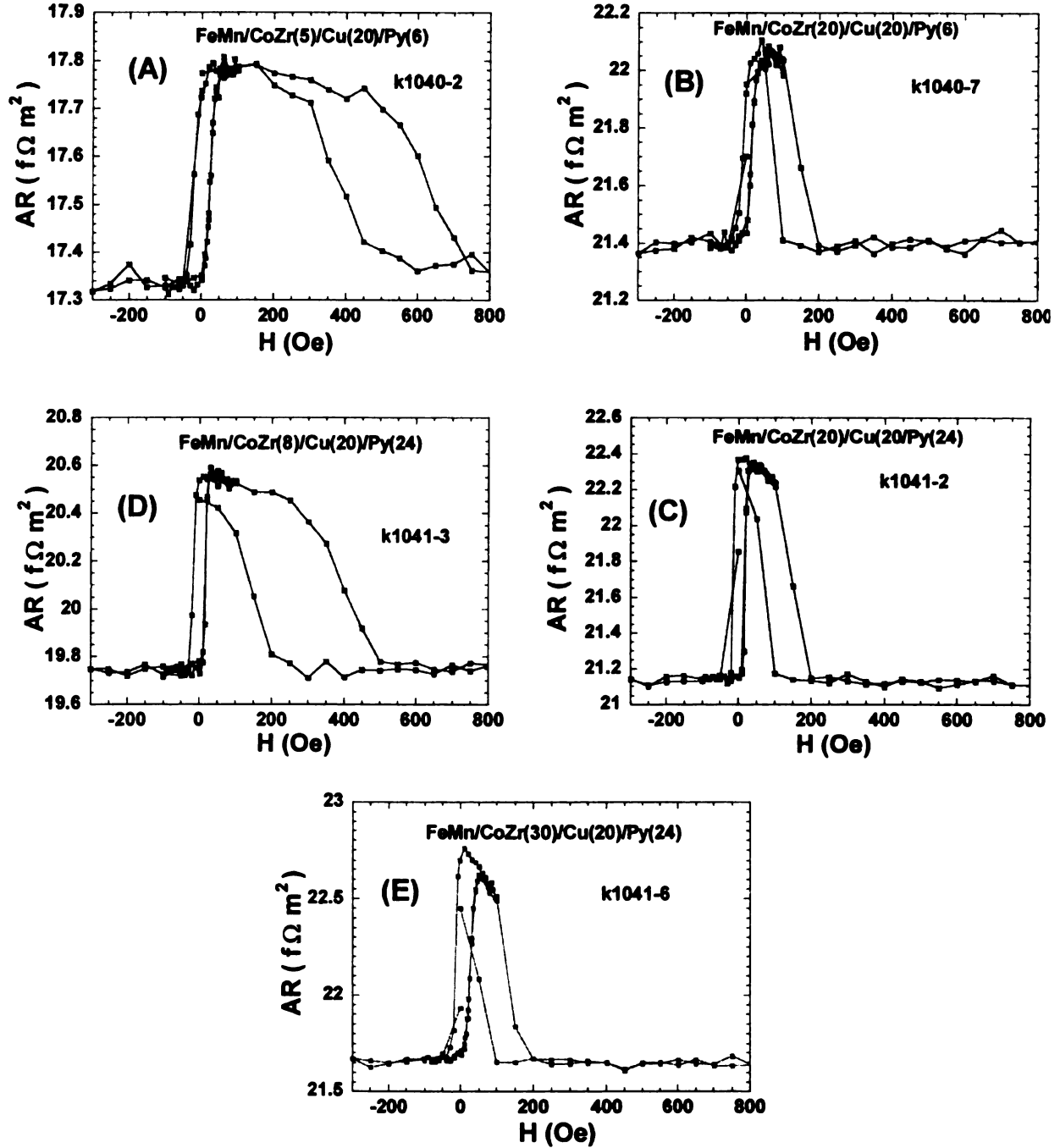


Fig. A.1. AR vs H for CoZr/Cu/Py asymmetric EBSVs. A good AP state is produced in samples with thin CoZr, while the samples with thicker CoZr show a poorer AP alignment. This behavior is common for both $t_{Py} = 6$ or 24 nm. Horizontal scale is the same for all samples to allow direct comparison of the switching fields.

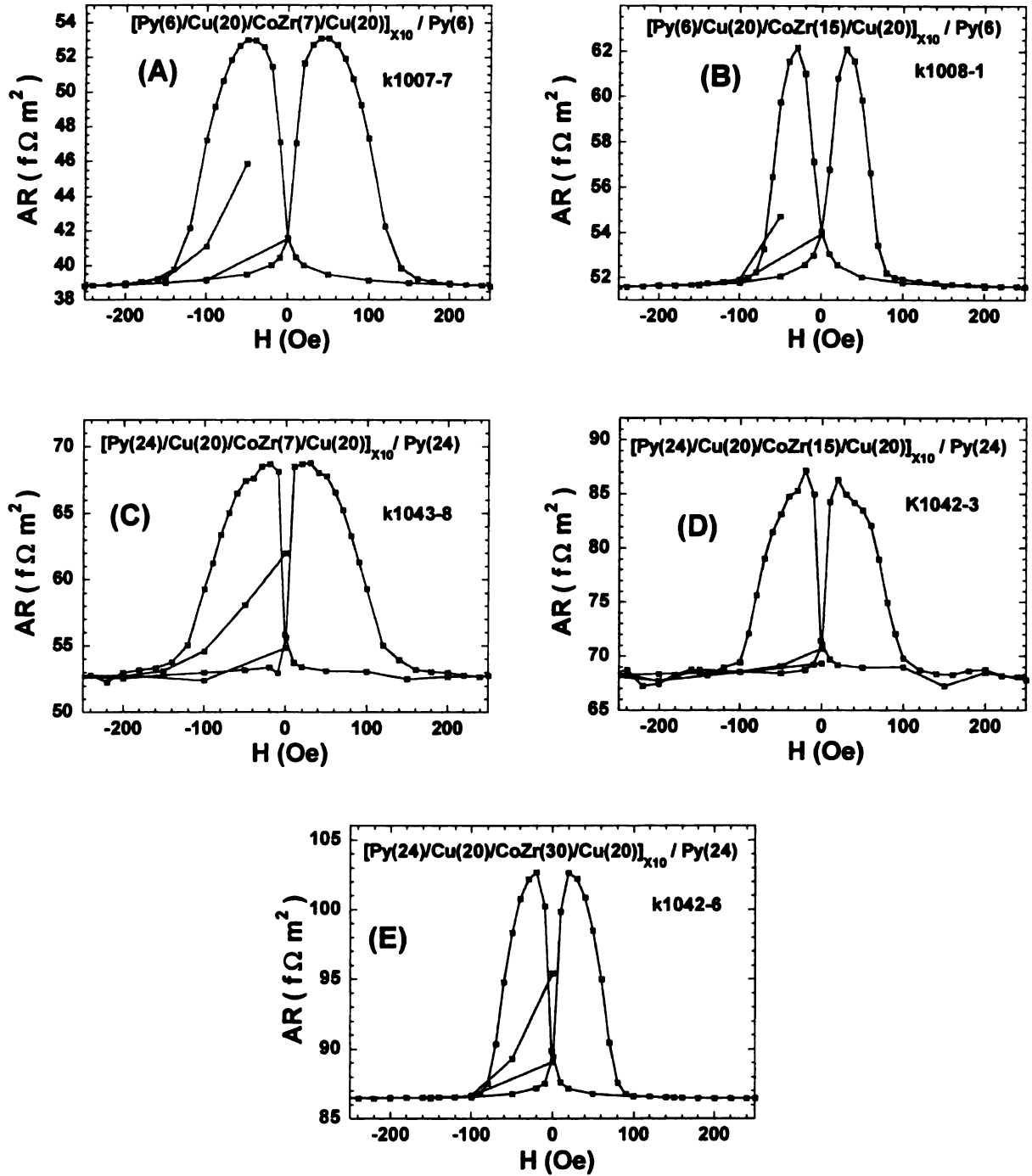


Fig. A.2. AR vs H for CoZr/Cu/Py hybrid spin valves. Curves are sharper for samples with thicker CoZr layers indicating the lack of a good AP alignment.

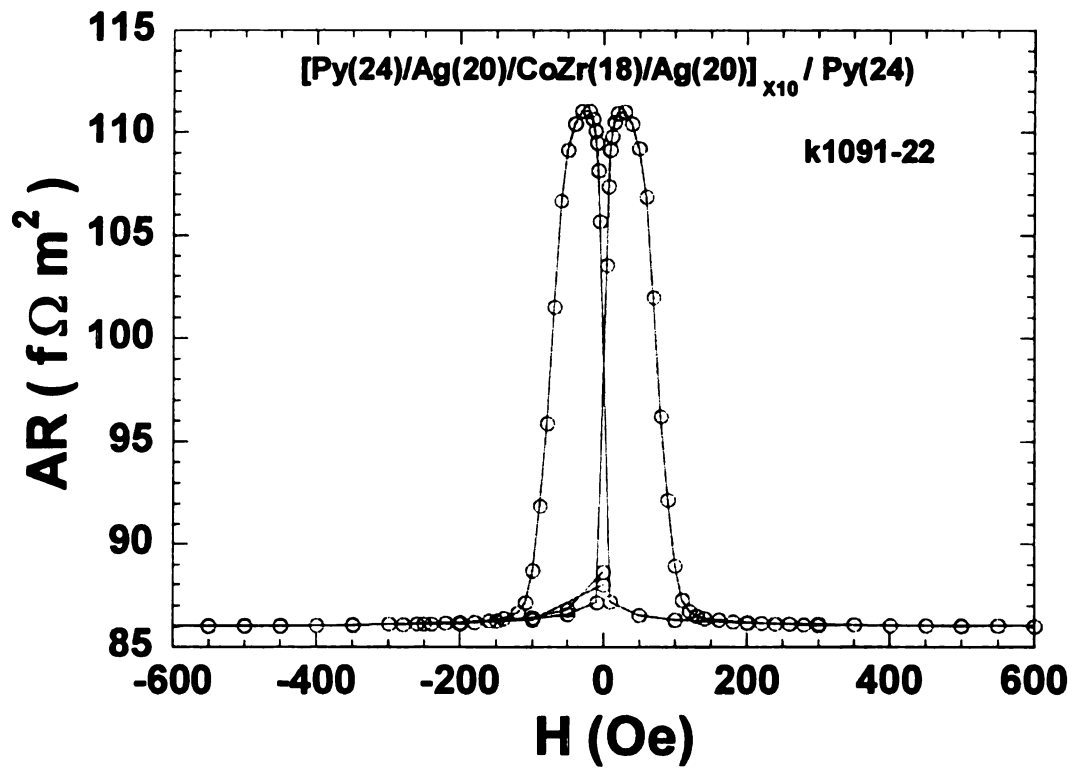
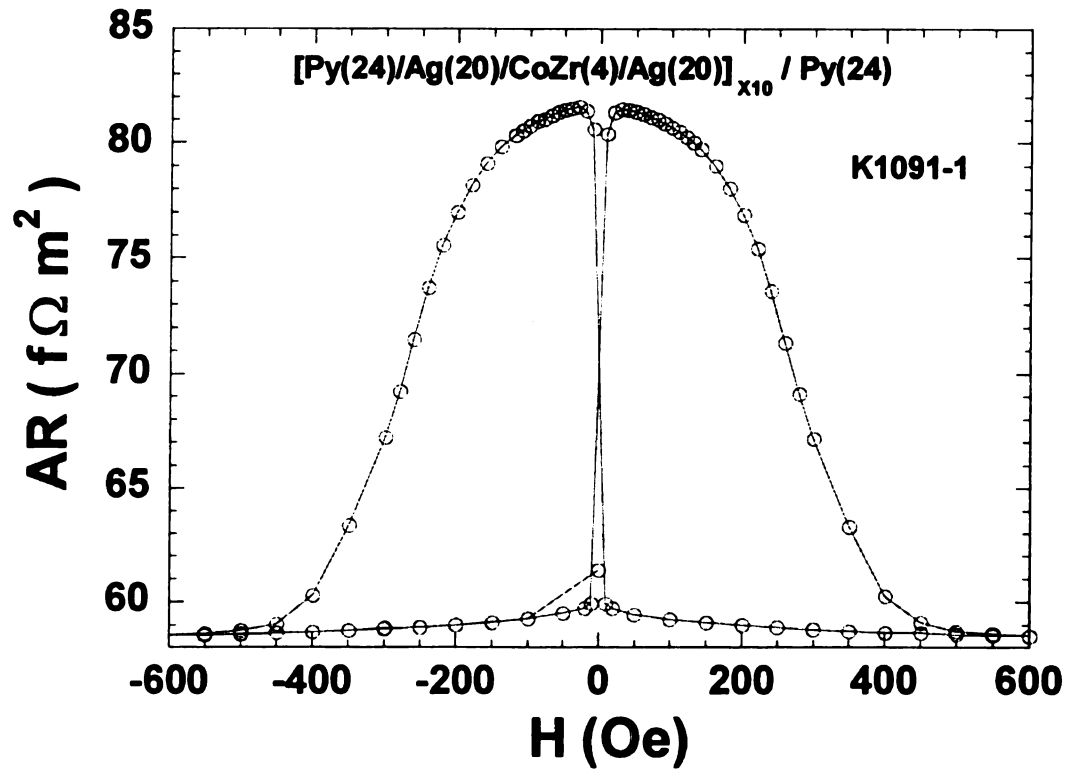


Fig. A.3. AR vs H for CoZr/Ag/Py hybrid spin valves. The AP alignment gets quite uncertain as the CoZr layers become thicker, as seen from the bottom part.

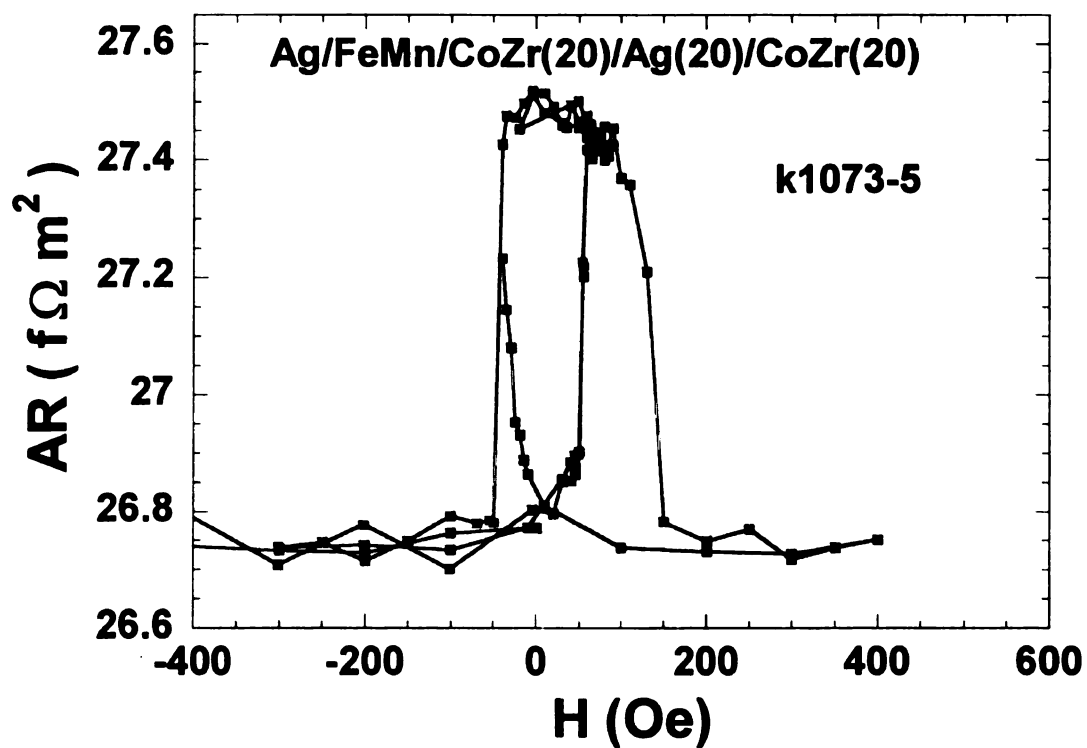
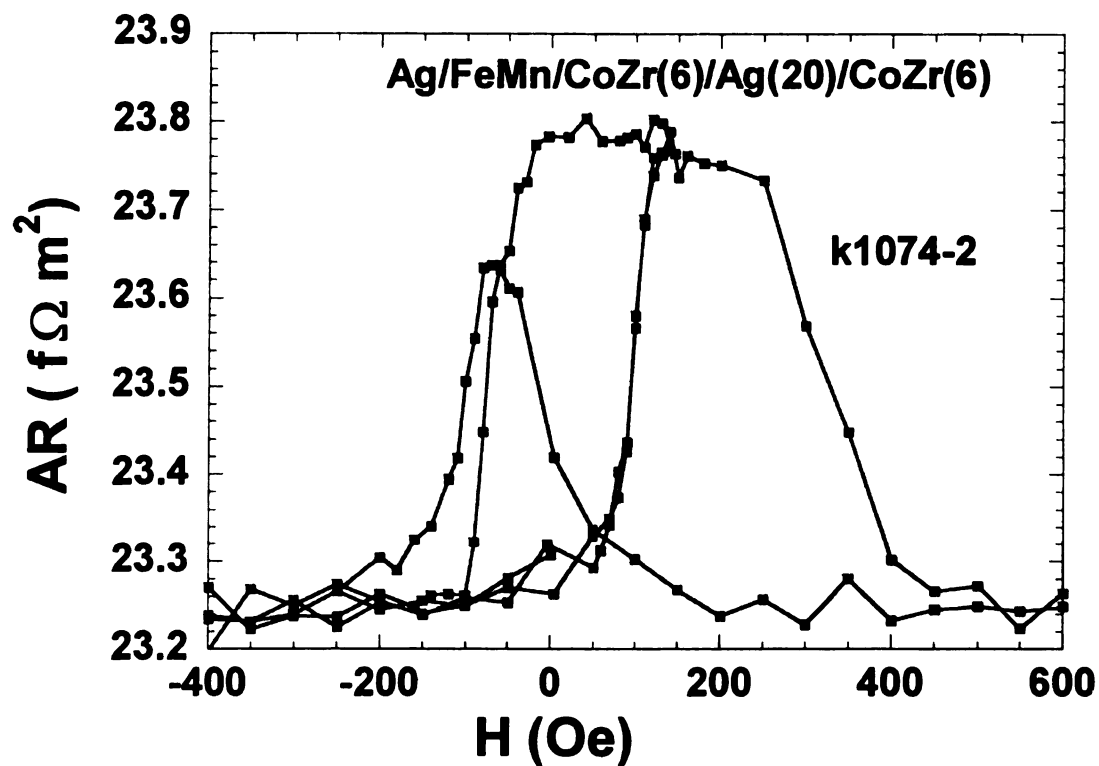


Fig. A.4. AR vs H for CoZr/Ag symmetric EBSVs. Unlike in the asymmetric and the hybrid spin valves that contain Py, the AP alignment seems good for both thin and thick CoZr in the symmetric EBSVs. Pinning is poorer than the Cu-based EBSVs (see Figs. 5.7 and 5.12).

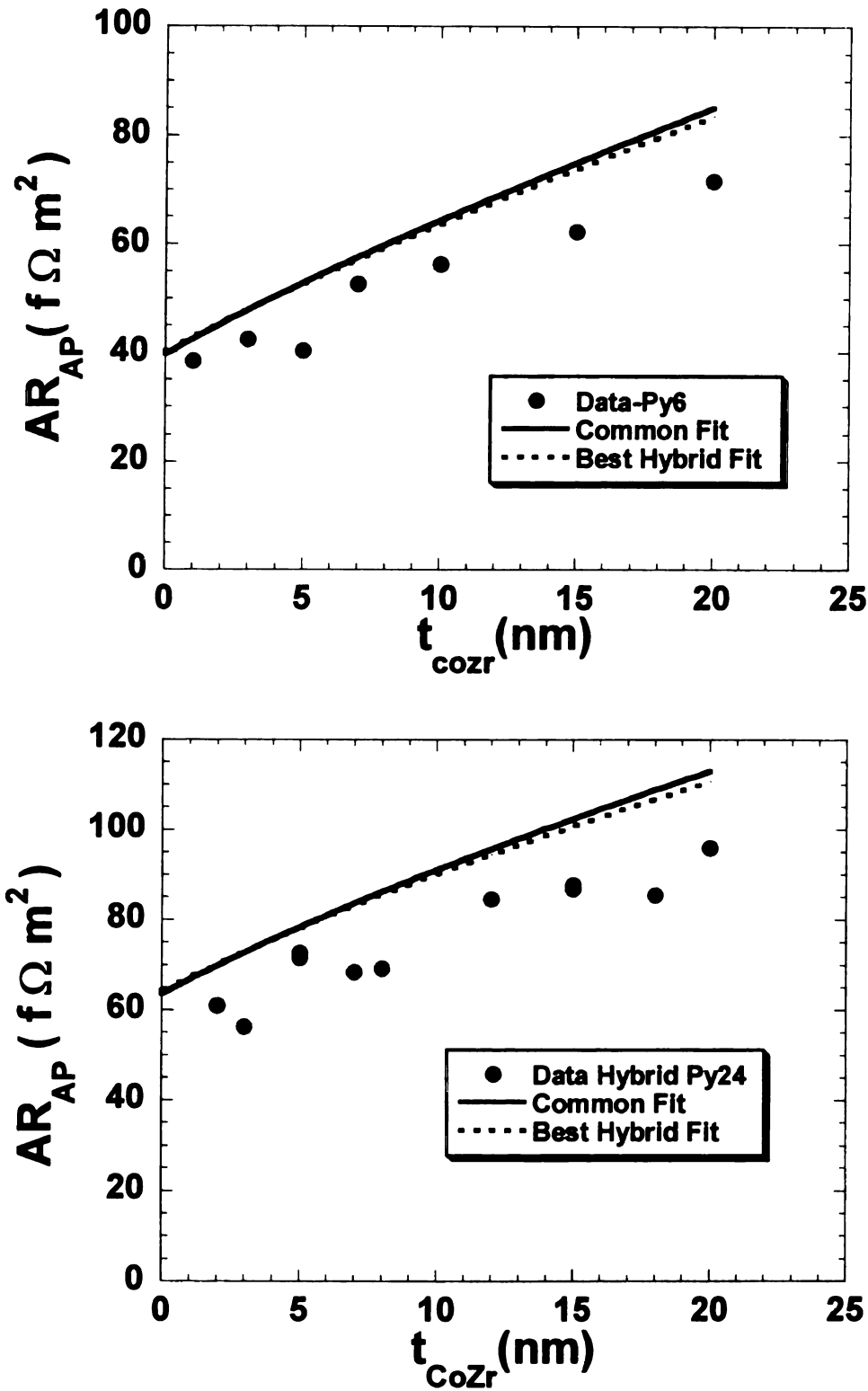


Fig. A.5. AR_{AP} vs t_{CoZr} for $[Py(t_{Py})/Cu(20)/CoZr(t)/Cu(20)]_n/Py(24)$ hybrid multilayers with $t_{Py} = 6$ nm (top) or 24 nm (bottom). The figure shows data, best common fit to all AR s of CoZr samples (solid line), and best fit to AR s of the hybrid samples alone (dotted line). The offset is most likely because the resistivity of Py is less than the value used in the fits.

References

- [1] M.N. Baibich, J.M Broto, A. Fert, F. Nguyen Van Dau, F. Petroff, P. Etienne, G. Creuzet, A. Friederich, and J. Chzelas, Phys. Rev. Lett. **61**, 2472 (1988).
- [2] G. Binash, P. Grunberg, F. Saurenbach, and W. Zinn, Phys. Rev. B **39**, 4828 (1989).
- [3] P.M. Levy, Solid State Physics, H. Ehrenreich and D. Turnbull, Eds., Academic Press, NY, **47**, 367 (1994).
- [4] M.A.M. Gijs and G.E.W. Bauer, Adv. in Phys. **46**, 285 (1997).
- [5] J. Bass and W.P. Pratt Jr., J. Magn. Magn. Mater. **200**, 274 (1999).
- [6] J.-Ph. Ansermet, J. Phys.: Condens. Matter **10** 223 (1998).
- [7] A. Barthelemy, A. Fert, R. Morel, and L. Steren, Physics World **7**, 34 (1994).
- [8] See IBM web page--www.ibm.com.
- [9] See Seagate web page--www.seagate.com.
- [10] P. Grunberg, R. Schreiber, Y. Pang, M.B. Brodsky, and H. Sowers, Phys. Rev. Lett. **57**, 2442 (1986).
- [11] D. H. Mosca, F. Petroff, A. Fert, P. A. Schroeder, W. P. Pratt, Jr., R. Loloee, and S. Lequien, J. Magn. Magn. Mater. **94** L1 (1991).
- [12] S.S. Parkin, N. More, and K.P. Roche, Phys. Rev. Lett. **64**, 2304 (1990).
- [13] S.S. Parkin, R. Bhadra, and K.P. Roche, Phys. Rev. Lett. **66**, 2152 (1991).
- [14] M.D. Stiles, J. Magn. Magn. Mater. **200**, 322 (1999).
- [15] J. Slonczewski, J. Magn. Magn. Mater. **159**, L1 (1996).
- [16] L. Berger, Phys. Rev. B **54**, 9353 (1996).
- [17] M. Tsoi, A.G.M. Jansen, J. Bass, W.-C. Chiang, M. Seck, V. Tsoi, and P. Wyder, Phys. Rev. Lett. **80**, 4281 (1998).
- [18] M. Tsoi, A. Jansen, J. Bass, W.C. Chiang, V. Tsoi, and P. Wyder, Nature (London) **406**, 6791 (2000).
- [19] E.B. Myers, D.C. Ralph, J.A. Katine, R.N. Louie, and R.A. Buhrman, Science **285**, 867 (1999).

- [20] J. Grollier, V. Cros, A. Hamzic, J.M. George, H. Jaffres, A. Fert, G. Faini, J. Ben Youssef, and H. Le Gall, *Appl. Phys. Lett.* **78**, 3663 (2001).
- [21] K. Bussmann, G.A. Prinz, R. Bass, J.-G Zhu, *Appl. Phys. Lett.* **78**, 2029 (2001).
- [22] Gary A. Prinz, *Phys. Today*, **48**, 58 (1995).
- [23] Gary A. Prinz, *Science*, **282**, 1660 (1998).
- [24] *R&D Magazine*, page 14, July 1999.
- [25] W.P. Pratt Jr., S.F. Lee, J.M. Slaughter, R. Loloee, P.A. Schroeder, and J. Bass, *Phys. Rev. Lett.* **66**, 3060 (1991).
- [26] S. Zhang, and P.M. Levy, *J. Appl. Phys.* **69**, 4786 (1991).
- [27] S.F. Lee, W.P. Pratt, Jr., Q. Yang, P. Holoday, R. Loloee, P.A. Schroeder, and J. Bass, *J. Magn. Magn. Mater.* **118**, L1 (1993).
- [28] S.F. Lee, Q. Yang, P. Holoday, R. Loloee, J.H. Hetherington, S. Mahmood, B. Ikegami, K. Vigen, L.L. Henry, P.A. Schroeder, W.P. Pratt, Jr., and J. Bass, *Phys. Rev. B* **52**, 15426 (1995).
- [29] C. Fierz, S.F. Lee, J. Bass, W.P. Pratt Jr., and P.A. Schroeder, *J. Phys. Cond. Matt.* **2**, 9701 (1990).
- [30] M.A.M. Gijs, S.K. Lenczowski, and J.B. Giesbers, *Phys. Rev. Lett.* **70**, 3343 (1993).
- [31] S.K. Lenczowski, et al., *J. Appl. Phys.* **75**, 5154 (1994).
- [32] J. Spallas, Y. Huai, S. Vernon, B. Fuchs, B. Law, D.R. Kania, D. Kroes, M. Thomas, D. Okane, Z.C.H. Tan, *IEEE Trans. Magn.*, **32**, 4710 (1996).
- [33] W. Vavra, S.F. Cheng, Antia Fink, J.J. Krebs, and G.A. Prinz, *Appl. Phys. Lett.* **66**, 2579 (1995).
- [34] A. Blondel, J.P. Meier, B. Doudin, and J.-Ph Ansermet, *Appl. Phys. Lett.* **65**, 3019 (1994).
- [35] B. Doudin, A. Blondel, and J.-Ph. Ansermet, *J. Appl. Phys.* **79**, 6090 (1996).
- [36] L. Piraux, J.M. George, J.F. Despres, C. Leroy, E. Ferain, R. Legras, K. Ounadjela, and A. Fert, *Appl. Phys. Lett.* **65**, 2484 (1994).

- [37] L. Piraux, S. Dubois, C. Marchal, J.M. Beuken, L. Filipozzi, J.F Despres, K. Ounadjela, and A. Fert, *J. Magn. Magn. Mater.* **156**, 317 (1996).
- [38] K. Liu, K. Nagodawithana, P.C. Searson, and C.L. Chhien, *Phys. Rev. B* **51**, 7381 (1995).
- [39] A. Fert and L. Piraux, *J. Magn. Magn. Mater.* **200**, 338 (1999).
- [40] T. Ono and T. Shinjo, *J. Phys. Soc. Jpn.* **64**, 363 (1994).
- [41] P.M. Levy, S. Zhang, T. Ono, and T. Shinjo, *Phys. Rev. B* **52**, 16, 049 (1995).
- [42] M.A.M. Gijs, M.T. Johnson, A. Reinders, P.E. Huisman, R.J.M. van de Veedronk, S.K.J. Lenczowski, and R.M.J. van Gansewinkel, *Appl. Phys. Lett.* **66**, 1839 (1995).
- [43] J. Bass, W.P. Pratt, and P.A. Schroeder, *Comments Cond. Matt. Phys.* **18**, 223 (1998).
- [44] Shang-Fan Lee, Ph.D. Dissertation, Michigan State University, 1994.
- [45] Qing Yang, Ph.D. Dissertation, Michigan State University, 1995.
- [46] I.A. Campbell and A. Fert, E.P. Wohlfarth (Ed.), *Ferromagnetic materials*, Vol. 3, North-Holland, Amsterdam, 1982, p. 751, Chapter 9.
- [47] T. Valet and A. Fert, *Phys. Rev. B* **48**, 7099 (1993).
- [48] P.C. van Son, H. van Kempen, and P. Wyder, *Phys. Rev. Lett.* **58**, 2271 (1987).
- [49] M. Johnson and R.H. Silsbee, *Phys. Rev. B* **37**, 5312 (1988).
- [50] Q. Yang, P. Holoday, S.-F. Lee, L.L. Henry, R. Loloee, P.A. Schroeder, W.P. Pratt Jr., and J. Bass, *Phys. Rev. Lett.* **72**, 3274 (1994).
- [51] J. Noguès and Ivan K. Schuller, *J. Magn. Magn. Mater.* **192**, 203 (1999).
- [52] B. Dieny, V. Speriosu, S. Metin, S.S.P. Parkin, B.A. Gurney, P. Baumgart, and D.R. Wilhoit, *J. Appl. Phys.* **69**, 4774 (1991).
- [53] K. Nagasaka, Y. Seyama, L. Varga, Y. Shimizu, and A. Tanaka, *J. Appl. Phys.* **89**, 6943 (2001).
- [54] Luc Thomas, Mahesh G. Samant, and Stuart S.P. Parkin, *Phys. Rev. Lett.* **84**, 1816 (2000).

- [55] Gary A. Prinz, *J. Magn. Magn. Mater.* **200**, 57 (1999).
- [56] K.J. Kirk, *Contemporary Physics* **41**, 61 (2000).
- [57] J.M. Daughton, J. Brown, E. Chen, R. Beech, A. Pohm, and W. Kude, *IEEE Trans. Magn.* **30**, 4608 (1994).
- [58] Robert Slater, Ph.D. Dissertation, Michigan State University, 2001.
- [59] W.A. Reed and E. Fawcett, *Phys. Rev.* **136**, A422 (1964).
- [60] S.J. Jin T.H. Tiefel, M. McCormack, R.A. Fastnacht, R. Ramesh, L.H. Chen, *Science*, **264** 413 (1994).
- [61] A.P. Ramirez, *J. Phys: Cond. Matt.* **9**, 8171 (1997).
- [62] Abstracts FD-01, FD-02, and FD-05, 46th Annual Conf. On Magn. & Magn. Mat., Seattle, Wash., Nov. 12-16 (2001).
- [63] J.S. Moodera, L.R. Kinder, T.M. Wong, and R. Meservey, *Phys. Rev. Lett.* **74**, 3273 (1995).
- [64] See, e.g. www.motorola.com (Search MRAM); New York Times, Jan. 18, 2001, Pg. D6.
- [65] D.D. Awschalom and N. Samarth, *J. Magn. Magn Mater.* **200**, 130 (1999).
- [66] J.A. Gupta, X. Peng, A.P. Alivisatos, D.D. Awschalom, *Phys. Rev. B* **59**, R10421 (1999).
- [67] S.A. Wolf, D.D. Awschalom, R.A. Buhrman, J.M. Daughton, S. von Molnar, M.L. Roukes, A.Y. Chtchelkanova, and D.M. Treger, *Science* **294** 1488 (2001).
- [68] J. Bass, P.A. Schroeder, W. P. Pratt Jr., S.F. Lee, Q. Yang, P. Holody, L.L. Henry, and R. Loloee, *Mat. Sci. & Eng. B* **31**, 77 (1995).
- [69] Richard Magno and Joe H. Pifer, *Phys. Rev. B* **10**, 3727 (1974).
- [70] R.H. Silsbee, A. Janossy, and P. Monod, *Phys. Rev. B* **19**, 4382 (1979).
- [71] P. Monod and S. Schultz, *J. Phys. (Paris)* **43**, 393 (1982).
- [72] A. Fert, J.-L. Duvail, and T. Valet, *Phys. Rev. B* **52**, 6513 (1995).
- [73] W. Park, D.V. Baxter, S. Steenwyk, I. Moraru, W.P. Pratt Jr., and J. Bass, *Phys. Rev. B* **62**, 1178 (2000).

- [74] S.D. Steenwyk, S.Y. Hsu, R. Loloee, J. Bass, and W.P. Pratt, Jr., *J. Magn. Magn. Mater.* **170**, L1 (1997).
- [75] W.P. Pratt, Jr., Q. Yang, L.L. Henry, P. Holody, W.-C. Chiang, P.A. Schroeder, and J. Bass, *J. Appl. Phys.* **79**, 5811 (1996).
- [76] L. Piraux, S. Dubois, A. Fert, and L. Belliard, *Euro. Phys. J. B* **4**, 413 (1998).
- [77] A.C. Reilly, W.-C. Chiang, W. Park, S.Y. Hsu, R. Loloee, S. Steenwyk, W.P. Pratt Jr., and J. Bass, *IEEE Trans. Magn.* **34**, 933 (1998).
- [78] C. Vouille, A. Fert, A. Barthelemy, S.Y. Hsu, R. Loloee, and P.A. Schroeder, *J. Appl. Phys.* **81**, 4573 (1997).
- [79] C. Vouille, A. Barthelemy, F. Elokani Mpondo, A. Fert, P.A. Schroeder, S.Y. Hsu, A. Reilly, and R. Loloee, *Phys. Rev. B* **60**, 6710 (1999).
- [80] P.A. Schroeder, P. Holody, R. Loloee, C. Vouille, A. Barthelemy, A. Fert, and S.Y. Hsu, *J. Magn. Magn. Mater.* **177-181**, 1464 (1998).
- [81] W. Park, R. Loloee, J.A. Caballero, W.P. Pratt, Jr., P.A. Schroeder, and J. Bass, *J. Appl. Phys.* **85**, 4542 (1999).
- [82] A.C. Reilly, W. Park, R. Slater, B. Ouaglal, R. Loloee, W.P. Pratt Jr., and J. Bass, *J. Magn. Magn. Mat.* **195**, L269 (1999).
- [83] W.-C. Chiang, Q. Yang, W.P. Pratt, Jr., R. Loloee, and J. Bass, *J. Appl. Phys.* **81**, 4570 (1997).
- [84] D. Bozec, M.J. Walker, B.J. Hickey, M.A. Howson, and Nathan Wiser, *Phys. Rev. B* **60**, 3037 (1999).
- [85] J.Y. Gu, S.D. Steenwyk, A.C. Reilly, W. Park, R. Loloee, J. Bass, and W.P. Pratt Jr., *J. Appl. Phys.* **87**, 4831 (2000).
- [86] C. Heide, *Phys. Rev. Lett.* **87**, 197201 (2001).
- [87] S. Zhang, P.M. Levy, and A. Fert, *Phys. Rev. Lett.* **88**, 236601 (2002)
- [88] X. Waintal, E. Myers, P. Bouwer, and D. Ralph, *Phys. Rev. B* **62**, 12317 (2000).
- [89] D. Bozec, M.A. Howson, B.J. Hickey, S. Shatz, N. Wiser, E.Y. Tsymbal, and D.G. Pettifor, *Phys. Rev. Lett.* **85**, 1314 (2000).
- [90] L.J. van der Pauw, *Philips Research Reports*, **13**, 1 (1958).

- [91] J. Bass, in *Metals, Electronic Transport Phenomena*, edited by K.H. Hellwege and J.L. Olson, Landolt-Bornstein, New Series, Group 3, **Vol. 15**, (Springer-Verlag, Berlin, 1982).
- [92] J.J. Krebs, W. Vavra, G.A. Prinz, S.F. Cheng, and A. Fink, *J. Appl. Phys.* **79**, 6084 (1996).
- [93] A. Fert and S.F. Lee, *Phys. Rev. B* **53**, 6554 (1996).
- [94] K.M. Schep, J.B.A.N. van Hoof, P.J. Kelly, G.E.W. Bauer, and J.E. Inglesfield, *Phys. Rev. B* **56**, 10805 (1997).
- [95] K. Xia, P.J. Kelly, G.E.W. Bauer, I. Turek, J. Kudrnovsky, and V. Drchal, *Phys. Rev. B* **63**, 64407 (2001).
- [96] M.D. Stiles and D.R. Penn, *Phys. Rev. B* **61**, 3200 (2000).
- [97] W.H. Butler, X.-G. Zhang, and J. M. MacLaren, *J. Appl. Phys.* **87**, 5173 (2000).
- [98] A. Shpiro and P.M. Levy, *Phys. Rev. B* **63**, 14419 (2000).
- [99] Y. Tsymbal and D.G. Pettifor, *Solid State Physics* **56**, 113 (2001).
- [100] J.A. Borchers, J.A. Dura, J. Unguris, D. Tulchinsky, M.H. Kelley, C.F. Majkrzak, S.Y. Hsu, R. Loloee, W.P. Pratt Jr., and J. Bass, *Phys. Rev. Lett.* **82**, 2796 (1999).
- [101] C.F. Majkrzak, *Physica B* **221**, 342 (1996).
- [102] S.K. Sinha, in *Neutron Scattering in Materials Science II*, Eds. D.A. Neumann, T.P. Russell, and B.J. Wuensch, *MRS Symp. Proc.* **376**, p 175 (1995).
- [103] J.A. Borchers, J.A. Dura, C.F. Majkrzak, S.Y. Hsu, R. Loloee, W.P. Pratt, Jr., and J. Bass, *Physica B* **283**, 162 (2000).
- [104] J.A. Borchers, P.M. Gehring, R.W. Erwin, J.F. Ankner, C.F. Majkrzak, T.L. Hylton, K.R. Coffey, M.A. Parker, and J.K. Howard, *Phys. Rev. B* **54**, 9870 (1996).
- [105] K. Eid, D. Portner, R. Loloee, W.P. Pratt Jr, and J. Bass, *J. Magn. Magn. Mat.* **224** L205 (2001).
- [106] K. Eid, M. Tsoi, D. Portner, R. Loloee, W.P. Pratt Jr., and J. Bass, *J. Magn. Magn. Mat.* **240**, 171 (2002).
- [107] A.C. Reilly, W.-C. Chiang, W. Park, S.Y. Hsu, R. Loloee, J. Bass, and W.P. Pratt Jr., *IEEE Trans. Magn.* **34**, 939 (1998).

- [108] K. Eid, D. Portner, J. Borchers, R. Loloee, M. AlHaj Darwish, M. Tsoi, H.Kurt, K.V. O'Donovan, W.P. Pratt Jr., and J. Bass, *Phys. Rev. B* **65**, 054424 (2002).
- [109] G. Suran, F. Machizaud, and M. Naili, *Rhys. Rev. B* **47**, 15007 (1993).
- [110] R. Mohammed Idrus and P J Grundy, *J. Phys. D: Appl. Phys.* **19**, 1245 (1986).
- [111] K. Bouziane, J. Ben Youssef, M. El Harfaoui, O. Koshkina, H. Le Gall, J. M. Desvignes, M. El Yamani, and A. Fert, *J. Magn. Magn. Mat.* **165**, 284 (1997).
- [112] K. Bouziane, M. Mamor, and M. Maaza, *Solid State Communications* **107**, 107 (1998).
- [113] M. El Harfaoui, M. Faris, A. Qachaou, J. Ben Youssef, H. Le Gall, and D. Meziane. Mtalsi, *J. Magn. Magn. Mat.* **223**, 81 (2001).
- [114] S. Wang, J.I. Guzman, and M.H. Kryder, *J. Appl. Phys.* **67**, 5114 (1990).
- [115] E. Jedryka, M. Wojcik, S. Nadolski, T. Stobiecki, and M. Czapkiewicz, *J. Magn. Magn. Mat.* **156**, 38 (1996).
- [116] W.P. Pratt, Jr., S.D. Steenwyk, S.Y Hsu, W.-C. Chiang, A.C. Schaefer, R. Loloee, and J. Bass, *IEEE Trans. Mag.* **33**, 3305 (1997).
- [117] J. Bass, K. Eid, R. Loloee, and W. P. Pratt Jr., *Bull. Am. Phys. Soc.* **45**, 223 (2000).
- [118] L.L. Henry, Q. Yang, W.-C. Chiang, P. Holody, R. Loloee, W. P. Pratt, Jr., and J. Bass, *Phys. Rev. B* **54**, 12336 (1996).
- [119] M. Pinarbasi, S. Metin, H. Gill, and M. Parker, *J. Appl. Phys.* **87**, 5714 (2000).
- [120] J. Chen, S.N. Mao, J. Fernandez-de-Castro, T.S. Choy, and S. Hershfield, *IEEE Trans. Mag.* **36**, 2885 (2000).
- [121] K. Meguro, H. Hoshiya, K. Watanabe, Y. Hamakawa, M. Fuyama, H. Fukui, *IEEE Trans. Mag.* **35**, 2925 (1999).
- [122] A. Dinia and K Rahmouni, *Phys. Lett. A* **264**, 482 (2000).
- [123] K. Rahmouni, A. Dinia, D. Stoeffler, K. Ounadjela, H.A.M. Van den Berg, and H. Rakoto, *Phys. Rev. B* **59**, 9475 (1999).
- [124] K. Eid, R. Fonck, M. AlHaj Darwish, W.P. Pratt, Jr., and J. Bass, *J. Appl. Phys.* **91**, 8102 (2002).

- [125] M. Wojcik, E. Jedryka, S. Nadolski, D. Kubinski, M. Parsons, and H. Holloway, *Acta Physica Polonica A* **97**, 551 (2000).
- [126] W.J. Antel, Jr., F. Perjeru, and G.R. Harp, *Phys. Rev. Lett.* **83**, 1439 (1999).
- [127] B.Y. Wong, C. Mitsumata, S. Prakash, D.E. Laughlin, and T. Kobayashi, *J. Appl. Phys.* **79**, 7897 (1996).
- [128] F. Taddei, S. Sanvito, J.H. Jefferson, and C.J. Lambert, *Phys. Rev. Lett.* **82**, 4938 (1999).
- [129] F. Taddei, S. Sanvito, and C.J. Lambert, *Phys. Rev. B* **63**, 012404 (2001).